Biophysical and mechanistic impacts of small molecule and polyanionic aggregation modulators on tau4RD

Ellie I. James

A dissertation

submitted in partial fulfillment of the

requirements for the degree of

Doctor of Philosophy

University of Washington

2025

Reading Committee:

Abhinav Nath, Chair

Miklos Guttman

Kelly K. Lee

Program Authorized to Offer Degree:

Molecular Engineering and Sciences

University of Washington

Abstract

Biophysical and mechanistic impacts of small molecule and polyanionic aggregation modulators on tau4RD

Ellie I. James

Chair of the Supervisory Committee:

Abhinav Nath

Department of Medicinal Chemistry

Tau is an intrinsically disordered protein (IDP) that pathologically aggregates in Alzheimer's disease and over twenty other neurodegenerative diseases known as tauopathies. Unlike structured proteins that exhibit one (or several) folded conformations, IDPs populate dynamic and interchanging conformational ensembles. This makes IDPs difficult to study structurally and challenging as drug targets. During aggregation, tau's ensemble is perturbed so that the disordered monomers assemble into ordered cross-beta-sheet amyloid structures. Recent advances in cryo-EM have revealed that many of the amyloid fibrils generated in different tauopathies display disease-specific morphologies. These morphologies are reproducible through prion-like seeding both in vivo and in vitro. While these observations imply that tau has a tunable self-assembly landscape, the structural and kinetic mechanisms that control tau's amyloid morphology remain unclear. Further, there could be great therapeutic potential in targeting species early in tau's aggregation pathway; aggregation intermediates (i.e., mid-stage oligomers) are considered toxic in neurodegenerative disease. Here, we describe the discovery and characterization of tryptanthrin and its synthetic analogs as extremely potent tau inhibitors that target the earliest stages of aggregation. We follow this with a pulsed hydrogen-deuterium exchange mass spectrometry (HDX-MS) investigation into the origins of tau's amyloid heterogeneity and find evidence that distinct amyloid morphologies are encoded at the start of aggregation. Together, these findings address critical open questions regarding drug development for IDPs and the timeline of amyloid structural divergence.

Table of Contents

List of Figures

1. Introduction

1.1 Intrinsic disorder in biology

1.1.1 The structure-function paradigm

The protein structure-function paradigm has been a prominent framework in structural biology over the last half-century. This framework states that a protein's function arises from its structure and that a three-dimensional native structure is imperative for a protein to perform its function. Today, this model is known as the 'sequence-structure-function' paradigm and recognizes that the amino acid sequence of a protein determines its structure[1,2]. At first glance, intrinsically disordered proteins (IDPs) appear to break the structure-function paradigm central to structural biology. In contrast to structured proteins that display one or a small set of dominant tertiary structures, IDPs populate dynamic conformational ensembles in which the protein chains undergo frequent rearrangement on a nanosecond to millisecond timescale.[2] The difference in structural propensity between disordered and structured proteins arises from the amino acid sequence of the protein chain in question. While structured proteins are enriched in hydrophobic amino acids (e.g. valine, phenylalanine, tryptophan) that promote the formation of a buried hydrophobic core, IDP sequences are depleted of hydrophobic residues and enriched in hydrophilic (i.e. charged) amino acids.[2,3] The sequence pattern of charged residues imparts behavioral propensities important for determining IDP function (readers are directed to Ref. 3 for a comprehensive discussion of this topic).[3] Thus, instead of thinking of IDPs as an exception to the structure-function paradigm, it is more helpful to recognize that IDPs exhibit a sequence-ensemble-function relationship that is influenced by the environment.

1.1.2 IDPs function as environmental reporters

Recent estimates suggest that 30-40% of the proteome has at least one intrinsically disordered region (IDR) of 30 residues or more, highlighting that disorder itself may play a crucial role in protein function.[3] The protein disorder spectrum encompasses well-folded proteins with disordered connecting loops or termini and extends to entirely unfolded random coil-like ensembles (Fig. 1.1).[2,3]

IDR ensembles can be characterized by properties such as compaction (e.g., radius of gyration, end-to-end distance) or local transient structure (helicity) propensity. Without a stabilizing hydrophobic core, IDR/IDP ensembles sensitively respond to changes in their local environment with changes in chain expansion and compaction. For example, disturbances in pH can result in protonation (Asp, Glu, His) or deprotonation (Lys, Tyr, His) of amino acid side chains, which in turn change the charge patterning of the sequence and can result in charge repulsion or attraction. Depending upon the sequence distribution of charged amino acids in an IDP, changes in environmental ionic strength give rise to or relieve electrostatic

shielding. Weak, nonspecific interactions between macromolecular crowders depend on the size of the crowder and can cause chain expansion (small crowders) or compaction (large crowders). These and other changes in environmental factors can perturb an IDR's conformational ensemble and result in functional consequences that alter downstream cellular function.[3] Consequently, IDPs/IDRs can quickly sense and respond to changes in cellular physiology or adapt to changes in cytoskeletal architecture. In contrast to structured proteins, IDPs can conformationally rearrange to interact with multiple binding partners, allowing a single IDP to serve as a cell signaling 'hub.'

1.1.3 Cellular function via molecular recognition and binding

Returning to the structure-function framework, the canonical model for molecular recognition (i.e., non-covalent interaction between different molecules) is one in which there is both chemical and structural complementarity. For structured proteins, this model works well to explain the selectivity with which a protein can bind to a specific biomolecule. As an extreme example, the non-covalent interaction between the protein streptavidin and its ligand, biotin, is one of the strongest in nature with a dissociation constant (K_D) of approximately 10^{-14} mol/L.[4] The strength of this interaction arises from the shape complementarity between the two molecules and the extensive network of hydrogen bonds that form between biotin and the streptavidin binding site. While this molecular recognition model works well to describe binding between structured proteins, it insufficiently describes the recognition between IDRs/IDPs and their binding partners (e.g., lipids, biopolymers, proteins), where one or both may exist as disordered ensembles in the "binding" interaction.

IDRs exhibit three main binding mechanisms: coupled binding and folding, fuzzy binding, and fully disordered complexation (Fig. 1.1).[3] The coupled binding and folding mechanism most closely aligns with the structured molecular recognition model and describes the process in which a disordered region folds to allow shape and chemical complementarity within the bound complex. This binding can involve various partners, including IDRs with other IDRs, structured proteins, or nucleic acids.[2] For example, the N-terminal IDR of p53 autoinhibits p53 transactivation in its disordered state but forms helices upon binding p53 regulatory proteins.[2,5,6] Fuzzy binding depends on the environmental context and binding partner in question and can lead to different bound ensembles that display various levels of heterogeneity. Of note for this work, fuzzy binding can be further subclassified due to the presence of static or dynamic disorder; the formation of amyloid fibrils from IDPs provides an example of static disorder in which one IDP forms conformationally distinct fibrils that do not interconvert. Finally, some IDRs/IDPs bind as fully disordered complexes, as is the case with the histone chaperone prothymosin alpha and the linker histone H1.0.[2] These proteins are strongly and oppositely charged, resulting in electrostatically driven binding that is sensitive to

changes in ionic strength. Although defining distinct binding modes is useful for conceptualization, the binding mechanisms of IDR to partners exist as a continuum, as illustrated by the "quasi-ordered" mechanism suggested by Clouser *et al.* that falls between the fuzzy binding and coupled folding and binding regimes.[7]

In addition to associating with other proteins, IDPs can bind numerous species including biopolymers, lipids, and metals. Extensive work within the last decade has highlighted that IDPs exhibit both functional (e.g., liquid-liquid phase separation - LLPS,[8] membrane poration[9]) and pathological self-association[10]. Self-association causes a concurrent decrease in disorder, resulting in diminished interconversion of IDP conformers and, sometimes, in the formation of pathological protein aggregates. IDP dysfunction is associated with diseases such as cancer (p53), diabetes (hiAPP), and Alzheimer's Disease (AD, amyloid-beta and microtubule-associated protein tau), the latter of which will be discussed in section 1.2.1.

1.1.4 Regulation through post-translational modification

The proteome is rich with post-translational modifications (PTMs) that impart chemical and structural diversity beyond that conferred by amino acid sidechains. PTM usually involves the enzymatic addition of a chemical functional group, such as phosphoryl, alkyl, glycosyl, or acyl groups, or the conjugation of a small protein, like ubiquitin or SUMO, to an amino acid sidechain.[11] IDPs exhibit a high rate of PTM and can have multiple copies of a single PTM or a combination of multiple different PTMs distributed along the protein sequence. The identity and distribution of PTMs result in altered conformational ensembles, which in turn modulate the interactions of IDPs with their binding partners and other cellular components. Regulation of IDPs by PTMs occurs by altering an IDP's chemistry (e.g., electrostatics), changing the IDP's propensity toward secondary structural elements, or by altering long-range tertiary contacts within the IDP or between the IDP and interaction partners.[11]

Phosphorylation is one of the most common PTMs, occurring in at least 30% of eukaryotic proteins and most often within IDRs. During phosphorylation, a neutral hydroxyl (OH) group is replaced with a doubly negative tetrahedral phosphoryl group (PO_4^{2-}). This results in large changes in the steric, electrostatic, and chemical properties of the sidechain that are partially recapitulated by phosphomimetic amino acid mutations to Asp or Glu. The introduction of a phosphoryl moiety often increases intra- and intermolecular electrostatic interactions through salt bridges or interactions with helix dipoles. In the case of microtubule-associated protein tau (MAPT, tau), hyperphosphorylation neutralizes tau's inherently positive charge, which destabilizes tau-microtubule binding and may promote tau's self-association.[12]

1.2 Tau biology and dysfunction

Tau is expressed at high levels (1-10 μM) in neurons and at low levels in glial cells.[13,14] Physiologically, tau plays a role in stabilizing microtubules and regulating their dynamic reconfiguration by weakly binding to tubulin dimers in addition to regulating axonic outgrowth in neurons. Tau is also purportedly involved in the insulin signaling pathway[15], iron homeostasis[16,17], and processes such as long-term synaptic signaling depression.[18,19] Studies of tau's interactome reveal interactions between tau and RNA, RNA-binding proteins, and species such as metal ions, other anionic biopolymers, and anionic lipids.[20,21] As mentioned previously, many of tau's interactions with other molecules are influenced by PTMs, and it has been shown that phosphorylation patterns differ between healthy patients and those with neurodegenerative diseases.

Tau is composed of 4 domains: the N-terminal projection domain, the proline-rich region, the microtubule-binding region (MTBR), and the C-terminal domain (Fig. 1.2). Alternative splicing of the *MAPT* gene results in six tau isoforms in the human central nervous system. The isoforms contain 0, 1, or 2 N-terminal inserts due to alternative splicing at exons 2 and 3 and contain 3 or 4 repeats in the MTBR due to the inclusion or exclusion of exon 10. The splice variants are known by the number of N-terminal inserts and MTBRs present; as such, 2N4R is the longest isoform at 441 amino acids and 0N3R is the shortest at 352 amino acids.[22] The expression and distribution of 3R and 4R tau isoforms are similar throughout healthy brains but this ratio is perturbed during disease.[20,23]

1.2.1 Tauopathies

To date, more than 26 tauopathies have been identified which are characterized as 3R (e.g., Pick's disease), 4R (e.g., Corticobasal degradation), or 3R/4R (e.g., AD) because of the predominant tau isoform(s) found in amyloid deposits.[20,23–25] Tau diseases are further classified into primary and secondary tauopathies based on whether tau's aggregation is a major constituent of pathology or thought to be a response to other pathological disruptions (e.g., amyloid-beta aggregation during AD).[12,20] There are several disease-associated mutations in the *MAPT* gene such as P301L/P301S or ΔK280. P301L is the most common MAPT mutation, but all three mutations are involved in frontotemporal dementia (FTD).[25] Although mutations in the *MAPT* gene are not linked to pathology in AD, mutations in genes such as *APOE*, *APP*, and *PSEN1/2* increase the risk of AD due to increased tau accumulation and changes in tau phosphorylation.[25] The fact that tau mutations are sufficient to induce neurodegenerative disease highlights the importance of tau in neuronal homeostasis.

Tauopathies present clinically as movement disorders, cognitive/behavioral or language disorders, dementia, or a mixed profile. Patients with movement disorders such as Progressive Supranuclear Palsy syndromes (PSPs) may exhibit postural instability, tremors, rigidity, gait freezing, bradykinesia (movement

slowing), or cerebellar ataxia (sudden loss of muscle coordination).[23] Some forms of PSP exhibit mixed clinical phenotypes, such as those observed in PSP-F, in which patients display disinhibition and apathy, PSP-RS in which patients develop mild dementia, and PSP-SL, in which patients exhibit labored speech and impaired grammar while maintaining comprehension. Like PSPs, FTD has several subclassifications that may or may not include parkinsonism. Chronic traumatic encephalopathy induces cognitive, motor, and psychiatric changes such as depression and suicidality.[26] AD, the most common and well-known tauopathy, results in amnesia, language deficits, and impaired executive function.[23]

Provisional diagnoses are given for these conditions because confirmatory examination of tau amyloid pathology can only be done post-mortem. Imaging techniques such as PET scan, MRI, and fMRI give clinicians the ability to detect pathological tau and its localization in the brain ante-mortem.[27–29] The distribution of pathological tau is often used to describe disease progression because the infiltration of tau pathology into a new brain region brings with it a further disruption of brain tissues and, therefore, further symptom development.

1.2.2 Amyloid formation and incomplete mitigation by molecular chaperones

A common feature of neurodegenerative diseases is the formation of amyloid fibrils. Amyloid aggregates are long fibrillar structures with a core of repeating beta-sheet units. Amyloid fibrils are held together by extensive hydrogen bonding networks and side-chain interactions between protein subunits. Amyloid aggregation follows a defined pathway in which soluble monomeric protein (IDPs, in this case) undergoes a change that results in an aggregation-competent activated monomer. These proteins then serve to template others, forming on-pathway oligomers. Further addition of monomers to oligomers leads to the formation of insoluble amyloid fibrils. Toxicity in some amyloid diseases arises from the extracellular deposition of amyloid fibrils (e.g., cardiac amyloid in transthyretin amyloidosis), but toxicity observed in neurodegenerative diseases more commonly arises from soluble oligomers.[30–34] The onset of neurodegenerative disease symptoms does not occur until early middle age or later, implying the presence of an innate mitigation system that prevents or slows amyloid formation. For example, several chaperones are known to interact with tau, and recent work has revealed different aggregation-delaying mechanisms exhibited by the molecular chaperones HspB1 and Hsc70.[35,36]

1.2.3 Prion-like seeding

Although chaperones might delay the onset of tau aggregation, there is evidence that tau pathology can spread from cell to cell in a prion-like manner. This behavior was first observed in cells that expressed fluorescently tagged tau, which localized into puncta after addition of tau amyloid fibrils to the cell media.[37]

Since then, the development of biosensor cell lines has facilitated the exploration and quantification of intracellular tau aggregation from unique 'seeds.'[38] Seeds, small pieces of amyloid fibril, propagate their own morphology by structurally templating the aggregation of monomeric tau. This behavior extends beyond *in vitro* studies; injection of well-characterized seeds into the brain of model mice expressing 1N4R-P301S tau resulted in the fidelitous transmission of seed morphology to progeny.[39] While the mechanism(s) behind the transcellular spread of pathological tau remains under investigation, these studies laid the foundation for determining the origins of amyloid heterogeneity.

1.2.4 Tau amyloid morphologies in vivo and in vitro

Pathological amyloid deposits are a hallmark of tauopathies. Although aggregation follows a similar pathway (i.e., disordered monomer to structured fibril) in each of these diseases, many of the resulting fibril morphologies are distinct, disease-specific, and reproducible through seeding. Some diseases exhibit multiple fibril types while others only display one predominant conformation. Fitzpatrick and Falcon provided unprecedented insight by cryo-EM into the unique morphologies tau fibrils exhibit in AD and Pick's disease.[40,41] Since then, there have been several attempts to structurally classify tau amyloid morphologies based on the identity and arrangement of tau domains in the fibril core (Fig. 1.10).[42–44]

Recently, Lövestam *et al.* have described and validated the generation of disease-relevant fibrils from recombinant tau,[45] while others have focused on the characterization of attributes unique to certain tau aggregation reactions.[46–48] Tau's *in vitro* aggregation often requires hyperphosphorylation or the addition of a polyanionic cofactor to overcome the electrostatic repulsion between the many lysine residues in tau's MTBR. These polyanions, called aggregation inducers, include RNA, polyphosphate, and the well-studied heparin. Comparisons of inducer-aggregated tau showed that the morphology of these fibrils is polymorphic, different than any morphology observed *in vivo*, and inducer-dependent.[46,47] This behavior also extends to seeding *in vitro*, which together offer the opportunity to explore the origins of and barriers to structural templating.

1.3 Structural studies of IDPs

1.3.1 Traditional solution-based techniques

Despite the inordinate amount of research that has been put toward tauopathies (AD in particular), the structural changes that occur *during* amyloid formation have not been described in detail. Notably, these intermediate species are thought to be responsible for toxicity in neurodegenerative diseases, so advancing our understanding of their structure and behavior is critical. A structural understanding of tau's aggregation intermediates could lead to disease-specific diagnostics and therapeutics aimed at preventing

neurodegeneration as opposed to responding to impairments it causes. The dearth of information surrounding amyloid intermediates is in large part due to the experimental difficulty associated with studying IDPs. While cryo-EM offers revolutionary high-resolution structural insight for structured proteins and end-stage amyloid fibrils, the technique is not suitable for studying dynamic species such as IDP ensembles or oligomers.

Despite the advantages of the techniques mentioned above in isolation and in concert, all have limitations. NMR studies are limited to proteins or complexes of ~100 kDa or less (e.g., tau 2N4R dimers) and are performed at protein concentrations an order of magnitude higher, or more, than in biology. While FRET and FCS are not limited by protein size and can be performed at physiologically relevant concentrations, both are constrained by the addition of an exogenous fluorophore that can perturb the conformational ensemble. To circumvent these limitations, mass spectrometry-based approaches are gaining popularity.

1.3.2 Hydrogen-deuterium exchange with mass spectrometry (HDX-MS)

Portions of this text have been reproduced from:
† James EI, Murphree TA, Vorauer C, Engen JR, Guttman M. Advances in Hydrogen/Deuterium Exchange Mass Spectrometry and the Pursuit of Challenging Biological Systems. Chem Rev. 2022 Apr 27;122(8):7562-7623. doi: 10.1021/acs.chemrev.1c00279. Epub 2021 Sep 7.

HDX-MS relies on the exchange of protein backbone amide protons for solvent deuterons. The reaction is allowed to proceed for predetermined amounts of time, after which HDX is quenched by acidifying the reaction to pH 2.5. The exchange of hydrogen for deuterium causes increased mass which can be localized to a particular amide bond through various fragmentation methods. Bottom-up HDX-MS, in which an intact protein is proteolyzed after HDX but prior to ionization, is the most common fragmentation strategy but is limited by the promiscuous cleavage specificity of acid-active proteases. Top-down HDX-MS circumvents this problem by utilizing gas-phase chemical reactions to fragment proteins with high spatial resolution and without the caveats of enzymatic cleavage. Middle-down HDX-MS experiments combine proteolysis and post-ionization top-down chemical reactions.

1.3.2.1 Global and top-down HDX-MS†

From the early years of HDX-MS, deuterium exchange kinetics have also been monitored on an intact protein level.[49–51] While this does not provide local information throughout the protein sequence, it does

offer a way to monitor the sum-total exchange of all amides on a global level. This approach has proven useful for a variety of applications over the years, including detecting conformational changes in different protein states, quantifying ligand-binding affinities, and enabling high throughput ligand binding screening for target proteins.[52–57] Global HDX-MS also has an inherent advantage of being well-suited for detecting subpopulations of conformers and tracking slow correlated protein conformational changes (EX1 kinetics) [reviewed in Ref. 58]. This later approach was used recently to track how detergents and ligand binding influence the global conformational profiles of membrane proteins.[59]

An emerging approach in proteomics has been the application of a top-down strategy for characterizing proteins.[60] The intact proteins are ionized and activated to generate a large series of fragment ions to track the sequence and map post-translational modifications throughout the sequence. An inherent advantage of examining the intact protein directly is the ability to resolve various populations resulting from different combinations of PTMs across the protein ("proteoforms") that would otherwise all be pooled together with a typical bottom-up approach (see Fig. 1.4 for an example). The advent of fragmentation techniques like ECD and ETD that have circumvented the issues of deuterium scrambling have paved the way for a top-down approach to enable high spatial resolution HDX-MS analysis from an intact protein analyte.[61,62] The mass shifts of all the *c* and *z* ions in the MS/MS spectra are used to calculate deuterium incorporation throughout the sequence (Fig. 1.3).

A major advantage of top-down analysis is the ability to mass-select different conformers within a sample of a protein based on global deuterium uptake. The mass-resolved conformers can then be individually characterized by their deuterium exchange profiles from all the fragment ions.[63,64] A similar mass-resolved top-down approach was used to study how different phosphorylation states influenced the conformational dynamics of calmodulin.[65] With four known phosphorylation sites, there are 16 possible phosphorylated calmodulin proteoforms. Using top-down fragmentation, it was found that only six of these potential species exist in vitro and that phosphorylation of these sites occurs in a sequential manner. Using a top-down HDX-MS approach, they discovered that structural differences only arise in the tetra-phosphorylated calmodulin, directly identifying how the degree and sites of phosphorylation affect conformational dynamics, which would not have been possible to resolve with a bottom-up approach (Fig. 1.4). Integration of capillary electrophoresis has proven a highly complementary tool when combined with HDX-MS.[66] Capillary electrophoresis (CE) under native conditions is used to resolve different conformers, which are then structurally characterized by top-down HDX-MS using ETD. The ability to both resolve and characterize conformationally distinct subpopulations through multiple means is a powerful increase for the comprehensive characterization of biopharmaceutical proteins.[67]

The frequent challenge with top-down studies is low sensitivity, which often necessitates collecting and averaging spectra over longer periods, which can be up to several minutes depending on the signal quality. To enable long collection times, several approaches have opted to use volatile buffers and directly analyze the quenched sample by mass spectrometry, thereby alleviating the need for a desalting or LC step. However, this imposes a restriction on which buffers can be incorporated for the protein labeling step, as most nonvolatile salts at even low mM levels can be problematic for MS analysis. Another complication with bypassing a desalting step is the inability to use high concentrations of reducing agents to reduce disulfide bonds, which present a barrier for effective ECD/ETD fragmentation. To this end, Wang et al. demonstrated using β2-microglobulin that even low concentrations of TCEP (5 mM) could be included in the infused protein sample to effectively reduce disulfide bonds while still being able to observe protein signal in the MS.[68] Another downside to not using a desalting step is that deuterium incorporated into side chain positions will not be washed away, meaning there can be variable numbers of deuterium on different residues according to the number of exchangeable positions at the side chains. Such data can be complex to analyze, whereas a short desalting step washes away deuterium in the side chains, leaving only exchanged deuterium at backbone amide positions, thereby simplifying data interpretation.

Whether or not a desalting step is used, minimizing back-exchange is critical for any top-down HDX-MS study. Deuterium loss during the MS acquisition will result in a mass shift that, when averaged, can artificially broaden the isotopic distribution and greatly complicate deuterium uptake calculations. To this end, several groups have adopted subzero cooling systems for top-down HDX-MS analysis that are capable of sufficiently reducing back-exchange to allow for collection of data for several minutes with stable deuterium levels.[69,70]

The spatial resolution obtainable with top-down analysis is determined by the number of fragment ions that are observed in the MS/MS spectra. Efficient fragmentation becomes increasingly challenging for larger proteins. To expand both sequence coverage and spatial resolution, bottom-up and top-down HDX-MS analyses can be combined.[71,72] A “middle-down” approach has also been used in proteomics to obtain better sequence coverage. Unlike a bottom-up approach, very highly specific proteases are used to predominantly generate large peptides, which are then typically analyzed by ETD/ECD.[73] For HDX-MS, all available proteases are relatively nonspecific, making it nearly impossible to achieve efficient proteolysis at only a limited set of sites on the protein. Pan et al. developed a middle-down HDX-MS approach to maximize coverage for Herceptin.[74] Limited pepsin digestion was achieved by not reducing disulfide bonds until after the digestion step to minimize the number of accessible cleavage sites. Pepsin was inhibited in the subsequent disulfide reduction step by the addition of pepstatin and produced three large fragments that could be well-resolved and produce a rich set of fragment ions (Fig. 1.5). The combination of top-down

and middle-down analysis yielded a coverage for the heavy chain of 95%, where with top-down alone it was only 50%.[70] Other proteases with more limited substrate specificity may offer another way to obtain limited fragmentation for middle-down HDX-MS analysis[75] (see section 2.3.1 of Ref. 76).

1.3.2.2 Theoretical considerations (for HDX-MS of IDPs)†

Of the available structural characterization techniques, HDX-MS is particularly well-suited to the study of IDPs because it can detect and resolve changes in protection resulting from weak or transient hydrogen bonding without perturbing the IDP structural ensemble.[76,77] Although HDX-MS experiments can offer valuable insight into IDPs, the detection of transient hydrogen bonding remains challenging. Very short time points (milliseconds) are often required to access relevant amide exchange kinetics for IDPs, a significant departure from the seconds–hours long time points used for typical HDX-MS samples. Furthermore, quantifying the level of transient hydrogen bonding in IDPs and IDRs requires an accurate intrinsic exchange rate (k_{ch}) for the fully unstructured state for comparison. In the case of IDPs, it is challenging to accurately create and measure the exchange of a truly unstructured reference.[77] The k_{ch} estimates are commonly calculated from values obtained from extensive NMR studies of unprotected amides. In this method, the intrinsic exchange rate for a particular amide is predicted by accounting for its position in the sequence and all relevant solution conditions.[78,79] Despite the sophisticated calculations established for accurately predicting k_{ch}, some studies have noted instances where the measured exchange rate of IDPs and IDRs is faster than the prediction (Fig. 1.6 A,B).[80–84] These findings have led to updates in the tools used for predictions of k_{ch} for proteins as outlined recently by Nguyen et al.[85] Walters introduced a similar empirical approach for accurately calculating local energetic differences in comparative HDX-MS studies without the need for estimated exchange rates.[86]

In an effort to alleviate possible mispredictions in k_{ch}, Al-Naqshabandi and Weis[84] developed a different approach to quantify the level of transient structure in IDPs. The authors introduce a strategy for empirically determining intrinsic exchange rates of IDPs using predigested peptides from the proteins of interest as references. By measuring protection in both the full protein and the peptides from the predigested protein, it is possible to directly calculate the protection ratio within each region independent of theoretical predictions. Although this value resembles a protection factor, the authors caution that thermodynamic interpretations applicable to protection factors may not hold in the case of protection ratios. The authors demonstrate the efficacy of this approach on the fully disordered ACTR and the molten globule CBP, finding that some predigested peptides exchange on a faster time scale than the experimental peptides (Fig. 1.6 C,D).

1.3.2.3 Methods for IDPs†

With IDRs and IDPs, at physiological conditions, amide exchange happens on the millisecond time scale.[79,80,87–89] Perturbing the experimental conditions by lowering the pH or temperature to slow the k_{ch} offers a way to probe the fast kinetics in both structured and unstructured proteins[89] but will likely reduce the physiological relevance of the study. The millisecond exchange time scale of IDPs and the desire to remain near physiologically relevant conditions has prompted the use of millisecond HDX. Traditional quench-flow systems are well-suited for tracking fast dynamics in proteins and have been employed for probing fast time scales for HDX-MS with high precision.[90–94] Simpler rapid mixing systems have also been described which are capable of probing time scales relevant to many disordered regions.[80] Deuterium exposure time in quench-flow or rapid mixing devices is varied by changing either the flow rate or the length of the deuteration loop between the D_2O/protein mixing stage and the introduction of quench in a second mixing chamber. Offline quench-flow HDX-MS sample preparation does not directly interface with the mass spectrometer; samples may be prepared and stored at −80 °C for later analysis. Keppel et al. made use of such an apparatus in their work on EGFR and HER3 to access time points from 108 ms to 2.033 s.[95] The authors also performed manual HDX-MS to extend their observations from 5 s to 2 h, showing the utility of this method for bridging time scales relevant to IDP exchange kinetics. More recently, chip-based rapid mixing devices have been fabricated using thiol–ene photochemistry that offer a convenient approach for rapid mixing and quenching with a time scale of 140 ms to 1.1 s.[96] Related to rapid mixing devices, automated sample handling systems have employed mixing strategies to also sample down the time ranges approaching 100 ms, adding another approach for probing fast time scales[97] (see automation section of Ref. 76).

A strategy that uses nested capillaries was also shown to be effective for monitoring exchange on very short labeling times. Time-resolved electrospray ionization (TRESI)-HDX, developed by Wilson and Konnerman in 2003,[98] consists of a nested capillary mixing system connected to a variable volume reaction chamber. The effluent from the reaction chamber is quenched and sprays directly into the mass spectrometer ESI source (i.e., an online method). This setup allows investigation of time scales ranging from 42 ms to 8 s, making it a powerful tool to resolve fast kinetics. More recent implementations have incorporated a pepsin digestion chamber to enable bottom-up analyses.[99] The main downside to spraying the quenched sample directly into the mass spectrometer is the potential for nonvolatile buffer components to interfere with MS analysis (see section 2.7 of Ref. 76). TRESI-HDX has recently been utilized to resolve fast kinetics on native and phospho-tau[100] and investigate the amyloidogenic shift attributed to tau phosphorylation.[101] These studies were able to detect increased exposure of the hexapeptide two region in phospho-tau, a key region for pathological tau aggregation.

1.3.2.4 Localizing disorder in proteins†

One of the most straightforward applications of HDX-MS is the ability to readily identify disordered regions within proteins. This approach continues to be utilized to pinpoint disordered regions in isolated proteins[95,102–105] and viral accessory proteins.[106,107] HDX-MS was also able to identify Ana2 as an IDP[108] and to confirm contraction is disordered in solution and thereby resolve a long-standing debate in the field.[109] Killoran et al.[110] used HDX-MS to assess the structure and dynamics of Cby, a wnt-signaling antagonist that had evaded previous structural characterization due to line broadening observed in NMR studies. In this case, the results allowed the authors to locate the boundaries of the Cby coiled-coil domain and to elucidate the role of the C-terminal disordered region in Cby solubility. HDX has also been effective for probing dynamics in large macromolecular complexes.[111–115] In many cases, HDX-MS was used in combination with other biophysical and biochemical characterization techniques to determine complex stoichiometry and the overall molecular architecture. HDX has also become an important tool for the structural characterization of aggregation prone IDPs such as α-synuclein[116] and antithrombin,[117] to investigate the structural effects of PTMs known to increase aggregation,[100,101] and to probe the influence of other protein domains on the aggregation properties.[118]

Identification of specific disordered segments has greatly aided efforts for full structural determination of proteins. Pantazatos et al.[119] demonstrated the application of HDX-MS to localize disordered regions of proteins to guide re-engineered protein constructs to enhance crystallography. This proof-of-concept work on 24 proteins from *Thermotoga maritima* demonstrated that some disorder-depleted proteins can maintain the integrity of their folded domains and thereby be amenable for crystallography studies. While this strategy does not work for all proteins, Fowler et al. recently showed the applicability of this technique in the identification and deletion of disordered regions of P14KIIIβ to create a construct amenable for crystallography.[120] They further demonstrated the role of HDX-MS in crystallography by comparing the dynamics of the wild-type P14KIIIβ and its disorder-depleted form, showing that the deuterium uptake for the remaining regions is unaffected, implying that the dynamics of the entire protein were not disturbed by the deletions.

HDX-MS has also been useful for resolving how residual structure of IDPs and IDRs are integral to their function and probe the influence of disordered regions on the other folded domains of the protein. Trabjerg et al.[121] investigated the opposing biological activity of dimerized proNGF and dimerized NGF by HDX-MS and found that the pro- region of proNGF is unstructured and, interestingly, protects mature (folded) regions of proNGF from exchange. In a similar investigation of the impact an unstructured region can exert on a structured region, Clouser et al. found that the N-terminal disordered region of HSPB1

dimerizes and binds to a single groove in multiple orientation-specific conformations.[7] Mutations in noncontiguous regions of the disordered domain influence the deuterium uptake observed elsewhere on HSPB1. Mysling et al.[122] observed that the N-terminal disordered region of GPIHBP1 functions to promote an encounter complex that results in tighter binding between the folded domain of GPIHBP1 and the LPL homodimer. On a similar theme, Saikusa et al.[123] used HDX-MS to study how histones H2A and H2B exhibit differences in dynamics between their wild type and disorder-depleted forms. The authors caution that deletion mutants should be characterized by HDX-MS to determine if deletion influences global protein structure or dynamics.

An array of recent studies has also shown that IDPs can be highly perturbed by mutations[124,125] and post-translational modifications, particularly phosphorylation.[126–129] IDPs generally exhibit disorder-to-order transitions upon binding,[130] however, Kacirova et al. noted that phosducin actually did not show ordering upon binding its regulatory partner 14–3–3 protein.[131] Papanastasiou et al. used similar methods to observe the difference between complement protein iC3b and its mature form C3b, finding that removing the immature portion of iC3b leads to a disorder-to-order transition, resulting in a structured CUB domain only observed in the mature C3b protein.[132] Other HDX-MS studies of IDPs have disorder-to-order transitions upon binding ligands such a metals,[133] small molecules,[57,134] and lipid membranes.[135]

Hamdi et al. exemplified the investigation of disorder-to-order transitions in IDPs in their study of ripening proteins HvASR1 (barley) and TtASR1 (wheat).[136] With a combination of Stoke's radius, SAXS, CD, and HDX-MS, the authors found that the addition of glycerol, zinc, and TFE can increase order within the proteins. By HDX, the authors determined that the addition of TFE alone does not affect HDX, but either zinc alone or TFE and zinc together induce global reductions in HDX due to increased structure formation (Fig. 1.7). The authors localized the area affected by the addition of TFE and zinc as residues 105–115 in HvASR1 and 104–113 in TtASR1, identifying these regions as bona fide molecular recognition elements and highlighting the applicability of HDX-MS for resolving factors that affect protein folding.

HDX-MS is well-suited for tracking ordering associated with complex formation. Ramirez et al. characterized a molten globule unfolding intermediate of the obligate homodimer phosphofructokinase-2, which exhibits strong coupling between dissociation and unfolding.[137] In a similar study, Dembinski et al. monitored the folding state of IκBα in a ternary complex with NFκB and found that IκBα begins to fold during the release of DNA. The authors resolved that two regions of IκBα remain partially unfolded in the ternary complex, which helps to explain line broadening observed in NMR experiments of the ternary complex.[138] De Vera et al. examined another DNA binding complex composed of SRC-2 and the PPARγ/RXRα heterodimer and concluded that ligand and DNA cooperatively recruit the SRC-2 interaction domain to the heterodimer.[139] Other groups have employed HDX to monitor domain-swapping of proteins

such as FoxP, which functions as a domain-swapped dimer. Medina et al. found that there are several intermediate domain-swapped states of FoxP that vary in the degree of disorder they exhibit.[140]

IDPs behave distinctly from structured proteins, and understanding their response to the cellular environment (e.g., crowding) is necessary to understand their biochemistry. Rusinga and Weis characterized the effects of molecular crowders on the IDP ATCR to interpret structural changes, which could previously not be sufficiently explained by volume exclusion theory.[141] Using predeuterated Ficoll as a crowding agent, they found that IDPs display complex behaviors in crowded environments that depend on the structure and concentration of the crowder. The concentration-dependent effects on secondary structure by crowded environments may play a functional role in modulating IDP activity.

1.3.2.5 Pulsed labeling HDX-MS and protein folding studies†

The HDX-MS described so far has been primarily continuous-labeling experiments in which the protein is exposed to D_2O while structural fluctuations occur. Deuteration levels in continuously labeled proteins integrate the number of molecules that behave dynamically during the labeling period, which can range from milliseconds to days. In contrast, in pulsed-labeling experiments, the duration of D_2O exposure is fixed and short compared to the time scale of structural changes. Short pulses of labeling can deuterate primarily unfolded regions, and this strategy has been shown to be applicable to all manner of unfolded proteins, including polypeptides that are in the process of conversion to/from the native structure through protein folding/unfolding as well as intrinsically disordered proteins (IDPs) (discussed in previous sections). Pulsed-labeling provides structural snapshots that can reveal the fraction of each region of the protein that is folded at different stages in the folding process and reveal intermediate folding states (Fig. 1.8).[50,92–94,142–144] In a recent review on the folding of apomyoglobin, Nishimura highlights the power of HDX in combination with NMR to probe these intermediate folding states.[145] Recent folding studies have detected a foldon pathway in cytochrome c consisting of units that exhibit the same energetic steps in both the forward and reverse reactions.[146]

Other groups have employed pulsed HDX experiments to identify interaction sites between protein subunits or binding partners. Many of the original intact-level protein folding studies were performed with pulsed labeling.[50,51,143] Short labeling times were shown to be more appropriate for revealing changes associated with protein interfaces.[91,147] In more recent years, pulsed HDX methods have been used to study the interfaces within potassium channels[148] and the interactions with lipoprotein lipase.[122,149] Dornan et al.[115] combine pulsed and continuous HDX experiments with electron microscopy to characterize the heterotrimeric PIKIIIα/TTC7B/FAM126A complex. By pulsed HDX, the authors determine the extent of

secondary structure throughout the protein complex, finding that regions unobserved in the EM structure appear dynamic by HDX.[115]

Benhaim et al.[150] used a pulsed HDX approach to monitor complex structural changes during the fusion activation of influenza hemagglutinin (HA) on the surface of intact infectious virions. Sequential local conformational changes in HA were tracked after activation to reveal two on-pathway intermediates during HA activation. The previous understanding of activation had been based on studies of the isolated soluble ectodomain of HA, and the study revealed how activation of the soluble HA ectodomain was distinct from that of the intact protein on the surface of the virion.

Pulsed HDX can provide critical structural information on the process of protein aggregation. Wang et al.[151] monitored the oligomerization and accompanying structural changes in CsgE, which is thought to act as a chaperone-like subunit active during amyloid formation of the curli protein. They found evidence of at least three intermediate oligomerization states and observed a large structural rearrangement upon CsgE oligomerization. In a study on CsgA, the major component of curli protein, Wang et al. deciphered the effects of deamidation of CsgA on aggregation.[152] Sabareesan and Udgaonkar[153] tracked the aggregation of the wild-type prion protein (PrP) to the N-terminal region of the protein, consistent with positions of mutations known to increase aggregation. Finally, Renawala et al.[154] studied calcitonin, an aggregation-prone therapeutic peptide hormone, to determine the effects of disulfide reduction on its aggregation kinetics. Interestingly, they found that reduced calcitonin aggregation involves different residues than wild-type (Fig. 1.9), demonstrating the utility of pulsed HDX approaches to therapeutic protein development.

Beyond providing structural and kinetic insight, pulse labeling has also been useful for characterization of protein ligand binding properties. By varying ligand concentration, it is possible to extract binding affinities[155,156] and assess the effects of numerous ligands on protein stability.[157,158] These approaches have paved the way to high throughput studies to identify inhibitors against therapeutic protein targets.[159]

Several methodological and data processing advances in pulsed HDX have been introduced in recent years. Pansca et al. mined existing pulsed HDX data from rapid folding experiments and found a correlation between the backbone rigidity of a sequence and early protection from HDX during folding.[160] Raimondi et al., introduced EFoldMine, an early folding prediction tool built on similar pulsed HDX-NMR data of early folding states.[161] The authors validated the EFoldMine predictions with pulsed HDX-MS experiments. On the experimental side, Makepeace et al. demonstrate that a 2.5 s deuterium pulse in the ligand bound and unbound states followed by intact protein MS can be used to estimate the number of exchange-competent amides in each state.[57] Finally, Tsirigotaki et al. described a pulsed HDX approach to study the non-native and disordered translocation-competent states of secretory proteins to identify short, structured regions.[162]

1.4 Drug discovery: tau as an example of disordered pharmacological targets

Historically, pharmacological interventions have focused on proteins that are integrally involved in disease onset and progression. Most of these proteins fall into the categories of kinases, receptors, or channels, all of which are structured, have hydrophobic binding pockets, and display functional changes after binding their intended ligand. In the case of small molecule drugs, having a known structure allows for rational drug design which speeds up the process of identifying 'hits' to pursue further. Experts then perform structure-activity relationship (SAR) studies to determine the important chemical features of a hit and develop it into a lead compound. To highlight the importance of protein structure in drug design, Xie *et al.* state that "…a lack of accurate structure information of undruggable proteins remains a significant obstacle in drug discovery."[163] How, then, do disordered proteins become drug targets?

1.4.1 Amyloid-targeted drugs

Despite their direct relevance to human disease, tau and other IDPs are challenging and uncommon drug targets because they populate dynamic structural ensembles rather than a single well-defined structure.[164] One approach to target amyloidogenic proteins is to use non-specific aggregation inhibitors (e.g., ECGC,[165] Congo Red,[166] CLR01,[167] methylene blue[168,169]) that interact with existing amyloid structures (i.e., act on protofibrils and fibrils). Although these compounds are excellent research tools, they have not proven effective therapeutics and have the added disadvantage of targeting multiple proteins.

Monoclonal antibodies (mAbs) raised against amyloid targets overcome the specificity problem posed by the compounds discussed above. Many mAbs have reached clinical trials, and several have been approved in recent years by the FDA for the treatment of early AD. While these mAbs (aducanamab, lecanemab, donanemab) have shown significant reductions of amyloid-beta plaques and soluble oligomers, they come at high risk to patients. Although all-cause mortality was similar between treatment groups (mAb vs. placebo) in clinical studies, participants treated with mAbs were at significantly higher risk for amyloid-related imaging abnormalities (ARIA) safety events.[170] Beyond concerns for ARIA, there was limited evidence of meaningful symptom reduction by these mAbs at the time of their approvals. Since then, meta-analysis has shown that none of the three reached the proposed threshold for clinically meaningful change on AD assessment scales, although the authors note that benefits may take longer to appear than the studies allowed.[170] This is somewhat unsurprising because targeting the later stages of aggregation means that an IDP has already lost its function and progressed through the toxic oligomeric species to the relatively inert amyloid fibrils. In fact, the same meta-analysis found that mAbs with lower binding affinity for amyloid-

beta monomer were associated with greater (though still not clinically meaningful) benefit and proposed that this was because of the protective effect of an intact monomer population.[170]

1.4.2 Targeting conformational ensembles

Although there could be great therapeutic potential in specifically targeting earlier, more disordered states of an IDP (e.g., interrupt self-association before formation of toxic or pathological species, selectivity for a particular disordered target), characterizing ligand interactions with tau and other IDPs remains challenging. Structurally agnostic high-throughput screening strategies avoid some of these pitfalls, but can labor- and material-intensive and have low success rates.[171,172] The development of enhanced computational sampling techniques (e.g., Replicate Exchange Molecular Dynamics,[173] metadynamics[174]) and refined Monte Carlo simulations[175] has provided unprecedented insight into IDP conformational ensembles. Readers are directed to references 176 and 177 for further discussion about *in silico* approaches to deciphering IDP conformations.[176,177] The ensembles can then be used to screen for novel ligands with computational docking approaches. The ligands generated by these approaches are expected to be more selective for the protein they were generated against, although the level of selectivity that can be achieved for a small molecule/IDP interaction remains an open question. A typical drug discovery workflow with these techniques consists of computationally modeling the IDP target, screening compound fragments against the ensemble *in silico*, and then selecting the top-scoring fragments or compounds for *in vitro* testing.

Several recent examples of rational ligand discovery for tau come from a pipeline developed in the Nath lab. Briefly, ligands were screened against a simulated tau conformational ensemble *in silico* and then assayed for *in vitro* activity against tau aggregation.[171] The authors also performed a small analogue study, noting that changing a single position from a tetrazole to a triazole abolished inhibitory activity, while retaining the tetrazole and altering distal parts of the molecule resulted in stronger inhibitory activity than the parent molecule,[178] suggesting that it is possible to systematically interrogate the origins of IDP-ligand interactions. My work, discussed in Chapter 2, extended this hypothesis with the discovery of tryptanthrin and its synthetic analogs as extremely potent tau aggregation inhibitors.[179]

1.5 Thesis Scope

Although many potential tau-targeted drugs (including small molecules and antibody-based therapeutics) have been identified *in vitro,* none have been approved after clinical trials. This is, in part, due to the challenges associated with characterizing interactions between ligands and IDPs. Similar challenges exist regarding characterizing changes in the IDP conformational ensembles during amyloid aggregation.

The primary goals of this work were to further our understanding of how small molecule inhibitors interact with tau and to elucidate the mechanisms underlying inducer-driven amyloid fibril polymorphism.

Chapter two explores a novel family of *in vitro* tau aggregation inhibitors. The tryptanthrin family exerts remarkable influence during the early stages of tau amyloid formation and was found to target the aggregation nucleus or its close precursor. Further, small changes to the tryptanthrin scaffold resulted in large changes in efficacy, reinforcing that SAR studies are applicable to IDP/ligand interactions.

Chapter three examines the origins of polymorphic tau amyloid fibrils. Despite the clear picture of amyloid endpoints that cryo-EM provides, we do not understand the structural or kinetic mechanisms that give rise to these diverse species. Herein we interrogate the conformational landscape of heparin- and polyphosphate-induced tau aggregation by pulsed HDX-MS and discover that polymorphism begins at nucleation.

Chapter four addresses the mechanism by which tryptanthrins inhibit tau aggregation. During studies about the impact of divalent metal ions on tau's aggregation, it became apparent that cysteine-free tau is resistant to tryptanthrin's effect. This discovery fortuitously tied the work of chapters two and three together when it became clear that the cysteine-free and wildtype tau nuclei were sufficiently different to cause their disparate responses to incubation with tryptanthrin. Taken together, this thesis provides a framework (with tau as an example) for studying ligand/IDP interactions and the structural changes that IDPs undergo during amyloid aggregation.

1.6 Figures

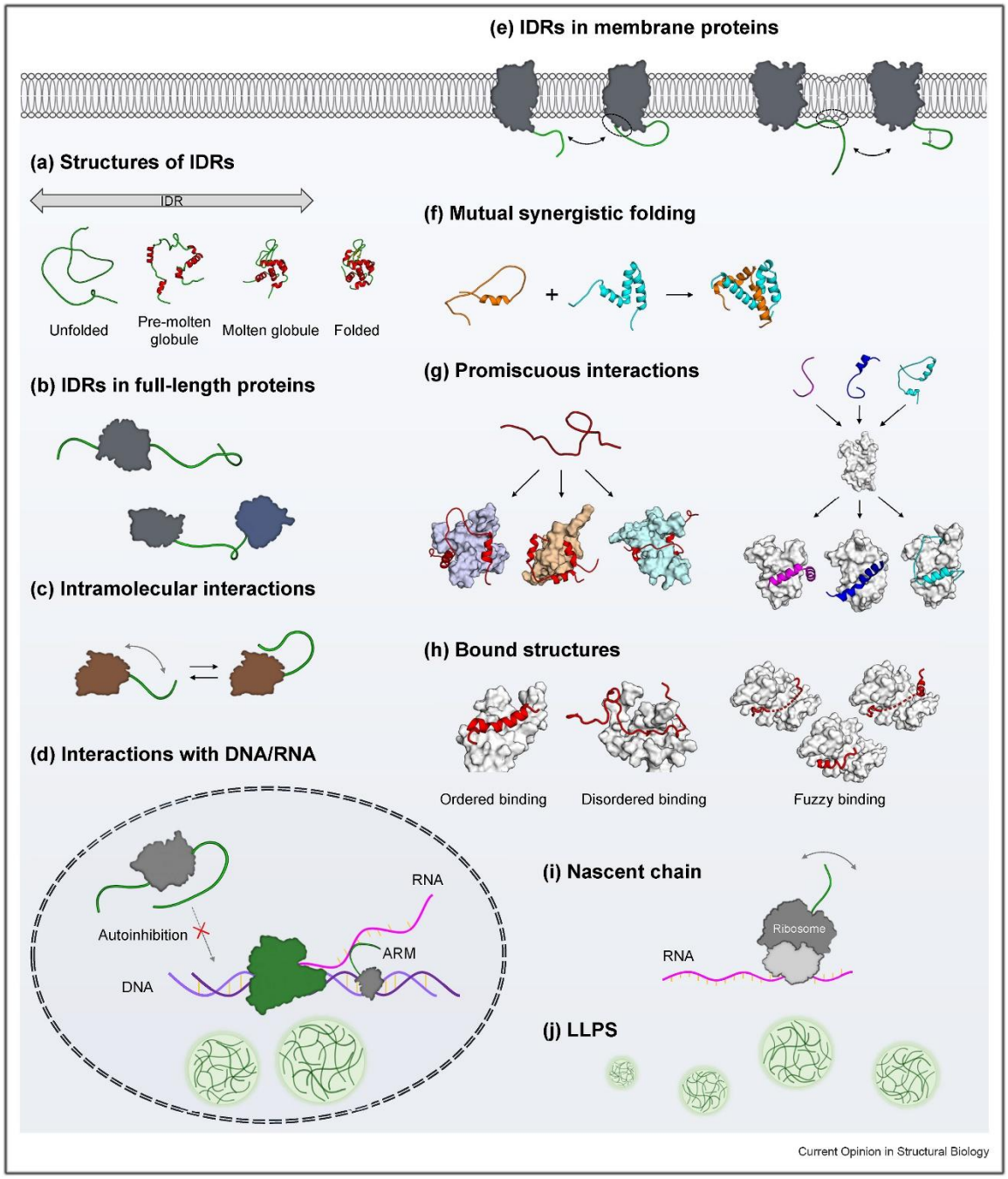

Figure 1.1: Diversity in the structure, dynamics and interactions of IDPs. (a) Structures of IDRs range from random coil-like unfolded ensembles to pre-molten globule ensembles to molten globule ensembles. **(b)** IDRs exist as N- or C-terminal tails or as linkers between folded domains in full-length proteins. **(c)** Intramolecular interactions involving IDRs in full-length proteins. **(d)** Interactions of IDPs with DNA/RNA. Intramolecular interactions in IDPs can autoinhibit DNA binding or suppress nonspecific DNA

binding [19,22,23]. Many transcription factors bind RNA using intrinsically disordered Arg-rich motifs (ARMs) [49]. **(e)** Intramolecular interactions involving IDRs in membrane proteins. The IDR of a GPCR interacts with its globular domain [24] (left). One element in the IDR of the membrane channel TRPV4 interacts exclusively with the membrane or another element in the IDR [25] (right). **(f)** Mutual synergistic folding by binding of two IDPs (ACTR and NCBD [PDB ID: 1KBH]). **(g)** Promiscuous interactions of IDPs. One IDP can bind different partners (p53 binding with TAZ2, NCBD and TAZ1 from the left [PDB ID: 5HPD, 2L14 and 5HOU, respectively]) (left). Different IDPs can competitively bind the same target (KIX binding with pKID, c-Myb and FOXO3a from the left [PDB ID: 1KDX, 1SB0 and 2LQH, respectively]) (right). **(h)** Bound structures of IDPs can be classified into ordered binding coupled with folding (PDB ID: 2AGH), disordered binding without folding (PDB ID: 2LM0), and fuzzy binding with different bound conformations and/or different binding sites (PDB ID: 5CSF, 5CSN and 5CSJ from the left). **(i)** The nascent chain during synthesis on the ribosome. **(j)** Many IDPs induce liquid-liquid phase separation (LLPS) by forming biomolecular condensates (also shown in **(d)**) that provide compartments for specific biochemical processes. Reprinted from Arai 2024 with permission from Elsevier with original citation numbering.[2]

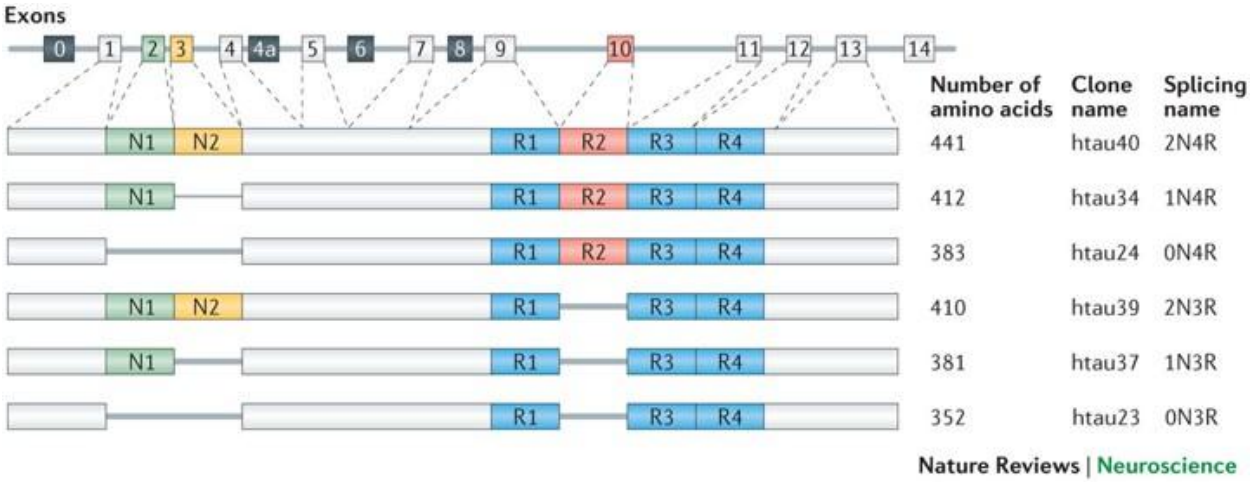

Figure 1.2: The human *MAPT* gene and the splice isoforms of tau in the human brain. *MAPT*, the gene encoding human tau, contains 16 exons[224]. Exon 1 (E1), E4, E5, E7, E9, E11, E12 and E13 are constitutive, whereas the others are subject to alternative splicing. E0 and E1 encode the 5′ untranslated sequences of *MAPT* mRNA, whereas E14 is part of the 3′ untranslated region. E0 is part of the promoter, which is transcribed but not translated. The translation initiation codon ATG is in E1. E4a, E6 and E8 are transcribed only in peripheral tissue. The six human brain tau isoforms are generated through alternative splicing of E2, E3 and E10 (Ref. 10). These tau isoforms differ according to the presence of 0, 1 or 2 near-amino-terminal inserts (0N, 1N or 2N, respectively) and the presence of repeat R2, yielding 3 or 4 carboxy-terminal repeat domain (3R or 4R, respectively) tau species. The expression of human tau is developmentally regulated: in the adult brain, six isoforms of tau are expressed, whereas in the fetal brain only the shortest tau is expressed. In the adult human brain, levels of the 3R and 4R forms are roughly equal and the 2N isoform is underrepresented compared with the others: the 0N, 1N and 2N tau isoforms comprise ~37%, ~54% and ~9% of total tau, respectively[21]. The expression of tau in the human brain shows considerable regional variation. The mRNA and protein levels of tau in the neocortex are twofold higher than those in the white matter and cerebellum[225]. The splicing of *MAPT* also exhibits regional differences; for example, the level of 0N3R tau is lower in the cerebellum than in other regions[225,226]. This variation of tau expression may contribute to the differential vulnerability of brain regions to tau pathology. Reproduced from Wang 2015 with permission from Springer Nature; citation numbers are original.[17]

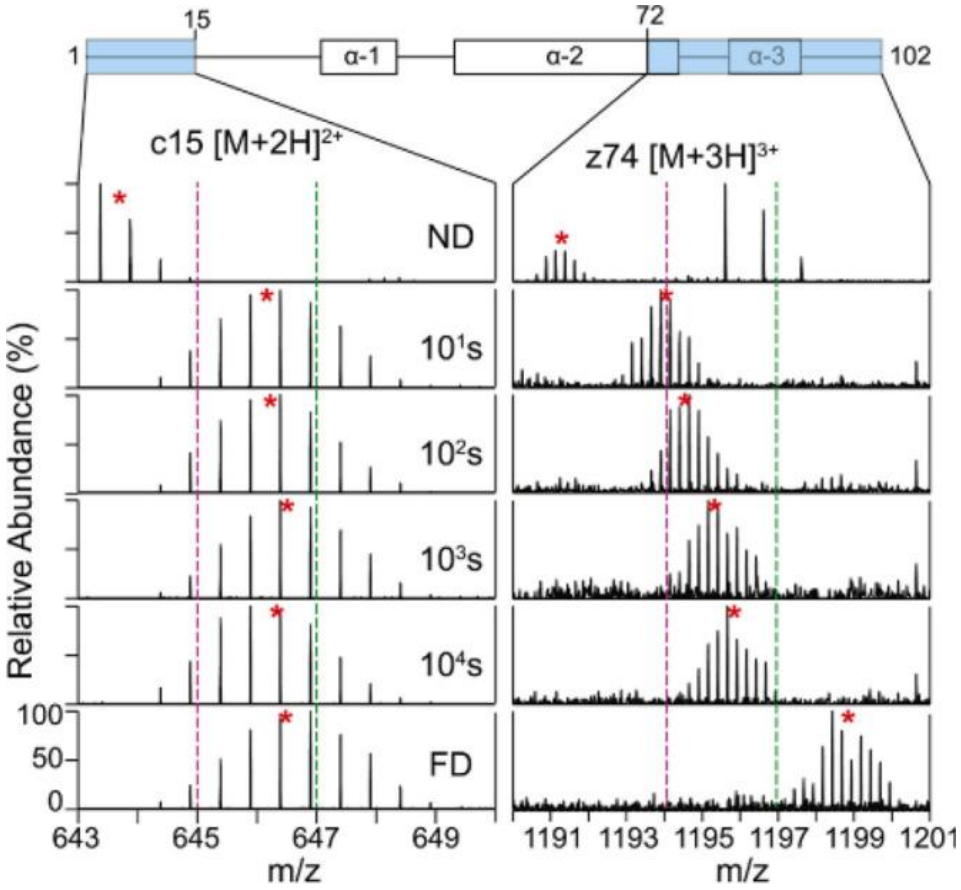

Figure 1.3: Example of top-down HDX-MS to study the dynamics of histone tails. The deuterium uptake for the *c*15 ion (left) and *z*74 ion (right) generated by ETD are shown for each deuterium exchange time point and the fully deuterated (FD) control. Reproduced with permission from Ref. 72. Copyright 2018 Elsevier.

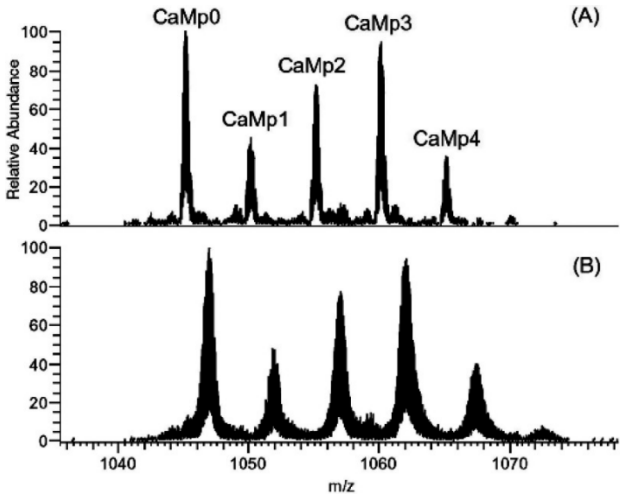

Figure 1.4: Top-down analysis of the various phosphorylated states of calmodulin. The top spectrum shows the unphosphorylated calmodulin (CaMp0) and four different phosphorylated proteoforms. The bottom spectrum is after 20 s of deuterium exchange. Each proteoform could be mass-isolated and the amide exchange characterized with high spatial resolution using ETD. Reproduced with permission from Ref. 65. Copyright 2016 from Elsevier.

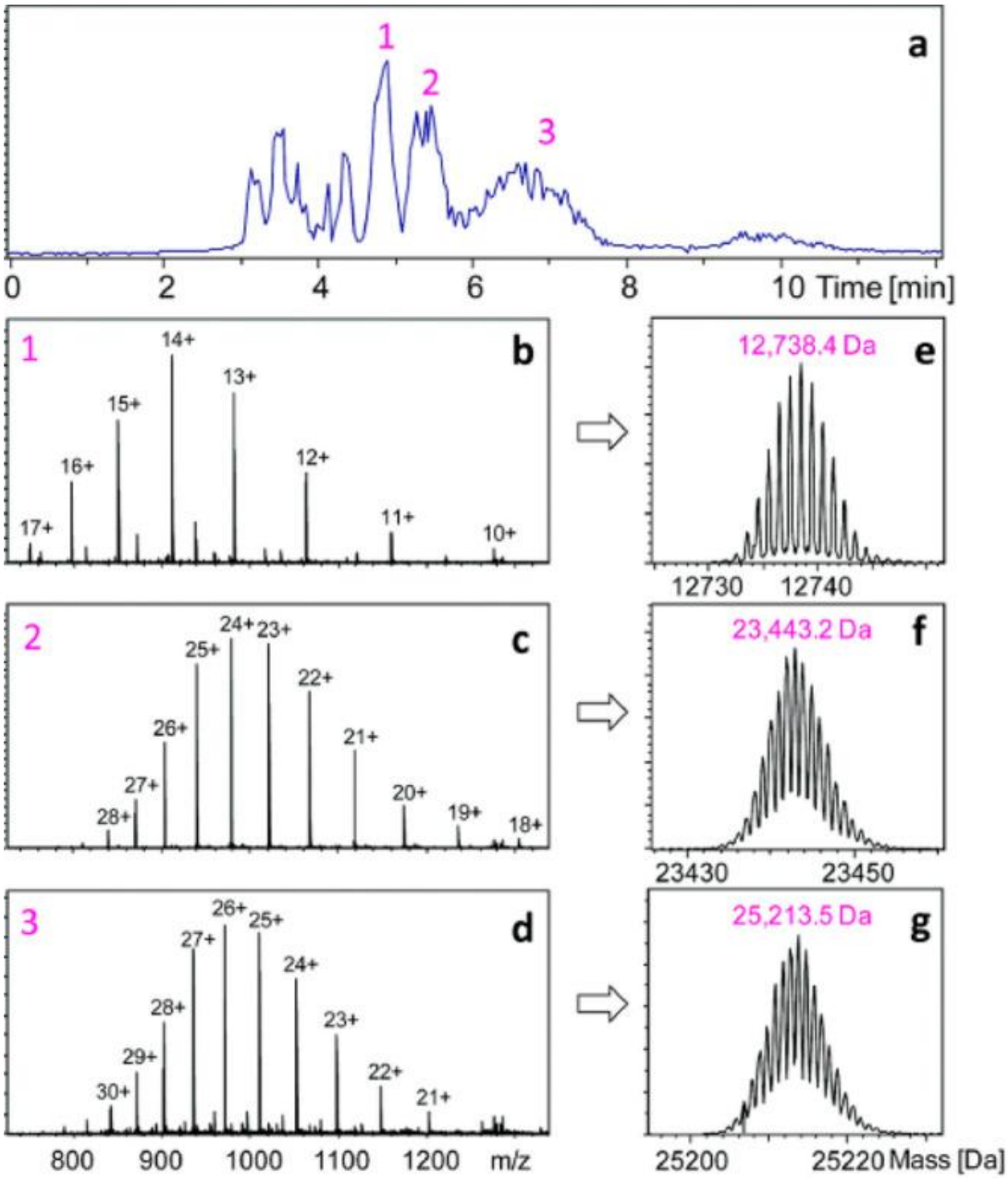

Figure 1.5: Middle-down HDX-MS was used to study herceptin. Limited pepsin digestion yielded three large fragments (1–3) that were resolved and independently analyzed by ETD to increase the sequence coverage that was obtained from direct top-down ETD analysis. Figure adapted from Ref. 74.

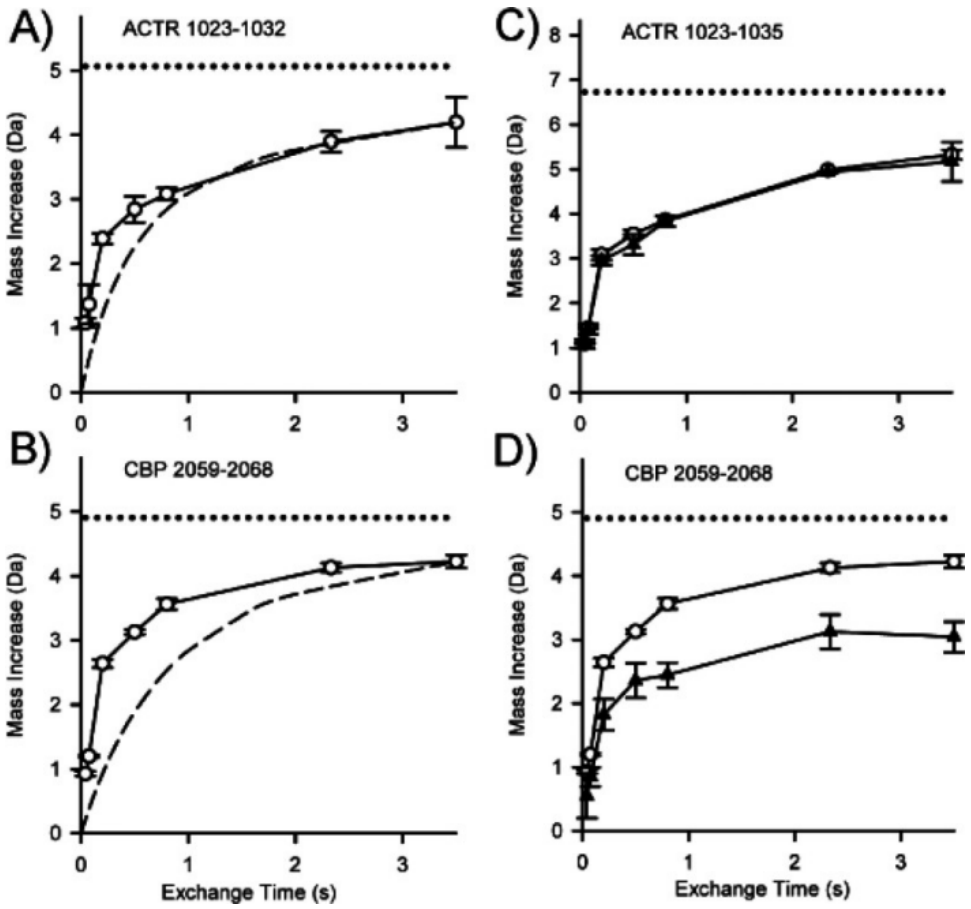

Figure 1.6: HDX-MS to measure residual structure in peptides. The exchange of two peptides compared to the predicted exchange rate is shown in (A) and (B). The predicted rates from k_{ch} are shown in dashed lines. (C,D) Exchange rates for predigested peptides (open circles) and peptide from intact protein (triangles) are compared directly to assess transient structure in the protein. Reproduced with permission from Ref. 84. Copyright 2017 American Chemical Society.

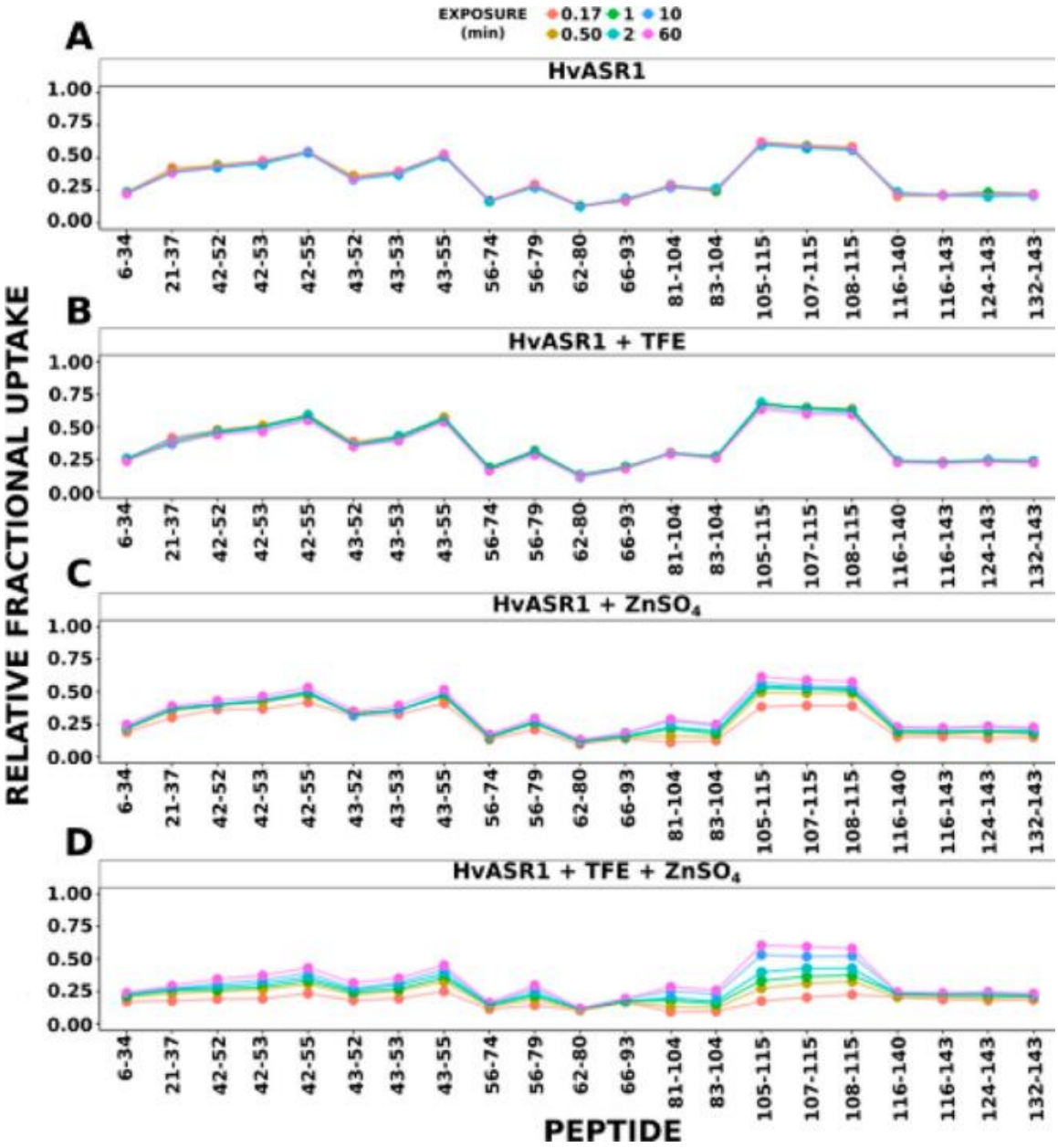

Figure 1.7: Deuterium uptake plots are shown for each peptide of unliganded HvASR1 (A), or bound to TFE (B), $ZnSO_4$ (C), or both TFE and $ZnSO_4$ (D). Points represented different time points of exchange denoted in the top of the figure. Figure adapted from Ref. 136.

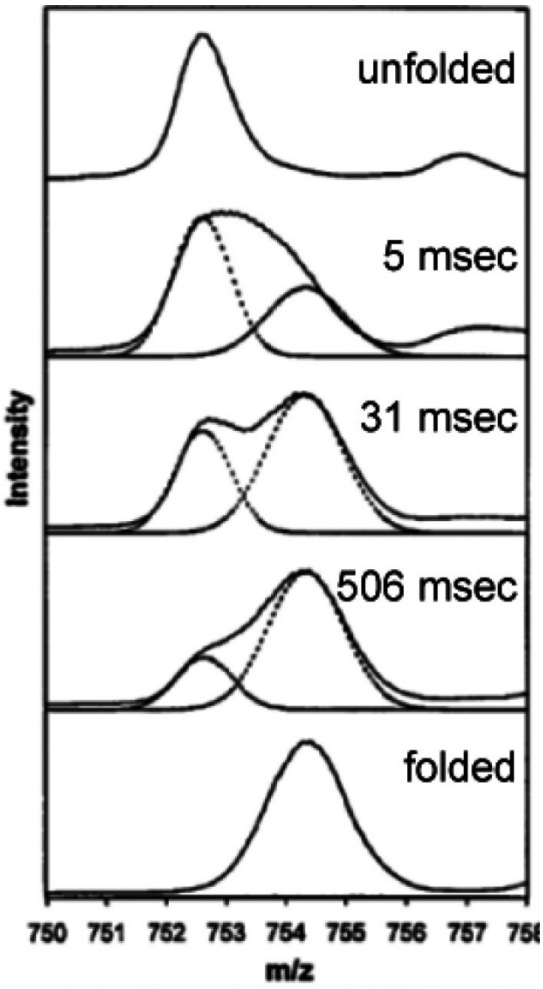

Figure 1.8: **Pulse labeling HDX-MS was used to study the folding kinetics of cytochrome c.** Fully deuterated unfolded protein was mixed with D_2O from 5 to 506 ms to initiate folding. The samples were then immediately pulse labeled with H_2O at pH 10.1 for 11 ms to rapidly label unstructured amides, followed by immediate quenching of the sample. The bimodal profiles during the folding process can be used to track the folding kinetics. The top and bottom panels are the controls for pulse labeling of the fully unfolded and folded states, respectively. Reproduced with permission from Ref. 92. Copyright 1997 American Chemical Society.

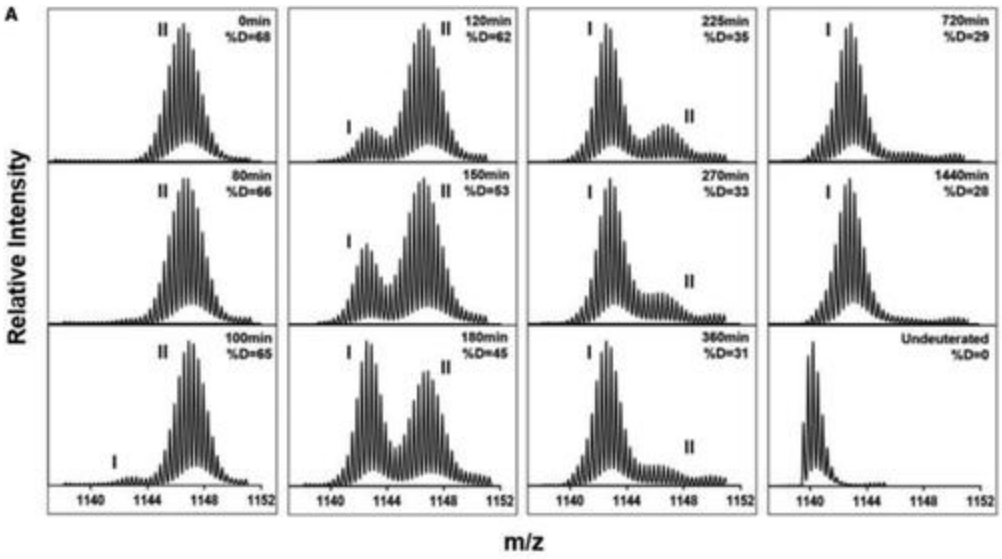

Figure 1.9: Pulse labeling HDX-MS used to track the aggregation of calcitonin. Each spectrum shows the deuteration profile (after a 2 min pulse of D2O) starting from initial conditions (0 min) to the final time point at 1440 min. Populations I and II are clearly resolved and shift as the aggregates form over time. Reproduced with permission from Ref. 154. Copyright 2021 Elsevier.

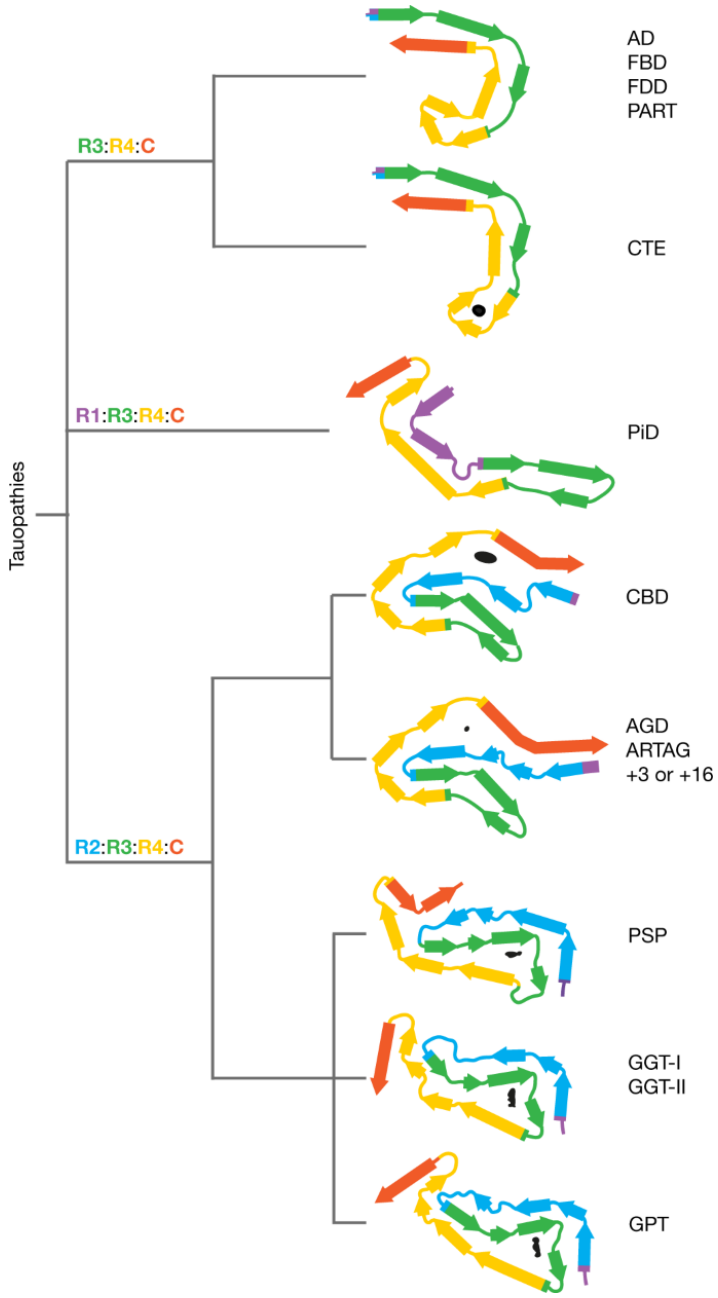

Figure 1.10: Structure-based classification of tauopathies. The dendrogram shows the proposed classification of tauopathies as described in the main text, with the corresponding folds displayed with the first β-strand in R3 oriented horizontally, except for the GGT and GPT folds, which are aligned to the PSP fold. Internal, non-proteinaceous densities are shown in black. R1 in purple, R2 in blue, R3 in green, R4 in yellow, C-terminal segment (C) in orange. AD, Alzheimer's disease; PiD, Pick's disease. Reproduced from Shi 2021 with permission from Springer Nature.[42]

1.7 References

(1) Koehler Leman, J.; Szczerbiak, P.; Renfrew, P. D.; Gligorijevic, V.; Berenberg, D.; Vatanen, T.; Taylor, B. C.; Chandler, C.; Janssen, S.; Pataki, A.; Carriero, N.; Fisk, I.; Xavier, R. J.; Knight, R.; Bonneau, R.; Kosciolek, T. Sequence-Structure-Function Relationships in the Microbial Protein Universe. Nat. Commun. 2023 141 2023, 14 (1), 1–11. https://doi.org/10.1038/S41467-023-37896-W.

(2) Arai, M.; Suetaka, S.; Ooka, K. Dynamics and Interactions of Intrinsically Disordered Proteins. Curr. Opin. Struct. Biol. 2024, 84, 102734. https://doi.org/10.1016/J.SBI.2023.102734.

(3) Holehouse, A. S.; Kragelund, B. B. The Molecular Basis for Cellular Function of Intrinsically Disordered Protein Regions. Nat. Rev. Mol. Cell Biol. 2024, 25 (3), 187–211. https://doi.org/10.1038/s41580-023-00673-0.

(4) Chivers, C. E.; Koner, A. L.; Lowe, E. D.; Howarth, M. How the Biotin–Streptavidin Interaction Was Made Even Stronger: Investigation via Crystallography and a Chimaeric Tetramer. Biochem. J. 2011, 435 (Pt 1), 55. https://doi.org/10.1042/BJ20101593.

(5) Sun, X.; Dyson, H. J.; Wright, P. E. A Phosphorylation-Dependent Switch in the Disordered P53 Transactivation Domain Regulates DNA Binding. Proc. Natl. Acad. Sci. U. S. A. 2020, 118 (1), e2021456118. https://doi.org/10.1073/PNAS.2021456118/SUPPL_FILE/PNAS.2021456118.SAPP.PDF.

(6) Krois, A. S.; Jane Dyson, H.; Wright, P. E. Long-Range Regulation of P53 DNA Binding by Its Intrinsically Disordered N-Terminal Transactivation Domain. Proc. Natl. Acad. Sci. U. S. A. 2018, 115 (48), E11302–E11310. https://doi.org/10.1073/PNAS.1814051115/SUPPL_FILE/PNAS.1814051115.SAPP.PDF.

(7) Clouser, A. F.; Baughman, H. E. R.; Basanta, B.; Guttman, M.; Nath, A.; Klevit, R. E. Interplay of Disordered and Ordered Regions of a Human Small Heat Shock Protein Yields an Ensemble of 'Quasi-Ordered' States. eLife 2019, 8. https://doi.org/10.7554/ELIFE.50259.

(8) Babinchak, W. M.; Surewicz, W. K. Liquid-Liquid Phase Separation and Its Mechanistic Role in Pathological Protein Aggregation. 2020. https://doi.org/10.1016/j.jmb.2020.03.004.

(9) Wang, B.; Zhang, L.; Dai, T.; Qin, Z.; Lu, H.; Zhang, L.; Zhou, F. Liquid–Liquid Phase Separation in Human Health and Diseases. Signal Transduct. Target. Ther. 2021 61 2021, 6 (1), 1–16. https://doi.org/10.1038/S41392-021-00678-1.

(10) Koo, E. H.; Lansbury, J.; Kelly, J. W. Amyloid Diseases: Abnormal Protein Aggregation in Neurodegeneration. Proc. Natl. Acad. Sci. U. S. A. 1999, 96 (18), 9989–9990. https://doi.org/10.1073/PNAS.96.18.9989/ASSET/4FAEF964-163C-41DD-9414-BB25E3573A87/ASSETS/GRAPHIC/PQ1892631001.JPEG.

(11) Bah, A.; Forman-Kay, J. D. Modulation of Intrinsically Disordered Protein Function by Post-Translational Modifications. J. Biol. Chem. 2016, 291 (13), 6696–6705. https://doi.org/10.1074/JBC.R115.695056.

(12) Hasegawa, M.; Wischik, C. M.; Harrington, C. Molecular Mechanisms in the Pathogenesis of Alzheimer's Disease and Tauopathies-Prion-Like Seeded Aggregation and Phosphorylation. Biomol. 2016 Vol 6 Page 24 2016, 6 (2), 24. https://doi.org/10.3390/BIOM6020024.

(13) Kanaan, N. M.; Grabinski, T. Neuronal and Glial Distribution of Tau Protein in the Adult Rat and Monkey. Front. Mol. Neurosci. 2021, 14, 607303. https://doi.org/10.3389/FNMOL.2021.607303/BIBTEX.

(14) Iqbal, K.; Liu, F.; Gong, C.-X.; Grundke-Iqbal, I. Tau in Alzheimer Disease and Related Tauopathies. Curr. Alzheimer Res. 2010, 7 (8), 656–664. https://doi.org/10.2174/156720510793611592.

(15) Marciniak, E.; Leboucher, A.; Caron, E.; Ahmed, T.; Tailleux, A.; Dumont, J.; Issad, T.; Gerhardt, E.; Pagesy, P.; Vileno, M.; Bournonville, C.; Hamdane, M.; Bantubungi, K.; Lancel, S.; Demeyer, D.; Eddarkaoui, S.; Vallez, E.; Vieau, D.; Humez, S.; Faivre, E.; Grenier-Boley, B.; Outeiro, T. F.; Staels, B.; Amouyel, P.; Balschun, D.; Buee, L.; Blum, D. Tau Deletion Promotes Brain Insulin Resistance. J. Exp. Med. 2017, 214 (8), 2257–2269. https://doi.org/10.1084/JEM.20161731.

(16) Kent, S. A.; Spires-Jones, T. L.; Durrant, C. S. The Physiological Roles of Tau and Aβ: Implications for Alzheimer's Disease Pathology and Therapeutics. Acta Neuropathol. (Berl.) 2020, 140 (4), 417. https://doi.org/10.1007/S00401-020-02196-W.
(17) Wang, Y.; Mandelkow, E. Tau in Physiology and Pathology. Nat. Rev. Neurosci. 2015 171 2015, 17 (1), 22–35. https://doi.org/10.1038/NRN.2015.1.
(18) Kimura, T.; Whitcomb, D. J.; Jo, J.; Regan, P.; Piers, T.; Heo, S.; Brown, C.; Hashikawa, T.; Murayama, M.; Seok, H.; Sotiropoulos, I.; Kim, E.; Collingridge, G. L.; Takashima, A.; Cho, K. Microtubule-Associated Protein Tau Is Essential for Long-Term Depression in the Hippocampus. Philos. Trans. R. Soc. B Biol. Sci. 2014, 369 (1633). https://doi.org/10.1098/RSTB.2013.0144.
(19) Ondrejcak, T.; Hu, N. W.; Qi, Y.; Klyubin, I.; Corbett, G. T.; Fraser, G.; Perkinton, M. S.; Walsh, D. M.; Billinton, A.; Rowan, M. J. Soluble Tau Aggregates Inhibit Synaptic Long-Term Depression and Amyloid β-Facilitated LTD in Vivo. Neurobiol. Dis. 2019, 127, 582–590. https://doi.org/10.1016/j.nbd.2019.03.022.
(20) Limorenko, G.; Lashuel, H. A. Revisiting the Grammar of Tau Aggregation and Pathology Formation: How New Insights from Brain Pathology Are Shaping How We Study and Target Tauopathies. Chem. Soc. Rev. 2022, 51 (2), 513–565. https://doi.org/10.1039/D1CS00127B.
(21) Kavanagh, T.; Halder, A.; Drummond, E. Tau Interactome and RNA Binding Proteins in Neurodegenerative Diseases. Mol. Neurodegener. 2022 171 2022, 17 (1), 1–17. https://doi.org/10.1186/S13024-022-00572-6.
(22) Buchholz, S.; Zempel, H. The Six Brain-Specific TAU Isoforms and Their Role in Alzheimer's Disease and Related Neurodegenerative Dementia Syndromes. Alzheimers Dement. 2024, 20 (5), 3606–3628. https://doi.org/10.1002/ALZ.13784.
(23) Zhang, Y.; Wu, K. M.; Yang, L.; Dong, Q.; Yu, J. T. Tauopathies: New Perspectives and Challenges. Mol. Neurodegener. 2022, 17 (1). https://doi.org/10.1186/s13024-022-00533-z.
(24) Sexton, C.; Snyder, H.; Beher, D.; Boxer, A. L.; Brannelly, P.; Brion, J. P.; Buée, L.; Cacace, A. M.; Chételat, G.; Citron, M.; DeVos, S. L.; Diaz, K.; Feldman, H. H.; Frost, B.; Goate, A. M.; Gold, M.; Hyman, B.; Johnson, K.; Karch, C. M.; Kerwin, D. R.; Koroshetz, W. J.; Litvan, I.; Morris, H. R.; Mummery, C. J.; Mutamba, J.; Patterson, M. C.; Quiroz, Y. T.; Rabinovici, G. D.; Rommel, A.; Shulman, M. B.; Toledo-Sherman, L. M.; Weninger, S.; Wildsmith, K. R.; Worley, S. L.; Carrillo, M. C. Current Directions in Tau Research: Highlights from Tau 2020. Alzheimers Dement. 2022, 18 (5), 988–1007. https://doi.org/10.1002/ALZ.12452.
(25) Langerscheidt, F.; Wied, T.; Al Kabbani, M. A.; van Eimeren, T.; Wunderlich, G.; Zempel, H. Genetic Forms of Tauopathies: Inherited Causes and Implications of Alzheimer's Disease-like TAU Pathology in Primary and Secondary Tauopathies. J. Neurol. 2024, 271 (6), 2992. https://doi.org/10.1007/S00415-024-12314-3.
(26) Mahar, I.; Alosco, M. L.; McKee, A. C. Psychiatric Phenotypes in Chronic Traumatic Encephalopathy. Neurosci. Biobehav. Rev. 2017, 83, 622–630. https://doi.org/10.1016/J.NEUBIOREV.2017.08.023.
(27) Knopman, D. S.; Amieva, H.; Petersen, R. C.; Chételat, G.; Holtzman, D. M.; Hyman, B. T.; Nixon, R. A.; Jones, D. T. Alzheimer Disease. Nat. Rev. Dis. Primer 2021 71 2021, 7 (1), 1–21. https://doi.org/10.1038/S41572-021-00269-Y.
(28) Chen, S. D.; Lu, J. Y.; Li, H. Q.; Yang, Y. X.; Jiang, J. H.; Cui, M.; Zuo, C. T.; Tan, L.; Dong, Q.; Yu, J. T.; Weiner, M. W.; Aisen, P.; Petersen, R.; Jack, C. R.; Jagust, W.; Trojanowki, J. Q.; Toga, A. W.; Beckett, L.; Green, R. C.; Saykin, A. J.; Morris, J. C.; Perrin, R. J.; Shaw, L. M.; Carrillo, M.; Potter, W.; Barnes, L.; Bernard, M.; González, H.; Ho, C.; Hsiao, J. K.; Jackson, J.; Masliah, E.; Masterman, D.; Okonkwo, O.; Ryan, L.; Silverberg, N.; Fleisher, A.; Sacrey, D. T.; Fockler, J.; Conti, C.; Veitch, D.; Neuhaus, J.; Jin, C.; Nosheny, R.; Ashford, M.; Flenniken, D.; Kormos, A.; Rafii, M.; Raman, R.; Jimenez, G.; Donohue, M.; Gessert, D.; Salazar, J.; Zimmerman, C.; Cabrera, Y.; Walter, S.; Miller, G.; Coker, G.; Clanton, T.; Hergesheimer, L.; Smith, S.; Adegoke, O.; Mahboubi, P.; Moore, S.; Pizzola, J.; Shaffer, E.; Sloan, B.; Harvey, D.; Forghanian-Arani, A.; Borowski, B.; Ward, C.;

Schwarz, C.; Jones, D.; Gunter, J.; Kantarci, K.; Senjem, M.; Vemuri, P.; Reid, R.; Fox, N. C.; Malone, I.; Thompson, P.; Thomopoulos, S. I.; Nir, T. M.; Jahanshad, N.; DeCarli, C.; Knaack, A.; Fletcher, E.; Tosun-Turgut, D.; Chen, S. R.; Choe, M.; Crawford, K.; Yushkevich, P. A.; Das, S.; Koeppe, R. A.; Reiman, E. M.; Chen, K.; Mathis, C.; Landau, S.; Cairns, N. J.; Householder, E.; Franklin, E.; Bernhardt, H.; Taylor-Reinwald, L.; Shaw, L. M.; Trojanowki, J. Q.; Korecka, M.; Figurski, M.; Crawford, K.; Neu, S.; Saykin, A. J.; Nho, K.; Risacher, S. L.; Apostolova, L. G.; Shen, L.; Foroud, T. M.; Nudelman, K.; Faber, K.; Wilmes, K.; Thal, L.; Khachaturian, Z.; Hsiao, J. K.; Silbert, L. C.; Lind, B.; Crissey, R.; Kaye, J. A.; Carter, R.; Dolen, S.; Quinn, J.; Schneider, L. S.; Pawluczyk, S.; Becerra, M.; Teodoro, L.; Dagerman, K.; Spann, B. M.; Brewer, J.; Vanderswag, H.; Fleisher, A.; Ziolkowski, J.; Heidebrink, J. L.; Zbizek-Nulph, L.; Lord, J. L.; Mason, S. S.; Albers, C. S.; Knopman, D.; Johnson, K.; Villanueva-Meyer, J.; Pavlik, V.; Pacini, N.; Lamb, A.; Kass, J. S.; Doody, R. S.; Shibley, V.; Chowdhury, M.; Rountree, S.; Dang, M.; Stern, Y.; Honig, L. S.; Mintz, A.; Ances, B.; Winkfield, D.; Carroll, M.; Stobbs-Cucchi, G.; Oliver, A.; Creech, M. L.; Mintun, M. A.; Schneider, S.; Geldmacher, D.; Love, M. N.; Griffith, R.; Clark, D.; Brockington, J.; Marson, D.; Grossman, H.; Goldstein, M. A.; Greenberg, J.; Mitsis, E.; Shah, R. C.; Lamar, M.; Samuels, P.; Duara, R.; Greig-Custo, M. T.; Rodriguez, R.; Albert, M.; Onyike, C.; Farrington, L.; Rudow, S.; Brichko, R.; Kielb, S.; Smith, A.; Raj, B. A.; Fargher, K.; Sadowski, M.; Wisniewski, T.; Shulman, M.; Faustin, A.; Rao, J.; Castro, K. M.; Ulysse, A.; Chen, S.; Sheikh, M. O.; Singleton-Garvin, J.; Doraiswamy, P. M.; Petrella, J. R.; James, O.; Wong, T. Z.; Borges-Neto, S.; Karlawish, J. H.; Wolk, D. A.; Vaishnavi, S.; Clark, C. M.; Arnold, S. E.; Smith, C. D.; Jicha, G. A.; El Khouli, R.; Raslau, F. D.; Lopez, O. L.; Oakley, M. A.; Simpson, D. M.; Porsteinsson, A. P.; Martin, K.; Kowalski, N.; Keltz, M.; Goldstein, B. S.; Makino, K. M.; Ismail, M. S.; Brand, C.; Thai, G.; Pierce, A.; Yanez, B.; Sosa, E.; Witbracht, M.; Kelley, B.; Nguyen, T.; Womack, K.; Mathews, D.; Quiceno, M.; Levey, A. I.; Lah, J. J.; Hajjar, I.; Cellar, J. S.; Burns, J. M.; Swerdlow, R. H.; Brooks, W. M.; Silverman, D. H. S.; Kremen, S.; Apostolova, L.; Tingus, K.; Lu, P. H.; Bartzokis, G.; Woo, E.; Teng, E.; Graff-Radford, N. R.; Parfitt, F.; Poki-Walker, K.; Farlow, M. R.; Hake, A. M.; Matthews, B. R.; Brosch, J. R.; Herring, S.; van Dyck, C. H.; Mecca, A. P.; Good, S. P.; MacAvoy, M. G.; Carson, R. E.; Varma, P.; Chertkow, H.; Vaitekunis, S.; Hosein, C.; Black, S.; Stefanovic, B.; Heyn, C.; Hsiung, G. Y. R.; Kim, E.; Mudge, B.; Sossi, V.; Feldman, H.; Assaly, M.; Finger, E.; Pasternak, S.; Rachinsky, I.; Kertesz, A.; Drost, D.; Rogers, J.; Grant, I.; Muse, B.; Rogalski, E.; Robson, J.; Mesulam, M. M.; Kerwin, D.; Wu, C. K.; Johnson, N.; Lipowski, K.; Weintraub, S.; Bonakdarpour, B.; Pomara, N.; Hernando, R.; Sarrael, A.; Rosen, H. J.; Miller, B. L.; Perry, D.; Turner, R. S.; Johnson, K.; Reynolds, B.; MCCann, K.; Poe, J.; Sperling, R. A.; Johnson, K. A.; Marshall, G. A.; Belden, C. M.; Atri, A.; Spann, B. M.; Clark, K. A.; Zamrini, E.; Sabbagh, M.; Killiany, R.; Stern, R.; Mez, J.; Kowall, N.; Budson, A. E.; Obisesan, T. O.; Ntekim, O. E.; Wolday, S.; Khan, J. I.; Nwulia, E.; Nadarajah, S.; Lerner, A.; Ogrocki, P.; Tatsuoka, C.; Fatica, P.; Fletcher, E.; Maillard, P.; Olichney, J.; DeCarli, C.; Carmichael, O.; Bates, V.; Capote, H.; Rainka, M.; Borrie, M.; Lee, T. Y.; Bartha, R.; Johnson, S.; Asthana, S.; Carlsson, C. M.; Burke, A.; Scharre, D. W.; Kataki, M.; Tarawneh, R.; Kelley, B.; Hart, D.; Zimmerman, E. A.; Celmins, D.; Miller, D. D.; Boles Ponto, L. L.; Smith, K. E.; Koleva, H.; Shim, H.; Nam, K. W.; Schultz, S. K.; Williamson, J. D.; Craft, S.; Cleveland, J.; Yang, M.; Sink, K. M.; Ott, B. R.; Drake, J.; Tremont, G.; Daiello, L. A.; Drake, J. D.; Sabbagh, M.; Ritter, A.; Bernick, C.; Munic, D.; Mintz, A.; O'Connelll, A.; Mintzer, J.; Wiliams, A.; Masdeu, J.; Shi, J.; Garcia, A.; Sabbagh, M.; Newhouse, P.; Potkin, S.; Salloway, S.; Malloy, P.; Correia, S.; Kittur, S.; Pearlson, G. D.; Blank, K.; Anderson, K.; Flashman, L. A.; Seltzer, M.; Hynes, M. L.; Santulli, R. B.; Relkin, N.; Chiang, G.; Lin, M.; Ravdin, L.; Lee, A.; Petersen, R.; Neylan, T.; Grafman, J.; Montine, T.; Petersen, R.; Hergesheimer, L.; Danowski, S.; Nguyen-Barrera, C.; Hayes, J.; Finley, S.; Donohue, M.; Bernstein, M.; Senjem, M.; Ward, C.; Chen, S. R.; Koeppe, R. A.; Foster, N.; Potkin, S.; Shen, L.; Faber, K.; Kim, S.; Nho, K.; Wilmes, K.; Spann, B. M.; Vanderswag, H.; Fleisher, A.; Sood, A.; Blanchard, K. S.; Fleischman, D.; Arfanakis, K.; Varon, D.; Greig, M. T.; Goldstein, B.; Martin, K. S.; Thai, G.; Pierce, A.; Reist, C.; Yanez, B.; Sosa, E.; Witbracht, M.; Sadowsky, C.; Martinez, W.;

Villena, T.; Rosen, H.; Marshall, G.; Nadarajah, S.; Peskind, E. R.; Petrie, E. C.; Li, G.; Yesavage, J.; Taylor, J. L.; Chao, S.; Coleman, J.; White, J. D.; Lane, B.; Rosen, A.; Tinklenberg, J.; Chiang, G.; Mackin, S.; Raman, R.; Jimenez-Maggiora, G.; Gessert, D.; Salazar, J.; Zimmerman, C.; Adegoke, O.; Mahboubi, P.; Drake, E.; Donohue, M.; Nelson, C.; Bickford, D.; Butters, M.; Zmuda, M.; Borowski, B.; Gunter, J.; Senjem, M.; Kantarci, K.; Ward, C.; Reyes, D.; Faber, K. M.; Nudelman, K. N.; Au, Y. H.; Scherer, K.; Catalinotto, D.; Stark, S.; Ong, E.; Fernandez, D.; Zmuda, M. Staging Tau Pathology with Tau PET in Alzheimer's Disease: A Longitudinal Study. Transl. Psychiatry 2021 111 2021, 11 (1), 1–12. https://doi.org/10.1038/S41398-021-01602-5.

(29) Franzmeier, N.; Neitzel, J.; Rubinski, A.; Smith, R.; Strandberg, O.; Ossenkoppele, R.; Hansson, O.; Ewers, M.; Weiner, M.; Aisen, P.; Petersen, R.; Jack, C. R.; Jagust, W.; Trojanowki, J. Q.; Toga, A. W.; Beckett, L.; Green, R. C.; Saykin, A. J.; Morris, J. C.; Shaw, L. M.; Liu, E.; Montine, T.; Thomas, R. G.; Donohue, M.; Walter, S.; Gessert, D.; Sather, T.; Jiminez, G.; Harvey, D.; Donohue, M.; Bernstein, M.; Fox, N.; Thompson, P.; Schuff, N.; DeCArli, C.; Borowski, B.; Gunter, J.; Senjem, M.; Vemuri, P.; Jones, D.; Kantarci, K.; Ward, C.; Koeppe, R. A.; Foster, N.; Reiman, E. M.; Chen, K.; Mathis, C.; Landau, S.; Cairns, N. J.; Householder, E.; Reinwald, L. T.; Lee, V.; Korecka, M.; Figurski, M.; Crawford, K.; Neu, S.; Foroud, T. M.; Potkin, S.; Shen, L.; Kelley, F.; Kim, S.; Nho, K.; Kachaturian, Z.; Frank, R.; Snyder, P. J.; Molchan, S.; Kaye, J.; Quinn, J.; Lind, B.; Carter, R.; Dolen, S.; Schneider, L. S.; Pawluczyk, S.; Beccera, M.; Teodoro, L.; Spann, B. M.; Brewer, J.; Vanderswag, H.; Fleisher, A.; Heidebrink, J. L.; Lord, J. L.; Petersen, R.; Mason, S. S.; Albers, C. S.; Knopman, D.; Johnson, K.; Doody, R. S.; Meyer, J. V.; Chowdhury, M.; Rountree, S.; Dang, M.; Stern, Y.; Honig, L. S.; Bell, K. L.; Ances, B.; Carroll, M.; Leon, S.; Householder, E.; Mintun, M. A.; Schneider, S.; OliverNG, A.; Griffith, R.; Clark, D.; Geldmacher, D.; Brockington, J.; Roberson, E.; Grossman, H.; Mitsis, E.; deToledo-Morrell, L.; Shah, R. C.; Duara, R.; Varon, D.; Greig, M. T.; Roberts, P.; Albert, M.; Onyike, C.; D'Agostino, D.; Kielb, S.; Galvin, J. E.; Pogorelec, D. M.; Cerbone, B.; Michel, C. A.; Rusinek, H.; de Leon, M. J.; Glodzik, L.; De Santi, S.; Doraiswamy, P. M.; Petrella, J. R.; Wong, T. Z.; Arnold, S. E.; Karlawish, J. H.; Wolk, D.; Smith, C. D.; Jicha, G.; Hardy, P.; Sinha, P.; Oates, E.; Conrad, G.; Lopez, O. L.; Oakley, M. A.; Simpson, D. M.; Porsteinsson, A. P.; Goldstein, B. S.; Martin, K.; Makino, K. M.; Ismail, M. S.; Brand, C.; Mulnard, R. A.; Thai, G.; Ortiz, C. M. A.; Womack, K.; Mathews, D.; Quiceno, M.; Arrastia, R. D.; King, R.; Weiner, M.; Cook, K. M.; DeVous, M.; Levey, A. I.; Lah, J. J.; Cellar, J. S.; Burns, J. M.; Anderson, H. S.; Swerdlow, R. H.; Apostolova, L.; Tingus, K.; Woo, E.; Silverman, D. H. S.; Lu, P. H.; Bartzokis, G.; Radford, N. R. G.; ParfittH, F.; Kendall, T.; Johnson, H.; Farlow, M. R.; Hake, A. M.; Matthews, B. R.; Herring, S.; Hunt, C.; van Dyck, C. H.; Carson, R. E.; MacAvoy, M. G.; Chertkow, H.; Bergman, H.; Hosein, C.; Black, S.; Stefanovic, B.; Caldwell, C.; Hsiung, G. Y. R.; Feldman, H.; Mudge, B.; Past, M. A.; Kertesz, A.; Rogers, J.; Trost, D.; Bernick, C.; Munic, D.; Kerwin, D.; Mesulam, M. M.; Lipowski, K.; Wu, C. K.; Johnson, N.; Sadowsky, C.; Martinez, W.; Villena, T.; Turner, R. S.; Johnson, K.; Reynolds, B.; Sperling, R. A.; Johnson, K. A.; Marshall, G.; Frey, M.; Yesavage, J.; Taylor, J. L.; Lane, B.; Rosen, A.; Tinklenberg, J.; Sabbagh, M. N.; Belden, C. M.; Jacobson, S. A.; Sirrel, S. A.; Kowall, N.; Killiany, R.; Budson, A. E.; Norbash, A.; Johnson, P. L.; Obisesan, T. O.; Wolday, S.; Allard, J.; Lerner, A.; Ogrocki, P.; Hudson, L.; Fletcher, E.; Carmichael, O.; Olichney, J.; DeCarli, C.; Kittur, S.; Borrie, M.; Lee, T. Y.; Bartha, R.; Johnson, S.; Asthana, S.; Carlsson, C. M.; Potkin, S. G.; Preda, A.; Nguyen, D.; Tariot, P.; Fleisher, A.; Reeder, S.; Bates, V.; Capote, H.; Rainka, M.; Scharre, D. W.; Kataki, M.; Adeli, A.; Zimmerman, E. A.; Celmins, D.; Brown, A. D.; Pearlson, G. D.; Blank, K.; Anderson, K.; Santulli, R. B.; Kitzmiller, T. J.; Schwartz, E. S.; SinkS, K. M.; Williamson, J. D.; Garg, P.; Watkins, F.; Ott, B. R.; Querfurth, H.; Tremont, G.; Salloway, S.; Malloy, P.; Correia, S.; Rosen, H. J.; Miller, B. L.; Mintzer, J.; Spicer, K.; Bachman, D.; Finger, E.; Pasternak, S.; Rachinsky, I.; Rogers, J.; Kertesz, A.; Drost, D.; Pomara, N.; Hernando, R.; Sarrael, A.; Schultz, S. K.; Ponto, L. L. B.; Shim, H.; Smith, K. E.; Relkin, N.; Chaing, G.; Raudin, L.; Smith, A.; Fargher, K.; Raj, B. A. Functional Brain Architecture Is Associated with the Rate of

Tau Accumulation in Alzheimer's Disease. Nat. Commun. 2020 111 2020, 11 (1), 1–17. https://doi.org/10.1038/S41467-019-14159-1.
(30) Almeida, Z. L.; Brito, R. M. M. Structure and Aggregation Mechanisms in Amyloids. Molecules 2020, 25 (5), 1195. https://doi.org/10.3390/MOLECULES25051195.
(31) Lee, M. C.; Yu, W. C.; Shih, Y. H.; Chen, C. Y.; Guo, Z. H.; Huang, S. J.; Chan, J. C. C.; Chen, Y. R. Zinc Ion Rapidly Induces Toxic, off-Pathway Amyloid-β Oligomers Distinct from Amyloid-β Derived Diffusible Ligands in Alzheimer's Disease. Sci. Rep. 2018 81 2018, 8 (1), 1–16. https://doi.org/10.1038/S41598-018-23122-X.
(32) Emin, D.; Zhang, Y. P.; Lobanova, E.; Miller, A.; Li, X.; Xia, Z.; Dakin, H.; Sideris, D. I.; Lam, J. Y. L.; Ranasinghe, R. T.; Kouli, A.; Zhao, Y.; De, S.; Knowles, T. P. J.; Vendruscolo, M.; Ruggeri, F. S.; Aigbirhio, F. I.; Williams-Gray, C. H.; Klenerman, D. Small Soluble α-Synuclein Aggregates Are the Toxic Species in Parkinson's Disease. Nat. Commun. 2022 131 2022, 13 (1), 1–15. https://doi.org/10.1038/S41467-022-33252-6.
(33) Lo Cascio, F.; Puangmalai, N.; Ellsworth, A.; Bucchieri, F.; Pace, A.; Palumbo Piccionello, A.; Kayed, R. Toxic Tau Oligomers Modulated by Novel Curcumin Derivatives. Sci. Rep. 2019 91 2019, 9 (1), 1–16. https://doi.org/10.1038/S41598-019-55419-W.
(34) Ward, S. M.; Himmelstein, D. S.; Lancia, J. K.; Binder, L. I. Tau Oligomers and Tau Toxicity in Neurodegenerative Disease. Biochem. Soc. Trans. 2012, 40 (4), 667. https://doi.org/10.1042/BST20120134.
(35) Baughman, H. E. R.; Clouser, A. F.; Klevit, R. E.; Nath, A. HspB1 and Hsc70 Chaperones Engage Distinct Tau Species and Have Different Inhibitory Effects on Amyloid Formation. J. Biol. Chem. 2018, 293 (8), 2687–2700. https://doi.org/10.1074/jbc.M117.803411.
(36) Baughman, H. E. R.; Pham, T. H. T.; Adams, C. S.; Nath, A.; Klevit, R. E. Release of a Disordered Domain Enhances HspB1 Chaperone Activity toward Tau. Proc. Natl. Acad. Sci. U. S. A. 2020, 117 (6), 2923–2929. https://doi.org/10.1073/PNAS.1915099117/-/DCSUPPLEMENTAL.
(37) Frost, B.; Jacks, R. L.; Diamond, M. I. Propagation of Tau Misfolding from the Outside to the Inside of a Cell. J. Biol. Chem. 2009, 284 (19), 12845–12852. https://doi.org/10.1074/JBC.M808759200.
(38) Holmes, B. B.; Furman, J. L.; Mahan, T. E.; Yamasaki, T. R.; Mirbaha, H.; Eades, W. C.; Belaygorod, L.; Cairns, N. J.; Holtzman, D. M.; Diamond, M. I. Proteopathic Tau Seeding Predicts Tauopathy in Vivo. Proc. Natl. Acad. Sci. U. S. A. 2014, 111 (41), E4376–E4385. https://doi.org/10.1073/PNAS.1411649111/SUPPL_FILE/PNAS.201411649SI.PDF.
(39) Sanders, D. W.; Kaufman, S. K.; DeVos, S. L.; Sharma, A. M.; Mirbaha, H.; Li, A.; Barker, S. J.; Foley, A. C.; Thorpe, J. R.; Serpell, L. C.; Miller, T. M.; Grinberg, L. T.; Seeley, W. W.; Diamond, M. I. Distinct Tau Prion Strains Propagate in Cells and Mice and Define Different Tauopathies. Neuron 2014, 82 (6), 1271–1288. https://doi.org/10.1016/J.NEURON.2014.04.047/ATTACHMENT/F7D577C0-9296-4685-B77D-84DDAB5259A5/MMC2.PDF.
(40) Fitzpatrick, A. W. P.; Falcon, B.; He, S.; Murzin, A. G.; Murshudov, G.; Garringer, H. J.; Crowther, R. A.; Ghetti, B.; Goedert, M.; Scheres, S. H. W. Cryo-EM Structures of Tau Filaments from Alzheimer's Disease. Nature 2017, 547 (7662), 185–190. https://doi.org/10.1038/NATURE23002.
(41) Falcon, B.; Zhang, W.; Murzin, A. G.; Murshudov, G.; Garringer, H. J.; Vidal, R.; Crowther, R. A.; Ghetti, B.; Scheres, S. H. W.; Goedert, M. Structures of Filaments from Pick's Disease Reveal a Novel Tau Protein Fold. Nature 2018, 561 (7721), 137–140. https://doi.org/10.1038/S41586-018-0454-Y.
(42) Shi, Y.; Zhang, W.; Yang, Y.; Murzin, A. G.; Falcon, B.; Kotecha, A.; van Beers, M.; Tarutani, A.; Kametani, F.; Garringer, H. J.; Vidal, R.; Hallinan, G. I.; Lashley, T.; Saito, Y.; Murayama, S.; Yoshida, M.; Tanaka, H.; Kakita, A.; Ikeuchi, T.; Robinson, A. C.; Mann, D. M. A.; Kovacs, G. G.; Revesz, T.; Ghetti, B.; Hasegawa, M.; Goedert, M.; Scheres, S. H. W. Structure-Based Classification of Tauopathies. Nature 2021, 598 (7880), 359. https://doi.org/10.1038/S41586-021-03911-7.

(43) Kovacs, G. G.; Ghetti, B.; Goedert, M. Classification of Diseases with Accumulation of Tau Protein. Neuropathol. Appl. Neurobiol. 2022, 48 (3), e12792. https://doi.org/10.1111/NAN.12792.
(44) Louros, N.; Wilkinson, M.; Tsaka, G.; Ramakers, M.; Morelli, C.; Garcia, T.; Gallardo, R.; D'Haeyer, S.; Goossens, V.; Audenaert, D.; Thal, D. R.; Mackenzie, I. R.; Rademakers, R.; Ranson, N. A.; Radford, S. E.; Rousseau, F.; Schymkowitz, J. Local Structural Preferences in Shaping Tau Amyloid Polymorphism. Nat. Commun. 2024 151 2024, 15 (1), 1–16. https://doi.org/10.1038/S41467-024-45429-2.
(45) Lövestam, S.; Koh, F. A.; van Knippenberg, B.; Kotecha, A.; Murzin, A. G.; Goedert, M.; Scheres, S. H. W. Assembly of Recombinant Tau into Filaments Identical to Those of Alzheimer's Disease and Chronic Traumatic Encephalopathy. eLife 2022, 11. https://doi.org/10.7554/eLife.76494.
(46) Despres, C.; Di, J.; Cantrelle, F. X.; Li, Z.; Huvent, I.; Chambraud, B.; Zhao, J.; Chen, J.; Chen, S.; Lippens, G.; Zhang, F.; Linhardt, R.; Wang, C.; Klärner, F. G.; Schrader, T.; Landrieu, I.; Bitan, G.; Smet-Nocca, C. Major Differences between the Self-Assembly and Seeding Behavior of Heparin-Induced and in Vitro Phosphorylated Tau and Their Modulation by Potential Inhibitors. ACS Chem. Biol. 2019, 14 (6), 1363–1379. https://doi.org/10.1021/ACSCHEMBIO.9B00325/SUPPL_FILE/CB9B00325_SI_001.PDF.
(47) Zhang, W.; Falcon, B.; Murzin, A. G.; Fan, J.; Crowther, R. A.; Goedert, M.; Scheres, S. H. W. Heparin-Induced Tau Filaments Are Polymorphic and Differ from Those in Alzheimer's and Pick's Diseases. eLife 2019, 8. https://doi.org/10.7554/ELIFE.43584.
(48) Townsend, D.; Fullwood, N. J.; Yates, E. A.; Middleton, D. A. Aggregation Kinetics and Filament Structure of a Tau Fragment Are Influenced by the Sulfation Pattern of the Cofactor Heparin. Biochemistry 2020, 59 (41), 4003–4014. https://doi.org/10.1021/ACS.BIOCHEM.0C00443/ASSET/IMAGES/LARGE/BI0C00443_0005.JPEG.
(49) Katta, V.; Chait, B. T. Hydrogen/Deuterium Exchange Electrospray Ionization Mass Spectrometry: A Method for Probing Protein Conformational Changes in Solution. J. Am. Chem. Soc. 1993, 115 (14), 6317–6321. https://doi.org/10.1021/JA00067A054/ASSET/JA00067A054.FP.PNG_V03.
(50) Miranker, A.; Robinson, C. V.; Radford, S. E.; Aplin, R. T.; Dobson, C. M. Detection of Transient Protein Folding Populations by Mass Spectrometry. Science 1993, 262 (5135), 896–900. https://doi.org/10.1126/SCIENCE.8235611.
(51) Robinson, C. V.; Groß, M.; Eyles, S. J.; Ewbank, J. J.; Mayhew, M.; Hartl, F. U.; Dobson, C. M.; Radford, S. E. Conformation of GroEL-Bound α-Lactalbumin Probed by Mass Spectrometry. Nat. 1994 3726507 1994, 372 (6507), 646–651. https://doi.org/10.1038/372646A0.
(52) Sperry, J. B.; Shi, X.; Rempel, D. L.; Nishimura, Y.; Akashi, S.; Gross, M. L. A Mass Spectrometric Approach to the Study of DNA-Binding Proteins: Interaction of Human TRF2 with Telomeric DNA. Biochemistry 2008, 47 (6), 1797–1807. https://doi.org/10.1021/BI702037P/ASSET/IMAGES/LARGE/BI702037PF00006.JPEG.
(53) Tong, Y.; Wuebbens, M. M.; Rajagopalan, K. V.; Fitzgerald, M. C. Thermodynamic Analysis of Subunit Interactions in Escherichia Coli Molybdopterin Synthase. Biochemistry 2005, 44 (7), 2595–2601. https://doi.org/10.1021/BI047762H/ASSET/IMAGES/LARGE/BI047762HF00005.JPEG.
(54) Xiao, H.; Kaltashov, I. A.; Eyles, S. J. Indirect Assessment of Small Hydrophobic Ligand Binding to a Model Protein Using a Combination of ESI MS and HDX/ESI MS. J. Am. Soc. Mass Spectrom. 2003, 14 (5), 506–515. https://doi.org/10.1016/S1044-0305(03)00135-1.
(55) Zhu, M. M.; Rempel, D. L.; Zhao, J.; Giblin, D. E.; Gross, M. L. Probing Ca2+-Induced Conformational Changes in Porcine Calmodulin by H/D Exchange and ESI-MS: Effect of Cations and Ionic Strength. Biochemistry 2003, 42 (51), 15388–15397. https://doi.org/10.1021/BI035188O/SUPPL_FILE/BI035188OSI20030707_100250.PDF.
(56) Kaltashov, I. A.; Bobst, C. E.; Abzalimov, R. R.; Berkowitz, S. A.; Houde, D. Conformation and Dynamics of Biopharmaceuticals: Transition of Mass Spectrometry-Based Tools from Academe to

Industry. J. Am. Soc. Mass Spectrom. 2009, 21 (3), 323. https://doi.org/10.1016/J.JASMS.2009.10.013.
(57) Makepeace, K. A. T.; Brodie, N. I.; Popov, K. I.; Gudavicius, G.; Nelson, C. J.; Petrotchenko, E. V.; Dokholyan, N. V.; Borchers, C. H. Ligand-Induced Disorder-to-Order Transitions Characterized by Structural Proteomics and Molecular Dynamics Simulations HHS Public Access. J Proteomics 2020, 211, 103544. https://doi.org/10.1016/j.jprot.2019.103544.
(58) Kaltashov, I. A.; Bobst, C. E.; Abzalimov, R. R. H/D Exchange and Mass Spectrometry in the Studies of Protein Conformation and Dynamics: Is There a Need for a Top-down Approach? Anal. Chem. 2009, 81 (19), 7892–7899. https://doi.org/10.1021/AC901366N/ASSET/IMAGES/LARGE/AC-2009-01366N_0001.JPEG.
(59) Möller, I. R.; Merkle, P. S.; Calugareanu, D.; Comamala, G.; Schmidt, S. G.; Loland, C. J.; Rand, K. D. Probing the Conformational Impact of Detergents on the Integral Membrane Protein LeuT by Global HDX-MS. J. Proteomics 2020, 225, 103845. https://doi.org/10.1016/J.JPROT.2020.103845.
(60) Patrie, S. M. Top-Down Mass Spectrometry: Proteomics to Proteoforms. Adv. Exp. Med. Biol. 2016, 919, 171–200. https://doi.org/10.1007/978-3-319-41448-5_8.
(61) Pan, J.; Han, J.; Borchers, C. H.; Konermann, L. Hydrogen/Deuterium Exchange Mass Spectrometry with Top-down Electron Capture Dissociation for Characterizing Structural Transitions of a 17 kDa Protein. J. Am. Chem. Soc. 2009, 131 (35), 12801–12808. https://doi.org/10.1021/JA904379W/ASSET/IMAGES/LARGE/JA-2009-04379W_0005.JPEG.
(62) Abzalimov, R. R.; Kaplan, D. A.; Easterling, M. L.; Kaltashov, I. A. Protein Conformations Can Be Probed in Top-Down HDX MS Experiments Utilizing Electron Transfer Dissociation of Protein Ions Without Hydrogen Scrambling. J. Am. Soc. Mass Spectrom. 2009, 20 (8), 1514–1517. https://doi.org/10.1016/J.JASMS.2009.04.006/SUPPL_FILE/JS8B03536_SI_004.PDF.
(63) Wang, G.; Abzalimov, R. R.; Bobst, C. E.; Kaltashov, I. A. Conformer-Specific Characterization of Nonnative Protein States Using Hydrogen Exchange and Top-down Mass Spectrometry. Proc. Natl. Acad. Sci. U. S. A. 2013, 110 (50), 20087–20092. https://doi.org/10.1073/PNAS.1315029110/SUPPL_FILE/PNAS.201315029SI.PDF.
(64) Pan, J.; Han, J.; Borchers, C. H.; Konermann, L. Structure and Dynamics of Small Soluble Aβ(1-40) Oligomers Studied by Top-down Hydrogen Exchange Mass Spectrometry. Biochemistry 2012, 51 (17), 3694–3703. https://doi.org/10.1021/BI3002049/ASSET/IMAGES/LARGE/BI-2012-002049_0009.JPEG.
(65) Pan, J.; Zhang, S.; Borchers, C. H. Protein Species-Specific Characterization of Conformational Change Induced by Multisite Phosphorylation. 2015. https://doi.org/10.1016/j.jprot.2015.12.002.
(66) Shen, Y.; Zhao, X.; Wang, G.; Chen, D. D. Y. Differential Hydrogen/Deuterium Exchange during Proteoform Separation Enables Characterization of Conformational Differences between Coexisting Protein States. Anal. Chem. 2019, 91 (6), 3805–3809. https://doi.org/10.1021/ACS.ANALCHEM.9B00558/ASSET/IMAGES/LARGE/AC-2019-00558B_0004.JPEG.
(67) Leurs, U.; Mistarz, U. H.; Rand, K. D. Getting to the Core of Protein Pharmaceuticals – Comprehensive Structure Analysis by Mass Spectrometry. Eur. J. Pharm. Biopharm. 2015, 93, 95–109. https://doi.org/10.1016/J.EJPB.2015.03.012.
(68) Wang, G.; Kaltashov, I. A. Approach to Characterization of the Higher Order Structure of Disulfide-Containing Proteins Using Hydrogen/Deuterium Exchange and Top-down Mass Spectrometry. Anal. Chem. 2014, 86 (15), 7293–7298. https://doi.org/10.1021/AC501789E/SUPPL_FILE/AC501789E_SI_001.PDF.
(69) Amon, S.; Trelle, M. B.; Jensen, O. N.; Jørgensen, T. J. D. Spatially Resolved Protein Hydrogen Exchange Measured by Subzero-Cooled Chip-Based Nanoelectrospray Ionization Tandem Mass Spectrometry. Anal. Chem. 2012, 84 (10), 4467–4473. https://doi.org/10.1021/AC300268R/SUPPL_FILE/AC300268R_SI_001.PDF.

(70) Pan, J.; Zhang, S.; Parker, C. E.; Borchers, C. H. Subzero Temperature Chromatography and Top-down Mass Spectrometry for Protein Higher-Order Structure Characterization: Method Validation and Application to Therapeutic Antibodies. J. Am. Chem. Soc. 2014, 136 (37), 13065–13071. https://doi.org/10.1021/JA507880W/SUPPL_FILE/JA507880W_SI_001.PDF.
(71) Huang, R. Y. C.; O'Neil, S. R.; Lipovšek, D.; Chen, G. Conformational Assessment of Adnectin and Adnectin-Drug Conjugate by Hydrogen/Deuterium Exchange Mass Spectrometry. J. Am. Soc. Mass Spectrom. 2018, 29 (7), 1524–1531. https://doi.org/10.1007/s13361-018-1966-2.
(72) Karch, K. R.; Coradin, M.; Zandarashvili, L.; Kan, Z.-Y.; Gerace, M.; Englander, S. W.; Black, B. E.; Garcia, B. A. Hydrogen-Deuterium Exchange Coupled to Top-and Middle-down Mass Spectrometry Reveals Histone Tail Dynamics before and after Nucleosome Assembly Graphical Abstract HHS Public Access eTOC Blurb. Structure 2018, 26 (12), 1651–1663. https://doi.org/10.1016/j.str.2018.08.006.
(73) Cristobal, A.; Marino, F.; Post, H.; Van Den Toorn, H. W. P.; Mohammed, S.; Heck, A. J. R. Toward an Optimized Workflow for Middle-Down Proteomics. Anal. Chem. 2017, 89 (6), 3318–3325. https://doi.org/10.1021/ACS.ANALCHEM.6B03756/ASSET/IMAGES/LARGE/AC-2016-03756G_0003.JPEG.
(74) Pan, J.; Zhang, S.; Chou, A.; Borchers, C. H. Higher-Order Structural Interrogation of Antibodies Using Middle-down Hydrogen/Deuterium Exchange Mass Spectrometry. Chem. Sci. 2016, 7 (2), 1480–1486. https://doi.org/10.1039/C5SC03420E.
(75) Papanastasiou, M.; Mullahoo, J.; DeRuff, K. C.; Bajrami, B.; Karageorgos, I.; Johnston, S. E.; Peckner, R.; Myers, S. A.; Carr, S. A.; Jaffe, J. D. Chasing Tails: Cathepsin-L Improves Structural Analysis of Histones by HX-MS,. Mol. Cell. Proteomics 2019, 18 (10), 2089–2098. https://doi.org/10.1074/MCP.RA119.001325.
(76) James, E. I.; Murphree, T. A.; Vorauer, C.; Engen, J. R.; Guttman, M. Advances in Hydrogen/Deuterium Exchange Mass Spectrometry and the Pursuit of Challenging Biological Systems. Chem. Rev. 2022, 122 (8), 7562–7623. https://doi.org/10.1021/ACS.CHEMREV.1C00279.
(77) Mitra, G. Emerging Role of Mass Spectrometry-Based Structural Proteomics in Elucidating Intrinsic Disorder in Proteins. Proteomics 2021, 21 (3–4). https://doi.org/10.1002/pmic.202000011.
(78) Molday, R. S.; Englander, S. W.; Kallen, R. G. Primary Structure Effects on Peptide Group Hydrogen Exchange. Biochemistry 1972, 11 (2), 150–158. https://doi.org/10.1021/BI00752A003/ASSET/BI00752A003.FP.PNG_V03.
(79) Bai, Y.; Milne, J. S.; Mayne, L.; Englander, S. W. Primary Structure Effects on Peptide Group Hydrogen Exchange. 1993. https://doi.org/10.1002/prot.340170110.
(80) Keppel, T. R.; Weis, D. D. Analysis of Disordered Proteins Using a Simple Apparatus for Millisecond Quench-Flow H/D Exchange. Anal. Chem. 2013, 85 (10), 5161–5168. https://doi.org/10.1021/AC4004979/SUPPL_FILE/AC4004979_SI_001.PDF.
(81) Zhang, Z.; Zhang, A.; Xiao, G. Improved Protein Hydrogen/Deuterium Exchange Mass Spectrometry Platform with Fully Automated Data Processing. Anal. Chem. 2012, 84 (11), 4942–4949. https://doi.org/10.1021/AC300535R/SUPPL_FILE/AC300535R_SI_002.XLS.
(82) Mori, S.; Van Zijl, P. C. M.; Shortle, D. Measurement of Water-Amide Proton Exchange Rates in the Denatured State of Staphylococcal Nuclease by a Magnetization Transfer Technique.
(83) Del Mar, C.; Greenbaum, E. A.; Mayne, L.; Englander, S. W.; Woods, V. L. Structure and Properties of α-Synuclein and Other Amyloids Determined at the Amino Acid Level. Proc. Natl. Acad. Sci. U. S. A. 2005, 102 (43), 15477–15482. https://doi.org/10.1073/PNAS.0507405102/ASSET/E3DEC232-0B0D-40F5-A145-3CB29A9D48F1/ASSETS/GRAPHIC/ZPQ0410597760004.JPEG.
(84) Al-Naqshabandi, M. A.; Weis, D. D. Quantifying Protection in Disordered Proteins Using Millisecond Hydrogen Exchange-Mass Spectrometry and Peptic Reference Peptides. Biochemistry 2017, 56 (31), 4064–4072. https://doi.org/10.1021/acs.biochem.6b01312.

(85) Nguyen, D.; Mayne, L.; Phillips, M. C.; Walter Englander, S. Reference Parameters for Protein Hydrogen Exchange Rates. J. Am. Soc. Mass Spectrom. 2018, 29 (9), 1936–1939. https://doi.org/10.1007/s13361-018-2021-z.
(86) Walters, B. T. Empirical Method to Accurately Determine Peptide-Averaged Protection Factors from Hydrogen Exchange MS Data. Anal. Chem. 2017, 89 (2), 1049–1053. https://doi.org/10.1021/ACS.ANALCHEM.6B03908/ASSET/IMAGES/LARGE/AC-2016-03908U_0004.JPEG.
(87) Keppel, T. R.; Howard, B. A.; Weis, D. D. Mapping Unstructured Regions and Synergistic Folding in Intrinsically Disordered Proteins with Amide H/D Exchange Mass Spectrometry. Biochemistry 2011, 50 (40), 8722–8732. https://doi.org/10.1021/bi200875p.
(88) Rob, T.; Liuni, P.; Gill, P. K.; Zhu, S.; Balachandran, N.; Berti, P. J.; Wilson, D. J. Measuring Dynamics in Weakly Structured Regions of Proteins Using Microfluidics-Enabled Subsecond H/D Exchange Mass Spectrometry. Anal. Chem. 2012, 84 (8), 3771–3779. https://doi.org/10.1021/AC300365U/SUPPL_FILE/AC300365U_SI_001.PDF.
(89) Goswami, D.; Devarakonda, S.; Chalmers, M. J.; Pascal, B. D.; Spiegelman, B. M.; Griffin, P. R. Time Window Expansion for HDX Analysis of an Intrinsically Disordered Protein. J. Am. Soc. Mass Spectrom. 2013, 24 (10), 1584–1592. https://doi.org/10.1007/s13361-013-0669-y.
(90) Rist, W.; Rodriguez, F.; Jørgensen, T. J. D.; Mayer, M. P. Analysis of Subsecond Protein Dynamics by Amide Hydrogen Exchange and Mass Spectrometry Using a Quenched-Flow Setup. Protein Sci. 2005, 14 (3), 626–632. https://doi.org/10.1110/ps.041098305.
(91) Dharmasiri, K.; Smith, D. L. Mass Spectrometric Determination of Isotopic Exchange Rates of Amide Hydrogens Located on the Surfaces of Proteins. Anal. Chem. 1996, 68 (14), 2340–2344. https://doi.org/10.1021/AC9601526/ASSET/IMAGES/MEDIUM/AC9601526E00001.GIF.
(92) Yang, H.; Smith, D. L. Kinetics of Cytochrome c Folding Examined by Hydrogen Exchange and Mass Spectrometry. Biochemistry 1997, 36 (48), 14992–14999. https://doi.org/10.1021/BI9717183/ASSET/IMAGES/LARGE/BI9717183F00004.JPEG.
(93) Deng, Y.; Zhang, Z.; Smith, D. L. FOCUS: H/D EXCHANGE OF PROTEINS IN SOLUTION Comparison of Continuous and Pulsed Labeling Amide Hydrogen Exchange/Mass Spectrometry for Studies of Protein Dynamics; 1999.
(94) Englander, S. W.; Mayne, L.; Kan, Z. Y.; Hu, W. Protein Folding - How and Why: By Hydrogen Exchange, Fragment Separation, and Mass Spectrometry. Annu. Rev. Biophys. 2016, 45, 135–152. https://doi.org/10.1146/annurev-biophys-062215-011121.
(95) Keppel, T. R.; Sarpong, K.; Murray, E. M.; Monsey, J.; Zhu, J.; Bose, R. Biophysical Evidence for Intrinsic Disorder in the C-Terminal Tails of the Epidermal Growth Factor Receptor (EGFR) and HER3 Receptor Tyrosine Kinases *. J. Biol. Chem. 2016, 292 (2), 597–610. https://doi.org/10.1074/jbc.M116.747485.
(96) Svejdal, R. R.; Dickinson, E. R.; Sticker, D.; Kutter, J. P.; Rand, K. D. Thiol-Ene Microfluidic Chip for Performing Hydrogen/Deuterium Exchange of Proteins at Subsecond Time Scales. Anal. Chem. 2019, 91 (2), 1309–1317. https://doi.org/10.1021/ACS.ANALCHEM.8B03050/ASSET/IMAGES/LARGE/AC-2018-03050Q_0006.JPEG.
(97) Chalmers, M. J.; Busby, S. A.; Pascal, B. D.; He, Y.; Hendrickson, C. L.; Marshall, A. G.; Griffin, P. R. Probing Protein Ligand Interactions by Automated Hydrogen/Deuterium Exchange Mass Spectrometry. Anal. Chem. 2006, 78 (4), 1005–1014. https://doi.org/10.1021/AC051294F/SUPPL_FILE/AC051294FSI20050720_053624.XLS.
(98) Wilson, D. J.; Konermann, L. A Capillary Mixer with Adjustable Reaction Chamber Volume for Millisecond Time-Resolved Studies by Electrospray Mass Spectrometry. Anal. Chem. 2003, 75 (23), 6408–6414. https://doi.org/10.1021/ac0346757.

(99) Resetca, D.; Wilson, D. J. Characterizing Rapid, Activity-Linked Conformational Transitions in Proteins via Sub-Second Hydrogen Deuterium Exchange Mass Spectrometry. FEBS J. 2013, 280 (22), 5616–5625. https://doi.org/10.1111/FEBS.12332.
(100) Lento, C.; Zhu, S.; Brown, K. A.; Knox, R.; Liuni, P.; Wilson, D. J. Time-Resolved ElectroSpray Ionization Hydrogen-Deuterium Exchange Mass Spectrometry for Studying Protein Structure and Dynamics. J. Vis. Exp. 2017, No. 122. https://doi.org/10.3791/55464-V.
(101) Zhu, S.; Shala, A.; Bezginov, A.; Sljoka, A.; Audette, G.; Wilson, D. J. Hyperphosphorylation of Intrinsically Disordered Tau Protein Induces an Amyloidogenic Shift in Its Conformational Ensemble. 2015. https://doi.org/10.1371/journal.pone.0120416.
(102) Cieplak-Rotowska, M. K.; Tarnowski, K.; Rubin, M.; Fabian, M. R.; Sonenberg, N.; Dadlez, M.; Niedzwiecka, A. Structural Dynamics of the GW182 Silencing Domain Including Its RNA Recognition Motif (RRM) Revealed by Hydrogen-Deuterium Exchange Mass Spectrometry. J. Am. Soc. Mass Spectrom. 2018, 29 (1), 158–173. https://doi.org/10.1007/S13361-017-1830-9/SUPPL_FILE/JS8B05674_SI_001.DOCX.
(103) Beveridge, R.; Phillips, A. S.; Denbigh, L.; Saleem, H. M.; Macphee, C. E.; Barran, P. E. Relating Gas Phase to Solution Conformations: Lessons from Disordered Proteins. Proteomics 2015, 15, 2872–2883. https://doi.org/10.1002/pmic.201400605.
(104) Tarczewska, A.; Kozłowska, M.; Dobryszycki, P.; Kaus-Drobek, M.; Dadlez, M.; Ożyhar, A. Insight into the Unfolding Properties of Chd64, a Small, Single Domain Protein with a Globular Core and Disordered Tails. 2015. https://doi.org/10.1371/journal.pone.0137074.
(105) Masson, G. R.; Perisic, O.; Burke, J. E.; Williams, R. L. The Intrinsically Disordered Tails of PTEN and PTEN-L Have Distinct Roles in Regulating Substrate Specificity and Membrane Activity. Biochem J 2016, 473, 135–144. https://doi.org/10.1042/BJ20150931.
(106) Mitchell, J. L.; Trible, R. P.; Emert-Sedlak, L. A.; Weis, D. D.; Lerner, E. C.; Applen, J. J.; Sefton, B. M.; Smithgall, T. E.; Engen, J. R. Functional Characterization and Conformational Analysis of the Herpesvirus Saimiri Tip-C484 Protein. J. Mol. Biol. 2007, 366 (4), 1282–1293. https://doi.org/10.1016/J.JMB.2006.12.026.
(107) Marcsisin, S. R.; Narute, P. S.; Emert-Sedlak, L. A.; Kloczewiak, M.; Smithgall, T. E.; Engen, J. R. On the Solution Conformation and Dynamics of the HIV-1 Viral Infectivity Factor. J. Mol. Biol. 2011, 410 (5), 1008–1022. https://doi.org/10.1016/J.JMB.2011.04.053.
(108) Fatalska, A.; Dzhindzhev, N. S.; Dadlez, M.; Glover, D. M. Interaction Interface in the C-Terminal Parts of Centriole Proteins Sas6 and Ana2: Interaction Interface of Sas6-Ana2. Open Biol. 2020, 10 (11). https://doi.org/10.1098/RSOB.200221/.
(109) Roberts, V. A.; Pique, M. E.; Hsu, S.; Li, S. Combining H/D Exchange Mass Spectrometry and Computational Docking to Derive the Structure of Protein-Protein Complexes. Biochemistry 2017, 56 (48), 6329–6342. https://doi.org/10.1021/ACS.BIOCHEM.7B00643/ASSET/IMAGES/LARGE/BI-2017-00643W_0001.JPEG.
(110) Killoran, R. C.; Sowole, M. A.; Halim, M. A.; Konermann, L.; Choy, W.-Y. Conformational Characterization of the Intrinsically Disordered Protein Chibby: Interplay between Structural Elements in Target Recognition. PROTEIN Sci. 2016, 25, 1420–1429. https://doi.org/10.1002/pro.2936.
(111) Dorosz, J.; Hyltoft Kristensen, L.; Aduri, N. G.; Mirza, osman; Lousen, R.; Bucciarelli, saskia; Mehta, V.; Sellés-Baiget, selene; Marie Øie solbak, sara; Bach, A.; Mesa, pablo; Alcon Hernandez, pablo; Montoya, G.; Nguyen, tam N.; Rand, K. D.; Boesen, thomas; Gajhede, M. Molecular Architecture of the Jumonji C Family Histone Demethylase KDM5B. https://doi.org/10.1038/s41598-019-40573-y.
(112) Shi, X.; Yokom, A. L.; Wang, C.; Young, L. N.; Youle, R. J.; Hurley, J. H. ULK Complex Organization in Autophagy by a C-Shaped FIP200 N-Terminal Domain Dimer. J. Cell Biol. 2020, 219 (7). https://doi.org/10.1083/JCB.201911047/151844.

(113) Mandacaru, S. C.; Do Vale, L. H. F.; Vahidi, S.; Xiao, Y.; Skinner, O. S.; Ricart, C. A. O.; Kelleher, N. L.; De Sousa, M. V.; Konermann, L. Characterizing the Structure and Oligomerization of Major Royal Jelly Protein 1 (MRJP1) by Mass Spectrometry and Complementary Biophysical Tools. Biochemistry 2017, 56 (11), 1645–1655. https://doi.org/10.1021/ACS.BIOCHEM.7B00020/ASSET/IMAGES/LARGE/BI-2017-000207_0008.JPEG.
(114) Su, M. Y.; Morris, K. L.; Kim, D. J.; Fu, Y.; Lawrence, R.; Stjepanovic, G.; Zoncu, R.; Hurley, J. H. Hybrid Structure of the RagA/C-Ragulator mTORC1 Activation Complex. Mol. Cell 2017, 68 (5), 835-846.e3. https://doi.org/10.1016/j.molcel.2017.10.016.
(115) Dornan, G. L.; Dalwadi, U.; Hamelin, D. J.; Hoffmann, R. M.; Yip, C. K.; Burke, J. E. Probing the Architecture, Dynamics, and Inhibition of the PI4KIIIα/TTC7/FAM126 Complex. 2018. https://doi.org/10.1016/j.jmb.2018.07.020.
(116) Brodie, N. I.; Popov, K. I.; Petrotchenko, E. V.; Dokholyan ID, N. V.; Borchers ID, C. H. Conformational Ensemble of Native α-Synuclein in Solution as Determined by Short-Distance Crosslinking Constraint-Guided Discrete Molecular Dynamics Simulations. 2019. https://doi.org/10.1371/journal.pcbi.1006859.
(117) Trelle, M. B.; Pedersen, S.; Østerlund, E. C.; Madsen, J. B.; Kristensen, S. R.; Jørgensen, T. J. D. An Asymmetric Runaway Domain Swap Antithrombin Dimer as a Key Intermediate for Polymerization Revealed by Hydrogen/Deuterium-Exchange Mass Spectrometry. Anal. Chem. 2017, 89 (1), 616–624. https://doi.org/10.1021/ACS.ANALCHEM.6B02518/ASSET/IMAGES/LARGE/AC-2016-02518T_0005.JPEG.
(118) Kaldmäe, M.; Leppert, A.; Chen, G.; Sarr, M.; Sahin, C.; Nordling, K.; Kronqvist, N.; Gonzalvo-Ulla, M.; Fritz, N.; Abelein, A.; Laín, S.; Biverstål, H.; Jörnvall, H.; Lane, D. P.; Rising, A.; Johansson, J.; Landreh, M. High Intracellular Stability of the Spidroin N-Terminal Domain in Spite of Abundant Amyloidogenic Segments Revealed by in-Cell Hydrogen/Deuterium Exchange Mass Spectrometry. FEBS J. 2020, 287 (13), 2823–2833. https://doi.org/10.1111/febs.15169.
(119) Pantazatos, D.; Kim, J. S.; Klock, H. E.; Stevens, R. C.; Wilson, I. A.; Lesley, S. A.; Woods, V. L. Rapid Refinement of Crystallographic Protein Construct Definition Employing Enhanced Hydrogen/Deuterium Exchange MS. Proc. Natl. Acad. Sci. U. S. A. 2004, 101 (3), 751–756. https://doi.org/10.1073/PNAS.0307204101/SUPPL_FILE/7204FIG5.PDF.
(120) Fowler, M. L.; Mcphail, J. A.; Jenkins, M. L.; Masson, G. R.; Rutaganira, F. U.; Shokat, K. M.; Williams, R. L.; Burke, J. E. Using Hydrogen Deuterium Exchange Mass Spectrometry to Engineer Optimized Constructs for Crystallization of Protein Complexes: Case Study of PI4KIIIb with Rab11. PROTEIN Sci. 2016, 25, 826–839. https://doi.org/10.1002/pro.2879.
(121) Esben Trabjerg, X.; Kartberg, F.; Christensen, S.; Rand, K. D. Conformational Characterization of Nerve Growth Factor-Reveals That Its Regulatory pro-Part Domain Stabilizes Three Loop Regions in Its Mature Part. 2017. https://doi.org/10.1074/jbc.M117.803320.
(122) Mysling, S.; Kristensen, K. K.; Larsson, M.; Beigneux, A. P.; Gå Rdsvoll, H.; Fong, L. G.; Bensadouen, A.; Jørgensen, T. J.; Young, S. G.; Ploug, M. The Acidic Domain of the Endothelial Membrane Protein GPIHBP1 Stabilizes Lipoprotein Lipase Activity by Preventing Unfolding of Its Catalytic Domain. https://doi.org/10.7554/eLife.12095.001.
(123) Saikusa, K.; Nagadoi, A.; Hara, K.; Fuchigami, S.; Kurumizaka, H.; Nishimura, Y.; Akashi, S. Mass Spectrometric Approach for Characterizing the Disordered Tail Regions of the Histone H2A/H2B Dimer. Anal. Chem. 2015, 87 (4), 2220–2227. https://doi.org/10.1021/AC503689W/SUPPL_FILE/AC503689W_SI_001.PDF.
(124) Deredge, D. J.; Huang, W.; Hui, C.; Matsumura, H.; Yue, Z.; Moënne-Loccoz, P.; Shen, J.; Wintrode, P. L.; Wilks, A. Ligand-Induced Allostery in the Interaction of the Pseudomonas Aeruginosa Heme Binding Protein with Heme Oxygenase. Proc. Natl. Acad. Sci. U. S. A. 2017, 114

(13), 3421–3426. https://doi.org/10.1073/PNAS.1606931114/SUPPL_FILE/PNAS.201606931SI.PDF.
(125) Tischer, A.; Brehm, M. A.; Machha, V. R.; Moon-Tasson, L.; Benson, L. M.; Nelton, K. J.; Leger, R. R.; Obser, T.; Martinez-Vargas, M.; Whitten, S. T.; Chen, D.; Pruthi, R. K.; Robert, H.; Iii, B.; Cruz, M. A.; Schneppenheim, R.; Auton, M. Evidence for the Misfolding of the A1 Domain within Multimeric von Willebrand Factor in Type 2 von Willebrand Disease. J. Mol. Biol. 2020, 432, 305–323. https://doi.org/10.1016/j.jmb.2019.09.022.
(126) Zhu, S.; Khatun, R.; Lento, C.; Sheng, Y.; Wilson, D. J. Enhanced Binding Affinity via Destabilization of the Unbound State: A Millisecond Hydrogen-Deuterium Exchange Study of the Interaction between P53 and a Pleckstrin Homology Domain. Biochemistry 2017, 56 (32), 4127–4133. https://doi.org/10.1021/acs.biochem.7b00193.
(127) Betts, G. N.; Van Der Geer, P.; Komives, E. A. Structural and Functional Consequences of Tyrosine Phosphorylation in the LRP1 Cytoplasmic Domain *. 2008. https://doi.org/10.1074/jbc.M709514200.
(128) Li, X.; Eyles, S. J.; Lynmarie, X.; Thompson, K. Hydrogen Exchange of Chemoreceptors in Functional Complexes Suggests Protein Stabilization Mediates Long-Range Allosteric Coupling. J Biol Chem 2019, 294 (44), 16062–16079. https://doi.org/10.1074/jbc.RA119.009865.
(129) Okuda, M.; Nishimura, Y. Extended String Binding Mode of the Phosphorylated Transactivation Domain of Tumor Suppressor P53. J Am Chem Soc 2014, 17, 2021. https://doi.org/10.1021/ja506351f.
(130) Van Der Lee, R.; Buljan, M.; Lang, B.; Weatheritt, R. J.; Daughdrill, G. W.; Dunker, A. K.; Fuxreiter, M.; Gough, J.; Gsponer, J.; Jones, D. T.; Kim, P. M.; Kriwacki, R. W.; Oldfield, C. J.; Pappu, R. V.; Tompa, P.; Uversky, V. N.; Wright, P. E.; Babu, M. M. Classification of Intrinsically Disordered Regions and Proteins. Chem. Rev. 2014, 114 (13), 6589–6631. https://doi.org/10.1021/CR400525M/ASSET/IMAGES/MEDIUM/CR-2013-00525M_0005.GIF.
(131) Kacirova, M.; Kosek, D.; Kadek, A.; Man, P.; Vecer, J.; Herman, P.; Obsilova, V.; Obsil, T. Structural Characterization of Phosducin and Its Complex with the 14-3-3 Protein *. 2015. https://doi.org/10.1074/jbc.M115.636563.
(132) Papanastasiou, M.; Koutsogiannaki, S.; Sarigiannis, Y.; Geisbrecht, B. V.; Ricklin, D.; Lambris, J. D. Structural Implications for the Formation and Function of the Complement Effector Protein iC3b 1 HHS Public Access. J Immunol 2017, 198 (8), 3326–3335. https://doi.org/10.4049/jimmunol.1601864.
(133) Skorupska, A.; Bystranowska, D.; Dąbrowska, K.; Ożyhar, A. Calcium Ions Modulate the Structure of the Intrinsically Disordered Nucleobindin-2 Protein. 2020. https://doi.org/10.1016/j.ijbiomac.2020.03.110.
(134) Dickinson, E. R.; Jurneczko, E.; Nicholson, J.; Hupp, T. R.; Zawacka-Pankau, J.; Selivanova, G.; Barran, P. E. The Use of Ion Mobility Mass Spectrometry to Probe Modulation of the Structure of P53 and of MDM2 by Small Molecule Inhibitors. Front. Mol. Biosci. 2015, 2 (JUL), 39. https://doi.org/10.3389/fmolb.2015.00039.
(135) Pirrone, G. F.; Emert-Sedlak, L. A.; Wales, T. E.; Smithgall, T. E.; Kent, M. S.; Engen, J. R. The Membrane-Associated Conformation of HIV-1 Nef Investigated with Hydrogen Exchange Mass Spectrometry at a Langmuir Monolayer HHS Public Access. Anal Chem 2015, 87 (14), 7030–7035. https://doi.org/10.1021/acs.analchem.5b01725.
(136) Hamdi, K.; Salladini, E.; O'brien, D. P.; Brier, S.; Chenal, A.; Yacoubi, I.; Longhi, S. Structural Disorder and Induced Folding within Two Cereal, ABA Stress and Ripening (ASR) Proteins OPEN. https://doi.org/10.1038/s41598-017-15299-4.
(137) Ramirez-Sarmiento, C. A.; Komives, E. A. Hydrogen-Deuterium Exchange Mass Spectrometry Reveals Folding and Allostery in Protein-Protein Interactions. https://doi.org/10.1016/j.ymeth.2018.04.001.
(138) Dembinski, H. E.; Wismer, K.; Vargas, J. D.; Suryawanshi, G. W.; Kern, N.; Kroon, G.; Dyson, H. J.; Hoffmann, A.; Komives, E. A. Functional Importance of Stripping in NFκB Signaling Revealed by

a Stripping-Impaired IκBα Mutant. Proc. Natl. Acad. Sci. U. S. A. 2017, 114 (8), 1916–1921. https://doi.org/10.1073/pnas.1610192114.
(139) Mitchelle, I.; De Vera, S.; Zheng, J.; Novick, S.; Shang, J.; Hughes, T.; Brust, R.; Munoz-Tello, P.; Gardner, W. J.; Marciano, D. P.; Kong, X.; Griffin, P. R.; Kojetin, D. J. Synergistic Regulation of Coregulator/Nuclear Receptor Interaction by Ligand and DNA HHS Public Access. Structure 2017, 25 (10), 1506–1518. https://doi.org/10.1016/j.str.2017.07.019.
(140) Medina, E.; Villalobos, P.; Hamilton, G. L.; Komives, E. A.; Sanabria, H.; Ramírez-Sarmiento, C. A.; Babul, J. Intrinsically Disordered Regions of the DNA-Binding Domain of Human FoxP1 Facilitate Domain Swapping. J. Mol. Biol. 2020, 432 (19), 5411–5429. https://doi.org/10.1016/j.jmb.2020.07.017.
(141) Rusinga, F. I.; Weis, D. D. Soft Interactions and Volume Exclusion by Polymeric Crowders Can Stabilize or Destabilize Transient Structure in Disordered Proteins Depending on Polymer Concentration. Proteins Struct. Funct. Bioinforma. 2017, 85 (8), 1468–1479. https://doi.org/10.1002/prot.25307.
(142) Georgescauld, F.; Wales, T. E.; Engen, J. R. Hydrogen Deuterium Exchange Mass Spectrometry Applied to Chaperones and Chaperone-Assisted Protein Folding. Expert Rev. Proteomics 2019, 16 (7), 613–625. https://doi.org/10.1080/14789450.2019.1633920.
(143) Miranker, A.; Robinson, C. V.; Radford, S. E.; Dobson, C. M. Investigation of Protein Folding by Mass Spectrometry. FASEB J. 1996, 10 (1), 93–101. https://doi.org/10.1096/FASEBJ.10.1.8566553.
(144) Deng, Y.; Smith, D. L. Rate and Equilibrium Constants for Protein Unfolding and Refolding Determined by Hydrogen Exchange-Mass Spectrometry. Anal. Biochem. 1999, 276 (2), 150–160. https://doi.org/10.1006/ABIO.1999.4347.
(145) Nishimura, C.; Beppu, T. Review Folding of Apomyoglobin: Analysis of Transient Intermediate Structure during Refolding Using Quick Hydrogen Deuterium Exchange and NMR. https://doi.org/10.2183/pjab.93.002.
(146) Hu, W.; Kan, Z. Y.; Mayne, L.; Englander, S. W. Cytochrome c Folds through Foldon-Dependent Native-like Intermediates in an Ordered Pathway. Proc. Natl. Acad. Sci. U. S. A. 2016, 113 (14), 3809–3814. https://doi.org/10.1073/pnas.1522674113.
(147) Mandell, J. G.; Falick, A. M.; Komives, E. A. Identification of Protein-Protein Interfaces by Decreased Amide Proton Solvent Accessibility. Proc. Natl. Acad. Sci. U. S. A. 1998, 95 (25), 14705–14710. https://doi.org/10.1073/PNAS.95.25.14705/ASSET/325D6664-2DD2-453C-8D2A-ECD199FCEA03/ASSETS/GRAPHIC/PQ2483803007.JPEG.
(148) Chen, J.; Liu, Z.; Creagh, J.; Zheng, R.; Thomas McDonald, X. V. Physical and Functional Interaction Sites in Cytoplasmic Domains of KCNQ1 and KCNE1 Channel Subunits. Am J Physiol Heart Circ Physiol 2020, 318, 212–222. https://doi.org/10.1152/ajpheart.00459.2019.-The.
(149) Mysling, S.; Kristensen, K. K.; Larsson, M.; Kovrov, O.; Bensadouen, A.; Jørgensen, T. J. D.; Olivecrona, G.; Young, S. G.; Ploug, M. The Angiopoietin-like Protein Angptl4 Catalyzes Unfolding of the Hydrolase Domain in Lipoprotein Lipase and the Endothelial Membrane Protein Gpihbp1 Counteracts This Unfolding. eLife 2016, 5 (DECEMBER2016), 18. https://doi.org/10.7554/ELIFE.20958.
(150) Benhaim, M. A.; Mangala Prasad, V.; Garcia, N. K.; Guttman, M.; Lee, K. K. Structural Monitoring of a Transient Intermediate in the Hemagglutinin Fusion Machinery on Influenza Virions. Sci. Adv. 2020, 6 (18). https://doi.org/10.1126/SCIADV.AAZ8822/SUPPL_FILE/AAZ8822_SM.PDF.
(151) Wang, H.; Shu, Q.; Rempel, D. L.; Frieden, C.; Gross, M. L. Continuous and Pulsed Hydrogen-Deuterium Exchange and Mass Spectrometry Characterize CsgE Oligomerization. Biochemistry 2015, 54 (42), 6475–6481. https://doi.org/10.1021/ACS.BIOCHEM.5B00871/ASSET/IMAGES/LARGE/BI-2015-00871M_0006.JPEG.
(152) Wang, H.; Shu, Q.; Frieden, C.; Gross, M. L. Deamidation Slows Curli Amyloid-Protein Aggregation. Biochemistry 2017, 56 (23), 2865–2872.

https://doi.org/10.1021/ACS.BIOCHEM.7B00241/ASSET/IMAGES/LARGE/BI-2017-00241U_0007.JPEG.
(153) Sabareesan, A. T.; Udgaonkar, J. B. Pathogenic Mutations within the Disordered Palindromic Region of the Prion Protein Induce Structure Therein and Accelerate the Formation of Misfolded Oligomers. 2016. https://doi.org/10.1016/j.jmb.2016.08.015.
(154) Renawala, H. K.; Chandrababu, K. B.; Topp, E. M. Fibrillation of Human Calcitonin and Its Analogs: Effects of Phosphorylation and Disulfide Reduction. Biophysj 2021, 120, 86–100. https://doi.org/10.1016/j.bpj.2020.11.009.
(155) Zhu, M. M.; Rempel, D. L.; Du, Z.; Gross, M. L. Quantification of Protein-Ligand Interactions by Mass Spectrometry, Titration, and H/D Exchange: PLIMSTEX. J. Am. Chem. Soc. 2003, 125 (18), 5252–5253. https://doi.org/10.1021/JA029460D/SUPPL_FILE/JA029460DSI20030228_083725.PDF.
(156) Tu, T.; Drăguşanu, M.; Petre, B. A.; Rempel, D. L.; Przybylski, M.; Gross, M. L. Protein-Peptide Affinity Determination Using an H/D Exchange Dilution Strategy: Application to Antigen-Antibody Interactions. J. Am. Soc. Mass Spectrom. 2010, 21 (10), 1660–1667. https://doi.org/10.1016/J.JASMS.2010.03.030.
(157) Hopper, E. D.; Pittman, A. M. C.; Tucker, C. L.; Campa, M. J.; Patz, E. F.; Fitzgerald, M. C. Hydrogen/Deuterium Exchange- and Protease Digestion-Based Screening Assay for Protein - Ligand Binding Detection. Anal. Chem. 2009, 81 (16), 6860–6867. https://doi.org/10.1021/AC900854T/SUPPL_FILE/AC900854T_SI_001.PDF.
(158) Ghaemmaghami, S.; Fitzgerald, M. C.; Oas, T. G. A Quantitative, High-Throughput Screen for Protein Stability. Proc. Natl. Acad. Sci. U. S. A. 2000, 97 (15), 8296–8301. https://doi.org/10.1073/PNAS.140111397/ASSET/0F5760EE-2A03-498C-A56F-4BD494A52A58/ASSETS/GRAPHIC/PQ1401113004.JPEG.
(159) Masson, G. R.; Maslen, S. L.; Williams, R. L. Analysis of Phosphoinositide 3-Kinase Inhibitors by Bottom-up Electron-Transfer Dissociation Hydrogen/Deuterium Exchange Mass Spectrometry. 2017. https://doi.org/10.1042/BCJ20170127.
(160) Pancsa, R.; Raimondi, D.; Cilia, E.; Vranken, W. F. Article Early Folding Events, Local Interactions, and Conservation of Protein Backbone Rigidity. Biophysj 2016, 110, 572–583. https://doi.org/10.1016/j.bpj.2015.12.028.
(161) Raimondi, D.; Orlando, G.; Pancsa, R.; Khan, T.; Vranken, W. F. Exploring the Sequence-Based Prediction of Folding Initiation Sites in Proteins OPEN. 2017. https://doi.org/10.1038/s41598-017-08366-3.
(162) Tsirigotaki, A.; Papanastasiou, M.; Trelle, M. B.; Jørgensen, T. J. D.; Economou, A. Analysis of Translocation-Competent Secretory Proteins by HDX-MS. https://doi.org/10.1016/bs.mie.2016.09.028.
(163) Xie, X.; Yu, T.; Li, X.; Zhang, N.; Foster, L. J.; Peng, C.; Huang, W.; He, G. Recent Advances in Targeting the “Undruggable” Proteins: From Drug Discovery to Clinical Trials. Signal Transduct. Target. Ther. 2023 81 2023, 8 (1), 1–71. https://doi.org/10.1038/S41392-023-01589-Z.
(164) Uversky, V. N. REVIEW A Decade and a Half of Protein Intrinsic Disorder: Biology Still Waits for Physics. 2013. https://doi.org/10.1002/pro.2261.
(165) Ehrnhoefer, D. E.; Duennwald, M.; Markovic, P.; Wacker, J. L.; Engemann, S.; Roark, M.; Legleiter, J.; Marsh, J. L.; Thompson, L. M.; Lindquist, S.; Muchowski, P. J.; Wanker, E. E. Green Tea (-)-Epigallocatechin-Gallate Modulates Early Events in Huntingtin Misfolding and Reduces Toxicity in Huntington’s Disease Models. Hum. Mol. Genet. 2006, 15 (18), 2743–2751. https://doi.org/10.1093/HMG/DDL210.
(166) Lendel, C.; Bertoncini, C. W.; Cremades, N.; Waudby, C. A.; Vendruscolo, M.; Dobson, C. M.; Schenk, D.; Christodoulou, J.; Toth, G. On the Mechanism of Nonspecific Inhibitors of Protein Aggregation: Dissecting the Interactions of Alpha-Synuclein with Congo Red and Lacmoid. Biochemistry 2009, 48 (35), 8322–8334. https://doi.org/10.1021/BI901285X.

(167) Taha, H. B.; Chawla, E.; Bitan, G. IM-MS and ECD-MS/MS Provide Insight into Modulation of Amyloid Proteins Self-Assembly by Peptides and Small Molecules. J. Am. Soc. Mass Spectrom. 2023, 34 (10), 2066–2086. https://doi.org/10.1021/JASMS.3C00065/ASSET/IMAGES/LARGE/JS3C00065_0011.JPEG.
(168) Lee, B. I.; Suh, Y. S.; Chung, Y. J.; Yu, K.; Park, C. B. Shedding Light on Alzheimer's β-Amyloidosis: Photosensitized Methylene Blue Inhibits Self-Assembly of β-Amyloid Peptides and Disintegrates Their Aggregates. Sci. Rep. 2017 71 2017, 7 (1), 1–10. https://doi.org/10.1038/S41598-017-07581-2.
(169) Dubey, T.; Gorantla, N. V.; Chandrashekara, K. T.; Chinnathambi, S. Photoexcited Toluidine Blue Inhibits Tau Aggregation in Alzheimer's Disease. ACS Omega 2019. https://doi.org/10.1021/ACSOMEGA.9B02792/ASSET/IMAGES/MEDIUM/AO9B02792_M001.GIF.
(170) Avgerinos, K. I.; Manolopoulos, A.; Ferrucci, L.; Kapogiannis, D. Critical Assessment of Anti-Amyloid-β Monoclonal Antibodies Effects in Alzheimer's Disease: A Systematic Review and Meta-Analysis Highlighting Target Engagement and Clinical Meaningfulness. Sci. Rep. 2024 141 2024, 14 (1), 1–12. https://doi.org/10.1038/S41598-024-75204-8.
(171) Baggett, D. W.; Nath, A. The Rational Discovery of a Tau Aggregation Inhibitor. Biochemistry 2018, 57 (42), 6099–6107. https://doi.org/10.1021/ACS.BIOCHEM.8B00581/ASSET/IMAGES/LARGE/BI-2018-00581Y_0004.JPEG.
(172) Bulic, B.; Pickhardt, M.; Mandelkow, E. M.; Mandelkow, E. Tau Protein and Tau Aggregation Inhibitors. Neuropharmacology 2010, 59 (4–5), 276–289. https://doi.org/10.1016/J.NEUROPHARM.2010.01.016.
(173) Scheraga, H. A.; Khalili, M.; Liwo, A. Protein-Folding Dynamics: Overview of Molecular Simulation Techniques. Annu. Rev. Phys. Chem. 2007, 58, 57–83. https://doi.org/10.1146/ANNUREV.PHYSCHEM.58.032806.104614.
(174) Leone, V.; Marinelli, F.; Carloni, P.; Parrinello, M. Targeting Biomolecular Flexibility with Metadynamics. Curr. Opin. Struct. Biol. 2010, 20 (2), 148–154. https://doi.org/10.1016/J.SBI.2010.01.011.
(175) Nath, A.; Sammalkorpi, M.; Dewitt, D. C.; Trexler, A. J.; Elbaum-Garfinkle, S.; O'Hern, C. S.; Rhoades, E. The Conformational Ensembles of α-Synuclein and Tau: Combining Single-Molecule FRET and Simulations. Biophys. J. 2012, 103 (9), 1940. https://doi.org/10.1016/J.BPJ.2012.09.032.
(176) Huang, J.; MacKerell, A. D. Force Field Development and Simulations of Intrinsically Disordered Proteins. Curr. Opin. Struct. Biol. 2018, 48, 40–48. https://doi.org/10.1016/J.SBI.2017.10.008.
(177) Erdős, G.; Dosztányi, Z. Deep Learning for Intrinsically Disordered Proteins: From Improved Predictions to Deciphering Conformational Ensembles. Curr. Opin. Struct. Biol. 2024, 89, 102950. https://doi.org/10.1016/J.SBI.2024.102950.
(178) Baggett, D. W.; Nath, A. Structure-Activity Relationships of Novel Tau Ligands: Passive Fibril Binders and Active Aggregation Inhibitors. ACS Chem. Biol. 2022, 17 (3), 701–708. https://doi.org/10.1021/ACSCHEMBIO.2C00012/ASSET/IMAGES/LARGE/CB2C00012_0006.JPEG.
(179) James, E. I.; Baggett, D. W.; Chang, E.; Schachter, J.; Nixey, T.; Choi, K.; Guttman, M.; Nath, A. Tryptanthrin Analogs Substoichiometrically Inhibit Seeded and Unseeded Tau4RD Aggregation. eLife 2024, 13. https://doi.org/10.7554/ELIFE.98227.1.

2. Tryptanthrin Analogs Substoichiometrically Inhibit Seeded and Unseeded Tau4RD Aggregation

This text has been reproduced with limited changes from:

James, E. I.; Baggett, D. W.; Chang, E.; Schachter, J.; Nixey, T.; Choi, K.; Guttman, M.; Nath, A. Tryptanthrin Analogs Substoichiometrically Inhibit Seeded and Unseeded Tau4RD Aggregation. *eLife* **2024**, *13*. https://doi.org/10.7554/ELIFE.98227.1.

2.1 Abstract

Microtubule-associated protein tau is an intrinsically disordered protein (IDP) that forms characteristic fibrillar aggregates in several diseases, the most well-known of which is Alzheimer's disease (AD). Despite keen interest in disrupting or inhibiting tau aggregation to treat AD and related dementias, there are currently no FDA-approved tau-targeting drugs. This is due, in part, to the fact that tau and other IDPs do not exhibit a single well-defined conformation but instead populate a fluctuating conformational ensemble that precludes finding a stable "druggable" pocket. Despite this challenge, we previously reported the discovery of two novel families of tau ligands, including a class of aggregation inhibitors, identified through a protocol that combines molecular dynamics, structural analysis, and machine learning. Here we extend our exploration of tau druggability with the identification of tryptanthrin and its analogs as potent, substoichiometric aggregation inhibitors, with the best compounds showing potencies in the low nanomolar range even at a ~100-fold molar excess of tau4RD (a truncated tau construct). Moreover, conservative changes in small molecule structure can have large impacts on inhibitory potency, demonstrating that similar structure-activity relationship (SAR) principles as used for traditional drug development also apply to tau and potentially to other IDPs.

2.2 Introduction

Intrinsically disordered proteins (IDPs) play important structural and signaling roles *in vivo*.[1] IDPs lack a single stable folded structure and often fulfill their roles by dynamically rearranging to interact with multiple different protein or macromolecular binding partners.[2,3] This conformational plasticity also makes IDPs prone to misfolding and aggregation. Aggregation of specific IDPs into amyloid-type fibrils and a variety of smaller cytotoxic species is a hallmark of proteopathic diseases such as Alzheimer's disease (AD), Parkinson's disease, and Type II diabetes mellitus.[4–7]

Microtubule-associated protein tau, an IDP that stabilizes neuronal axons, exhibits pathological dysfunction and aggregation in a group of ~20 neurodegenerative diseases that are collectively called tauopathies. Tau consists of six isoforms in the human brain that vary in their number of N-terminal inserts and repeat sequences in the microtubule binding region (MTBR). In primary tauopathies such as Pick's disease, frontotemporal dementia with parkinsonism in chromosome 17, and progressive supranuclear palsy, amyloid deposition of one or more tau isoforms is the predominant pathological characteristic. Secondary tauopathies such as AD and Lewy body dementia (LBD) are characterized by the extensive deposition of both tau and one or more other aggregation-prone proteins (e.g., amyloid-β [Aβ] in AD, alpha-synuclein in LBD).[5,8–12]

Tauopathies and related neurodegenerative proteinopathies present a stark challenge to human health, affecting tens of millions globally, with very few effective therapeutic options.[8–13] However, recently developed anti-Aβ therapeutic antibodies for AD can slow disease progression, albeit modestly and with a substantial risk of side effects.[14,15] While these treatments are far from ideal, they do demonstrate that disease-modifying therapies targeting protein aggregation are indeed feasible, further supporting the idea that inhibiting tau aggregation could advance the treatment of both primary and secondary tauopathies. In particular, small molecule tau aggregation inhibitors could be made orders of magnitude more bioavailable in the brain than antibody drugs,[16] and are better suited to target intracellular tau species. Accordingly, there is active interest in developing both antibody-based and small molecule tau aggregation inhibitors.

Despite this interest, tau and other IDP targets present unique challenges to rational drug design. First, the lack of well-defined structure in the physiological state prevents conventional structure-based discovery and design. Second, the specificity and strength of structure-activity relationships (SAR) for IDP/small molecule interactions remain open questions. For folded proteins, it is axiomatic that the chemical structure of a candidate therapeutic can be systematically modified to improve activity (e.g., selectivity, inhibition) by altering the physicochemical interaction between the ligand and protein target. It remains to be seen whether and how altering the 3D conformation of a small molecule modifies activity towards a disordered target.

Our approach differs from efforts to develop broad-spectrum aggregation inhibitors, whether based on natural products,[17,18] molecular tweezer[19] or designed peptide scaffolds,[20–22] that target later oligomeric or fibrillar states. Instead, we target disordered, monomeric states with the goals of (1) achieving specificity for tau vs. other aggregation-prone proteins, and (2) interrupting aggregation before cytotoxic oligomers are populated.[23,24] In previous work, we developed a novel enhanced sampling technique, repeated simulated annealing molecular dynamics (ReSA-MD), to generate a conformer library of the tau MTBR (tau4RD).[25] A subset of these conformers displaying locally persistent structure was used as docking targets for *in silico* compound screening. To date, we have identified a novel family of tau4RD aggregation inhibitors, and a second family of compounds that potently binds to tau4RD fibrils without affecting the kinetics of aggregation.[25,26] With this discovery pipeline, we now identify the tryptanthrin (TA) family as potent, substoichiometric inhibitors of tau4RD aggregation. Though TA, a plant alkaloid, is known to have anti-microbial,[27–30] anti-inflammatory,[31,32] anti-fungal,[33,34] and anti-cancer activity,[35–38] our work is the first demonstration of TA as an anti-amyloid agent. Here we describe the SAR of TA analogs against tau4RD aggregation and identify the mechanism by which they inhibit aggregation.

2.3 Results

2.3.1 Design, synthesis, and screening of TA analogs

We began by mining a 284,463-compound proprietary library using a regression model trained on our previous *in silico*/*in vitro* screening effort[21] to identify compounds likely to modulate tau aggregation. Characterizing heparin-induced tau4RD aggregation at a 1:2 protein:compound molar ratio using a thioflavin T (ThT) fluorescence assay revealed that TA (**1**) and three of its analogs (**2**–**4**) were among the most potent inhibitors (Fig. 2.1). ThT is widely used as a probe of protein aggregation, but is neither perfectly specific nor selective for amyloid aggregates. Therefore, orthogonal label-free assays were used to confirm that TA analogs are *bona fide* aggregation inhibitors, increasing the amount of tau4RD remaining in solution at the end of the reaction (SI Fig. 2.1). Several other chemically distinct screened compounds showed reasonable aggregation inhibition (compounds **S1**–**S20**; SI Fig. 2.2), further demonstrating the value of ReSA-MD-guided screening in targeting disordered proteins such as tau. However, this study focuses on the TA scaffold, both because these compounds displayed the greatest activity, and because they afforded an excellent opportunity to explore the structure-activity relationship of a novel family of tau aggregation inhibitors.

A 14-compound library (**5**–**18**) was synthesized based on 8-chloroTA (**3**), the most potent of the first four compounds, exploring the effects of modifications to the quinazoline ring (Fig. 2.2A). Synthesis from commercially available precursors used a one-step process driven by visible light in the presence of the dye

Rose Bengal.[39] The activity of **1** synthesized in-house was comparable to that of samples obtained from two different commercial vendors (SI Fig. 2.3). All of these compounds strongly (10 of 13 compounds: **5**, **6**, **8**, **10**, **11**, **13**–**18**) or moderately (3 of 13: **7**, **9**, **12**) inhibited tau4RD aggregation (Fig. 2.2B/C) at 5 μM. A subsequent 12 compounds (**19**–**30**) were synthesized based on 1,8-dichloroTA (**16**), selected based on its inhibitory properties and relatively low levels of cytotoxicity (SI Fig. 2.4), to explore the effect of modifications to the indole ring. Three compounds (**20**, **24**, **25**) were dropped due to solubility issues, but seven of the remaining nine (**19**, **22**, **23**, **27**–**30**) inhibited tau aggregation more strongly than **3**.

2.3.2 Potency of TA analogs

Evaluating and quantifying the potency of aggregation inhibitors from dose response experiments requires consideration of certain experimental design factors. The first is the ratio of inhibitor to other species involved in aggregation: in this case, tau4RD and the aggregation inducer heparin. Dose response aggregation assays yield a half-maximal effective concentration EC_{50}, distinct from a dissociation constant K_D or an inhibitor binding constant K_I. The EC_{50} would be expected to change if either the tau4RD or heparin concentrations were altered. It is important to recognize that the ratio of the EC_{50} to tau4RD concentration is more relevant in this context than the K_D or K_I itself. A stoichiometric inhibitor (i.e., one that must bind 1:1 to tau4RD for activity) would have a EC_{50} equal to the tau4RD concentration regardless of how low its K_D for tau4RD might be. Dose response assays were conducted at a concentration of 5 μM tau4RD and 5 μM heparin (with an average molecular weight of 3 kDa), in the presence of 1% DMSO, while compound concentrations varied from 62.5 nM to 5 μM.

A second factor is the choice of parameter used to quantify compound effects. TA analogs were seen to affect both the midpoint of the aggregation time course (t_{50}) and the maximal fluorescence achieved at the end of the reaction ($F_{plateau}$). Accordingly, we quantify dose response based on the ThT fluorescence at the t_{50} of the *vehicle* trace (F_{50}; Fig. 2.3). This approach captures compound effects on both t_{50} and $F_{plateau}$.

A third consideration is accurately estimating the uncertainty in EC_{50} values obtained from dose response assays. Many sources of error can contribute to this uncertainty, and not all of them are normally distributed. Accordingly, a resampling procedure was used to more rigorously capture the range of parameter values consistent with observations. Briefly, a quadratic dose response equation (Eq. 2) was used to fit F_{50} vs. compound concentration data. Then, 100 synthetic 'decoy' dose response curves were generated using the best-fit values of EC_{50} with random noise added to match experimentally observed scatter in F_{50} values. The synthetic data sets were then re-fit using Eq. 2, and confidence intervals were then determined from the resulting distribution of re-fit EC_{50} values. We report the best-fit EC_{50} value from the experimental data, along with the 95% confidence interval, as a conservative estimate of the potency of

each of the TA analogs. Equation 2 properly accounts for arbitrarily potent inhibition, and also yields as an additional global parameter T_{target}, the concentration of species within the tau4RD population ensemble targeted by TA-family compounds.

Remarkably, dose-response studies revealed that many of these compounds are active at nanomolar concentrations even when tau is present in a significant molar excess. For example, **16** and **27** both have EC_{50} values below 100 nM in our assay (11 nM and 16 nM, with 95% C.I. upper bounds of 23 nM and 30 nM respectively). In other words, these compounds are able to block aggregation even when tau4RD is present in over a 100-fold molar excess. This clear substoichiometric activity suggests that TA analogs may be able to selectively target a sub-population of tau species that drive aggregation. T_{target} (2.3 nM, 95% C.I. upper bound 22 nM) is also well below the concentration of tau4RD, consistent with substoichiometric activity. The mechanistic implications of this selective engagement with particular protein species are explored below.

Furthermore, TA and its analogs exhibit strong structure-activity relationships. Conservative changes to the substituents of the quinazoline ring can either abrogate inhibitory activity (for example, compare **11** to positional isomers **7** and **12**) or enhance it (e.g., **16** vs. **6**, **8** and **14**). Similarly, comparing **22** vs. **26** or **29** vs. **23** illustrates the effects that positional isomers and substitutions on the indole ring can have on activity. This pattern of SAR indicates that the interactions between TA analogs and tau4RD are specific and rationalizable, despite the intrinsic disorder of tau4RD, which is consistent with our previous work.[22]

2.3.3 Mechanism of aggregation inhibition by TA analogs

Given the potency and substoichiometric inhibition of tau4RD aggregation demonstrated by TA-family compounds, we turned our attention to understanding the mechanism driving their activity. Our design and discovery strategy targets monomeric states of tau4RD, meaning that TA analogs would be expected to target the earliest stages of the aggregation pathway. To test this idea, we performed delayed addition experiments. Briefly, instead of being included at the start of an aggregation reaction, TA analogs or vehicle were introduced at defined timepoints within the lag, elongation, and plateau phases of aggregation (Fig. 2.4). The delayed addition results show that TA analogs inhibited aggregation when added during the lag phase (where primary nucleation is the dominant process), but did not inhibit aggregation when added later in the elongation phase (where fibril growth and secondary nucleation predominate). From this data, we concluded that because TA analogs are more potent inhibitors when added immediately after aggregation initiation, TA analogs primarily act on tau4RD nucleation. The ability to selectively target nucleating species, or their precursors, would nicely explain the strongly substoichiometric activity of TA analogs.

To directly determine whether TA analogs have any effect on the tau4RD elongation rate, we performed seeded aggregation assays. Seeding tau4RD with preformed fibrils bypasses the nucleation phase, allowing direct observation of elongation kinetics. We performed seeded aggregation assays with tau4RD:TA stoichiometries between 1:2 and 1:0.125. We observed a dose-dependent decrease in tau4RD elongation rate (k_{obs}, AU/min) with increased stoichiometric equivalents of TA analogs (Fig. 2.5). The dose response of the observed elongation rate indicated that TA analogs inhibit seeded tau4RD aggregation with mid-nM potency.

2.4 Discussion

The development of potent, specific small-molecule aggregation inhibitors for tau and other aggregation-prone IDPs remains a major open challenge. Our work here demonstrates that computationally-guided screening followed by focused analog design can, at least in this case, provide a solution. TA and its analogs are an attractive scaffold for further development for several reasons.

TA-family compounds display remarkable potency and substoichiometric activity, at levels that have never (as far as we are aware) been reported for small-molecule tau aggregation inhibitors. At least two compounds (**16** and **27**) are active at concentrations well below 100 nM, and inhibit unseeded aggregation of tau4RD at >50-fold molar excess. As discussed above, when it comes to aggregation inhibition, the substoichiometric nature of this activity is even more exciting than raw potency or binding affinity. For a target like tau, with a total concentration of ~2 μM in the neuron,[8] it would be much more tractable to deliver nM concentrations of a substoichiometric therapeutic to the brain than μM concentrations of a stoichiometric one.[40] Although we have not conducted experiments to determine if TA analogs impair tau's native microtubule binding function, the concentration difference between inhibitor and tau is such that even with off-target binding to native tau, there would remain a large fraction of unbound native tau. Moreover, TA-family compounds demonstrate that dramatic changes in activity can result from conservative changes to small-molecule structure, even with a target as disordered as tau. Firstly, this finding confirms that the interactions between tau and the small molecules presented here are specific in nature. Secondly, it suggests that iterative analog optimization is a feasible strategy to generate high-affinity ligands of disordered proteins, following similar paradigms well-established for structured protein targets.[41]

Mechanistic studies shed light on how exactly TA and its analogs modulate tau aggregation. TA-family compounds more potently inhibit unseeded than seeded tau4RD aggregation, with EC_{50} values for the latter higher by about an order of magnitude. (Note that the inhibition of seeded aggregation is still substoichiometric, with EC_{50}s about 10-fold lower than tau4RD concentration.) In nucleation-dependent polymerization (NDP) models, seeded aggregation is driven by elongation (i.e., monomers adding on to

existing fibrils) and secondary nucleation processes (by which existing fibrils generate new fibril growth sites).[42] Unseeded aggregation is driven by primary nucleation (*de novo* formation of nuclei or fibrillar seeds from soluble material) in addition to elongation and secondary nucleation. Accordingly, the difference in potency towards unseeded and seeded reactions indicates that TA-family compounds preferentially target early stages of tau4RD aggregation. This is clearly backed up by delayed addition experiments that demonstrate a loss of activity if aggregation is allowed to continue unchecked for defined periods of time before compounds are added. Moreover, the strongly substoichiometric activity of TA analogs indicates that they must bind selectively and tightly to either the aggregation nucleus or a close precursor (whether monomeric or oligomeric). This raises the exciting prospect that characterizing TA analogs' effects on tau conformation could shed light on these enigmatic species.

The discovery and functional characterization of novel TA inhibitors of tau aggregation positions us to pursue important future questions. On the one hand, it will be important to determine where TA analogs bind to tau and how they affect its conformation. Given the disordered nature of the target, X-ray crystallography or cryo-EM are unlikely to be useful,[2,3] and multidimensional NMR would require intractably high concentrations of TA analogs in solution. Accordingly, we are developing hydrogen/deuterium exchange mass spectrometry (HDX-MS) methods to characterize tau/small-molecule complexes.[43,44] On the other hand, establishing the biological activity of TA-family compounds is the essential next step in their development as potential tau-targeting therapeutics. Studying their effects on tau aggregation in cells or *in vivo*, and their ability to slow the propagation of tau pathology from neuron to neuron, would reveal whether and how the intriguing *in vitro* activity of tryptanthrin and its analogs translates to the biological environment.

2.5 Materials and Methods

2.5.1 Protein Expression and Purification

Tau4RD was expressed and purified from *E. coli* BL-21 (DE3) as previously reported.[21] Briefly, a plasmid containing the His-tagged tau4RD gene with a TEV cleavage site was gifted from the Rhoades lab at the University of Pennsylvania (Philadelphia, PA). To express protein, BL-21 cells containing the tau4RD gene were grown at 37 °C until the OD reached 0.6-0.7. The temperature was then lowered to 16 °C and protein expression was induced with the addition of Isopropyl B-D-1-thiogalactopyranoside to a final concentration of 0.4 mM. The culture was allowed to grow overnight, then cells were harvested by centrifugation. Expressions were resuspended, flash frozen, and stored at -80 °C in lysis buffer [50 mM Tris, 500 mM NaCl, and 10 mM imidazole (pH 8 at 4 °C)]. Upon thawing for purification, Halt Protease inhibitor cocktail (Life Technologies), DNase, RNase, and phenylmethanesulfonylfluoride in ethanol were added to cells before lysis with a French press. The lysate was centrifuged at 2800*g* for 45 minutes, then the supernatant was passed through 0.4 μm filters and loaded onto a 5 mL Ni-NTA agarose column. The protein was eluted by increasing the concentration of imidazole, then the eluent was dialyzed against a 10 μM imidazole buffer during an overnight incubation with 1 mM dithiothreitol and 100 μL of 8.64 mg/mL TEV protease (expressed in *E. coli*) at 4 °C. This solution was loaded onto a Ni-NTA column and the flow-through was collected and concentrated to 1-2 mL with a 3 kDa molecular weight cutoff centrifugal filter. The concentrate was fractionated using a 25 mL S200 extended gel-filtration column as previously described.[25] Protein purity was confirmed by precast 12% Bis-Tris SDS-PAGE gels (Invitrogen). Protein was concentrated, aliquoted, and flash-frozen before storage at –80 °C. Protein concentrations were determined using the Pierce BCA Protein Assay Kit (Thermo Fisher Scientific).

2.5.2 Aggregation Assays

Unseeded: All aggregation assays were performed at 37 °C and pH 7.4 in filtered (0.22 μm) aggregation buffer containing 20 mM Tris, 50 mM NaCl, 1 mM TCEP, 1 mM EDTA. EDTA was added to aggregation assays because the presence of trace divalent metal cations was found to affect tau4RD aggregation.[45,46] Aggregation buffer was made fresh and passed through a 0.22 μm syringe filter before use. (Tau4RD, TA analogs, and heparin were not filtered because filtration of these components resulted in spurious aggregation results.) Aggregation assays were performed at 5 μM tau4RD, 5 μM ~3 kDa heparin, and 5 μM TA analog unless otherwise indicated. DMSO concentration in all assays was 0.1% unless otherwise stated. Because tau4RD does not aggregate in the absence of an oppositely-charged cofactor, heparin was used to induce tau4RD aggregation. Heparin-induced tau and tau4RD aggregation is well-characterized.

Solutions of tau4RD and TA analogs (or an equivalent volume of DMSO) were prepared at 2.105x the desired final concentrations in aggregation buffer, and 95 μL aliquots of each were then added to the wells of a 96-well black flat-bottom non-binding plate (Corning). A 1 mM stock of ThT in aggregation buffer was passed through a 0.22 μm syringe filter, and then 10 μL of this solution was added to the wells for a final concentration of 50 μM ThT. Immediately before beginning fluorescent readings, 95 μL of 5 μM unfractionated ~3 kDa heparin (MP Biomedicals, Irvine, CA) dissolved in aggregation buffer was added to each well, bringing the total well volume to 200 μL. The plate was covered with a piece of polyolefin or polypropylene sealing tape (Thermo Fisher Scientific) and monitored with a BioTek Synergy HTX plate reader (Agilent, Santa Clara, CA). Intrinsic fluorescence from TA analogs did not interfere with monitoring reaction progress by the increase in ThT fluorescence (λ_{ex} = 440 nm, λ_{em} = 485 nm). Reads were taken every 5 min after linear agitation (300 rpm) for 1 min. Experiments were performed with at least three technical replicates. Baseline correction was performed by subtracting the fluorescence value (A.U.) of the buffer/DMSO trace from experimental traces.

Seeded: Pre-formed tau4RD seeds were generated by harvesting tau4RD fibrils after 17 h of aggregation. Briefly, wells containing tau4RD and DMSO from unseeded aggregation assays were transferred to individual snap-cap tubes and centrifuged at 21,000*g* for 30 min at 4 °C. 100 μL of supernatant was discarded, then 100 μL of fresh aggregation buffer was added to each tube. Each 200 μL aliquot was sonicated on ice for 5 rounds of 2 sec (Cole-Parmer 4710 Series Ultrasonic Homogenizer, 50% output) to disrupt tau4RD amyloid fibrils. Seeds were added to aggregation assays at 5% (v/v). Aggregation assays were then performed as above, except that 10 μL of tau4RD seeds or aggregation buffer was added to the wells after addition of 85 μL of heparin.

Delayed addition: Delayed addition aggregation assays were prepared similarly to unseeded aggregation reactions except that DMSO and TA analogs were not included in the tau4RD aliquots introduced to the wells. TA analogs were diluted in DMSO to 1 mM and held until the appropriate time point. Tau4RD, ThT, and heparin were prepared as above and plated in the stated order. At t = 0, 120, 240, or 480 min, 1 μL of 1 mM TA analog or 1 μL of DMSO were pipetted into the appropriate wells to create three technical replicates of each condition. To do so, the plate was removed from the plate reader and unsealed at each time point, then resealed and replaced after the addition and allowed to continue incubating. Well volume was 201 μL after addition. Reaction progress was monitored as above.

2.5.3 Gel Densitometry

Aggregation assays were stopped at the indicated time and wells were pipetted into individual snap-cap tubes. The tubes were centrifuged 21,000*g* for 30 min at 4 °C, after which 15 μL of supernatant was

added to 3 μL of 5x SDS loading dye. Concentration standards were prepared at 5 μM, 3 μM, and 1 μM and t = 0 samples were prepared with 5 μM final concentration of both tau4RD and the respective TA analog. Samples were boiled for 45 sec, cooled on ice, and 15 uL was added to precast 12% Bis-Tris SDS-PAGE gels. Gels were imaged with a Li-Cor Odyssey CLx gel scanner and band intensity was determined using ImageJ.[47] Experiments consisted of 3 technical replicates and the results were averaged (mean).

2.5.4 EC_{50} Determination and Resampling

Unseeded aggregation assays were performed as above with 5 μM tau4RD and TA analog at concentrations between 62.5 nM and 10 μM. DMSO content was 0.25% for experiments involving **20**, **24**, and **25** and 0.1% for experiments involving all other compounds. ThT fluorescence traces were baseline corrected and averaged. Non-linear least squares fitting in Prism 9.0 (GraphPad Software, Boston, MA) was used to determine t_{50}, the midpoint of the aggregation curve, from the vehicle control trace from the following equation:

$$F(t) = F(0) + \frac{(F_{max} - F(0))}{1 + e^{-k(t - t_{50})}} \quad \text{.....(1)}$$

Here, $F(0)$ is the baseline fluorescence at the start of the reaction, F_{max} is the maximal fluorescence at the plateau after aggregation is complete, and k is a rate parameter that describes the steepness of the transition.

We then define $F_{50}(C)$ as the ThT fluorescence in the presence of a given concentration C of a TA analog at the t_{50} (midpoint) *of the vehicle control trace*. F_{50} values measured over a range of compound concentrations were fit to the following quadratic dose-response equation to determine analog EC_{50}:

$$\frac{F_{50}(C)}{F_{50}(0)} = 1 - \frac{T_{target} + C + EC_{50} - \sqrt{(T_{target} + C + EC_{50})^2 - 4T_{target}C}}{2T_{target}} \quad \text{.....(2)}$$

Here, $F_{50}(0)$ is the fluorescence of the vehicle control trace at its t_{50} (i.e., in the absence of compound), and T_{target} is the concentration of species within the tau4RD ensemble that are targeted by the compound. The value of T_{target} was globally shared across all dose response fitted curves.

To estimate the 95% confidence interval of the mean EC_{50} values, 100 synthetic "decoy" datasets were generated based on the best-fit values obtained from Equation 2. Gaussian noise equal to the RMSE observed in the EC_{50} fit was applied to the decoys which were each then fit to Equation 2. The upper and lower 95% confidence intervals were determined by binning the EC_{50} values of the decoy datasets.

2.5.5 TA Synthesis, Purification, and Storage

Following the protocol of Hou et al., TA analogs were synthesized by reacting isatin derivatives (1.0 eq) with benzoxazine-2,4-dione derivatives (1.2 eq) in the presence of Rose Bengal (0.050 eq) and

potassium carbonate (1.0 eq) at ambient temperature under illumination for 18h. TA analogs were purified by reverse-phase HPLC followed by supercritical fluid chromatography, characterized by ^{1}H NMR and/or mass spectrometry, and lyophilized. Details on the synthesis, purification, and characterization of each TA analog are presented in Supplementary Material. DMSO stocks of TA analogs were prepared, aliquoted, and stored at –20 °C until use.

2.6 Acknowledgments

This work was supported by the NIH (T32GM007750 to E.I.J.) and the Seattle Partnership for Research on Innovative Therapies (to A.N.). The authors gratefully acknowledge Elena Arroyo Holland and Mia Cervantes for assistance with protein expression, as well as Dr. Cathy Tralau-Stewart and Dr. C. Alex Goddard (Takeda Pharmaceuticals) for administrative support. The authors also gratefully acknowledge helpful discussions with Prof. Brian Kraemer, Prof. Tuomas Knowles, and Prof. Michele Vendrusculo.

2.7 Author contributions

E.I.J., D.W.B. and A.N. conceived the project. E.I.J. performed *in vitro* aggregation assays. D.W.B., E.I.J. and A.N. performed the computational work. E.D.C., T.N. and K.C. were responsible for the synthesis and validation of TA analogs. J.S. was responsible for cytotoxicity assays. E.I.J., and A.N. drafted the manuscript, and all authors participated in editing.

2.8 Figures

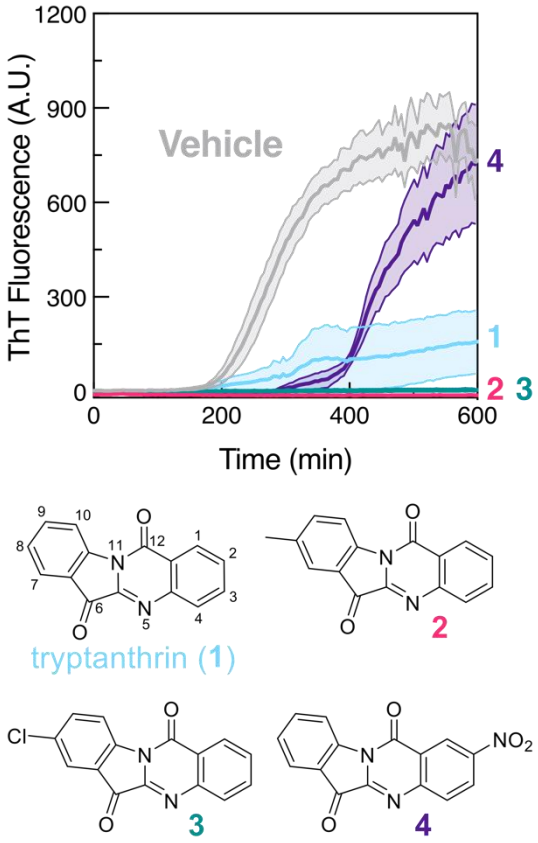

Figure 2.1: Inhibition of heparin-induced tau4RD aggregation by tryptanthrin and analogs, discovered by computationally-guided screening. Tau4RD (5 μM) aggregation in the presence of 5 μM 3 kDa heparin, with 5 μM of TA, analogs **2**–**4**, or vehicle control. (*n* = 3, error bands shown mean +/- SEM.)

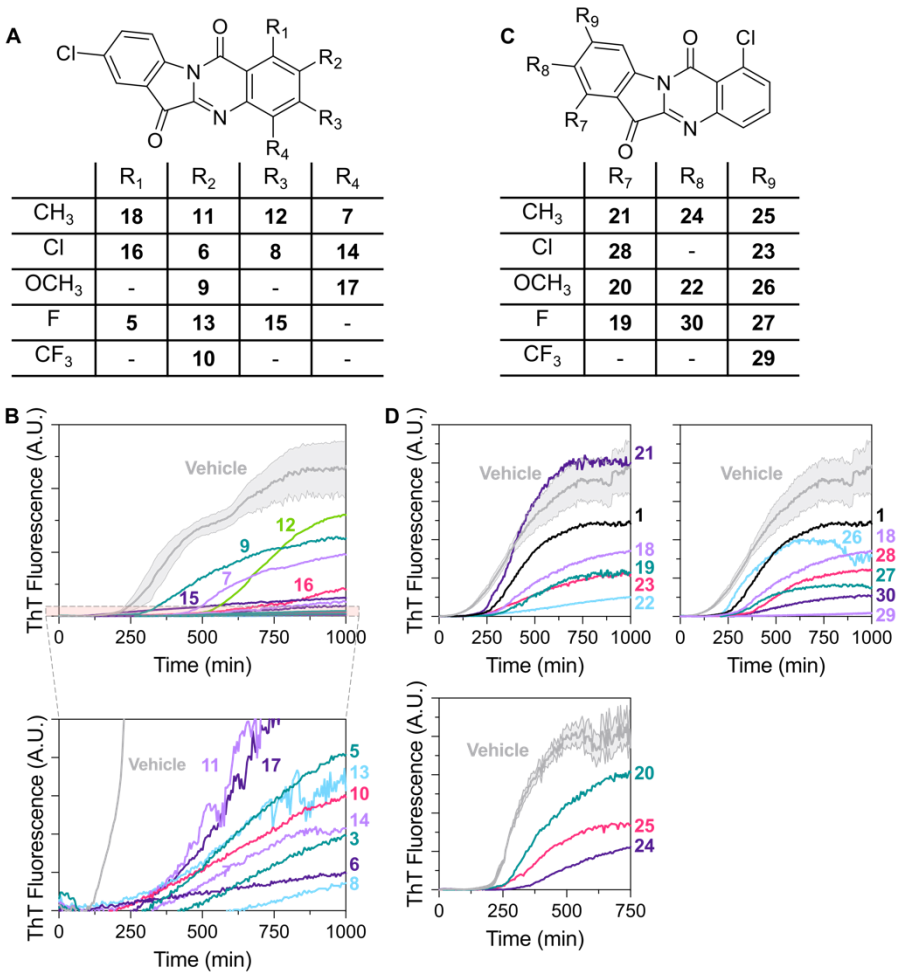

	R_1	R_2	R_3	R_4
CH_3	**18**	**11**	**12**	**7**
Cl	**16**	**6**	**8**	**14**
OCH_3	-	**9**	-	**17**
F	**5**	**13**	**15**	-
CF_3	-	**10**	-	-

	R_7	R_8	R_9
CH_3	**21**	**24**	**25**
Cl	**28**	-	**23**
OCH_3	**20**	**22**	**26**
F	**19**	**30**	**27**
CF_3	-	-	**29**

Figure 2.2: Effects of second and third generation TA analogs on heparin-induced tau4RD aggregation. A) Structures of second generation TA analogs **5-17**, with the table indicating substituents present at specified positions on the quinazoline ring for each analog. B) Tau4RD aggregation under standard conditions in the presence of second generation TA analog (5 μM) or vehicle control. The means (n = 3 or 4 technical replicates) are displayed for each trace. For visual clarity, error bands (mean +/- SEM) are displayed only for the vehicle trace. Other traces showed similar or lower technical variability. C) Structures of third generation analogs **19–30** derived from **16**. D) Tau4RD aggregation in the presence of third generation TA analog (5 μM) or vehicle control. Traces and error bands are formatted as in panel B. Compounds **20**, **24**, and **25** (lower panel) were conducted at a DMSO concentration of 0.25% v/v, while all other experiments were conducted at 0.1% v/v DMSO.

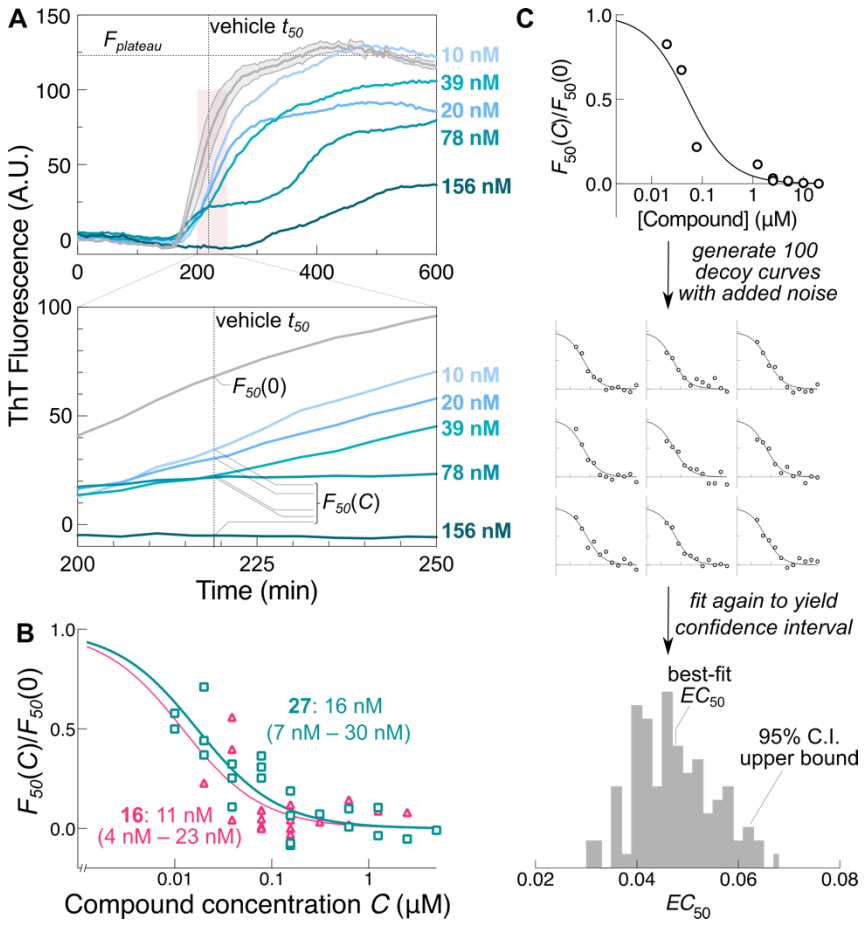

Figure 2.3: TA analogs inhibit tau4RD aggregation in a substoichiometric, dose-dependent manner. A) Tau4RD aggregation under standard conditions in the presence of varying concentrations of the third generation compound **27** or vehicle control (n = 3 or 4, mean displayed for all analog traces, S.E.M. error band displayed solely for the vehicle trace). F_{50} is defined as the fluorescence measured at the transition midpoint of the vehicle trace (t_{50}), whether in the absence [$F_{50}(0)$] or presence [$F_{50}(C)$] of varying concentrations of compound. B) Dose-response curves of $F_{50}(C)$ normalized to $F_{50}(0)$ measured on the same plate for compounds **16** and **27**, demonstrating nanomolar potency. Best-fit EC_{50} values are shown, with 95% confidence intervals estimated from resampling shown in parentheses. C) Schematic of resampling protocol used to estimate confidence intervals of best-fit EC_{50} values.

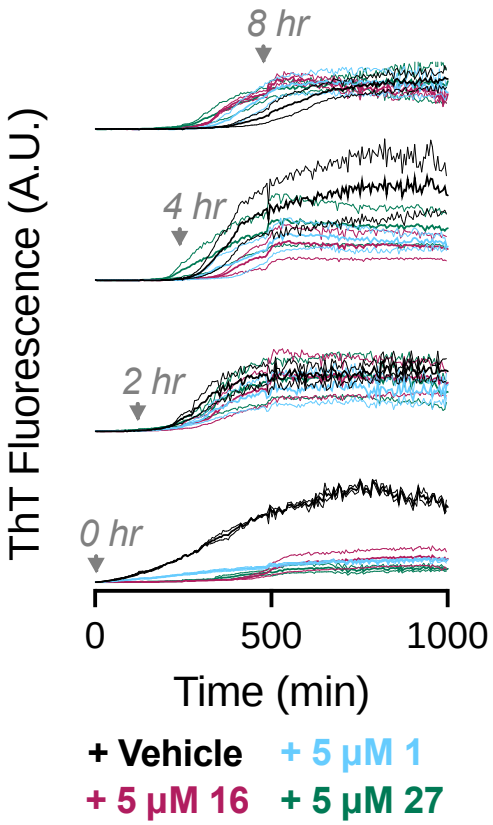

Figure 2.4: TA analogs are most active early in the aggregation process. Tau4RD aggregation with delayed addition of 5 µM TA analog at t = 0, 2, 4, or 8 hours (*n* = 3, mean +/- SEM). Inhibition was observed when analogs were added early in the aggregation lag phase but not once the elongation phase began. This suggests that TA analogs preferentially inhibit primary nucleation.

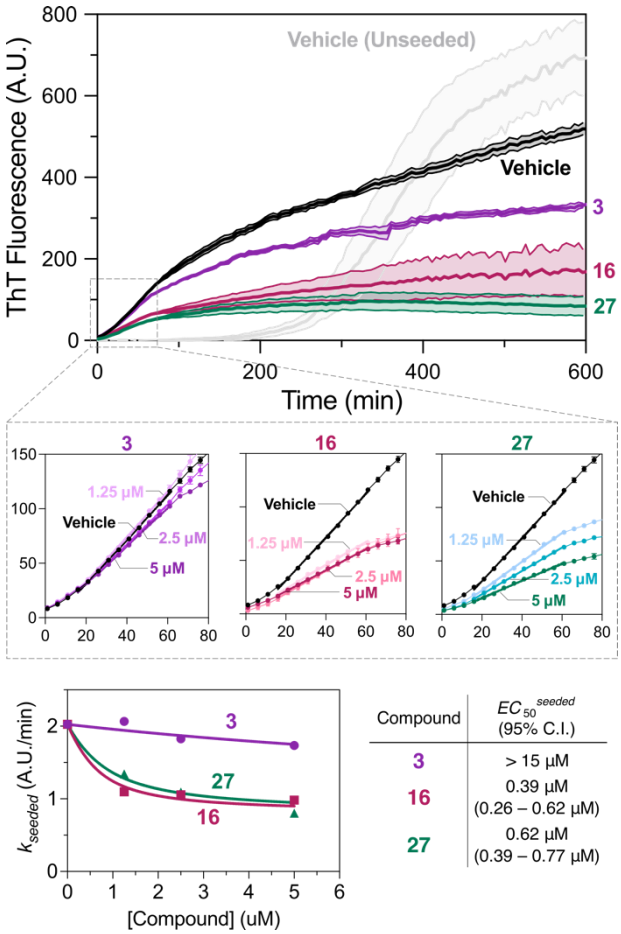

Figure 2.5: Inhibition of seeded tau4RD aggregation by TA analogs. A) Aggregation of 5 µM tau4RD and 5 µM 3 kDa heparin, seeded with 5% (w/w) pre-formed fibril in the presence of 5 µM TA analog or vehicle control. Traces indicate mean +/- SEM (n = 3 or 4). B) Seeded elongation measured over a range of compound concentrations, with linear fits (bold lines) used to estimate elongation rates. Traces indicate mean +/- SEM (n = 3 or 4). C) k_{seeded} rates from B plotted against compound concentration and fit to Equation 2, with 95% C.I. estimated by resampling.

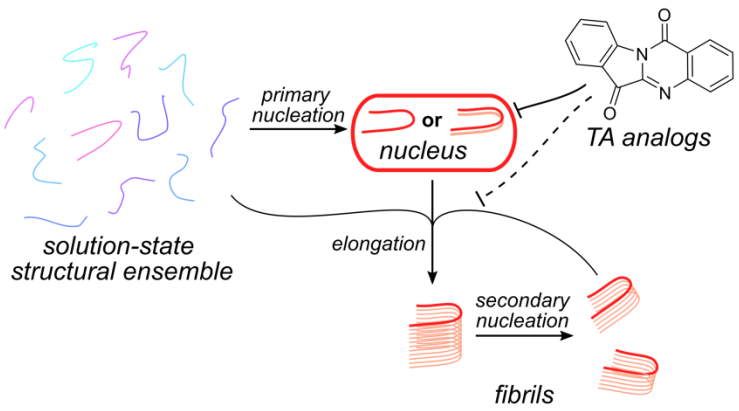

Figure 2.6: Proposed mechanism of action of tryptanthrin and its analogs. Substoichiometric inhibition of early-stage aggregation indicates that TA analogs bind selectively and tightly to tau aggregation nuclei or their close precursors. Substoichiometric inhibition of seeded aggregation indicates that TA analogs can also inhibit subsequent elongation or secondary nucleation, albeit with lower potency.

2.9 Supplementary Material

2.9.1 Synthesis and Characterization of Tryptanthrin Analogs

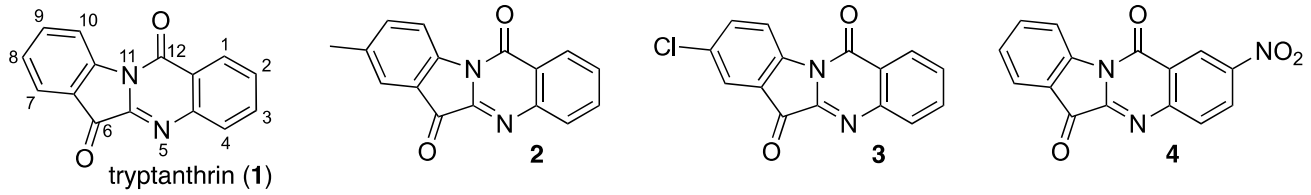

Compounds **1**–**4** were sourced from Axcelead Drug Discovery Partners (Fujisawa, Japan). Additional **1** was purchased from Sigma Aldrich (St. Louis, MO) and MedChemExpress (Monmouth Junction, NJ).

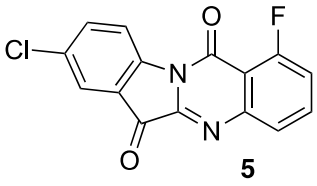

Compound **5** (8-chloro-1-fluoro-indolo[2,1-b]quinazoline-6,12-dione) was synthesized as follows: a solution of 5-fluoro-1H-3,1-benzoxazine-2,4-dione (1.2 eq, 26 mg, 0.13 mmol), Rose Bengal (0.050 eq, 5.6 mg, 0.0055 mmol) and DMA (0.9 mL) was added to a 4 mL vial containing 5-chloroisatin (1.0 eq, 20 mg, 0.11 mmol) and potassium carbonate (1.0 eq, 15 mg, 0.11 mmol). The resulting mixture was stirred (uncapped) at ambient temperature under a 100 lumen white LED light (Milwaukee Tool, Brookfield, WI) for 18h. DMSO (1 mL) was added to solubilize the mixture, which was then filtered and purified by HPLC (Phenomenex Gemini® C18, 5 µm, ID 30 mm x 150 mm, eluting with 10-90% acetonitrile (0.035% TFA)/water (0.05% TFA), and then dried *in vacuo*. The resulting solid was repurified by supercritical fluid chromatography (2-PIC column (30 x 150mm, 5 micron), eluting with 5-50% MeOH/CO_2:methanol, MeOH modified with 0.1% ammonium hydroxide) to give 8-chloro-1-fluoro-indolo[2,1-b]quinazoline-6,12-dione (2.1 mg, 6.4 % yield). ESI-MS m/z [M+H]+ calc'd for $C_{15}H_6ClFN_2O_2$ 300.0; found 300.9.

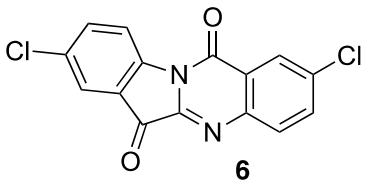

6

Compound **6** (2,8-dichloroindolo[2,1-b]quinazoline-6,12-dione) was synthesized (1.7 mg, 4.9 % yield) using 6-chloro-1H-3,1-benzoxazine-2,4-dione as a starting material and the analogous procedure described for Compound **5** above. ^{1}H NMR (400 MHz, chloroform-*d*) δ ppm 7.76 - 7.80 (m, 1 H) 7.81 - 7.85 (m, 1 H) 7.89 - 7.92 (m, 1 H) 7.98 - 8.02 (m, 1H) 8.41 - 8.44 (m, 1 H) 8.59 - 8.63 (m, 1 H). ESI-MS $[M+H]^{+}$ calc'd for $C_{15}H_6Cl_2N_2O_2$, 316.0; found, 316.9.

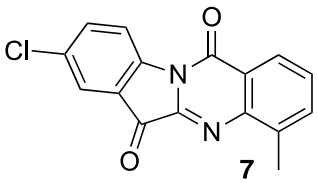

7

Compound 7 (8-chloro-4-methyl-indolo[2,1-b]quinazoline-6,12-dione) was synthesized (13 mg, 38 % yield) using 8-methyl-1H-3,1-benzoxazine-2,4-dione as a starting material and the analogous procedure described for Compound **5**. ESI-MS m/z [M+H]+ calc'd for $C_{16}H_9ClN_2O_2$ 296.0; found 297.0.

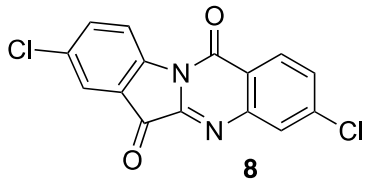

8

Compound **8** (3,8-dichloroindolo[2,1-b]quinazoline-6,12-dione) was synthesized (2.8 mg, 7.3 % yield) using 7-chloro-1H-3,1-benzoxazine-2,4-dione as a starting material and the analogous procedure described for Compound **5**. ^{1}H NMR (400 MHz, chloroform-*d*) δ ppm. 7.65 - 7.69 (m, 1 H) 7.76 - 7.80 (m, 1 H) 7.89 - 7.92 (m, 1 H) 8.02 - 8.05 (m, 1 H) 8.37 - 8.41 (m, 1 H) 8.58 - 8.62 (m, 1 H) ESI-MS m/z [M+H]+ calc'd for $C_{15}H_6Cl_2N_2O_2$ 316.0; found 316.9.

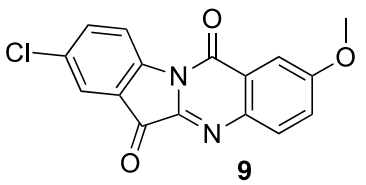

9

Compound **9** (8-chloro-2-methoxy-indolo[2,1-b]quinazoline-6,12-dione) was synthesized (1.2 mg, 3.5 % yield) using 6-methoxy-1H-3,1-benzoxazine-2,4-dione as a starting material and the analogous procedure described for Compound **5**. ESI-MS m/z [M+H]+ calc'd for $C_{16}H_9ClN_2O_3$ 312.0; found 313.0.

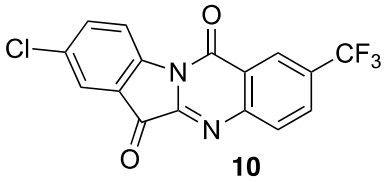

10

Compound **10** (8-chloro-2-(trifluoromethyl)indolo[2,1-b]quinazoline-6,12-dione) was synthesized (7.9 mg, 19 % yield) using 6-(trifluoromethyl)-1H-3,1-benzoxazine-2,4-dione as a starting material and the analogous procedure described for Compound **5**. ESI-MS m/z [M+H]+ calc'd for $C_{16}H_6ClF_3N_2O_2$ 350.0; found 350.9.

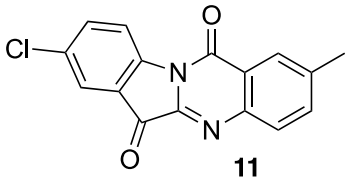

11

Compound **11** (8-chloro-2-methyl-indolo[2,1-b]quinazoline-6,12-dione) was synthesized (9.3 mg, 27 % yield) using 6-methyl-1H-3,1-benzoxazine-2,4-dione as a starting material and the analogous procedure described for Compound **5**. ESI-MS m/z [M+H]+ calc'd for $C_{16}H_9ClN_2O_2$ 296.0; found 297.00.

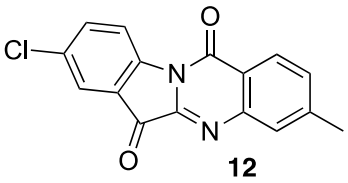

12

Compound **12** (8-chloro-3-methyl-indolo[2,1-b]quinazoline-6,12-dione) was synthesized (2.4 mg, 7.3 % yield) using 7-methyl-1H-3,1-benzoxazine-2,4-dione as a starting material and the analogous procedure described for Compound **5**. ESI-MS m/z [M+H]+ calc'd for $C_{16}H_9ClN_2O_2$ 296.0; found 297.0.

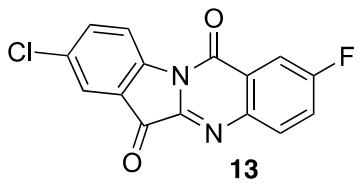

13

Compound **13** (8-chloro-2-fluoro-indolo[2,1-b]quinazoline-6,12-dione) was synthesized (3.9 mg, 11 % yield) using 6-fluoro-1H-3,1-benzoxazine-2,4-dione as a starting material and the analogous procedure described for Compound **5**. ^{1}H NMR (400 MHz, chloroform-*d*) δ ppm 7.36 - 7.42 (m, 1 H) 7.55 - 7.59 (m, 1 H) 7.68 - 7.72 (m, 1 H) 7.84 - 7.92 (m, 2H) 8.39 - 8.42 (m, 1 H). ESI-MS m/z [M+H]+ calc'd for $C_{15}H_6ClFN_2O_2$ 300.0; found 301.0.

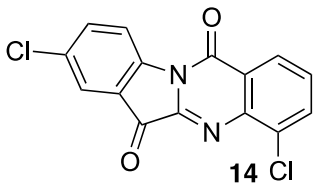

14

Compound **14** (4,8-dichloroindolo[2,1-b]quinazoline-6,12-dione) was synthesized (7.3 mg, 20 % yield) using 8-chloro-1H-3,1-benzoxazine-2,4-dione as a starting material and the analogous procedure described for Compound **5**. ESI-MS m/z [M+H]+ calc'd for $C_{15}H_6Cl_2N_2O_2$ 316.0; found 316.9.

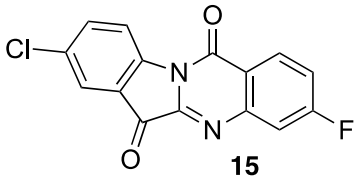

15

Compound **15** (8-chloro-3-fluoro-indolo[2,1-b]quinazoline-6,12-dione) was synthesized (12.6 mg, 36 % yield) using 7-fluoro-1H-3,1-benzoxazine-2,4-dione as a starting material and the analogous procedure described for Compound **5**. ^{1}H NMR (400 MHz, chloroform-*d*) δ ppm. 7.18 - 7.25 (m, 1 H) 7.47 - 7.53 (m, 1 H) 7.55 - 7.59 (m, 1 H) 7.67 - 7.71 (m, 1 H) 8.24 - 8.30 (m, 1H) 8.37 - 8.42 (m, 1 H). ESI-MS m/z [M+H]+ calc'd for $C_{15}H_6ClFN_2O_2$ 300.0; found 301.0.

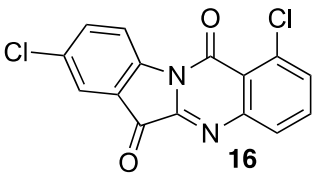

16

Compound **16** (1,8-dichloroindolo[2,1-b]quinazoline-6,12-dione) was synthesized (1.1 mg, 3.1 % yield) using 5-chloro-1H-3,1-benzoxazine-2,4-dione as a starting material and the analogous procedure described for Compound **5**. ESI-MS m/z [M+H]+ calc'd for $C_{15}H_6Cl_2N_2O_2$ 316.0; found 316.9.

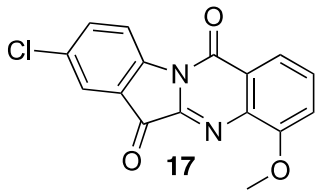

17

Compound **17** (8-chloro-4-methoxy-indolo[2,1-b]quinazoline-6,12-dione) was synthesized (3.9 mg, 11 % yield) using 8-methoxy-1H-3,1-benzoxazine-2,4-dione as a starting material and the analogous procedure described for Compound **5**. ESI-MS m/z [M+H]+ calc'd for $C_{16}H_9ClN_2O_3$ 312.0; found 313.0.

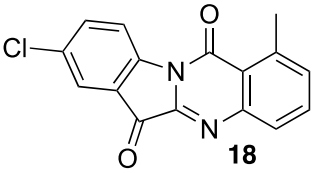

18

Compound **18** (8-chloro-1-methyl-indolo[2,1-b]quinazoline-6,12-dione) was synthesized using 5-methyl-1H-3,1-benzoxazine-2,4-dione as starting material using the analogous procedure described for Compound **5**. 1H NMR (400 MHz, chloroform-*d*) δ ppm 2.97 (s, 3 H) 7.44 (d, J=7.53 Hz, 1 H) 7.68 - 7.78 (m, 2 H) 7.86 - 7.90 (m, 2 H) 8.62 (d, J=8.53 Hz, 1 H). ESI-MS m/z [M+H]+ calc'd for $C_{16}H_9ClN_2O_2$ 296.04; found 296.90.

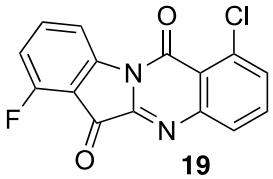

19

Compound **19** (1-chloro-7-fluoro-indolo[2,1-b]quinazoline-6,12-dione) was synthesized as follows: a solution of 5-chloro-1H-3,1-benzoxazine-2,4-dione (1.00 eq, 20 mg, 0.101 mmol), Rose Bengal (0.0500 eq, 5.2 mg, 0.00506 mmol) and DMA (0.9000 mL) was added to a 4 mL vial containing 4-fluoroindoline-

2,3-dione (1.2 eq, 26.1 mg, 0.12 mmol) and potassium carbonate (1.00 eq, 14 mg, 0.101 mmol). The resulting mixture was stirred (uncapped) at ambient temperature under a 100 lumen white LED light (Milwaukee Tool, Brookfield, WI) for 18h. Purification by HPLC and SFC were performed as for Compound **5**. ^{1}H NMR (400 MHz, methanol-d_4) δ ppm 7.12 (t, J=8.41 Hz, 1 H) 7.68 - 7.72 (m, 1 H) 7.72 - 7.78 (m, 1 H) 7.81 (td, J=8.31, 5.46 Hz, 1 H) 7.99 (dd, J=7.91, 1.38 Hz, 1 H) 8.52 (d, J=8.03 Hz, 1 H). ESI-MS m/z [M+H]+ calc'd for $C_{15}H_6ClFN_2O_2$ 300.01; found 300.90.

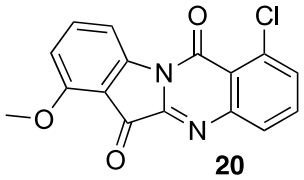

20

Compound **20** (1-chloro-7-methoxy-indolo[2,1-b]quinazoline-6,12-dione) was synthesized using 4-methoxyindoline-2,3-dione as starting material using the analogous procedure described for Compound **19**. 1H NMR (400 MHz, chloroform-*d*) δ ppm 4.10 (s, 3 H) 6.94 (d, *J*=8.53 Hz, 1 H) 7.64 - 7.77 (m, 3 H) 7.98 (dd, *J*=7.97, 1.32 Hz, 1 H) 8.28 (d, *J*=7.91 Hz, 1 H). ESI-MS m/z [M+H]+ calc'd for $C_{16}H_9ClN_2O_3$ 312.03; found 313.00.

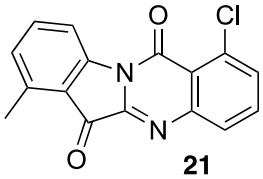

21

Compound **21** (1-chloro-7-methyl-indolo[2,1-b]quinazoline-6,12-dione) was synthesized using 4-methyl-2,3-dihydro-1H-indole-2,3-dione as starting material using the analogous procedure described for Compound **19**. ^{1}H NMR (400 MHz, methanol-d_4) δ ppm 2.77 (s, 3 H) 7.22 (d, J=7.78 Hz, 1 H) 7.62 - 7.70 (m, 2 H) 7.70 - 7.75 (m, 1 H) 7.97 (dd, J=7.97, 1.32 Hz, 1 H) 8.53 (d, J=8.03 Hz, 1 H). ESI-MS m/z [M+H]+ calc'd for $C_{16}H_9ClN_2O_2$ 296.04; found 297.00.

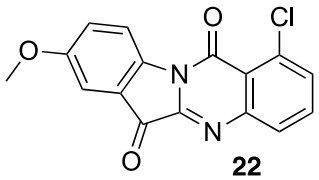

22

Compound **22** (1-chloro-8-methoxy-indolo[2,1-b]quinazoline-6,12-dione) was synthesized using 5-methoxy-2,3-dihydro-1H-indole-2,3-dione as starting material using the analogous procedure described for Compound **19**. 1H NMR (400 MHz, chloroform-*d*) δ ppm 3.92 (s, 3 H) 7.33 (d, *J*=8.28 Hz, 1 H) 7.40 (d,

J=2.76 Hz, 1 H) 7.65 - 7.69 (m, 1 H) 7.69 - 7.75 (m, 1 H) 7.96 (d, *J*=7.75 Hz, 1 H) 8.58 (d, *J*=8.78 Hz, 1 H). ESI-MS m/z [M+H]+ calc'd for $C_{16}H_9ClN_2O_3$ 312.03; found 312.95.

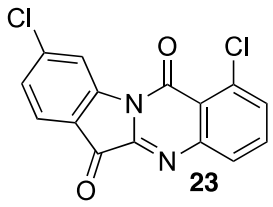

23

Compound **23** (1,9-dichloroindolo[2,1-b]quinazoline-6,12-dione) was synthesized using 6-chloroindoline-2,3-dione as starting material using the analogous procedure described for Compound **19**. ^{1}H NMR (400 MHz, chloroform-*d*) δ ppm 7.44 (dd, *J*=8.16, 1.76 Hz, 1 H) 7.66 (dd, *J*=8.53, 2.01 Hz, 1 H) 7.87 (d, *J*=8.03 Hz, 1 H) 8.02 (d, *J*=2.01 Hz, 1 H) 8.38 (d, *J*=8.53 Hz, 1 H) 8.68 (d, *J*=1.76 Hz, 1 H). ESI-MS m/z [M+H]+ calc'd for $C_{15}H_6Cl_2N_2O_2$ 315.98; found 316.95.

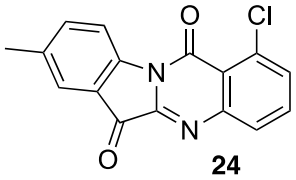

24

Compound **24** (1-chloro-8-methyl-indolo[2,1-b]quinazoline-6,12-dione) was synthesized using 5-methyl-2,3-dihydro-1H-indole-2,3-dione as starting material using the analogous procedure described for Compound **19**. ^{1}H NMR (400 MHz, chloroform-d) δ ppm 2.48 (s, 3 H) 7.62 (d, J=8.16 Hz, 1 H) 7.65 - 7.69 (m, 1 H) 7.69 - 7.75 (m, 2 H) 7.97 (dd, J=7.91, 1.38 Hz, 1 H) 8.55 (d, J=8.28 Hz, 1 H). ESI-MS m/z [M+H]+ calc'd for $C_{16}H_9ClN_2O_2$ 296.04; found 297.00.

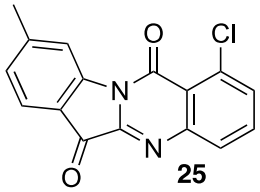

25

Compound **25** 1-chloro-9-methyl-indolo[2,1-b]quinazoline-6,12-dione was synthesized using 6-methylindoline-2,3-dione as starting material using the analogous procedure described for Compound **19**. ^{1}H NMR (400 MHz, methanol-d_4) δ ppm 2.56 (s, 3 H) 7.19 - 7.26 (m, 1 H) 7.60 - 7.68 (m, 1 H) 7.68 - 7.75 (m, 1 H) 7.81 (d, J=7.78 Hz, 1 H) 7.96 (d, J=7.98 Hz, 1 H) 8.50 - 8.55 (m, 1 H). ESI-MS m/z [M+H]+ calc'd for C16H9ClN2O2 296.04; found 296.95.

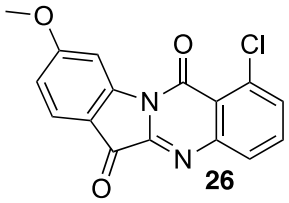

26

Compound **26** (1-chloro-9-methoxy-indolo[2,1-b]quinazoline-6,12-dione) was synthesized using 6-methoxyindoline-2,3-dione as starting material using the analogous procedure described for Compound **19**. ^{1}H NMR (400 MHz, chloroform-*d*) δ ppm 4.04 (s, 3 H) 6.92 (dd, *J*=8.53, 2.26 Hz, 1 H) 7.67 (dd, *J*=7.97, 1.32 Hz, 1 H) 7.73 (t, *J*=7.97 Hz, 1 H) 7.87 (d, *J*=8.53 Hz, 1 H) 7.97 (dd, *J*=7.91, 1.25 Hz, 1 H) 8.25 (d, *J*=2.13 Hz, 1 H). ESI-MS m/z [M+H]+ calc'd for $C_{16}H_9ClN_2O_3$ 312.03; found 312.95.

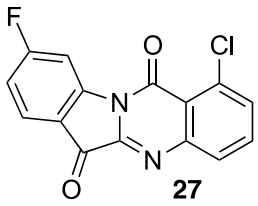

27

Compound **27** (1-chloro-9-fluoro-indolo[2,1-b]quinazoline-6,12-dione) was synthesized using 6-fluoro-2,3-dihydro-1H-indole-2,3-dione as starting material using the analogous procedure described for Compound **19**. ^{1}H NMR (400 MHz, chloroform-*d*) δ ppm 7.15 (td, J=8.47, 2.26 Hz, 1 H) 7.68 - 7.72 (m, 1 H) 7.76 (t, J=7.60 Hz, 1 H) 7.95 - 8.00 (m, 2 H) 8.45 (d, J=2.13 Hz, 1 H). ESI-MS m/z [M+H]+ calc'd for $C_{15}H_6ClFN_2O_2$ 300.01; found 301.00.

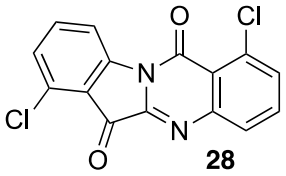

28

Compound **28** (1,7-dichloroindolo[2,1-b]quinazoline-6,12-dione) was synthesized using 4-chloroindoline-2,3-dione as starting material using the analogous procedure described for Compound **19**. ^{1}H NMR (400 MHz, chloroform-*d*) δ ppm 7.41 (d, J=8.16 Hz, 1 H) 7.68 - 7.78 (m, 3 H) 7.99 (dd, J=7.91, 1.25 Hz, 1 H) 8.66 (d, J=8.03 Hz, 1 H). ESI-MS m/z [M+H]+ calc'd for $C_{15}H_6Cl_2N_2O_2$ 315.98; found 316.90.

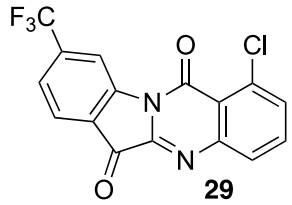

29

Compound **29** (1-chloro-9-(trifluoromethyl)indolo[2,1-b]quinazoline-6,12-dione) was synthesized using 6-(trifluoromethyl)indoline-2,3-dione as starting material using the analogous procedure described for Compound **19**. ESI-MS $[M+H]^+$ calc'd for $C_{16}H_6ClF_3N_2O_2$, 350.0; found, 350.90.

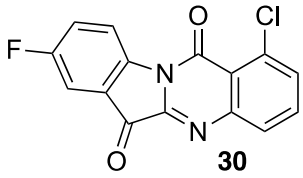

30

Compound **30** (1-chloro-8-fluoro-indolo[2,1-b]quinazoline-6,12-dione) was synthesized using 5-fluorisatin as starting material using the analogous procedure described for Compound **19**. ^{1}H NMR (400 MHz, chloroform-*d*) δ ppm 7.51 (td, J=8.66, 2.76 Hz, 1 H) 7.61 (dd, J=6.53, 2.76 Hz, 1 H) 7.68 - 7.72 (m, 1 H) 7.72 - 7.77 (m, 1 H) 7.98 (dd, J=7.91, 1.38 Hz, 1 H) 8.71 (dd, J=8.85, 4.08 Hz, 1 H) . ESI-MS m/z [M+H]+ calc'd for $C_{15}H_6ClFN_2O_2$ 300.01; found 300.95.

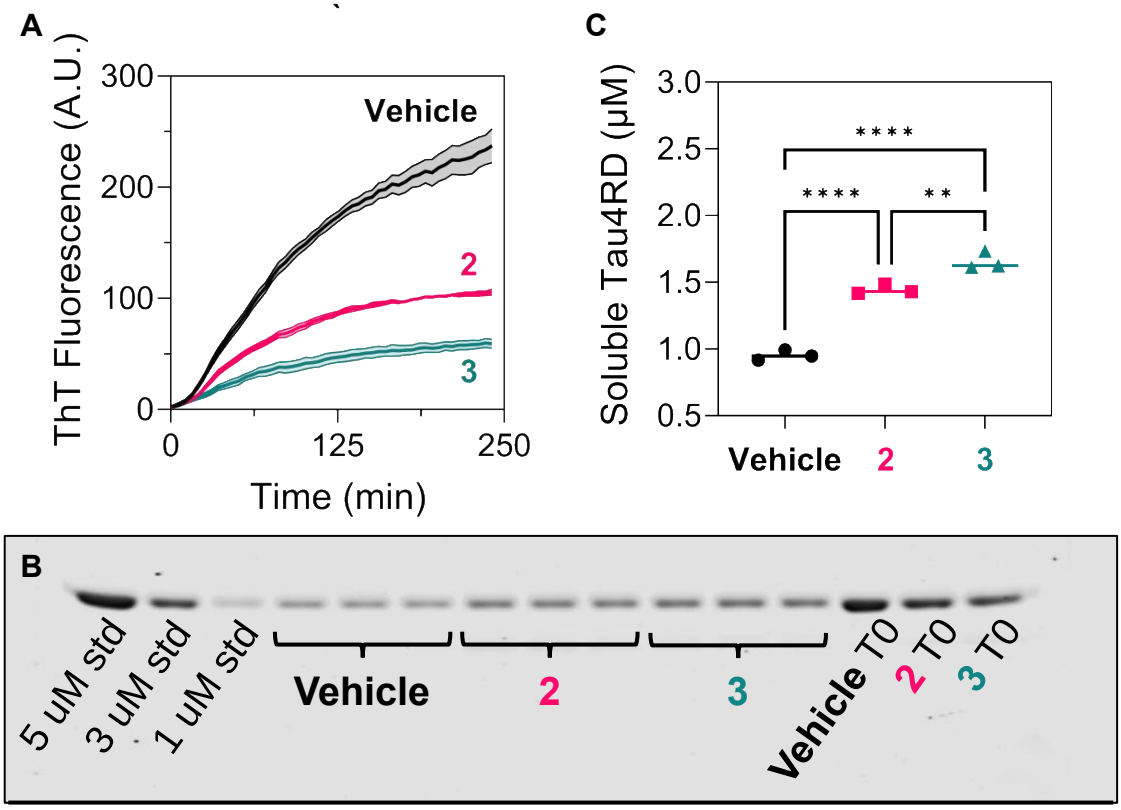

SI Fig. 2.1: Confirmation of TA analog activity by label-free centrifugation assays. A) Tau4RD (5 μM) aggregation kinetics in the presence of 5 μM 3 kDa heparin and either 10 μM **2**, 5 μM **3**, or vehicle control, in filtered buffer containing 20 mM Tris, 50 mM NaCl, and 1 mM TCEP. (*n* = 3 or 4, error bands show mean +/- SEM.) B) SDS-PAGE gel densitometry of soluble tau4RD remaining at *t* = 240 min from panel A, including additional Tau4RD concentration standards. C) Soluble tau4RD remaining at *t* = 240 min calculated from the results of panel B.

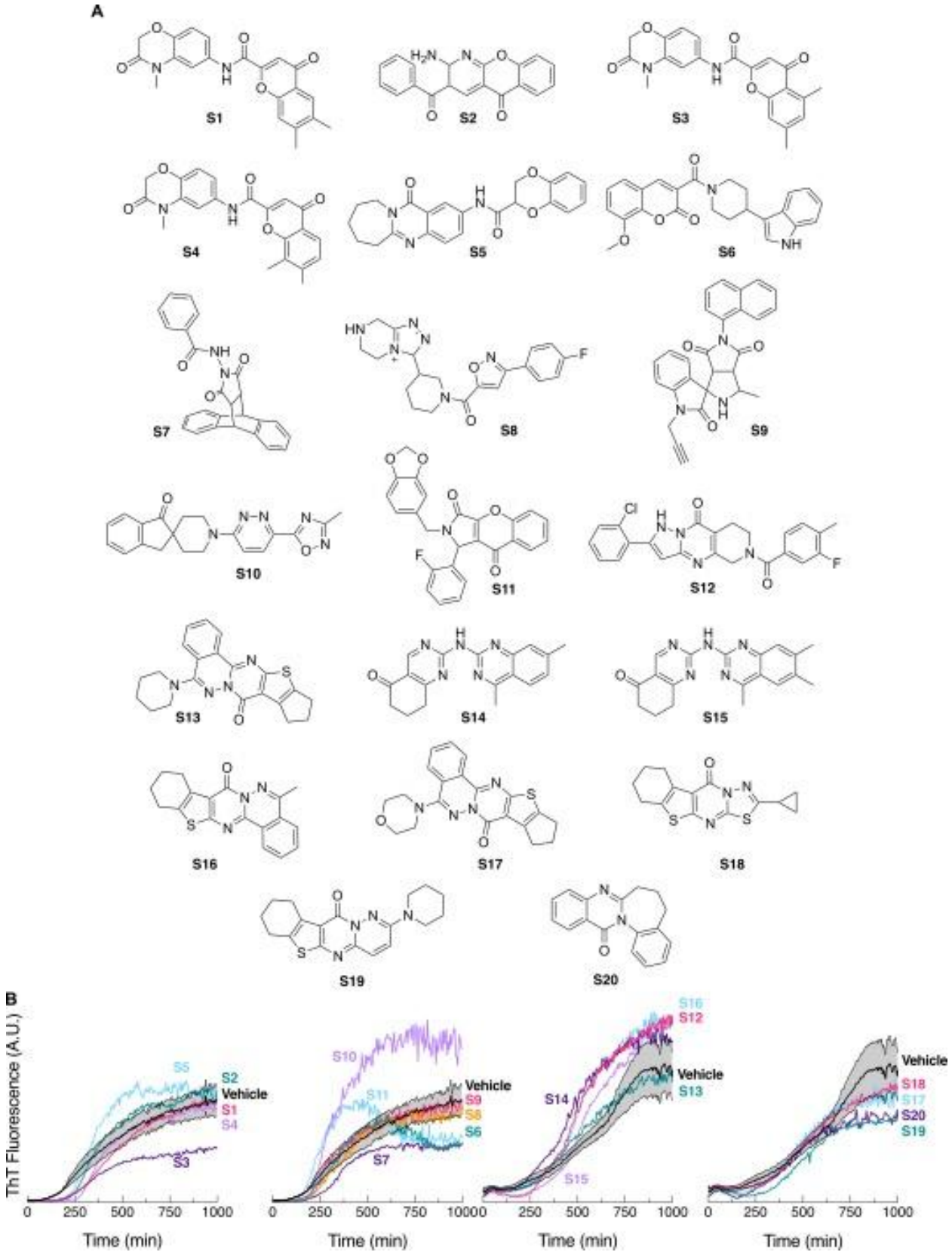
A
S1
S2
S3
S4
S5
S6
S7
S8
S9
S10
S11
S12
S13
S14
S15
S16
S17
S18
S19
S20
B
ThT Fluorescence (A.U.)
Time (min)
Vehicle
S1
S2
S3
S4
S5
S6
S7
S8
S9
S10
S11
S12
S13
S14
S15
S16
S17
S18
S19
S20

SI Fig. 2.2: Structures (A) and aggregation inhibition activity (B) of non-tryptanthrin compounds in screen. Conditions and formatting match those for Fig. 2.1.

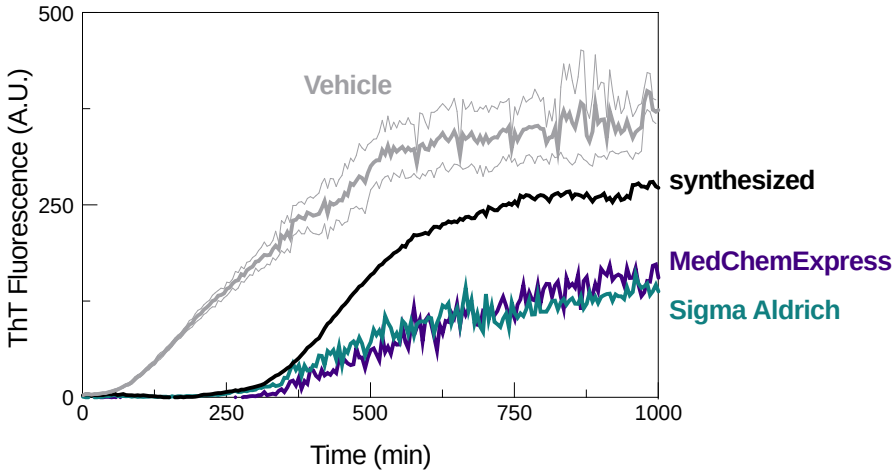

SI Fig. 2.3: Comparison of synthesized vs. commercially available tryptanthrin (1). Aggregation of 5 μM tau4RD is inhibited to similar extents by 0.31 μM **1** synthesized in-house or acquired from Sigma Aldrich (St. Louis, MO) or MedChemExpress (Monmouth Junction, NJ).

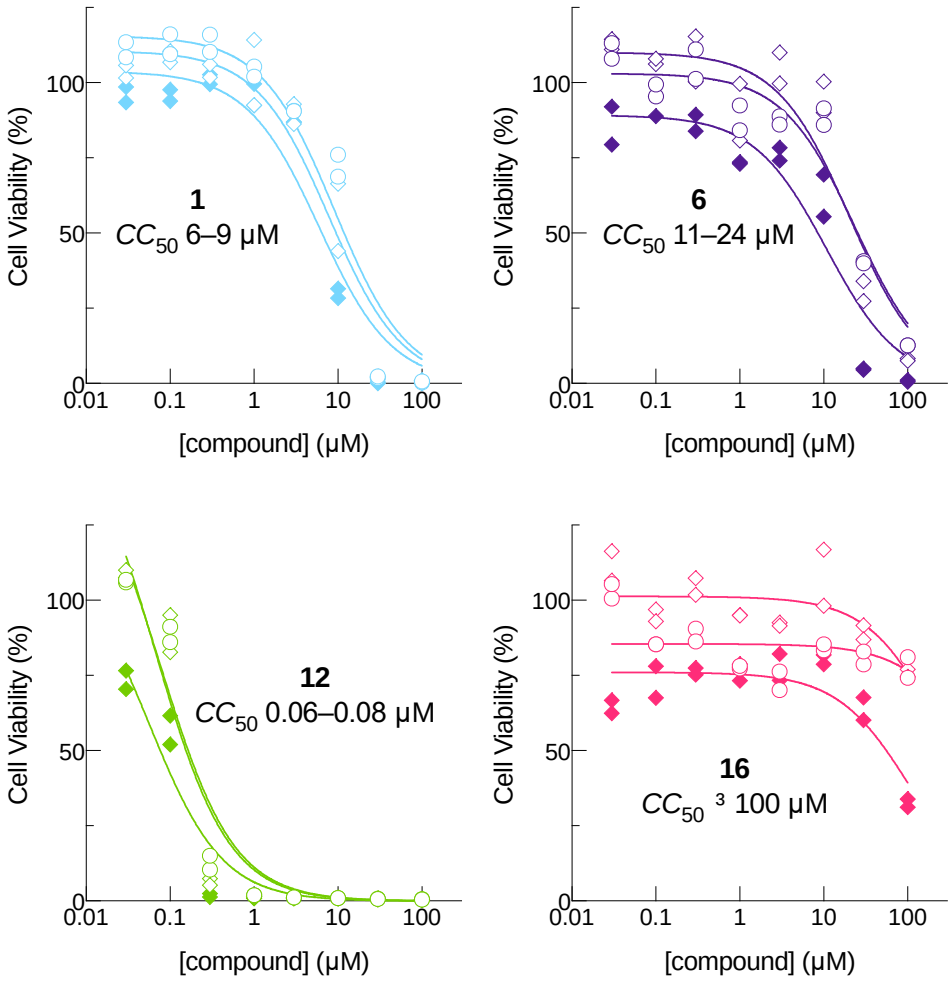

SI Fig. 2.4: Cytotoxicity of selected TA analogs towards HepG2 human hepatocellular carcinoma cells in culture. Cytotoxicity assays were conducted by Eurofins Discovery Services (Fremont, CA) using the following protocol: cells were plated in 384-well plates at a density of 3000 cells/well, cultured overnight at 37ºC, and transferred into assay media. These media included TA analogs at concentrations ranging from 0.03–100 μM in modified Eagle's medium without phenol red, 1% fetal bovine serum, 2 mM L-glutamine, 50 U/mL penicillin, 50 μg/mL streptomycin, supplemented with glucose (circles) or galactose (diamonds). Cell viability was measured in duplicate after 24 h (open symbols) or 72 h (closed symbols) using the Cell Titer Glo assay (Promega Corp., Madison, WI).

2.10 References

(1) Sharma, R.; Raduly, Z.; Miskei, M.; Fuxreiter, M. Fuzzy Complexes: Specific Binding without Complete Folding. FEBS Letters 2015, 589 (19), 2533–2542. https://doi.org/10.1016/J.FEBSLET.2015.07.022.

(2) van der Lee, R.; Buljan, M.; Lang, B.; Weatheritt, R. J.; Daughdrill, G. W.; Dunker, A. K.; Fuxreiter, M.; Gough, J.; Gsponer, J.; Jones, D. T.; Kim, P. M.; Kriwacki, R. W.; Oldfield, C. J.; Pappu, R. V.; Tompa, P.; Uversky, V. N.; Wright, P. E.; Babu, M. M. Classification of Intrinsically Disordered Regions and Proteins. Chem. Rev. 2014, 114 (13), 6589–6631. https://doi.org/10.1021/cr400525m.

(3) Wright, P. E.; Dyson, H. J. Intrinsically Disordered Proteins in Cellular Signalling and Regulation. Nat Rev Mol Cell Biol 2015, 16 (1), 18–29. https://doi.org/10.1038/nrm3920.

(4) Koo, E. H.; Lansbury, P. T.; Kelly, J. W. Amyloid Diseases: Abnormal Protein Aggregation in Neurodegeneration. Proc. Natl. Acad. Sci. U.S.A. 1999, 96 (18), 9989–9990. https://doi.org/10.1073/pnas.96.18.9989.

(5) Midic, U.; Oldfield, C.; Dunker, A.; Obradovic, Z.; Uversky, V. Unfoldomics of Human Genetic Diseases: Illustrative Examples of Ordered and Intrinsically Disordered Members of the Human Diseasome. PPL 2009, 16 (12), 1533–1547. https://doi.org/10.2174/092986609789839377.

(6) Götz, J.; Halliday, G.; Nisbet, R. M. Molecular Pathogenesis of the Tauopathies. Annu. Rev. Pathol. Mech. Dis. 2019, 14 (1), 239–261. https://doi.org/10.1146/annurev-pathmechdis-012418-012936.

(7) Uversky, V. N.; Oldfield, C. J.; Dunker, A. K. Intrinsically Disordered Proteins in Human Diseases: Introducing the D2 Concept. Annual Review of Biophysics 2008, 37 (1), 215–246. https://doi.org/10.1146/annurev.biophys.37.032807.125924.

(8) Iqbal, K.; Liu, F.; Gong, C.-X.; Grundke-Iqbal, I. Tau in Alzheimer Disease and Related Tauopathies. CAR 2010, 7 (8), 656–664. https://doi.org/10.2174/156720510793611592.

(9) Hasegawa, M. Molecular Mechanisms in the Pathogenesis of Alzheimer's Disease and Tauopathies-Prion-like Seeded Aggregation and Phosphorylation. Biomolecules 2016, 6 (2), 24. https://doi.org/10.3390/biom6020024.

(10) Goedert, M.; Jakes, R.; Spillantini, M. G. The Synucleinopathies: Twenty Years On. JPD 2017, 7 (s1), S51–S69. https://doi.org/10.3233/JPD-179005.

(11) Zhang, Y.; Wu, K.-M.; Yang, L.; Dong, Q.; Yu, J.-T. Tauopathies: New Perspectives and Challenges. Mol Neurodegeneration 2022, 17 (1), 28. https://doi.org/10.1186/s13024-022-00533-z.

(12) Limorenko, G.; Lashuel, H. A. Revisiting the Grammar of Tau Aggregation and Pathology Formation: How New Insights from Brain Pathology Are Shaping How We Study and Target Tauopathies. Chem. Soc. Rev. 2022, 51 (2), 513–565. https://doi.org/10.1039/D1CS00127B.

(13) Long, J. M.; Holtzman, D. M. Alzheimer Disease: An Update on Pathobiology and Treatment Strategies. Cell 2019, 179 (2), 312–339. https://doi.org/10.1016/j.cell.2019.09.001.

(14) Sims, J. R.; Zimmer, J. A.; Evans, C. D.; Lu, M.; Ardayfio, P.; Sparks, J.; Wessels, A. M.; Shcherbinin, S.; Wang, H.; Monkul Nery, E. S.; Collins, E. C.; Solomon, P.; Salloway, S.; Apostolova, L. G.; Hansson, O.; Ritchie, C.; Brooks, D. A.; Mintun, M.; Skovronsky, D. M.; TRAILBLAZER-ALZ 2 Investigators; Abreu, R.; Agarwal, P.; Aggarwal, P.; Agronin, M.; Allen, A.; Altamirano, D.; Alva, G.; Andersen, J.; Anderson, A.; Anderson, D.; Arnold, J.; Asada, T.; Aso, Y.; Atit, V.; Ayala, R.; Badruddoja, M.; Badzio-jagiello, H.; Bajacek, M.; Barton, D.; Bear, D.; Benjamin, S.; Bergeron, R.; Bhatia, P.; Black, S.; Block, A.; Bolouri, M.; Bond, W.; Bouthillier, J.; Brangman, S.; Brew, B.; Brisbin, S.; Brisken, T.; Brodtmann, A.; Brody, M.; Brosch, J.; Brown, C.; Brownstone, P.; Bukowczan, S.; Burns, J.; Cabrera, A.; Capote, H.; Carrasco, A.; Cevallos Yepez, J.; Chavez, E.; Chertkow, H.; Chyrchel-paszkiewicz, U.; Ciabarra, A.; Clemmons, E.; Cohen, D.; Cohen, R.; Cohen, I.; Concha, M.; Costell, B.; Crimmins, D.; Cruz-pagan, Y.; Cueli, A.; Cupelo, R.; Czarnecki, M.; Darby, D.; Dautzenberg, P. l. j.; De Deyn, P.; De La Gandara, J.; Deck, K.; Dibenedetto, D.; Dibuono, M.; Dinnerstein, E.; Dirican, A.; Dixit, S.; Dobryniewski, J.; Drake, R.; Drysdale, P.; Duara, R.; Duffy, J.; Ellenbogen, A.; Faradji, V.; Feinberg, M.; Feldman, R.; Fishman, S.; Flitman, S.; Forchetti,

C.; Fraga, I.; Frank, A.; Frishberg, B.; Fujigasaki, H.; Fukase, H.; Fumero, I.; Furihata, K.; Galloway, C.; Gandhi, R.; George, K.; Germain, M.; Gitelman, D.; Goetsch, N.; Goldfarb, D.; Goldstein, M.; Goldstick, L.; Gonzalez Rojas, Y.; Goodman, I.; Greeley, D.; Griffin, C.; Grigsby, E.; Grosz, D.; Hafner, K.; Hart, D.; Henein, S.; Herskowitz, B.; Higashi, S.; Higashi, Y.; Ho, G.; Hodgson, J.; Hohenberg, M.; Hollenbeck, L.; Holub, R.; Hori, T.; Hort, J.; Ilkowski, J.; Ingram, K. J.; Isaac, M.; Ishikawa, M.; Janu, L.; Johnston, M.; Julio, W.; Justiz, W.; Kaga, T.; Kakigi, T.; Kalafer, M.; Kamijo, M.; Kaplan, J.; Karathanos, M.; Katayama, S.; Kaul, S.; Keegan, A.; Kerwin, D.; Khan, U.; Khan, A.; Kimura, N.; Kirk, G.; Klodowska, G.; Kowa, H.; Kutz, C.; Kwentus, J.; Lai, R.; Lall, A.; Lawrence, M.; Lee, E.; Leon, R.; Linker, G.; Lisewski, P.; Liss, J.; Liu, C.; Losk, S.; Lukaszyk, E.; Lynch, J.; Macfarlane, S.; Macsweeney, J.; Mannering, N.; Markovic, O.; Marks, D.; Masdeu, J.; Matsui, Y.; Matsuishi, K.; Mcallister, P.; Mcconnehey, B.; Mcelveen, A.; Mcgill, L.; Mecca, A.; Mega, M.; Mensah, J.; Mickielewicz, A.; Minaeian, A.; Mocherla, B.; Murphy, C.; Murphy, P.; Nagashima, H.; Nair, A.; Nair, M.; Nardandrea, J.; Nash, M.; Nasreddine, Z.; Nishida, Y.; Norton, J.; Nunez, L.; Ochiai, J.; Ohkubo, T.; Okamura, Y.; Okorie, E.; Olivera, E.; O'mahony, J.; Omidvar, O.; Ortiz-Cruz, D.; Osowa, A.; Papka, M.; Parker, A.; Patel, P.; Patel, A.; Patel, M.; Patry, C.; Peckham, E.; Pfeffer, M.; Pietras, A.; Plopper, M.; Porsteinsson, A.; Poulin Robitaille, R.; Prins, N.; Puente, O.; Ratajczak, M.; Rhee, M.; Ritter, A.; Rodriguez, R.; Rodriguez Ables, L.; Rojas, J.; Ross, J.; Royer, P.; Rubin, J.; Russell, D.; Rutgers, S. M.; Rutrick, S.; Sadowski, M.; Safirstein, B.; Sagisaka, T.; Scharre, D.; Schneider, L.; Schreiber, C.; Schrift, M.; Schulz, P.; Schwartz, H.; Schwartzbard, J.; Scott, J.; Selem, L.; Sethi, P.; Sha, S.; Sharlin, K.; Sharma, S.; Shiovitz, T.; Shiwach, R.; Sladek, M.; Sloan, B.; Smith, A.; Solomon, P.; Sorial, E.; Sosa, E.; Stedman, M.; Steen, S.; Stein, L.; Stolyar, A.; Stoukides, J.; Sudoh, S.; Sutton, J.; Syed, J.; Szigeti, K.; Tachibana, H.; Takahashi, Y.; Tateno, A.; Taylor, J. D.; Taylor, K.; Tcheremissine, O.; Thebaud, A.; Thein, S.; Thurman, L.; Toenjes, S.; Toji, H.; Toma, M.; Tran, D.; Trueba, P.; Tsujimoto, M.; Turner, R.; Uchiyama, A.; Ussorowska, D.; Vaishnavi, S.; Valor, E.; Vandersluis, J.; Vasquez, A.; Velez, J.; Verghese, C.; Vodickova-borzova, K.; Watson, D.; Weidman, D.; Weisman, D.; White, A.; Willingham, K.; Winkel, I.; Winner, P.; Winston, J.; Wolff, A.; Yagi, H.; Yamamoto, H.; Yathiraj, S.; Yoshiyama, Y.; Zboch, M. Donanemab in Early Symptomatic Alzheimer Disease: The TRAILBLAZER-ALZ 2 Randomized Clinical Trial. JAMA 2023, 330 (6), 512. https://doi.org/10.1001/jama.2023.13239.

(15) van Dyck, C. H.; Swanson, C. J.; Aisen, P.; Bateman, R. J.; Chen, C.; Gee, M.; Kanekiyo, M.; Li, D.; Reyderman, L.; Cohen, S.; Froelich, L.; Katayama, S.; Sabbagh, M.; Vellas, B.; Watson, D.; Dhadda, S.; Irizarry, M.; Kramer, L. D.; Iwatsubo, T. Lecanemab in Early Alzheimer's Disease. N Engl J Med 2023, 388 (1), 9–21. https://doi.org/10.1056/NEJMoa2212948.

(16) Pardridge, W. M. Blood-Brain Barrier and Delivery of Protein and Gene Therapeutics to Brain. Front. Aging Neurosci. 2020, 11, 373. https://doi.org/10.3389/fnagi.2019.00373.

(17) Calcul, L.; Zhang, B.; Jinwal, U. K.; Dickey, C. A.; Baker, B. J. Natural Products as a Rich Source of Tau-Targeting Drugs for Alzheimer's Disease. Future Med Chem 2012, 4 (13), 1751–1761. https://doi.org/10.4155/fmc.12.124.

(18) Khan, S.; Hassan, Md. I.; Shahid, M.; Islam, A. Nature's Toolbox against Tau Aggregation: An Updated Review of Current Research. Ageing Research Reviews 2023, 87, 101924. https://doi.org/10.1016/j.arr.2023.101924.

(19) Sinha, S.; Lopes, D. H. J.; Du, Z.; Pang, E. S.; Shanmugam, A.; Lomakin, A.; Talbiersky, P.; Tennstaedt, A.; McDaniel, K.; Bakshi, R.; Kuo, P.-Y.; Ehrmann, M.; Benedek, G. B.; Loo, J. A.; Klärner, F.-G.; Schrader, T.; Wang, C.; Bitan, G. Lysine-Specific Molecular Tweezers Are Broad-Spectrum Inhibitors of Assembly and Toxicity of Amyloid Proteins. J. Am. Chem. Soc. 2011, 133 (42), 16958–16969. https://doi.org/10.1021/ja206279b.

(20) Sievers, S. A.; Karanicolas, J.; Chang, H. W.; Zhao, A.; Jiang, L.; Zirafi, O.; Stevens, J. T.; Münch, J.; Baker, D.; Eisenberg, D. Structure-Based Design of Non-Natural Amino-Acid Inhibitors of Amyloid Fibril Formation. Nature 2011, 475 (7354), 96–100. https://doi.org/10.1038/nature10154.

(21) Seidler, P. M.; Boyer, D. R.; Rodriguez, J. A.; Sawaya, M. R.; Cascio, D.; Murray, K.; Gonen, T.; Eisenberg, D. S. Structure-Based Inhibitors of Tau Aggregation. Nature Chemistry 2017, 10 (2), 170–176. https://doi.org/10.1038/nchem.2889.
(22) Kaffy, J.; Berardet, C.; Mathieu, L.; Legrand, B.; Taverna, M.; Halgand, F.; Van Der Rest, G.; Maillard, L. T.; Ongeri, S. Helical Γ-peptide Foldamers as Dual Inhibitors of Amyloid-β Peptide and Islet Amyloid Polypeptide Oligomerization and Fibrillization. Chem. Eur. J. 2020, 26 (64), 14612–14622. https://doi.org/10.1002/chem.202001716.
(23) Last, N. B.; Schlamadinger, D. E.; Miranker, A. D. A Common Landscape for Membrane Active Peptides. Protein Science 2013, 22 (7), 870–882. https://doi.org/10.1002/pro.2274.
(24) Kagan, B. L.; Jang, H.; Capone, R.; Teran Arce, F.; Ramachandran, S.; Lal, R.; Nussinov, R. Antimicrobial Properties of Amyloid Peptides. Mol. Pharmaceutics 2012, 9 (4), 708–717. https://doi.org/10.1021/mp200419b.
(25) Baggett, D. W.; Nath, A. The Rational Discovery of a Tau Aggregation Inhibitor. Biochemistry 2018, 57 (42), 6099–6107. https://doi.org/10.1021/acs.biochem.8b00581.
(26) Baggett, D. W.; Nath, A. Structure–Activity Relationships of Novel Tau Ligands: Passive Fibril Binders and Active Aggregation Inhibitors. ACS Chem. Biol. 2022, 17 (3), 701–708. https://doi.org/10.1021/acschembio.2c00012.
(27) Hwang, J.-M.; Oh, T.; Kaneko, T.; Upton, A. M.; Franzblau, S. G.; Ma, Z.; Cho, S.-N.; Kim, P. Design, Synthesis, and Structure–Activity Relationship Studies of Tryptanthrins as Antitubercular Agents. J. Nat. Prod. 2013, 76 (3), 354–367. https://doi.org/10.1021/np3007167.
(28) Iwata, T.; Watanabe-Yanai, A.; Tamamura-Andoh, Y.; Arai, N.; Akiba, M.; Kusumoto, M. Tryptanthrin Reduces Campylobacter Jejuni Colonization in the Chicken Gut by a Bactericidal Mechanism. Appl Environ Microbiol 2023, 89 (2), e01701-22. https://doi.org/10.1128/aem.01701-22.
(29) Olson, J. A.; Terryn, R. J.; Stewart, E. L.; Baum, J. C.; Novak, M. J. New Insight into the Action of Tryptanthrins against Plasmodium Falciparum: Pharmacophore Identification via a Novel Submolecular QSAR Descriptor. Journal of Molecular Graphics and Modelling 2018, 80, 138–146. https://doi.org/10.1016/j.jmgm.2017.12.013.
(30) Bandekar, P. P.; Roopnarine, K. A.; Parekh, V. J.; Mitchell, T. R.; Novak, M. J.; Sinden, R. R. Antimicrobial Activity of Tryptanthrins in Escherichia Coli. J. Med. Chem. 2010, 53 (9), 3558–3565. https://doi.org/10.1021/jm901847f.
(31) Agafonova, I. G.; Moskovkina, T. V. Studies on Anti-Inflammatory Action of Tryptanthrin, Using a Model of DSS-Induced Colitis of Mice and Magnetic Resonance Imaging. Appl Magn Reson 2015, 46 (7), 781–791. https://doi.org/10.1007/s00723-015-0674-3.
(32) Kirpotina, L. N.; Schepetkin, I. A.; Hammaker, D.; Kuhs, A.; Khlebnikov, A. I.; Quinn, M. T. Therapeutic Effects of Tryptanthrin and Tryptanthrin-6-Oxime in Models of Rheumatoid Arthritis. Front. Pharmacol. 2020, 11, 1145. https://doi.org/10.3389/fphar.2020.01145.
(33) Peng, J.-W.; Yin, X.-D.; Li, H.; Ma, K.-Y.; Zhang, Z.-J.; Zhou, R.; Wang, Y.-L.; Hu, G.-F.; Liu, Y.-Q. Design, Synthesis, and Structure–Activity Relationship of Quinazolinone Derivatives as Potential Fungicides. J. Agric. Food Chem. 2021, 69 (16), 4604–4614. https://doi.org/10.1021/acs.jafc.0c05475.
(34) Hesse-Macabata, J.; Morgner, B.; Elsner, P.; Hipler, U.-C.; Wiegand, C. Tryptanthrin Promotes Keratinocyte and Fibroblast Responses in Vitro after Infection with Trichophyton Benhamiae DSM6916. Sci Rep 2020, 10 (1), 1863. https://doi.org/10.1038/s41598-020-58773-2.
(35) Zou, Y.; Zhang, G.; Li, C.; Long, H.; Chen, D.; Li, Z.; Ouyang, G.; Zhang, W.; Zhang, Y.; Wang, Z. Discovery of Tryptanthrin and Its Derivatives and Its Activities against NSCLC in Vitro via Both Apoptosis and Autophagy Pathways. IJMS 2023, 24 (2), 1450. https://doi.org/10.3390/ijms24021450.
(36) Yu, S.; Chern, J.; Chen, T.; Chiu, Y.; Chen, H.; Chen, Y. Cytotoxicity and Reversal of Multidrug Resistance by Tryptanthrin-Derived Indoloquinazolines. Acta Pharmacol Sin 2010, 31 (2), 259–264. https://doi.org/10.1038/aps.2009.198.

(37) Yang, S.; Li, X.; Hu, F.; Li, Y.; Yang, Y.; Yan, J.; Kuang, C.; Yang, Q. Discovery of Tryptanthrin Derivatives as Potent Inhibitors of Indoleamine 2,3-Dioxygenase with Therapeutic Activity in Lewis Lung Cancer (LLC) Tumor-Bearing Mice. J. Med. Chem. 2013, 56 (21), 8321–8331. https://doi.org/10.1021/jm401195n.
(38) Zeng, Q.; Luo, C.; Cho, J.; Lai, D.; Shen, X.; Zhang, X.; Zhou, W. Tryptanthrin Exerts Anti-Breast Cancer Effects Both in Vitro and in Vivo through Modulating the Inflammatory Tumor Microenvironment. Acta Pharmaceutica 2021, 71 (2), 245–266. https://doi.org/10.2478/acph-2021-0020.
(39) Hou, H.; Li, H.; Han, Y.; Yan, C. Synthesis of Visible-Light Mediated Tryptanthrin Derivatives from Isatin and Isatoic Anhydride under Transition Metal-Free Conditions. Org. Chem. Front. 2018, 5 (1), 51–54. https://doi.org/10.1039/C7QO00740J.
(40) Pardridge, W. M. A Historical Review of Brain Drug Delivery. Pharmaceutics 2022, 14 (6), 1283. https://doi.org/10.3390/pharmaceutics14061283.
(41) Saurabh, S.; Nadendla, K.; Purohit, S. S.; Sivakumar, P. M.; Cetinel, S. Fuzzy Drug Targets: Disordered Proteins in the Drug-Discovery Realm. ACS Omega 2023, 8 (11), 9729–9747. https://doi.org/10.1021/acsomega.2c07708.
(42) Buell, A. K.; Dobson, C. M.; Knowles, T. P. J. The Physical Chemistry of the Amyloid Phenomenon: Thermodynamics and Kinetics of Filamentous Protein Aggregation. Essays In Biochemistry 2014, 56, 11–39. https://doi.org/10.1042/bse0560011.
(43) James, E. I.; Murphree, T. A.; Vorauer, C.; Engen, J. R.; Guttman, M. Advances in Hydrogen/Deuterium Exchange Mass Spectrometry and the Pursuit of Challenging Biological Systems. Chemical Reviews 2021. https://doi.org/10.1021/acs.chemrev.1c00279.
(44) Wagner, W. J.; Gross, M. L. Using Mass Spectrometry-based Methods to Understand Amyloid Formation and Inhibition of Alpha-synuclein and Amyloid Beta. Mass Spectrometry Reviews 2022, mas.21814. https://doi.org/10.1002/mas.21814.
(45) Wang, L.; Yin, Y.-L.; Liu, X.-Z.; Shen, P.; Zheng, Y.-G.; Lan, X.-R.; Lu, C.-B.; Wang, J.-Z. Current Understanding of Metal Ions in the Pathogenesis of Alzheimer's Disease. Transl Neurodegener 2020, 9 (1), 10. https://doi.org/10.1186/s40035-020-00189-z.
(46) Kim, A.; Lim, S.; Kim, Y. Metal Ion Effects on Aβ and Tau Aggregation. IJMS 2018, 19 (1), 128. https://doi.org/10.3390/ijms19010128.
(47) Schneider, C. A.; Rasband, W. S.; Eliceiri, K. W. NIH Image to ImageJ: 25 Years of Image Analysis. Nature Methods 2012, 9 (7), 671–675. https://doi.org/10.1038/nmeth.2089.

3. Tau4RD fibril polymorphism is imprinted during early aggregation

This chapter will be adapted for publication as a manuscript with the following author list:
Ellie I. James, Mason Saunders, Kelly K. Lee, Miklos Guttman, Abhinav Nath

Author contributions: E.I.J, M.G., and A.N. conceived the project. E.I.J performed *in vitro* aggregation assays, limited proteolysis, and pulsed HDX. M.S. generated nsEM data, which was analyzed by M.S. and K.K.L. E.I.J. drafted the manuscript with input from K.K.L., M.G., and A.N.

3.1 Abstract

Microtubule-associated protein tau forms characteristic fibrillar species in many neurodegenerative diseases. Neurofibrillary tangles, tau deposits observed in Alzheimer's disease (AD), contain a mixture of amyloid-type polymorphic fibrils called paired helical filaments (PHFs) and straight filaments. The formation of heterogenous fibril populations is observed in other diseases and when tau aggregation is induced *in vitro* with polyanionic species. This suggests that tau's structural transition from a conformational ensemble to various amyloid morphologies is a controlled and, therefore, controllable process. Despite many years of work toward describing aggregation intermediates that could address open questions such as whether fibril polymorphism is imprinted at the start of aggregation or arises due to conformational conversions, our understanding of amyloid structure remains predominantly based on observations of mature fibrils. It is unclear whether these processes are mutually exclusive and to what extent we can bias intermediate conformations toward less toxic states. Here to address the challenge of studying aggregation intermediates and tau's structural conversion, we apply pulsed hydrogen-deuterium exchange with mass spectrometry (pulsed HDX-MS), which revealed differences in the subpopulations formed by tau4RD (a truncated tau construct) within seconds of initiating aggregation with polyphosphate and within hours of heparin-induction. This work begins to address the gap in knowledge regarding whether amyloid polymorphism is directly imprinted during nucleation or results from structural rearrangement during later stages of aggregation.

3.2 Introduction

Tau and other intrinsically disordered proteins (IDPs) that lack a well-ordered overall conformation are prone to pathological misfolding and aggregation due to their conformational plasticity. The formation and deposition of fibrillar protein aggregates are hallmarks of many neurodegenerative diseases, including tauopathies like Alzheimer's Disease (AD) and chronic traumatic encephalopathy.[1,2] In these diseases, microtubule-associated protein tau's structural role in stabilizing neuronal axons is disrupted and tau begins to self-associate into amyloid-type fibrils with canonical cross-beta sheet morphology. Many of the more than 26 tauopathies described to date exhibit distinct fibrillar aggregates in *ex vivo* samples.[3,4] Recent studies suggest that the pattern of post-translational modifications (PTMs) on tau is reflective of the tauopathy causing fibrillization.[5,6] While PTMs are commonly associated with pathological aggregation, the sequence of events leading to PTM enrichment in tauopathies is unclear.[2,7,8]

Amyloidogenic aggregation can be modeled as a defined pathway in which a functional monomer undergoes an activating event that results in an aggregation-competent nucleus to which additional monomers add. This generates oligomers, which further develop into protofibrils and mature fibrils. Inducing tau aggregation *in vitro* often requires phosphorylation or the addition of polyanionic species such as RNA, polyphosphate, or heparin to overcome the positive electrostatic charge spread across the MTBR.[9–11] Changes in the tau conformational ensemble caused by aggregation initiation are first evident in a short hexapeptide, ^{306}VQIVYK^{311}, known as PHF6 which has been identified as a nucleation driver. PHF6 is present in all tau isoforms and has been found both necessary and sufficient for tau's aggregation.[12–14]

Although nucleation begins in the same handful of residues, distinct fibril morphologies result from tau's incubation with various aggregation inducers.[11,15,16] In the case of heparin, three fibril polymorphs develop within a single reaction.[16] Furthermore, aggregation *in vitro* is quite sensitive to changes in parameters such as reaction temperature, buffer composition, and agitation, which results in a broad range of aggregate morphologies even in the presence of a single polyanion.[17,18] Taken together, these observations suggest that there are points of control along tau's aggregation pathway that bias the amyloid conformation toward one morphology versus another. This remains an important open question in amyloid research, namely whether amyloid conformations are imprinted at the onset of aggregation or whether differences derive from conformational conversion further along the aggregation pathway.

We have limited insight into the evolution of structure during IDP aggregation, a fact that potentially hampers the development of diagnostics and therapeutics targeted at early intervention. Because oligomers are thought to be toxic in amyloidogenic diseases,[19–24] it would be of great benefit to therapeutically intervene at the monomeric or intermediate stage and thereby prevent additional neuronal damage. Despite extensive knowledge of fibril morphology due to advances in structural techniques such as cryo-EM,[16,25–

[27] this knowledge is not transferable to the dynamic and transient species present during aggregation that elude characterization. Recently, Lövestam *et al.* have pushed the limit by characterizing tau amyloid intermediates by cryo-EM, although their chosen approach provided limited kinetic information.[28] Pulsed HDX-MS is a solution state technique that is size-agnostic and can inform on the profile of structural order throughout a protein even as it populates transient and disordered species.[29,30] It can be used to simultaneously identify subpopulations within a reaction (e.g., monomer, oligomer A, oligomer B) and deconvolve aggregation kinetics, facilitating meaningful comparisons about the temporal and structural changes that occur during protein aggregation.[31,32] Here, we apply pulsed HDX-MS to track the propagation of heparin- or polyphosphate-induced structural differences along tau's aggregation pathway and find that distinct fibril morphologies appear to be biased during nucleation rather than occurring through a conformational conversion mechanism during mid-to-late aggregation.

3.3 Results

3.3.1 Generation of conformationally distinct recombinant tau4RD fibrils

It has been shown that inducing tau aggregation with different polyanions generates conformationally distinct fibrillar species.[9,11,27] Indeed, in our hands, fibrils generated by the addition of heparin or polyphosphate to recombinant tau4RD are morphologically distinct by negative stain EM (nsEM). Differences in branching, helicity, and fibril diameter were observed (Fig. 3.1A/B, SI Fig. 3.1). Other factors that could influence fibril morphology, such as temperature, buffer composition, and mechanical agitation, were held constant in these experiments. Limited proteolysis MS/MS experiments supported the inference that tauR4D adopts different conformations since qualitative differences in fibril digestion patterns between monomer, heparin-induced fibrils, and polyphosphate-induced fibrils were clearly evident (SI Fig. 3.1). We do not interpret the limited proteolysis MS/MS data beyond the qualitative statement that the cleavage products (defined only by c-terminal residue) are different between heparin- and polyphosphate-induced fibrils. While further analysis could reveal additional insight into the amyloid morphologies present in each sample, we do not seek to characterize the fibrils, only their intermediates.

3.3.2 Characterization of divergent aggregation pathways

An open question in the amyloid field is whether amyloid structure is imprinted upon aggregation initiation or whether amyloid differentiation occurs through conformational conversion during later stages of the aggregation process. To monitor time-dependent structural changes in tau4RD structure in the presence of polyphosphate or heparin, we employed pulsed HDX-MS. Figure 3.1C shows a cartoon of a pulsed HDX-MS experiment in which the fibril core is tightly packed and hydrogen bonded, which prevents

residues in this region from undergoing HDX. In comparison, the monomer is solvent-exposed and unstructured, making it highly susceptible to HDX. By applying a 3-sec deuterium pulse and observing the peptide-level deuterium uptake, we can discern which regions of tau are monomer-like vs. fibril-like at various points during tau4RD aggregation. Despite attempting to dissociate tau4RD amyloid fibrils with very harsh HDX quench conditions (7 M guanidine HCl), the fibril populations could not be effectively disassembled and were thus not amenable to digestion. Therefore, the populations observed omit the contribution of any fibrils but accurately measure the monomeric and protofibrillar subspecies.

Tau4RD exhibits a decrease in deuterium incorporation during both heparin-induced and polyphosphate-induced aggregation that correlates with amyloid formation monitored by increased ThT fluorescence (Fig. 3.2A, inset). Tau4RD and inducer concentrations were identical for ThT fluorescence assays and HDX assays, which were performed side-by-side on the same 96-well plate. The only difference in composition between the two assays was the inclusion of 10 μL of ThT solution versus 10 μL of buffer. Without heparin or polyphosphate, there was no decrease in deuterium uptake, indicating that the changes in tau4RD's deuteration profile are caused by the addition of aggregation inducer (Fig. 3.2A, dashed grey lines). Protection from HDX and changes in the tau4RD ensemble caused by heparin-induced aggregation appear by 240 min of aggregation (Fig. 3.2A, inset); at this time, protection appears between residues 284-323 (Fig. 3.2A, 3.3D, SI Figs. 3.2/3.4). Polyphosphate-induced tau4RD aggregation occurs much more quickly than heparin-induced tau4RD aggregation and lacks a distinct lag phase under our experimental conditions (Fig. 3.2A, inset). However, the resulting structures are clearly fibrillar (Fig. 3.1B), and the process is irreversible, indicating that we are observing *bona fide* fibril formation rather than amorphous aggregation or liquid-liquid phase separation. By 15 sec after aggregation initiation (early elongation), pulsed HDX-MS detects protection in peptides ^{260}IGS…KKL^{282}, ^{291}CGS…VYK^{311}, and ^{308}IVYKPVDLSK^{317} (Fig. 3.2A). While Fig. 3.2A, an alternate visualization of an HDX uptake heatmap, provides a per-residue (averaged) overview of the kinetic and structural differences between heparin- and polyphosphate-induced fibril formation, it obscures key differences in deuteration levels that result from distinct populations in the samples. Figs. 3.2B/C depict the final pulsed HDX time point for each condition. Protection from HDX (less deuteration) is more widespread throughout the tau4RD sequence (x-axis) during polyphosphate-induced than during heparin-induced aggregation, particularly near the termini. Note the absence of low-exchanging subpopulations in the heparin condition near residues 240-257 and 350-372 (Fig. 3.2B, SI Fig. 3.13/3.14). In both cases, the polyphosphate fibril core extends further than is apparent in Fig. 3.2A.

One advantage of pulsed HDX-MS is its ability to differentiate the number of conformational subpopulations that exist simultaneously within a sample by quantifying differences in their level of

protection. The isotopic distributions in the spectra can reveal the existence of more than the two conformational subpopulations expected when observing a transition like aggregate forming from monomer. HXExpress v3[33] was used to fit one or more binomial distributions to the mass envelopes of 26 peptides common to heparin- and polyphosphate-induced tau4RD fibrils. Multimodal tau4RD spectra occur throughout the heparin-induced fibril core, including in peptides ^{260}IGS…KKL^{282} and ^{291}CGS…VYK^{311} (Fig. 3.3A). These multimodal distributions can be fit with two binomials that represent monomer-like (high-exchanging, unprotected) and fibril-like (low-exchanging, protected) states in peptides across the tau4RD sequence. This single protected species accounts for ~ 33% of the population 360 min after initiation with heparin (Fig. 3.3A).

In contrast to our observations of peptides ^{260}IGS…KKL^{282} and ^{291}CGS…VYK^{311} in heparin-induced tau4RD aggregation, the mass envelope of these peptides cannot be adequately explained by two binomials in the polyphosphate aggregation condition. Applying a multimodal (three binomials) fit to the mass envelope of these peptides results in a statistically justified fit (p-value = 4.0×10^{-5}, Fig. 3.3A, SI Fig. 3.6), indicating the presence of at least two distinct protected populations (i.e., fibril morphs). By comparing the multimodal analyses of peptide ^{291}CGS…SVQ^{307} and redundant peptide ^{291}CGS…SVQIVYK^{311}, we can confidently say that residues ^{308}IVYK^{311} in the PHF6 aggregation-driving region are distinct in the two fibril forms (Fig. 3.3A). Residues beyond the four in this segment may also be distinct in the fibrils but lack of overlapping peptides precludes determining the exact stretch of relevant residues. Further, by comparing the subpopulation distribution between these redundant peptides throughout aggregation, we can determine that at 60 min of aggregation, morph B accounts for 29 ± 0% of the tau4RD population while a second morph accounts for 26 ± 1% of the population and begins in the PHF6 region (Fig. 3.3B/C). Strikingly, the relative population fractions of these two protected states remain constant throughout aggregation, suggesting that each subpopulation represents a stable protofibril conformation instead of an intermediate species converting into the final conformation (Fig. 3.3C). The medium- and low-exchanging species seen in Fig. 3.2C represent separate polyphosphate-induced tau4RD fibril morphs that account for a total of approx. 57% of the population at the final time point.

3.3.3 Effect of a potent aggregation inhibitor

We have recently demonstrated that tryptanthrin and several synthetic analogs are potent inhibitors of tau4RD aggregation that act primarily by inhibiting tau4RD nucleation.[34] Here, we investigated whether inhibiting nucleation with tryptanthrin changes the resulting fibril morphologies for either heparin- or polyphosphate-induced tau4RD aggregation. As previously described, the substoichiometric (1:2) addition of tryptanthrin to heparin-induced tau4RD aggregation delayed the onset (longer lag phase) and strongly

decreased the rate (decreased transition steepness) and extent (decreased plateau fluorescence) of tau4RD aggregation (Fig. 3.4A, inset). However, pulsed HDX-MS comparison reveals that tryptanthrin does not cause conformational changes in the core of fibrils formed in the presence of heparin, although peptides at the C-terminal edge of the core shift from weakly multimodal to unimodal (e.g., Fig. 3.4B/C peptide 341-353) due to the overall reduction in aggregation, resulting in these low abundance populations falling below the limit of detection.

Incubation with substoichiometric tryptanthrin (1:2) modestly decreases the extent of polyphosphate-induced tau4RD aggregation (Fig. 3.5B, inset) but does not result in changes to the fibril core observed by pulsed HDX-MS (Fig. 3.5B/C). Like the effect observed on the C-terminal side of the heparin fibril core, peptides with low abundance multimodal character (e.g. peptide 350-372, SI Fig. 3.13) become unimodal after incubation with tryptanthrin. This likely results from the suppression of aggregation rather than a change in the polyphosphate-induced fibril conformations. Moreover, the relative population distribution of morph B and morph C throughout polyphosphate-induced aggregation with tryptanthrin is unchanged (SI Fig. 3.10), providing additional evidence that the fibril morphs observed during polyphosphate-induced aggregation are unchanged by tryptanthrin and are conformationally distinct from heparin-induced fibrils. Further, it is clear from this data that tryptanthrin does not preferentially inhibit one polyphosphate-induced nucleus compared to the other, which would result in a skewed population distribution compared to the vehicle-controlled state.

3.4 Discussion

Although amyloid aggregation is a complex process, it can be simplified with the application of nomenclature that describes relevant steps in the aggregation process. For example, “nucleation” is the transition that a monomer undergoes to make it aggregation-prone, and “elongation” describes the process by which additional monomers add to existing fibril ends. The microscopic processes involved in amyloid formation (e.g., primary nucleation, fibril fragmentation) are characteristic of an individual protein’s self-assembly landscape and can change depending on the environmental conditions.[17,18,27,35–39] For example, heparin- and polyphosphate-induced tau4RD aggregation exhibit strikingly different kinetics. Nucleation of tau4RD in the presence of heparin occurs much more slowly than in the presence of polyphosphate, made apparent by the approximately 150-minute lag phase observed in heparin-induced aggregation and the absence of a lag phase during polyphosphate-induced aggregation (Fig. 3.2 inset). The rate-limiting step of heparin-induced aggregation is nucleation, while that of polyphosphate-induced aggregation is fibril elongation. Although these differences are reflected in the shape of the aggregation curve, they are also represented by the total duration of aggregation. Tau4RD aggregation takes more than twice as long to

plateau when initiated with heparin versus polyphosphate, and the shape of the curves indicates a much higher fibril elongation rate (steeper transition slope) observed during polyphosphate-induced aggregation. Although polyphosphate and heparin are both highly negatively charged and have similar charge density per unit length (-0.31 e/Å vs. -0.27 e/ Å), they differ in the chemistry and arrangement of their negative charge (phosphate vs. sulfates/carboxyl).[18] This results in distinct aggregation kinetics as well as the formation of distinct amyloid species when used to initiate tau4RD aggregation *in vitro.* Both nsEM and limited trypsin/lys-C proteolysis of the polyphosphate- and heparin-induced tau4RD fibrils confirmed that differences exist in the final amyloid structures formed between the two conditions (Fig. 3.1A/B, SI Fig. 3.1).

Despite the clear picture of endpoint tau fibril morphologies observed by cryo-electron microscopy,[16,25–27] the transient nature of amyloid intermediates has, until recently, limited their structural characterization and precluded the determination of when amyloid conformations diverge. Lövestam *et al.* applied time-resolved cryo-EM to monitor the amyloid formation of a truncated tau construct consisting of residues 297-391. The authors discovered a species they termed the FIA (first amyloid intermediate), the first intermediate structured enough to resolve with cryo-EM. During further monitoring, the authors observed maturation and conformational conversion of the FIA into polymorphic intermediates, some of which were shared amongst aggregation conditions.[28] Although this cryo-EM data provides structural insight into the origin of amyloid polymorphism, it does not provide kinetic details about the assembly reactions.

Pulsed HDX-MS addresses this concern because it can track the kinetics and structural conversions of aggregation *in situ*. Another powerful advantage of pulsed HDX-MS in the study of aggregation intermediates is its ability to discern the prevalence of conformational subpopulations.[29,33] Unlike the data in Fig. 3.2A, which is based on the averaged deuterium shift approximated to single residues through all observable peptides, the data in Fig. 3.3A shows the mass envelope for a given peptide and has been analyzed to discern distinct populations.[33] This format lends itself to the determination of subpopulations such as the protected (purple, lower mass) and unprotected (teal, higher mass) observed in peptides spanning residues 260-353 for heparin and 240-372 for polyphosphate. Protection extending further than residue 323 is not apparent in the centroided, per-residue deuteration levels in Fig. 3.2B due to the small and poorly resolved population fractions, emphasizing the importance of multimodal fitting to extract the full scope of information contained within the data. The low abundance protected populations observed at the termini are not artifacts; they are never observed in the monomer injections in which no aggregation has occurred. They also do not appear in earlier time points or in blank injections, which would be expected if they were the result of carryover from fibrils sticking to the protease column and slowly disassembling which would cause apparent protected subpopulations in subsequent runs.

Multimodal fitting of peptide ^{291}CGS…VYK^{311} revealed the evolution of multiple protected subpopulations during polyphosphate-induced aggregation and a single protected population during heparin-induced aggregation (Fig. 3.3A). Remarkably, both polyphosphate-specific protected subpopulations were detected 15 seconds after the addition of polyphosphate and increased in population fraction concurrently (Fig. 3.3C), lending support to our hypothesis that fibril polymorphism is imprinted early in the aggregation process rather than occurring through a conformational conversion process. This comparison highlights the power of pulsed HDX-MS to interrogate the conformational differences between separate aggregation pathways as well as the differences that develop within a single aggregation reaction.

After establishing pulsed HDX-MS as an experimental tool capable of detecting structural differences between aggregation intermediates, we sought structural and mechanistic information about tryptanthrin-mediated aggregation inhibition. To facilitate detectable levels of aggregation, a substoichiometric (1:2) molar ratio of tryptanthrin to tau4RD was chosen. As expected, heparin-induced aggregation was greatly diminished by the inclusion of tryptanthrin, but somewhat surprisingly, the resulting aggregation intermediates and fibril core were the same as in the control condition. Unlike with heparin, tryptanthrin only mildly inhibits polyphosphate-induced tau4RD aggregation (SI Fig. 3.7). Once again, tryptanthrin was found not to change the core of either polyphosphate-induced fibril morph or the ratio of their populations to each other, supporting that both polyphosphate-induced polymorphs are distinct from that observed during heparin-induced aggregation and neither is preferentially inhibited by tryptanthrin.

While our data is extremely revealing, there remain some limits to its interpretation. First, polyphosphate-induced tau4RD aggregation proceeds so quickly that there are sizeable changes in the subpopulation fractions of, e.g., peptide ^{291}CGS…VYK^{311} between within samples collected in the first minute after initiating aggregation. It was not possible to collect duplicate samples in this time regime due to these changes, so a single data point was collected at 15-sec and 30-sec post-initiation. This limitation is alluded to in Fig. 3.3B/C and can be seen in more detail in SI Fig. 3.11. Despite this, both protected subpopulations are visible at the earliest time point in the first replicate (SI Fig. 3.11), indicating that polymorphism has fully evolved by 15-sec after the start of polyphosphate-induced aggregation.

Second, our pulsed HDX experiments lacked a deuterium exposure control (internal exchange reporter). Although 3-sec deuterium pulses were performed with the aid of a metronome,[40] there are likely small variations in deuterium exposure between samples. We have mitigated this shortcoming by choosing a pulse duration that adequately separates monomeric and structured tau4RD populations and through our analysis of subpopulation prevalence rather than by comparing %D across samples. Although HXExpress v3 can confidently assign peptide spectra as unimodal, bimodal, trimodal, etc., it cannot deconvolute poorly resolved subpopulation fractions. For this reason, we have taken a conservative approach to inter- and intra-

inducer comparisons, focusing on the statistically justified differences in the number of subpopulations detected in key regions of the tau4RD sequence.

Finally, mature amyloid fibrils are not amenable to pulsed HDX-MS in our hands because they cannot be solubilized for LC-MS analysis. We see no changes in the relative signal intensities during LC-MS of peptides in the fibril core versus those at the extreme N- and C-termini in monomeric digests, early aggregation digests, or digests performed during the mid-to-late elongation phase, suggesting that fibrils are not disproportionately contributing to peptide signal at the termini. Negating the contribution of fully formed fibrils means that we do not have a fully quantitative picture of the populations present, but we do still get a complete picture of the early intermediates that lead to fibrils. Fortunately, these are the high-value targets that we wanted to structurally characterize.

Here we have presented a comparative structural analysis of heparin- and polyphosphate-induced tau4RD aggregation. We highlight differences in the extent of the tau4RD sequence involved in the fibril core and differences in conformational polymorphism, specifically observed in regions 260-282 and 291-321 in polyphosphate-induced samples. Our results support the conclusion that tau fibril polymorphism is imprinted during nucleation; we see no evidence of conformational conversion through the course of fibril formation and maturation. This, at first glance, appears to contradict the findings of Lövestam *et al.* who found evidence of an intermediate common to two separate tau aggregation reactions and determined that differences in fibril polymorphism arose through the structural maturation of the FIA. None of the protection profiles we observed are consistent with the FIA, although this is unsurprising due to the different systems our two studies used to induce tau's aggregation. There are many possible explanations for the disparate conclusions we have reached. Namely, their work and ours made use of different tau constructs which could cause differences in aggregation mechanism. The construct we use (tau4RD, residues 244-372) contains PHF6*, a second hexapeptide motif known to drive aggregation; the construct used by Lövestam *et al.* does not contain PHF6* but does comprise all the residues that form the proteolytically-stable core of PHFs observed in *post-mortem* AD patient samples. The differences in polymorphic behavior we observed could simply be intrinsic to these different tau constructs. Alternatively, the timeline of polyphosphate-induced tau4RD aggregation is far removed from that observed in the Lövestam study or in our own heparin-induced aggregation. It could be that *in vitro* polyphosphate-induced aggregation is kinetically controlled and proceeds without the thermodynamically stable FIA, but conditions that promote an aggregation lag phase allow time for the FIA to arise and mature into separate polymorphs. Regardless, these discrepancies clearly indicate that we need to deepen our understanding of the origin of amyloid polymorphism to create a unified framework.

3.5 Materials and Methods

3.5.1 Protein Expression and Purification

Tau4RD was generated in-house as recently described. In brief, tau4RD was expressed and purified in *E. coli* BL-21 (DE3) from a plasmid gifted by the Rhoades lab at the University of Pennsylvania (Philadelphia, PA). In brief, a three-step purification consisting of two Ni-NTA agarose column steps followed by fractionation with a 25 mL S200 extended gel filtration column. Tau4RD purity was confirmed by precast 12% Bis-Tris SDS-PAGE gels (Invitrogen). Protein was concentrated, aliquoted, and flash-frozen before storage at -80 °C. Protein concentrations were determined using the Pierce BCA Protein Assay Kit (Thermo Fisher Scientific).

3.5.2 Aggregation Assays

Tau4RD aggregation assays were completed as previously described with the following changes.[34] Tau4RD and the aggregation inducers were prepared at 2.105x the desired final concentration in a buffer consisting of 20 mM MOPS, 50 mM NaCl, 1 mM TCEP, 1 mM EDTA mixed in optima H2O, pH = 7.44. The buffer was not filtered prior to use. Tau4RD and tryptanthrin (or an equivalent volume of DMSO) aliquots were thawed and diluted to 10.526 μM (tau4RD) and 5.263 μM (tryptanthrin), respectively, in a combined final volume of 460 μL per experimental condition. For each condition, 95 μL of tau4RD sample was plated into each of n = 3 or 4 wells on a black 96-well plate with a multi-channel pipette. Then, 10 μL of 1 mM filtered (0.22 μm) ThT stock was added to each well with a multi-channel pipette (final concentration of 50 μM ThT). Finally, 95 μL of heparin at 10.526 μM or 95 μL of polyphosphate (Kerafast, medium chain) at 21.05 μg/mL was added to each well for a final concentration of 5 μM heparin or 10 μg/mL polyphosphate (approx. 7 μM when average polyphosphate chain length (mode) is 75 units). The plate was then covered with a polypropylene or polyolefin film and placed into a BioTek Synergy HTXplate reader pre-heated to 37 °C. Aggregation was monitored until completion (overnight, ~17 h unless stated otherwise) by ThT fluorescence (λ_{ex} = 440 nm, λ_{em} = 485 nm). Fluorescence readings were collected every 5 minutes following 1 minute of linear shaking at 540 rpm. All ThT fluorescence assays were performed with non-binding black 96-well flat-bottom plates (Corning). A blank sample was prepared as above but without tau4RD. The blank was used to correct baseline fluorescence.

3.5.3 Gel Densitometry

Aggregation assays were stopped at the indicated time and wells were pipetted into individual 1.5 mL tubes. The tubes were centrifuged at 21,000*g* for 30 min at 4 °C, after which 15 μL of supernatant was added to 3 μL of 5x SDS loading dye. Concentration standards were prepared at 5 μM, 2.5 μM, and 1.25 μM and included on the plate during the aggregation assay. Samples and standards were boiled for 45 sec,

cooled on ice, then 15 uL was added to precast 12% Bis-Tris SDS-PAGE gels. Gels were imaged with a Li-Cor Odyssey CLx gel scanner and band intensity was determined using GelAnalyzer 23.1.1 (available at www.gelanalyzer.com) by Istvan Lazar Jr., PhD and Istvan Lazar Sr., PhD, CSc. N = 2 or 3 and results were averaged (mean).

3.5.4 Limited Proteolysis

3.5.4.1 Trypsin/Lys-C Digest

Tau4RD was prepared and aggregated as above, except additional aggregation buffer (10 μL) was added to the wells in place of ThT solution. At the end of aggregation, wells were pipetted individually into non-binding 1.5 mL tubes, then centrifuged at 21,000 g for 30 min at 4 °C. Fibril pellets were isolated by removing 175 μL of supernatant from each tube. Trypsin/Lys-C Protease Mix (Pierce, MS-Grade) was resuspended at 0.5 mg/mL in PBS buffer pH 7.4 (20 mM phosphate, 150 mM NaCl, 0.02% sodium azide, 1 mM EDTA), aliquoted, and stored at -20 °C until use. For tau4RD fibril digest, 0.4 μg of Trypsin/Lys-C mix was added to each tube. Initially, samples were incubated at 37 °C for 15, 30, 60, or 120 min. After comparing cleavage products, a 30-minute digestion was chosen for further experiments. Proteolysis was quenched and fibrils were disrupted with the addition of 8 M urea, pH 2.5, and 30-min incubation at 37 °C. Samples were cooled to room temperature, used immediately in an SDS-PAGE gel, or flash-frozen and stored at -80 °C until LC-MS/MS analysis.

3.5.4.2 LC-MS/MS

Samples were thawed at 5 °C for 4.5 minutes and injected using a custom LEAP robot integrated with an LC-MS system.[41] Peptides were trapped on a Waters XSelect CSH C18 trap cartridge column (2.1 x 5 mm 2.5 μm) and resolved over a CSH C18 column (1 x 50 mm 1.7 μm 130Å) using a linear gradient of 5 to 35% B (A: 0.1% FA, 0.025% TFA, 5% ACN; B: ACN with 0.1% FA) over 10 minutes and analyzed on a Thermo Orbitrap Ascend mass spectrometer at a resolution setting of 120,000. A series of washes over the trap column were used between injections to minimize carry-over as described previously. Data-dependent MS/MS acquisition was performed using rapid CID and HCD scans and processed in Byonic (Protein Metrics) with a digestion filter set to K/R and infinite missed cleavages. A score cutoff of 200 was used to identify peptides.

3.5.4.3 Peptide Mapping

Peptides identified from limited proteolysis-LC-MS/MS were filtered, sorted, and compared using an in-house Python script (available upon request). Briefly, each K/R position in tau4RD was assessed for proteolysis by totaling the XIC of peptides with K/R in the C-terminal position. K/R positions with XIC signals less than 1e5 were assigned an XIC value of 0. The XIC for each K/R position (per sample) was

then normalized to the average (mean) XIC of all K/R positions within the sample. This is a simplified workflow that neglects considering the starting residue of each cleavage product. If quantitative rather than qualitative cleavage readouts are necessary, we recommend a more in-depth analysis and comparison.

3.5.5 Pulsed HDX

Pulsed HDX experiments were designed to minimize perturbing aggregation by separating each time point into a different well on the plate. This means that duplicate samples are created from a single well for each time point, but each time point is pulled from a separate well (i.e., a separate aggregation reaction). As such, the extent of aggregation may vary slightly between time points even though aggregation was initiated at the same time.

Aggregation assays were prepared as described above. Samples for pulsed HDX-MS did not contain ThT (replaced with 10 µL of aggregation buffer), but n = 3 or 4 matched wells contained ThT to monitor aggregation progress during the pulsed HDX experiments. At each time point, the corresponding ThT-free well was transferred into a 1.5 mL lo-bind tube (Eppendorf) and held at 37 °C. The 96-well plate was returned to the plate reader for continued monitoring. Then, 20 µL of tau4RD/mixture was diluted into 80 µL of deuterated MOPS buffer (20 mM MOPS, 50 mM NaCl, 1 mM TCEP, 1 mM EDTA, 0.2 nM bradykinin, pH* 7.18, 70% D final) for 3 sec at 21 °C. Timing accuracy was facilitated using an electronic metronome set to 60 beats/min. After 3 sec, the sample was rapidly mixed with an equal volume of ice-cold quench (4 M urea, 0.2 % formic acid, 0.1% TFA) for a final pH of 2.51. Samples were immediately frozen on ethanol/dry ice and stored at -80 °C until LC-MS analysis. Samples were collected in duplicate at each aggregation time point. Fully deuterated samples were prepared by incubating monomeric tau4RD with deuterated buffer at 21 °C for 60 min. Samples were then quenched and frozen as above. Undeuterated samples were prepared alongside fully deuterated samples but with a matched deuterium-free buffer.

3.5.6 LC-MS for HDX samples

Of note, samples containing polyphosphate were challenging to assay via LC-MS and significant effort went into identifying suitable experimental conditions. Briefly, polyphosphate buildup on the trap and analytical columns prevented peptide binding, resulting in blank or extremely noisy mass spectra. A neutral-pH wash was passed over the trap and analytical columns between each sample injection to remove polyphosphate buildup. No carryover was detected in blanks injected between polyphosphate- or heparin-containing samples.

All HDX samples were subjected to LC-MS on a Thermo Orbitrap Ascend during an uninterrupted three-day period. Samples were thawed at 5 °C for 4.5 minutes and injected using a custom LEAP robot integrated with an LC-MS system.[41] The protein was first passed over a Nepenthesin II column (2.1 x 30

mm; AffiPro) at 400 µL/min for inline digestion with the protease column held at 20 °C. Peptides were then trapped, eluted, and analyzed as described above. A series of washes over the trap and protease columns was used between injections to minimize carry-over as described previously,[41] except the fourth wash which was replaced with 98% optima water/2% optima ACN (neutral pH). Data-dependent MS/MS acquisition was performed on an undeuterated sample using rapid CID and HCD scans and processed in Byonic (Protein Metrics) with a score cutoff of 200 to identify peptides. Deuterium incorporation was analyzed using HDExaminer v3 (Trajan Scientific). Peptide spectra were exported from HDExaminer and analyzed with HXExpress v3 for multimodal character.[33] Multiple binomials were fit to spectra based on the F-test p-value calculated in HXExpress v3. Multimodal spectra were plotted according to the solutions provided by HXExpress v3, regardless of the confidence associated with the subpopulation deconvolution. Only well-resolved or redundant spectra were used to assign population fractions.

3.5.7 nsEM

Tau4RD was prepared, aggregated, and pelleted as for limited proteolysis. Fibril pellets were isolated by removing 190 uL of supernatant from each tube. Fibrils were resuspended by gently pipetting the remaining 10 µL of buffer until the pellet was dispersed. Negative stain grids were made by applying 3.5 µl of dispersed fibrils to carbon film 400 mesh copper grids (Electron Microscopy Sciences) for one minute, blotting to dryness, washing with distilled water, blotting to dryness, staining using a 2% methylammonium tungstate solution (NanoW™; Nanoprobes) for one minute, and then blotting to dryness. nsEM was performed on a 120 kV Tecnai T12 TEM (FEI). Micrographs were collected at 67,000x magnification with a 1.60 Å/pixel size using the software Leginon[42] with defocus set to -2.0 µm and a total electron dose of 35.04 e−/Å.

3.6 Figures

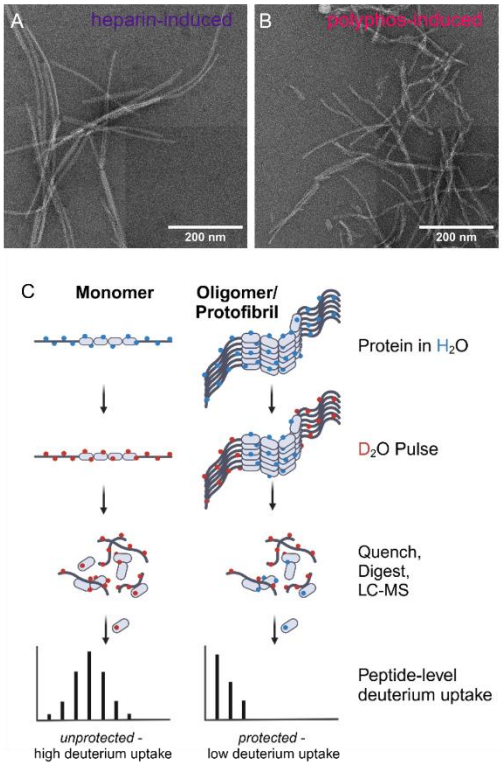

Figure 3.1: Heparin- and polyphosphate-induced tau4RD aggregation result in different fibril morphologies. A/B) nsEM of representative heparin- and polyphosphate-induced tau4RD fibrils highlighting differences in branching and helicity. Scale bar = 200 nm. C) Cartoon of pulsed HDX experiment showing how differences in protection arise during aggregation.

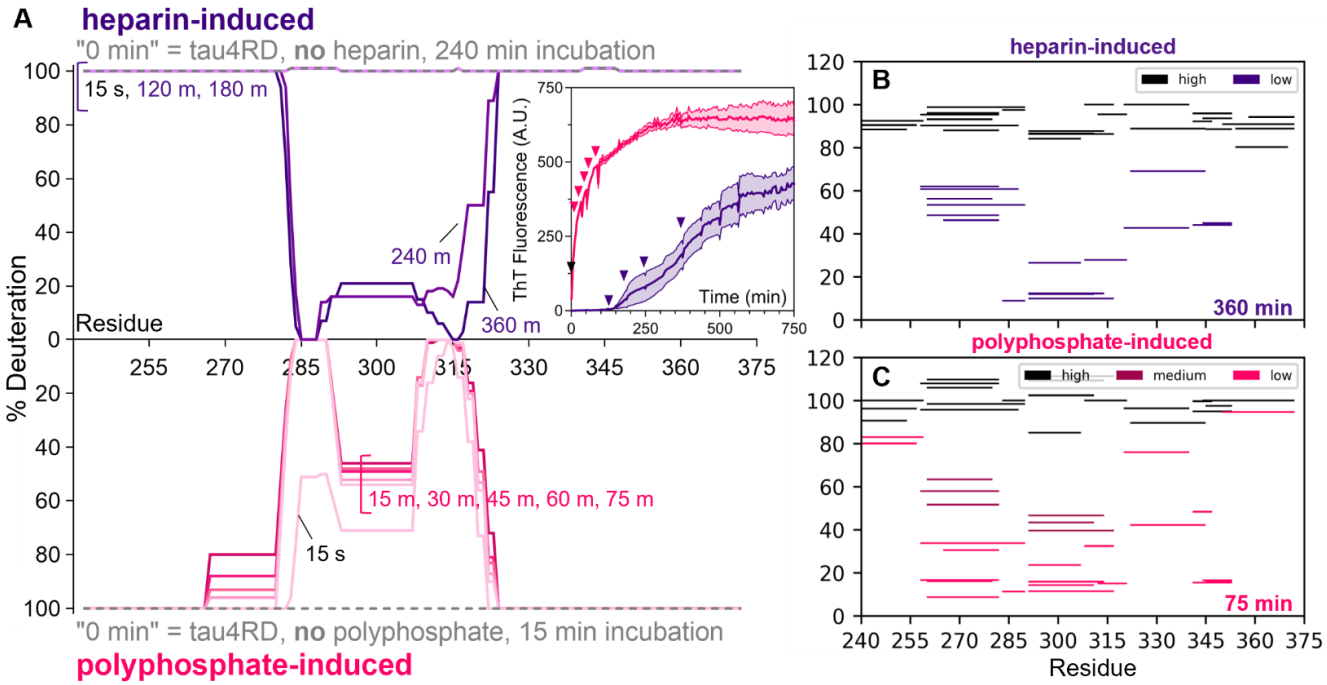

Figure 3.2: Pulsed HDX-MS detects conformational changes in tau4RD caused by amyloid aggregation. A) Deuteration level per residue of tau4RD following a 3-sec 70% D2O pulse at various aggregation durations. Darker colors indicate longer aggregation. Without inducer (grey dotted lines), tau4RD becomes completely deuterated with a 3-sec D2O pulse. Deuteration levels decrease across the fibril core as aggregation time increases in both the heparin- and polyphosphate-induced conditions. This data primarily reflects the protected (aggregated) population and includes small contributions from the unprotected (monomeric) population. Full peptide coverage information and traditional heat maps can be found in SI Figs. 2-3. Inset: ThT fluorescence monitoring of tau4RD (5 μM) aggregated with 5 μM of 3 kDa heparin or 10 μg/mL medium chain polyphosphate. N = 4, mean ± SEM. Pulsed-HDX sampling times are indicated with colored arrows. B) Woods plot showing deconvoluted % deuteration by peptide for the high-exchanging (monomer-like) and low-exchanging (aggregated) heparin-induced populations at t = 360 m. C) Woods plot showing deconvoluted % deuteration by peptide for the high-exchanging (monomer-like), medium-exchanging (aggregated), and low-exchanging (aggregated) populations at t = 75 m.

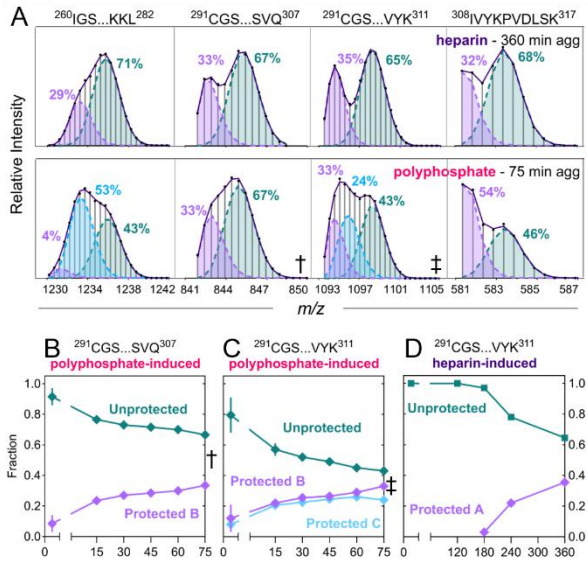

Figure 3.3: Multimodal deconvolution highlights structural and population differences between heparin- and polyphosphate-induced tau4RD fibril populations. A) Pulsed HDX mass envelopes for five peptides observed in heparin- (top) and polyphosphate- (bottom) induced tau4RD fibrils. In the presence of polyphosphate, peptides ^{260}IGS…KKL^{282} and ^{291}CGS…VYK^{311} (double dagger) exhibit trimodal character, indicating the existence of at least two stable protected species, while the same peptides display a single protected population in the presence of heparin. The unprotected population decreases over time with a concurrent increase in the protected population(s) under either condition. The F-test p-value for multiple binomial fits is less than 0.05 for all mass envelopes shown. B) Population distribution throughout polyphosphate-induced aggregation for peptide ^{291}CGS…SVQ^{307} (dagger) which has been fit to two binomials. C) Population distribution for redundant peptide ^{291}CGS…VYK^{311} (double dagger) reveals that a second protected population can be localized to residues near ^{308}IVYK^{311} during polyphosphate-induced aggregation. For polyphosphate-induced aggregation, protected B and protected C maintain stable relative population fractions to each other throughout aggregation, indicating that they are two distinct species. The dagger and double dagger symbols mark the time point shown in A. D) In contrast, peptide ^{291}CGS…VYK^{311} exhibits a single protected population throughout heparin-induced aggregation. N = 2, mean ± range, except for polyphosphate ^{291}CGS…VYK^{311} 75-min (n = 1).

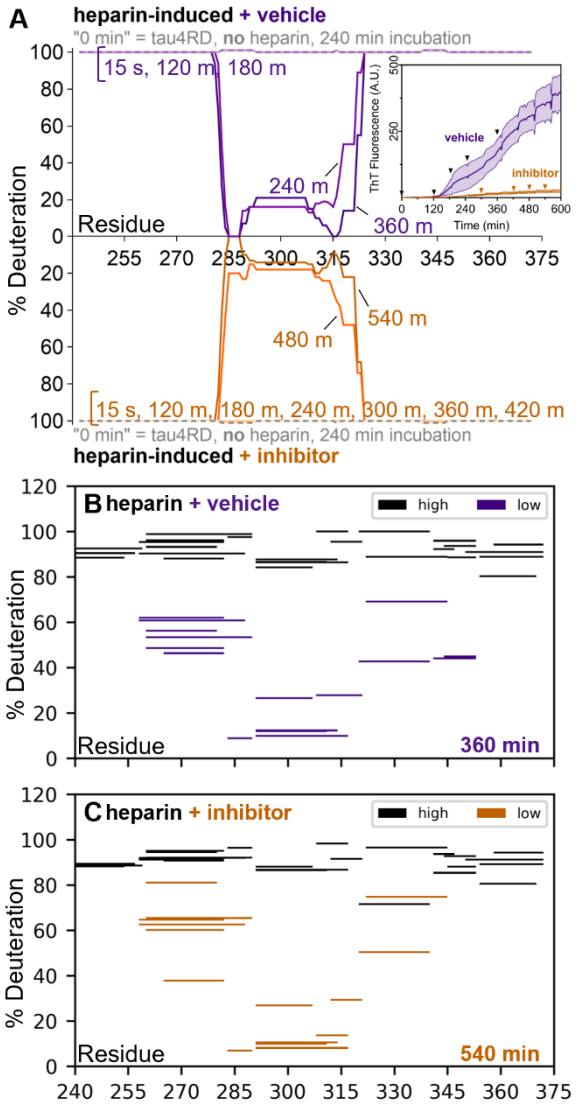

Figure 3.4: Inhibitor TK23 potently reduces heparin-induced aggregation kinetics but does not change resulting amyloid conformation. A) Deuteration level per residue of tau4RD following a 3-sec 70% D2O pulse at various aggregation durations in the absence or presence of inhibitor TK23. Darker colors indicate longer aggregation. Shared HDX sampling times are indicated in the inset ThT traces with black arrows; condition-specific sampling times are indicated with colored arrows. B/C) Woods plots showing deconvoluted deuterium uptake by peptide for the high-exchanging and low-exchanging (aggregated) populations when incubated with vehicle control (B) or inhibitor (C). Despite the marked

decrease in the rate and extent of heparin-induced tau4RD aggregation in the presence of inhibitor TK23 (inset, steepness of curve and decrease in plateau fluorescence), the region protected from HDX remains largely similar to that observed in the absence of inhibitor, except for peptides bordering the fibril core (e.g., 344-353).

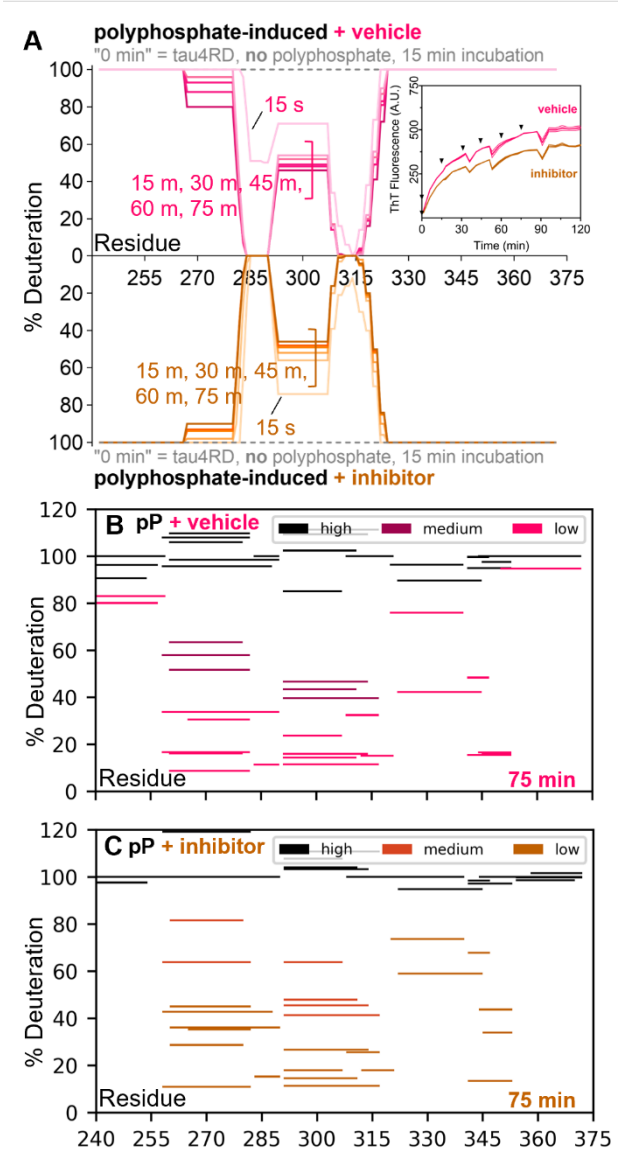

Figure 3.5: Inhibitor TK23 moderately decreases polyphosphate-induced aggregation but does not change resulting amyloid conformations. A) Deuteration level per residue of tau4RD following a 3-sec 70% D2O pulse at various aggregation durations in the absence or presence of inhibitor TK23. Darker colors indicate longer aggregation. Shared HDX sampling times are indicated in the inset ThT traces with black arrows. Inhibitor TK23 mildly decreases the final extent of polyphosphate-induced tau4RD aggregation (inset, decrease in plateau fluorescence), but has little impact on the rate of aggregation. E/F) Woods plots comparing tau4RD deuterium uptake of the high- (monomer-like), medium- (aggregated), and low-exchanging (aggregated) after aggregation with vehicle (E) or inhibitor (F). The region protected from

HDX remains largely unchanged in the presence of TK23, although peptides bordering the fibril core are not detectably multimodal in the presence of inhibitor (e.g., peptide 240-257).

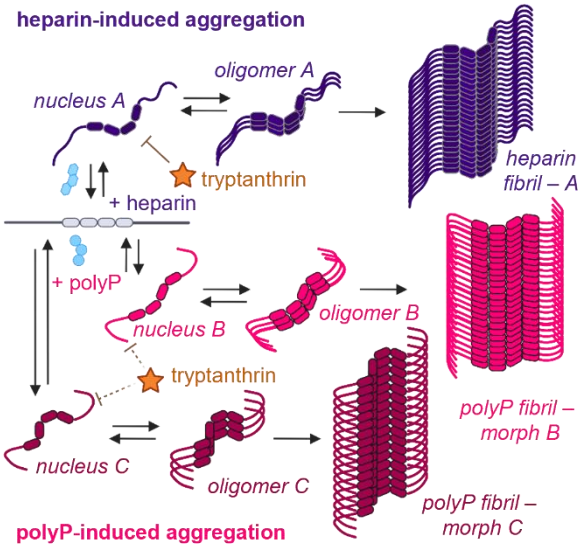

Figure 3.6: Nucleation proposed as the divergence point of both inter- and intra-inducer tau4RD amyloid polymorphism. Detection of multiple protected populations 15 sec after tau4RD aggregation induction with polyphosphate indicates that fibril polymorphism is imprinted extremely early during aggregation. Tryptanthrin, a potent tau4RD nucleation inhibitor, does not alter the resulting fibril core in heparin- or polyphosphate-induced aggregation. Polymorphic aggregation with stable population fractions is observed when tryptanthrin is incubated with polyphosphate and tau4RD.

3.7 Supplementary Material

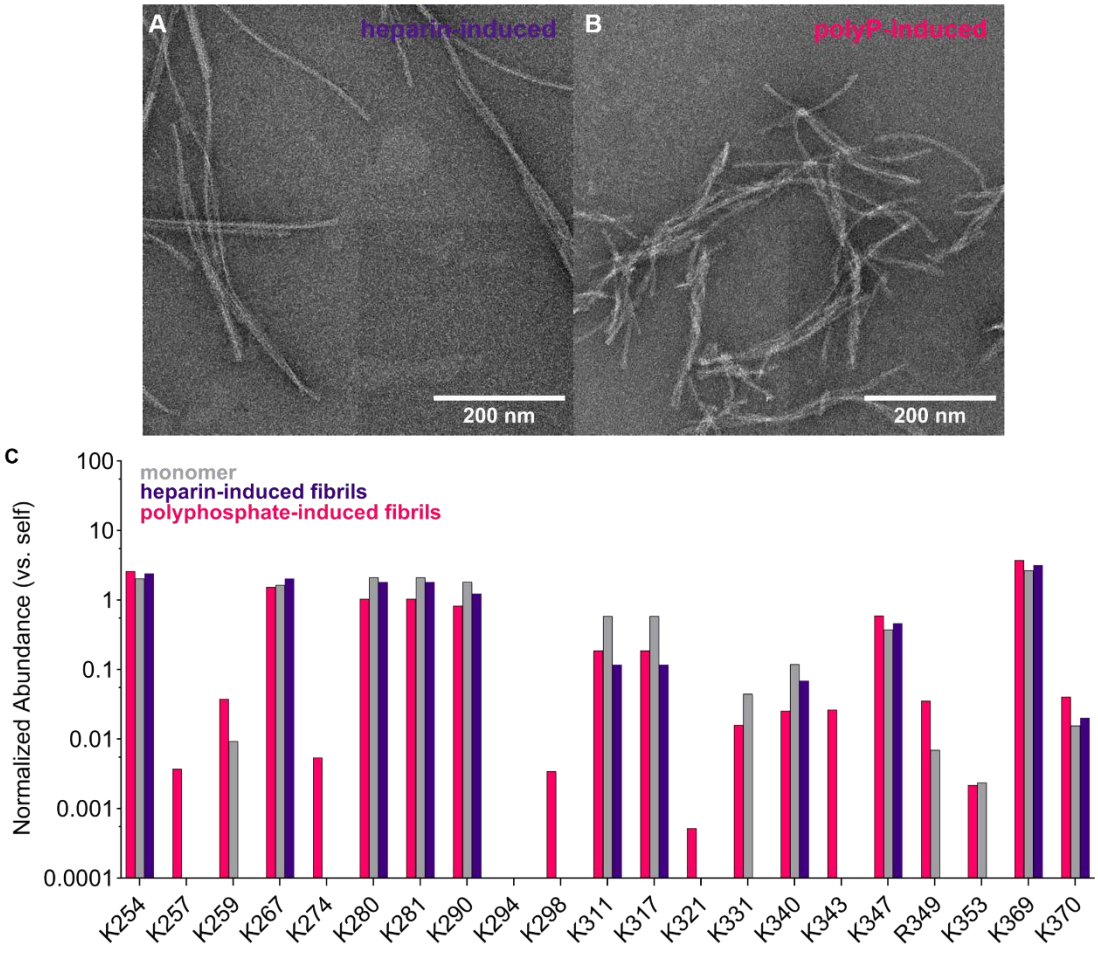

SI Fig. 3.1: Heparin- and polyphosphate-induced tau4RD fibrils have different morphologies. A/B) Additional representative nsEM of heparin- and polyphosphate-induced tau4RD fibrils. Scale bar = 200 nm. Median filter; 4 px/6.4Å. C) Trypsin limited proteolysis of tau4RD monomer and heparin- or polyphosphate-induced fibrils reveals different cleavage fingerprints, providing further confirmation that heparin- and polyphosphate-generated fibrils are conformationally distinct.

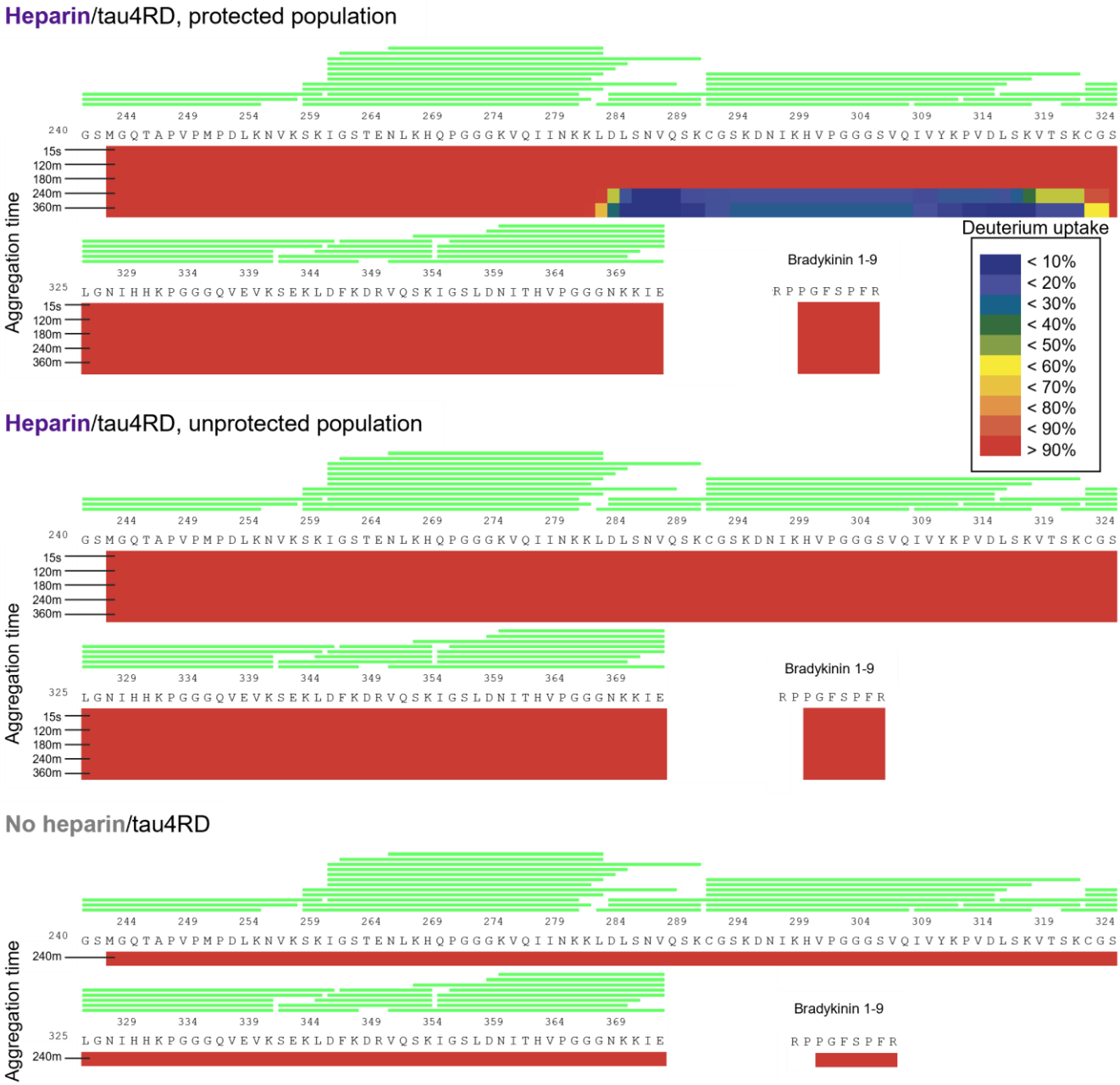

SI Fig. 3.2: Deuterium uptake heatmap for heparin-induced tau4RD throughout aggregation. Deuteration level per residue of tau4RD following a 3-sec 70% D2O pulse at various aggregation durations. This is a traditional visualization of the data displayed in Fig. 3.2A. Without inducer (no heparin condition), tau4RD monomer becomes completely deuterated with a 3-sec pulse. As aggregation proceeds, protection develops between residues 283-324. Note that the contribution of the protected and unprotected populations could not be completely deconvoluted in this analysis software (HD Examiner), so further fitting was performed on a subset of peptides with HXExpress v3.

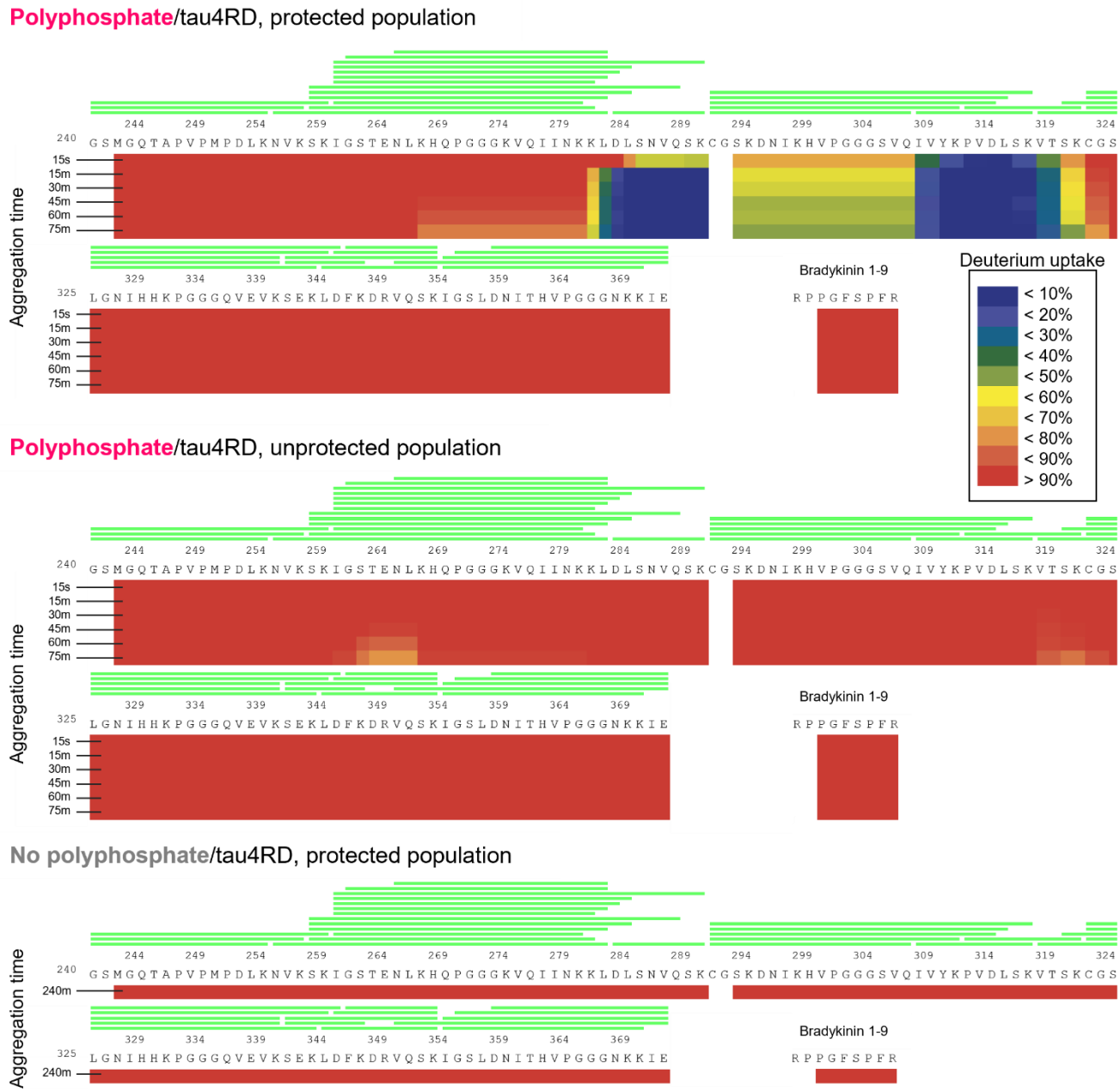

SI Fig. 3.3: Deuterium uptake heatmap for polyphosphate-induced tau4RD throughout aggregation. Deuteration level per residue of tau4RD following a 3-sec 70% D2O pulse at various aggregation durations. This is a traditional visualization of the data displayed in Fig. 3.2A. Without inducer (no polyphosphate condition), tau4RD monomer becomes completely deuterated with a 3-sec pulse. As aggregation proceeds, protection develops between residues 267-324. Note that the contribution of the protected and unprotected populations could not be completely deconvoluted in this analysis software (HD Examiner), so further fitting was performed on a subset of peptides with HXExpress v3.

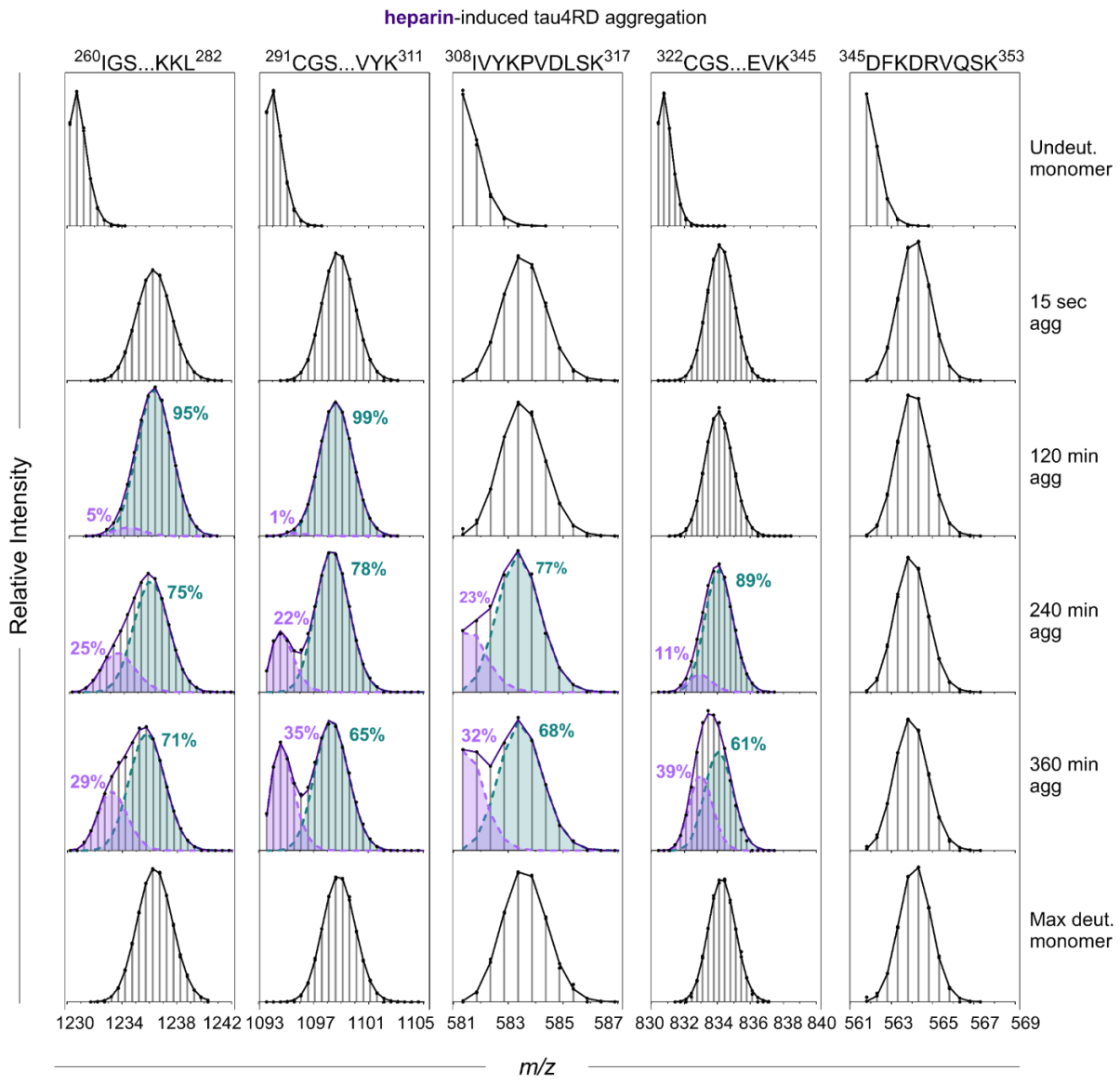

SI Fig. 3.4: Multimodal deconvolution of tau4RD/heparin pulsed HDX data reveals moderate sequence protection and a single protected population. Data for five pulsed HDX peptides common to heparin- and polyphosphate-induced tau4RD fibrils are displayed. Protected populations are detected as early as 120 min after aggregation initiation in two of the five peptides. Peptides I308-K317 and C322-D345 and D345-K353 do not develop protection until after 240 min of aggregation. Unlike in the polyphosphate-induced condition, peptide 345-353 never exhibits bimodal character when aggregated with heparin. F-test p-value is less than 0.05 for all mass envelopes fit with multiple binomials.

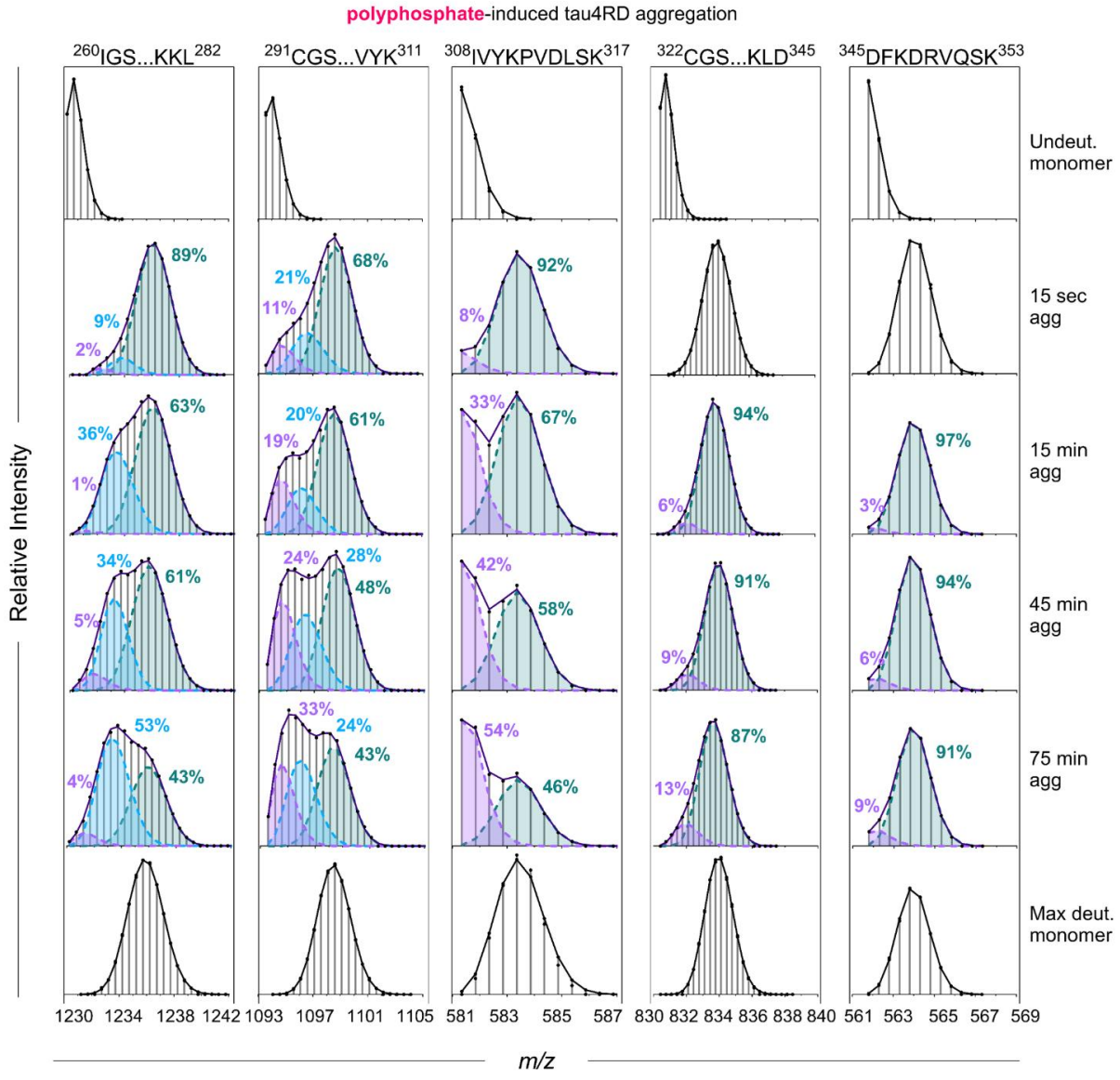

SI Fig. 3.5: Multimodal deconvolution of tau4RD/polyphosphate pulsed HDX data reveals extensive sequence protection and multiple protected populations. Data for five pulsed HDX peptides common to heparin- and polyphosphate-induced tau4RD fibrils are displayed. Protected populations are detected as early as 15 s after aggregation initiation in three of the five peptides. Peptides C322-D345 and D345-K353 do not develop protection until after 15 sec of aggregation and exhibit a lower protected population fraction than the other three peptides. Protection is observed in all five peptides. Peptides I260-L282 and C291-K311 exhibits trimodal character throughout aggregation, indicating the presence of at least two different fibril polymorphs. The protected population fraction of each peptide increases as aggregation proceeds. F-test p-value is less than 0.05 for all mass envelopes fit with multiple binomials.

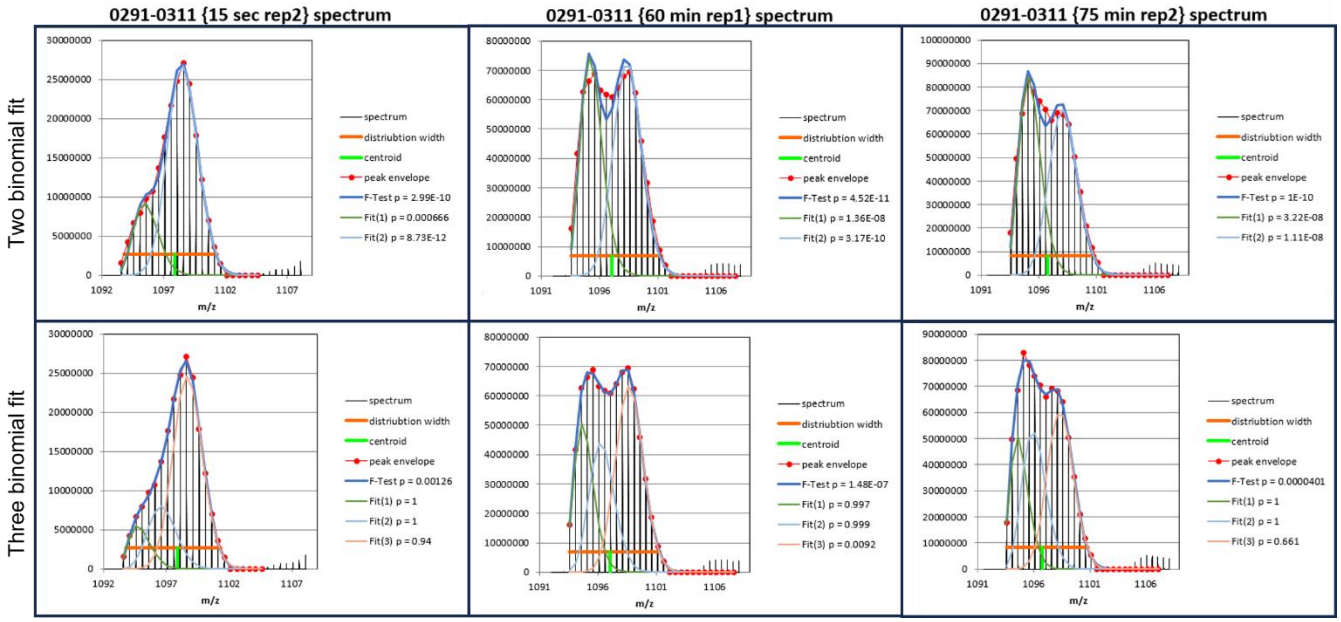

SI Fig. 3.6: Justification of multimodal (three binomial) fits for polyphosphate-induced tau4RD peptide ^{291}CGS…VYK^{311}. Mass spectra of peptide ^{291}CGS…VYK^{311} at t = 15 sec, 60 min, 75 min after aggregation initiation. Mass envelopes have been fit to two binomials in the top row and three binomials in the bottom row. While the subpopulations cannot be accurately deconvoluted with a three-binomial fit, a two-binomial fit does not sufficiently describe the data (e.g., mass envelope not accounted for in the two-binomial fit of 60 min rep1). Note that the F-test p-value remains statistically significant after three binomial fits, even with the substantial penalty applied for adding an additional degree of freedom. Fitting and plots from HXExpress v3.

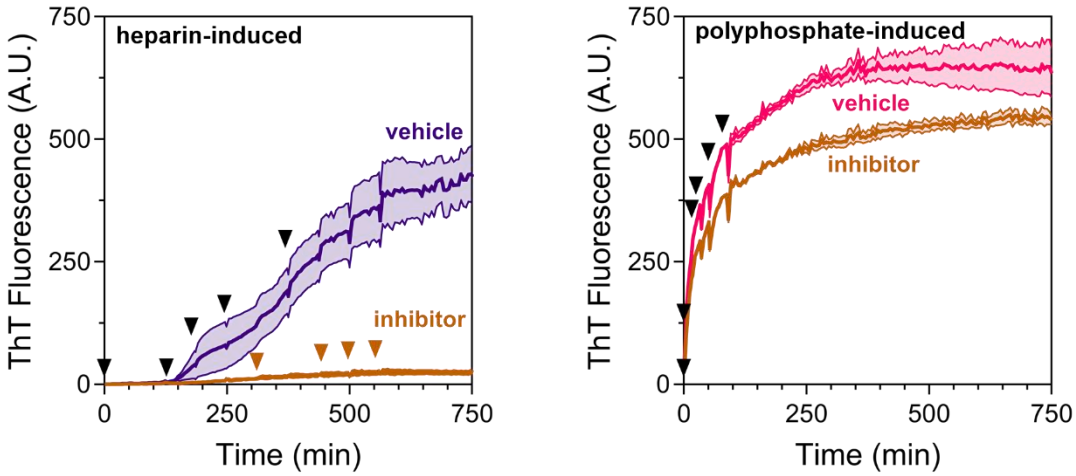

SI Fig. 3.7: Tryptanthrin inhibits heparin- and polyphosphate-induced tau4RD aggregation. ThT traces for heparin- (left) and polyphosphate-induced (right) tau4RD aggregation in the presence of inhibitor (1:2) or vehicle control. Aggregation inhibitor increases the lag time and strongly decreases the plateau height of heparin-induced tau4RD aggregation. Addition of inhibitor to polyphosphate-induced tau4RD aggregation results in no change to the lag time but results in a moderate decrease of the plateau height.

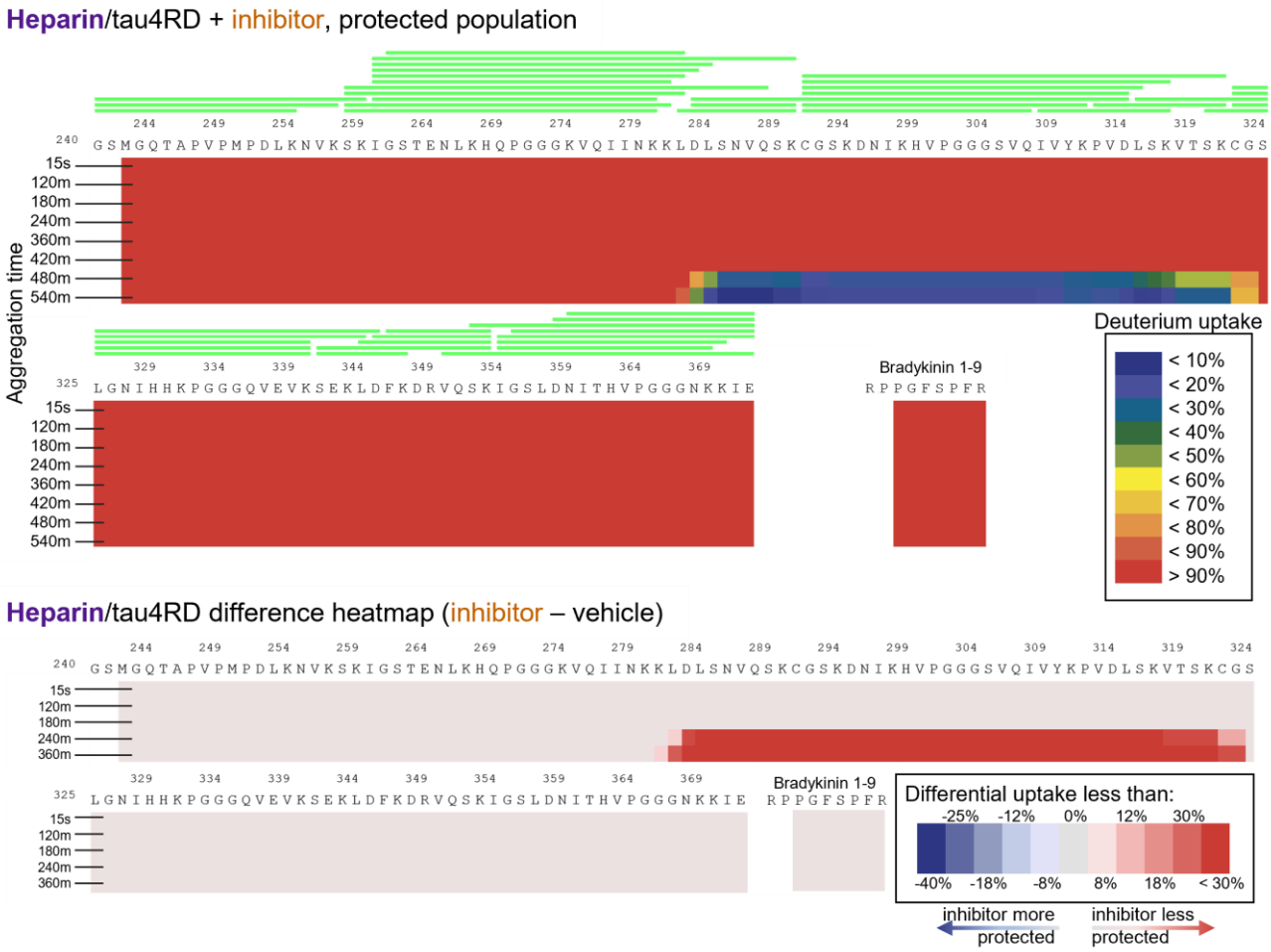

SI Fig. 3.8: Deuterium uptake heatmap for heparin-induced tau4RD incubated with tryptanthrin (inhibitor). Top) Deuteration level per residue of tau4RD following a 3-sec 70% D2O pulse at various aggregation durations. This is a traditional visualization of the data displayed in Fig. 3.4A. As aggregation proceeds, protection develops between residues 267-324. Note that the contribution of the protected and unprotected populations could not be completely deconvoluted in this analysis software (HD Examiner), so further fitting was performed on a subset of peptides with HXExpress v3. Bimodal populations were detected at 15-sec (thought to be caused by inhibitor binding) after HXExpress deconvolution. See SI Figs. 12 and 14. Bottom) Difference heatmap showing that the inhibited condition is less protected (less aggregated) at 240 m and 360 m.

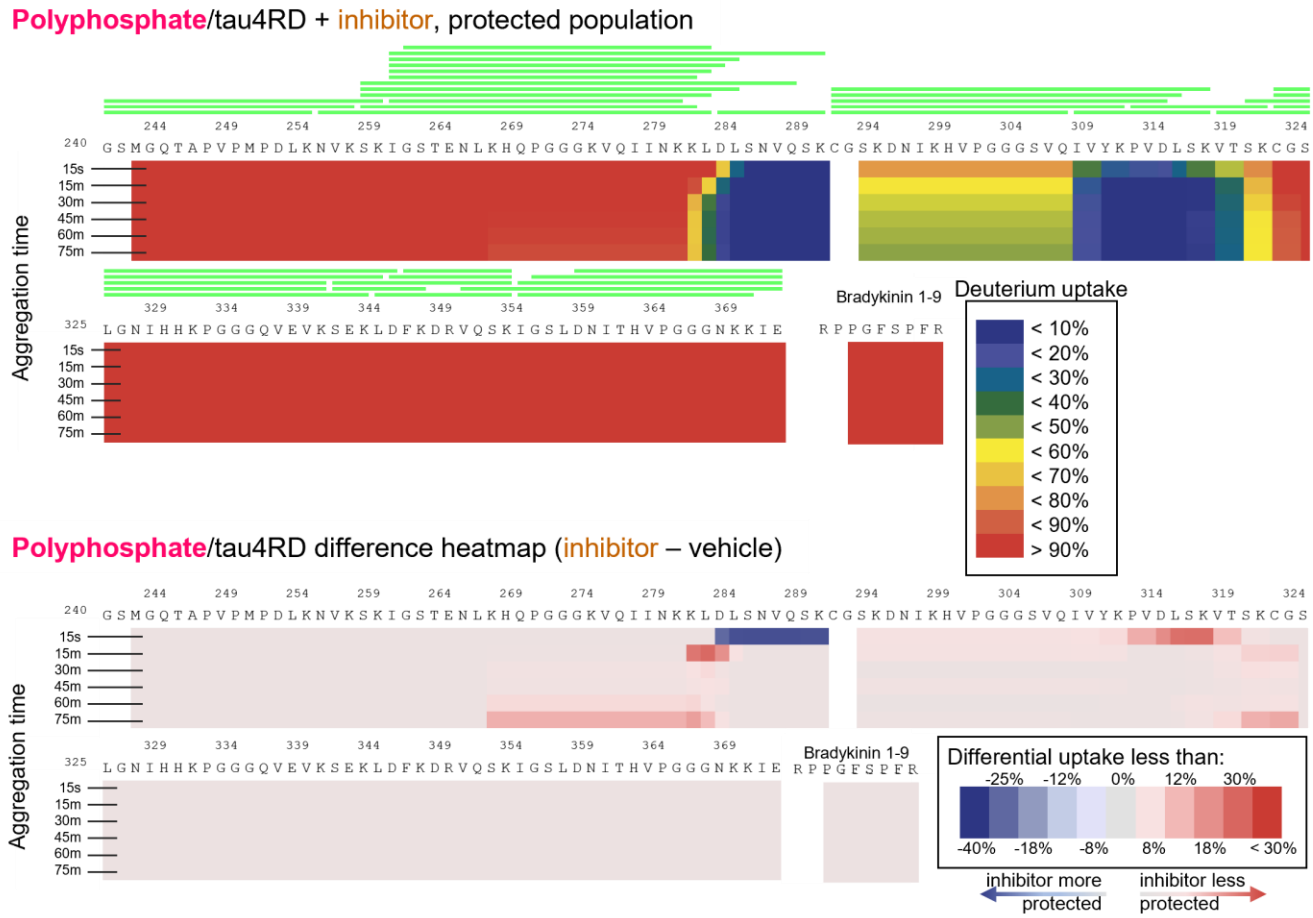

SI Fig. 3.9: Deuterium uptake heatmap for polyphosphate-induced tau4RD incubated with inhibitor. Top) Deuteration level per residue of tau4RD following a 3-sec 70% D2O pulse at various aggregation durations. This is a traditional visualization of the data displayed in Fig. 3.5A. As aggregation proceeds, protection develops between residues 267-324. Note that the contribution of the protected and unprotected populations could not be completely deconvoluted in this analysis software (HD Examiner), so further fitting was performed on a subset of peptides with HXExpress v3. Bottom) Difference heat map showing that tau4RD incubated with inhibitor is generally slightly less protected (less aggregated) than the vehicle control. Note the exception between residues 284-290, which exhibit substantial protection in the presence of inhibitor at the 15-sec time point. We attribute this protection to inhibitor binding.

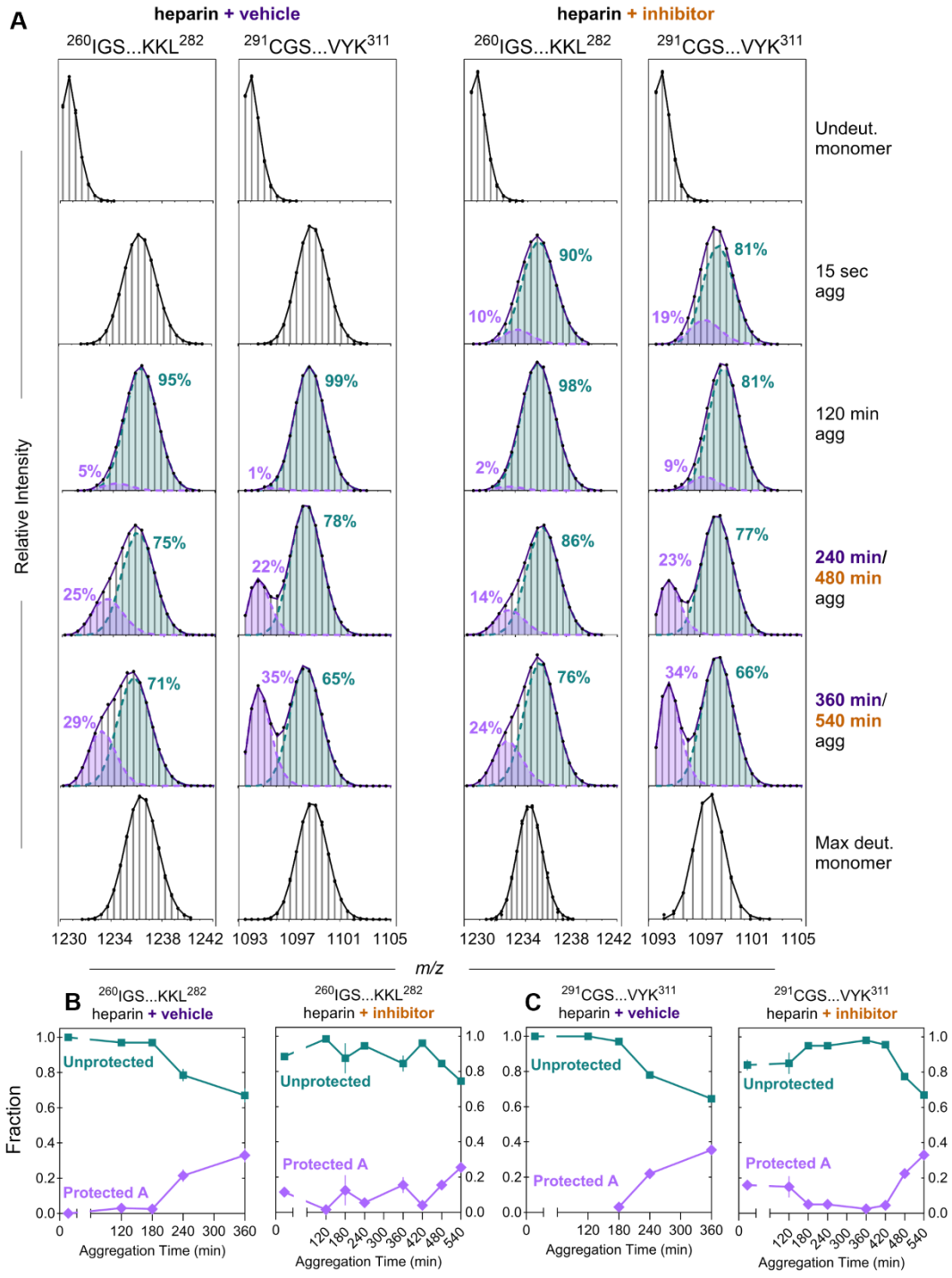

SI Fig. 3.10: Addition of inhibitor does not change the multimodal behavior observed during heparin-induced tau4RD aggregation. A) Data for two peptides in the absence (vehicle) or presence of tryptanthrin (inhibitor). Although the addition of tryptanthrin substantially delays and reduces heparin-induced tau4RD aggregation, it does not result in changes to the fibril core. F-test p-value is less than 0.05 for all mass

envelopes fit with multiple binomials. B/C) Population fraction for the aggregated (protected) and monomer-like (unprotected) populations for peptides I260-L282 and C291-K311.

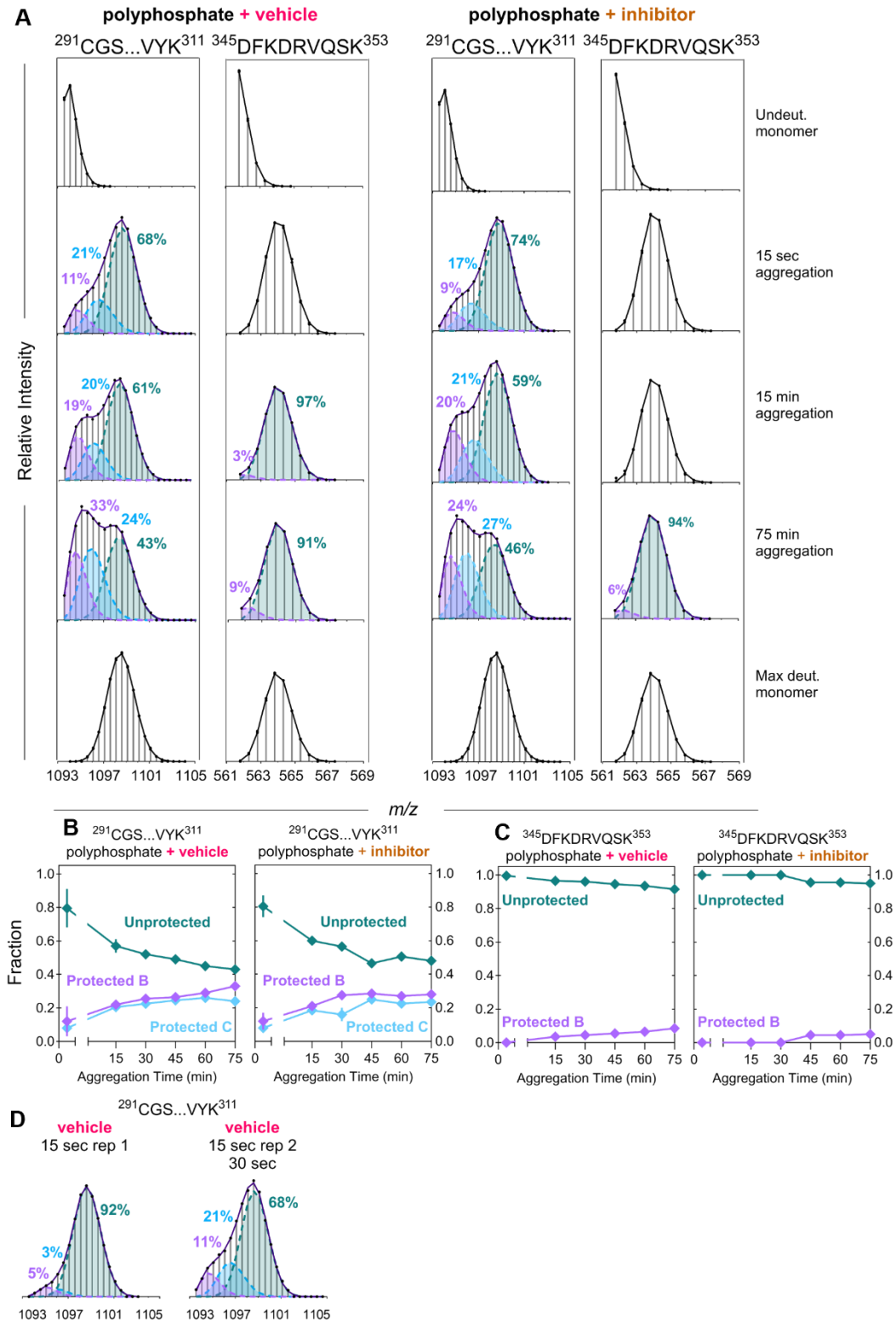
A
polyphosphate + vehicle
polyphosphate + inhibitor
291CGS...VYK311
345DFKDRVQSK353
Undeut. monomer
15 sec aggregation
15 min aggregation
75 min aggregation
Max deut. monomer
Relative Intensity
21%
68%
11%
17%
74%
9%
20%
61%
19%
21%
59%
20%
97%
3%
33%
24%
43%
24%
27%
46%
91%
9%
94%
6%
1093 1097 1101 1105 561 563 565 567 569
m/z
B
291CGS...VYK311
polyphosphate + vehicle
polyphosphate + inhibitor
Unprotected
Protected B
Protected C
Fraction
Aggregation Time (min)
C
345DFKDRVQSK353
D
vehicle
15 sec rep 1
vehicle
15 sec rep 2
30 sec
92%
3%
5%
21%
68%
11%

SI Fig. 3.11: Addition of inhibitor does not change the multimodal behavior observed during polyphosphate-induced tau4RD aggregation. A) Data for two peptides in the absence (vehicle) or presence of tryptanthrin (inhibitor). Although the addition of tryptanthrin mildly reduces polyphosphate-induced tau4RD aggregation, it does not result in changes to the fibril core. F-test p-value is less than 0.05 for all mass envelopes fit with multiple binomials. B/C) Population fraction for the aggregated (protected) and monomer-like (unprotected) populations for peptides C291-K311 and D345-K353. D) Duplicate sampling at 15 sec results in substantially different subpopulation profiles due to the speed at which polyphosphate-induced aggregation progresses.

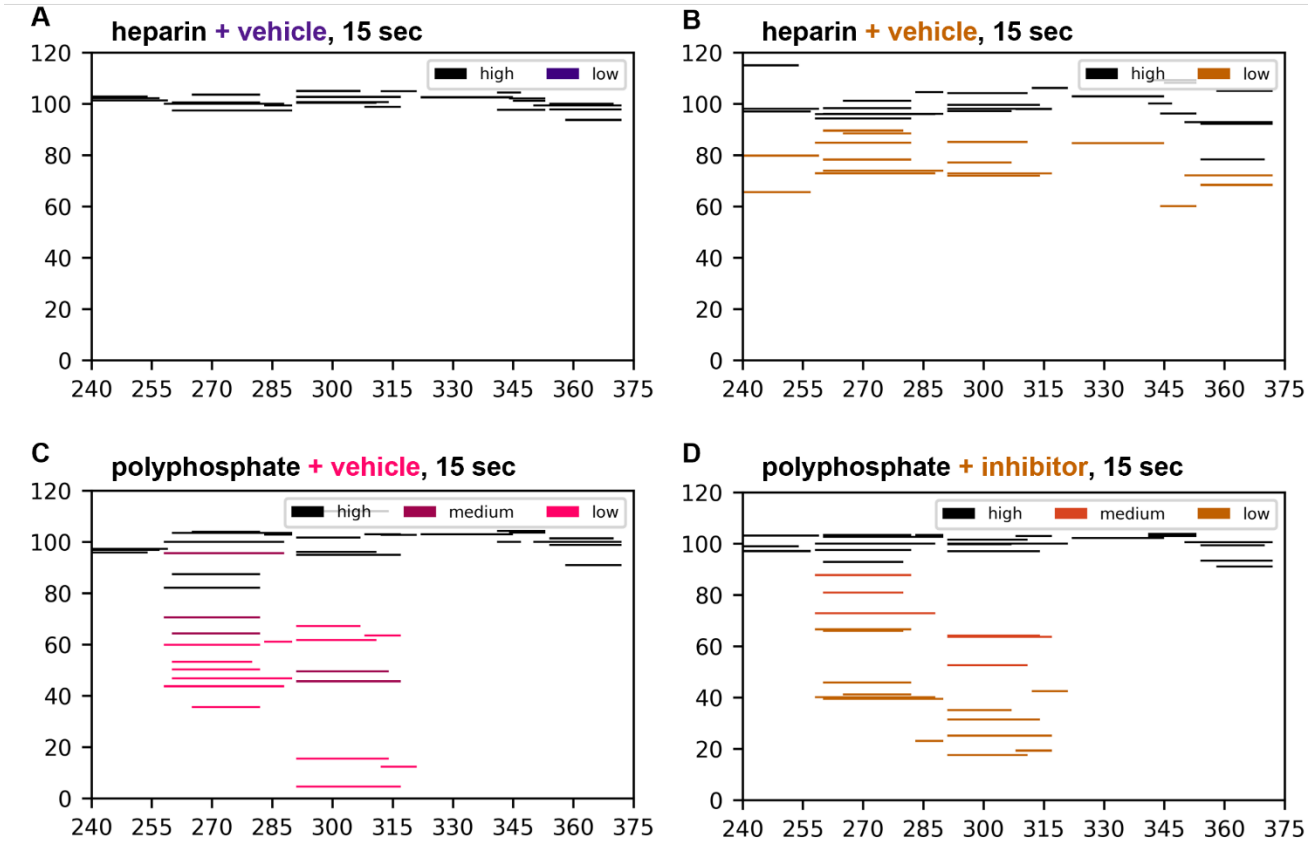

SI Fig. 3.12: HDX Woods plots for heparin- and polyphosphate-induced tau4RD incubated with inhibitor for 15-sec. A) Woods plot revealing only a high-exchanging (monomer-like) population when heparin-induced tau4RD is incubated with vehicle. B) In contrast, a Woods plot of heparin-induced tau4RD incubated with inhibitor shows both a high-exchanging (monomer-like) and low-exchanging (protected) population. The pattern of protection caused by the inhibitor does not match the pattern of protection caused by the heparin fibril core, suggesting that the protection observed at 15-sec is due to structural changes associated with the inhibitor binding tau4RD. C) Woods plot revealing both morph B and morph C are present 15-sec after the beginning of polyphosphate-induced tau4RD aggregation. D) The addition of inhibitor to polyphosphate-induced tau4RD aggregation does not change the pattern of protection.

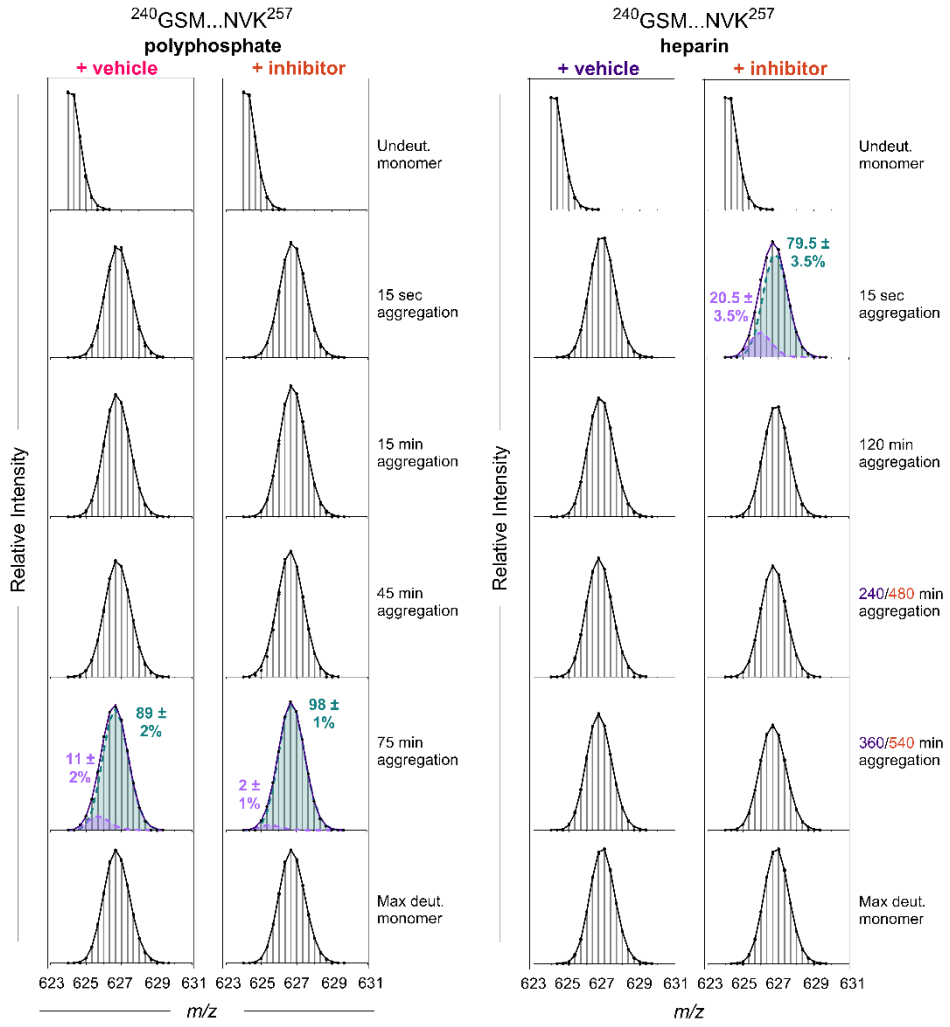

SI Fig. 3.13: Addition of inhibitor does not change the low abundance aggregated subpopulation observed in peptide 240-257 under polyphosphate-initiated aggregation. A) Data for one peptide in the absence (vehicle) or presence of tryptanthrin (inhibitor) when tau4RD aggregation is induced with polyphosphate. Note that the low-abundance population is not detected until 75 min in either case. This likely represents fibril maturation. F-test p-value is less than 0.05 for all mass envelopes fit with multiple binomials. B) Peptide 240-257 when incubated in the absence (vehicle) or presence (inhibitor) of tryptanthrin. Note that there appears to be a low abundance protected population at 15 sec in the presence of inhibitor; this could be due to inhibitor binding and causing rearrangements in the tau4RD backbone. Note that there is no evidence of an aggregated subpopulation at the final time point (360 min for vehicle, 540 min for inhibitor). Subpopulation abundance values are the average (mean) ± difference between duplicate samples.

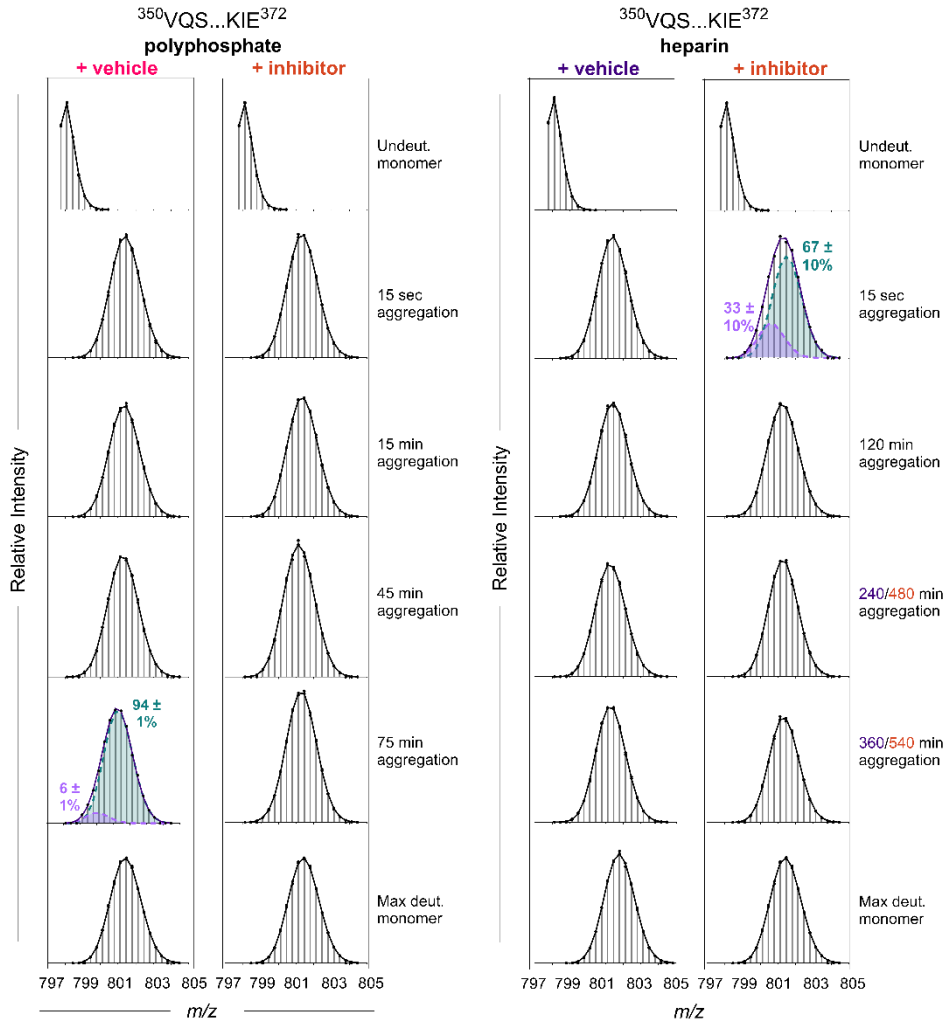

SI Fig. 3.14: Inhibitor reduces the low abundance aggregated subpopulation observed during polyphosphate-induced tau4RD aggregation at peptide 350-372. A) Spectra for peptide 350-372 with vehicle or inhibitor when tau4RD aggregation is induced with polyphosphate. Note that the low-abundance population is not detected until 75 min with vehicle. This likely represents fibril maturation. There is not evidence of an aggregated subpopulation at 75 min when tau4RD is incubated with tryptanthrin. This is likely due to a reduction in overall aggregation and not due to a conformational change caused by tryptanthrin. F-test p-value is less than 0.05 for all mass envelopes fit with multiple binomials. B) Peptide 350-372 incubated with vehicle or inhibitor and aggregation is induced with heparin. Note that there appears to be a low abundance protected population at 15 sec in the presence of inhibitor; this could be due to inhibitor binding and causing rearrangements in the tau4RD backbone. Note that there is no evidence of an aggregated subpopulation at the final time point (360 min for vehicle, 540 min for inhibitor). Subpopulation abundance values are the average (mean) ± difference between duplicate samples.

3.8 References

(1) Zhang, Y.; Wu, K. M.; Yang, L.; Dong, Q.; Yu, J. T. Tauopathies: New Perspectives and Challenges. *Mol. Neurodegener.* **2022**, *17* (1). https://doi.org/10.1186/s13024-022-00533-z.

(2) Limorenko, G.; Lashuel, H. A. Revisiting the Grammar of Tau Aggregation and Pathology Formation: How New Insights from Brain Pathology Are Shaping How We Study and Target Tauopathies. *Chem. Soc. Rev.* **2022**, *51* (2), 513–565. https://doi.org/10.1039/D1CS00127B.

(3) Shi, Y.; Zhang, W.; Yang, Y.; Murzin, A. G.; Falcon, B.; Kotecha, A.; van Beers, M.; Tarutani, A.; Kametani, F.; Garringer, H. J.; Vidal, R.; Hallinan, G. I.; Lashley, T.; Saito, Y.; Murayama, S.; Yoshida, M.; Tanaka, H.; Kakita, A.; Ikeuchi, T.; Robinson, A. C.; Mann, D. M. A.; Kovacs, G. G.; Revesz, T.; Ghetti, B.; Hasegawa, M.; Goedert, M.; Scheres, S. H. W. Structure-Based Classification of Tauopathies. *Nature* **2021**, *598* (7880), 359. https://doi.org/10.1038/S41586-021-03911-7.

(4) Kovacs, G. G.; Ghetti, B.; Goedert, M. Classification of Diseases with Accumulation of Tau Protein. *Neuropathol. Appl. Neurobiol.* **2022**, *48* (3), e12792. https://doi.org/10.1111/NAN.12792.

(5) Wesseling, H.; Mair, W.; Kumar, M.; Schlaffner, C. N.; Tang, S.; Beerepoot, P.; Fatou, B.; Guise, A. J.; Cheng, L.; Takeda, S.; Muntel, J.; Rotunno, M. S.; Dujardin, S.; Davies, P.; Kosik, K. S.; Miller, B. L.; Berretta, S.; Hedreen, J. C.; Grinberg, L. T.; Seeley, W. W.; Hyman, B. T.; Steen, H.; Steen, J. A. Tau PTM Profiles Identify Patient Heterogeneity and Stages of Alzheimer's Disease. *Cell* **2020**, *183* (6), 1699-1713.e13. https://doi.org/10.1016/J.CELL.2020.10.029.

(6) Kyalu Ngoie Zola, N.; Balty, C.; Pyr dit Ruys, S.; Vanparys, A. A. T.; Huyghe, N. D. G.; Herinckx, G.; Johanns, M.; Boyer, E.; Kienlen-Campard, P.; Rider, M. H.; Vertommen, D.; Hanseeuw, B. J. Specific Post-Translational Modifications of Soluble Tau Protein Distinguishes Alzheimer's Disease and Primary Tauopathies. *Nat. Commun. 2023 141* **2023**, *14* (1), 1–17. https://doi.org/10.1038/S41467-023-39328-1.

(7) Mirbaha, H.; Chen, D.; Mullapudi, V.; Terpack, S. J.; White, C. L.; Joachimiak, L. A.; Diamond, M. I. Seed-Competent Tau Monomer Initiates Pathology in a Tauopathy Mouse Model. *J. Biol. Chem.* **2022**, *298* (8), 102163. https://doi.org/10.1016/J.JBC.2022.102163.

(8) Li, L.; Nguyen, B. A.; Mullapudi, V.; Li, Y.; Saelices, L.; Joachimiak, L. A. Disease-Associated Patterns of Acetylation Stabilize Tau Fibril Formation. *Structure* **2023**, *31* (9), 1025-1037.e4. https://doi.org/10.1016/J.STR.2023.05.020.

(9) Wickramasinghe, S. P.; Lempart, J.; Merens, H. E.; Murphy, J.; Huettemann, P.; Jakob, U.; Rhoades, E. Polyphosphate Initiates Tau Aggregation through Intra- and Intermolecular Scaffolding. *Biophys. J.* **2019**, *117* (4), 717–728. https://doi.org/10.1016/J.BPJ.2019.07.028.

(10) Chakraborty, P.; Rivière, G.; Liu, S.; de Opakua, A. I.; Dervişoğlu, R.; Hebestreit, A.; Andreas, L. B.; Vorberg, I. M.; Zweckstetter, M. Co-Factor-Free Aggregation of Tau into Seeding-Competent RNA-Sequestering Amyloid Fibrils. *Nat. Commun.* **2021**, *12* (1). https://doi.org/10.1038/s41467-021-24362-8.

(11) Abskharon, R.; Sawaya, M. R.; Cao, Q.; Nguyen, B. A.; Boyer, D. R.; Cascio, D.; Eisenberg, D. S. Cryo-EM Structure of RNA-Induced Tau Fibrils Reveals a Small C-Terminal Core That May Nucleate Fibril Formation. *Proc. Natl. Acad. Sci. U. S. A.* **2022**, *119* (15), e2119952119. https://doi.org/10.1073/PNAS.2119952119/SUPPL_FILE/PNAS.2119952119.SAPP.PDF.

(12) Von Bergen, M.; Friedhoff, P.; Biernat, J.; Heberle, J.; Mandelkow, E. M.; Mandelkow, E. Assembly of τ Protein into Alzheimer Paired Helical Filaments Depends on a Local Sequence Motif (306VQIVYK311) Forming β Structure. *Proc. Natl. Acad. Sci. U. S. A.* **2000**, *97* (10), 5129–5134. https://doi.org/10.1073/PNAS.97.10.5129/ASSET/7E919641-17A6-4468-A582-4672B009D09E/ASSETS/GRAPHIC/PQ0904029008.JPEG.

(13) Ganguly, P.; Do, T. D.; Larini, L.; Lapointe, N. E.; Sercel, A. J.; Shade, M. F.; Feinstein, S. C.; Bowers, M. T.; Shea, J. E. Tau Assembly: The Dominant Role of PHF6 (VQIVYK) in Microtubule Binding Region Repeat R3. *J. Phys. Chem. B* **2015**, *119* (13), 4582–4593. https://doi.org/10.1021/ACS.JPCB.5B00175/SUPPL_FILE/JP5B00175_SI_001.PDF.

(14) Smit, F. X.; Luiken, J. A.; Bolhuis, P. G. Primary Fibril Nucleation of Aggregation Prone Tau Fragments PHF6 and PHF6. *J. Phys. Chem. B* **2017**, *121* (15), 3250–3261. https://doi.org/10.1021/ACS.JPCB.6B07045/ASSET/IMAGES/LARGE/JP-2016-070454_0013.JPEG.
(15) Despres, C.; Di, J.; Cantrelle, F. X.; Li, Z.; Huvent, I.; Chambraud, B.; Zhao, J.; Chen, J.; Chen, S.; Lippens, G.; Zhang, F.; Linhardt, R.; Wang, C.; Klärner, F. G.; Schrader, T.; Landrieu, I.; Bitan, G.; Smet-Nocca, C. Major Differences between the Self-Assembly and Seeding Behavior of Heparin-Induced and in Vitro Phosphorylated Tau and Their Modulation by Potential Inhibitors. *ACS Chem. Biol.* **2019**, *14* (6), 1363–1379. https://doi.org/10.1021/ACSCHEMBIO.9B00325/SUPPL_FILE/CB9B00325_SI_001.PDF.
(16) Zhang, W.; Falcon, B.; Murzin, A. G.; Fan, J.; Crowther, R. A.; Goedert, M.; Scheres, S. H. W. Heparin-Induced Tau Filaments Are Polymorphic and Differ from Those in Alzheimer's and Pick's Diseases. *eLife* **2019**, *8*. https://doi.org/10.7554/ELIFE.43584.
(17) Axell, E.; Hu, J.; Lindberg, M.; Dear, A. J.; Ortigosa-Pascual, L.; Andrzejewska, E. A.; Šneideriene, G.; Thacker, D.; Knowles, T. P. J.; Sparr, E.; Linse, S. The Role of Shear Forces in Primary and Secondary Nucleation of Amyloid Fibrils. *Proc. Natl. Acad. Sci. U. S. A.* **2024**, *121* (25), e2322572121. https://doi.org/10.1073/PNAS.2322572121/SUPPL_FILE/PNAS.2322572121.SAPP.PDF.
(18) Montgomery, K. M.; Carroll, E. C.; Thwin, A. C.; Quddus, A. Y.; Hodges, P.; Southworth, D. R.; Gestwicki, J. E. Chemical Features of Polyanions Modulate Tau Aggregation and Conformational States. *J. Am. Chem. Soc.* **2023**, *145* (7), 3926–3936. https://doi.org/10.1021/jacs.2c08004.
(19) Emin, D.; Zhang, Y. P.; Lobanova, E.; Miller, A.; Li, X.; Xia, Z.; Dakin, H.; Sideris, D. I.; Lam, J. Y. L.; Ranasinghe, R. T.; Kouli, A.; Zhao, Y.; De, S.; Knowles, T. P. J.; Vendruscolo, M.; Ruggeri, F. S.; Aigbirhio, F. I.; Williams-Gray, C. H.; Klenerman, D. Small Soluble α-Synuclein Aggregates Are the Toxic Species in Parkinson's Disease. *Nat. Commun. 2022 131* **2022**, *13* (1), 1–15. https://doi.org/10.1038/S41467-022-33252-6.
(20) Ward, S. M.; Himmelstein, D. S.; Lancia, J. K.; Binder, L. I. Tau Oligomers and Tau Toxicity in Neurodegenerative Disease. *Biochem. Soc. Trans.* **2012**, *40* (4), 667. https://doi.org/10.1042/BST20120134.
(21) Ondrejcak, T.; Hu, N. W.; Qi, Y.; Klyubin, I.; Corbett, G. T.; Fraser, G.; Perkinton, M. S.; Walsh, D. M.; Billinton, A.; Rowan, M. J. Soluble Tau Aggregates Inhibit Synaptic Long-Term Depression and Amyloid β-Facilitated LTD in Vivo. *Neurobiol. Dis.* **2019**, *127*, 582–590. https://doi.org/10.1016/j.nbd.2019.03.022.
(22) Lee, M. C.; Yu, W. C.; Shih, Y. H.; Chen, C. Y.; Guo, Z. H.; Huang, S. J.; Chan, J. C. C.; Chen, Y. R. Zinc Ion Rapidly Induces Toxic, off-Pathway Amyloid-β Oligomers Distinct from Amyloid-β Derived Diffusible Ligands in Alzheimer's Disease. *Sci. Rep. 2018 81* **2018**, *8* (1), 1–16. https://doi.org/10.1038/S41598-018-23122-X.
(23) Lo Cascio, F.; Puangmalai, N.; Ellsworth, A.; Bucchieri, F.; Pace, A.; Palumbo Piccionello, A.; Kayed, R. Toxic Tau Oligomers Modulated by Novel Curcumin Derivatives. *Sci. Rep. 2019 91* **2019**, *9* (1), 1–16. https://doi.org/10.1038/S41598-019-55419-W.
(24) Almeida, Z. L.; Brito, R. M. M. Structure and Aggregation Mechanisms in Amyloids. *Molecules* **2020**, *25* (5), 1195. https://doi.org/10.3390/MOLECULES25051195.
(25) Fitzpatrick, A. W. P.; Falcon, B.; He, S.; Murzin, A. G.; Murshudov, G.; Garringer, H. J.; Crowther, R. A.; Ghetti, B.; Goedert, M.; Scheres, S. H. W. Cryo-EM Structures of Tau Filaments from Alzheimer's Disease. *Nature* **2017**, *547* (7662), 185–190. https://doi.org/10.1038/NATURE23002.
(26) Falcon, B.; Zhang, W.; Murzin, A. G.; Murshudov, G.; Garringer, H. J.; Vidal, R.; Crowther, R. A.; Ghetti, B.; Scheres, S. H. W.; Goedert, M. Structures of Filaments from Pick's Disease Reveal a Novel Tau Protein Fold. *Nature* **2018**, *561* (7721), 137–140. https://doi.org/10.1038/S41586-018-0454-Y.

(27) Lövestam, S.; Koh, F. A.; van Knippenberg, B.; Kotecha, A.; Murzin, A. G.; Goedert, M.; Scheres, S. H. W. Assembly of Recombinant Tau into Filaments Identical to Those of Alzheimer's Disease and Chronic Traumatic Encephalopathy. *eLife* **2022**, *11*. https://doi.org/10.7554/eLife.76494.
(28) Lövestam, S.; Li, D.; Wagstaff, J. L.; Kotecha, A.; Kimanius, D.; McLaughlin, S. H.; Murzin, A. G.; Freund, S. M. V.; Goedert, M.; Scheres, S. H. W. Disease-Specific Tau Filaments Assemble via Polymorphic Intermediates. *Nat. 2023 6257993* **2023**, *625* (7993), 119–125. https://doi.org/10.1038/S41586-023-06788-W.
(29) James, E. I.; Murphree, T. A.; Vorauer, C.; Engen, J. R.; Guttman, M. Advances in Hydrogen/Deuterium Exchange Mass Spectrometry and the Pursuit of Challenging Biological Systems. *Chem. Rev.* **2022**, *122* (8), 7562–7623. https://doi.org/10.1021/ACS.CHEMREV.1C00279.
(30) Kumar, H.; Udgaonkar, J. B. Mechanistic and Structural Origins of the Asymmetric Barrier to Prion-like Cross-Seeding between Tau-3R and Tau-4R. *J. Mol. Biol.* **2018**, *430* (24), 5304–5312. https://doi.org/10.1016/J.JMB.2018.09.010.
(31) Illes-Toth, E.; Rempel, D. L.; Gross, M. L. Pulsed Hydrogen-Deuterium Exchange Illuminates the Aggregation Kinetics of α-Synuclein, the Causative Agent for Parkinson's Disease. *ACS Chem. Neurosci.* **2018**, *9* (6), 1469–1476. https://doi.org/10.1021/ACSCHEMNEURO.8B00052/ASSET/IMAGES/MEDIUM/CN-2018-00052K_M006.GIF.
(32) Illes-Toth, E.; Meisl, G.; Rempel, D. L.; Knowles, T. P. J.; Gross, M. L. Pulsed Hydrogen-Deuterium Exchange Reveals Altered Structures and Mechanisms in the Aggregation of Familial Alzheimer's Disease Mutants. *ACS Chem. Neurosci.* **2021**, *12* (11), 1972–1982. https://doi.org/10.1021/ACSCHEMNEURO.1C00072/ASSET/IMAGES/LARGE/CN1C00072_0005.JPEG.
(33) Tuttle, L. M.; James, E. I.; Georgescauld, F.; Wales, T. E.; Weis, D. D.; Engen, J. R.; Nath, A.; Klevit, R. E.; Guttman, M. Rigorous Analysis of Multimodal HDX-MS Spectra. *J. Am. Soc. Mass Spectrom.* **2025**. https://doi.org/10.1021/JASMS.4C00471/ASSET/IMAGES/LARGE/JS4C00471_0005.JPEG.
(34) James, E. I.; Baggett, D. W.; Chang, E.; Schachter, J.; Nixey, T.; Choi, K.; Guttman, M.; Nath, A. Tryptanthrin Analogs Substoichiometrically Inhibit Seeded and Unseeded Tau4RD Aggregation. *eLife* **2024**, *13*. https://doi.org/10.7554/ELIFE.98227.1.
(35) Tanaka, G.; Yamanaka, T.; Furukawa, Y.; Kajimura, N.; Mitsuoka, K.; Nukina, N. Sequence- and Seed-Structure-Dependent Polymorphic Fibrils of Alpha-Synuclein. *Biochim. Biophys. Acta BBA - Mol. Basis Dis.* **2019**, *1865* (6), 1410–1420. https://doi.org/10.1016/J.BBADIS.2019.02.013.
(36) Yoo, J. M.; Lin, Y.; Heo, Y.; Lee, Y. H. Polymorphism in Alpha-Synuclein Oligomers and Its Implications in Toxicity under Disease Conditions. *Front. Mol. Biosci.* **2022**, *9*, 959425. https://doi.org/10.3389/FMOLB.2022.959425/BIBTEX.
(37) Meisl, G.; Rajah, L.; Cohen, S. A. I.; Pfammatter, M.; Šarić, A.; Hellstrand, E.; Buell, A. K.; Aguzzi, A.; Linse, S.; Vendruscolo, M.; Dobson, C. M.; Knowles, T. P. J. Scaling Behaviour and Rate-Determining Steps in Filamentous Self-Assembly. *Chem. Sci.* **2017**, *8* (10), 7087–7097. https://doi.org/10.1039/c7sc01965c.
(38) Knowles, T. P. J.; Waudby, C. A.; Devlin, G. L.; Cohen, S. I. A.; Aguzzi, A.; Vendruscolo, M.; Terentjev, E. M.; Welland, M. E.; Dobson, C. M. An Analytical Solution to the Kinetics of Breakable Filament Assembly. *Science* **2009**, *326* (5959), 1533–1537. https://doi.org/10.1126/SCIENCE.1178250.
(39) Cohen, S. I. A.; Vendruscolo, M.; Dobson, C. M.; Knowles, T. P. J. From Macroscopic Measurements to Microscopic Mechanisms of Protein Aggregation. *J. Mol. Biol.* **2012**, *421* (2–3), 160–171. https://doi.org/10.1016/j.jmb.2012.02.031.
(40) Benhaim, M. A.; Mangala Prasad, V.; Garcia, N. K.; Guttman, M.; Lee, K. K. Structural Monitoring of a Transient Intermediate in the Hemagglutinin Fusion Machinery on Influenza Virions. *Sci. Adv.* **2020**, *6* (18). https://doi.org/10.1126/SCIADV.AAZ8822/SUPPL_FILE/AAZ8822_SM.PDF.

(41) Watson, M. J.; Harkewicz, R.; Hodge, E. A.; Vorauer, C.; Palmer, J.; Lee, K. K.; Guttman, M. Simple Platform for Automating Decoupled LC-MS Analysis of Hydrogen/Deuterium Exchange Samples. *J. Am. Soc. Mass Spectrom.* **2021**, *32* (2), 597–600. https://doi.org/10.1021/JASMS.0C00341/SUPPL_FILE/JS0C00341_SI_001.PDF.
(42) Suloway, C.; Pulokas, J.; Fellmann, D.; Cheng, A.; Guerra, F.; Quispe, J.; Stagg, S.; Potter, C. S.; Carragher, B. Automated Molecular Microscopy: The New Leginon System. *J. Struct. Biol.* **2005**, *151* (1), 41–60. https://doi.org/10.1016/j.jsb.2005.03.010.

4. Cysteine mutants of tau4RD confer resistance to tryptanthrin aggregation inhibitors

This chapter will be adapted for publication as a manuscript with the following author list:
Ellie I. James, Julien Dagan, Madison Hanahan, Abhinav Nath

Author contributions: E.I.J. and A.N. conceived the project. E.I.J. and M.H. expressed and purified protein. J.D. and E.I.J. performed *in vitro* aggregation assays and limited proteolysis. A.N. and E.I.J. drafted the manuscript with input from J.D.

4.1 Abstract

We recently developed a family of remarkably potent and substoichiometric tau aggregation inhibitors based on the tryptanthrin scaffold. We subsequently mapped the conformational effects of tryptanthrins on tau4RD (the four-repeat domain of tau, consisting of residues 244–372) in solution and throughout the aggregation pathway. Designed tryptanthrin analogs preferentially inhibit the earliest stages of aggregation with potency as low as 11 nM and also inhibit seeded aggregation with potency as low as 0.3 μM. Here, we pursue the intriguing observation that mutation of one of tau's naturally occurring cysteine residues to serine virtually abolishes the inhibitory activity of tryptanthrins. Importantly, this dramatic difference is observed even under reducing conditions where tau4RD's native disulfide bond is not formed. The results presented here enrich our understanding of the mechanism by which tryptanthrins inhibit tau aggregation and validate the original computational design approach that yielded these novel inhibitors.

4.2 Introduction

Microtubule-associated protein tau is an intrinsically disordered protein (IDP) implicated in a range of neurodegenerative disorders, including Alzheimer's disease and chronic traumatic encephalopathy, collectively termed tauopathies.[1,2] Tau is present at low micromolar concentrations in neurons, where it is largely bound to microtubules.[3,4] However, a hallmark of tauopathies is that tau dissociates from microtubules and forms intracellular fibrillar aggregates termed neurofibrillary tangles (NFTs). Tau aggregation *in vivo* is associated with overall increases in phosphorylation and other post-translation modifications, although the order of operations is not established.[5,6] *In vitro*, tau is quite soluble, and its aggregation typically requires the addition of negatively charged inducers such as heparin or polyphosphate.[7–9] Much of the *in vitro* characterization of tau aggregation has relied on short constructs such as tau4RD (residues 244–372, also known as K18), which aggregate on more tractable timescales than full-length tau. Physiologically, tau is expressed in six isoforms through alternative splicing, the longest of which comprises 441 residues.[6,10]

There is an urgent need for potent, selective tau aggregation inhibitors. Treatment options for tauopathies are limited to non-existent. As a primarily intracellular protein, tau is challenging to target using therapeutic antibodies. However, the development of small molecule inhibitors has been hampered by tau's dynamic nature: as an IDP, tau lacks any well-defined three-dimensional structure that could be targeted by rational drug design. We approached this challenge using virtual screening, starting from the hypothesis that, despite being highly dynamic, tau preferentially samples locally structured transient states. We modeled these states by performing enhanced-sampling molecular dynamics simulations of tau4RD and then using local clustering to identify the most populated small (10-residue) structural motifs. Machine learning-guided iterative screening of large compound libraries yielded numerous high-affinity tau ligands, including several based on the tryptanthrin scaffold.[11]

Tryptanthrin is an aromatic natural product that is well-tolerated and bioavailable and is being explored for a variety of therapeutic applications.[12–21] We previously reported tryptanthrin's ability to inhibit tau4RD aggregation.[22] Through three rounds of analog design and synthesis, optimized inhibitors with potency as low as 11 nM and activity even with ≥100-fold excess of target protein were developed. Moreover, tryptanthrin and its analogs work best early on in tau4RD aggregation, during the lag phase when primary nucleation is the dominant process. This combination of activities indicates that tryptanthrin analogs selectively target either the aggregation nucleus or a close precursor. However, the precise mechanism of action of these compounds remains an open question. Computational docking provides a rough idea of where these compounds might bind, but specific residues involved in these interactions have not yet been resolved.

Here, we focus on the role of tau's two native cysteine residues in interactions with tryptanthrin and its analogs. Disulfide formation has a marked effect on tau aggregation under oxidizing conditions.[23–27] Meanwhile, under reducing conditions, tau's cysteine residues mediate interactions with divalent metal cations such as Zn^{2+} that can dramatically accelerate aggregation.[28–33] Exploring how cysteine mutants affect susceptibility to tryptanthrins yields important mechanistic insights into this promising new class of tau aggregation inhibitors.

4.3 Results

4.3.1 Tau4RD constructs with or without the native cysteines aggregate on similar timescales under reducing conditions.

Tau contains two native cysteine residues, 291 and 322. Under oxidizing conditions *in vitro*, fibrillization is accelerated by the formation of both intramolecular and intermolecular disulfide bonds, resulting in heterogenous amyloid fibrils. Wild-type versions of both full-length tau and shorter constructs such as tau4RD aggregate more quickly than the corresponding C291A/S;C322A/S double mutants. However, under reducing conditions, the aggregation kinetics of wild-type and cysteine double mutant constructs are similar.[23–27] We confirmed that, in our hands, heparin-induced fibril formation of tau4RD and tau4RD-C291S;C322S double mutants (henceforth referred to as 4RD-Cysless) proceed on similar timescales as assessed by t_{50} (aggregation midpoint), although the lag phase of 4RD-Cysless is approximately half of that observed for tau4RD (Fig. 4.1, SI Fig. 4.1).

4.3.2 As expected, 4RD-Cysless aggregation is not accelerated by Zn^{2+}.

Tau fibril formation is very sensitive to environmental factors, including the presence of low concentrations of metal ions. In particular, low micromolar concentrations of Zn^{2+} are sufficient to dramatically accelerate tau4RD aggregation and alter aggregate morphology. The mechanism of acceleration by Zn^{2+} is thought to depend on metal ion chelation by cysteine residues. Indeed, as expected, 4RD-Cysless fibril formation is much less susceptible to acceleration by Zn^{2+} than tau4RD, resulting in accelerations (measured by t_{50}) of 4.4x and 21x for 4RD-Cysless and tau4RD respectively (Fig. 4.2, SI Fig. 4.2).

4.3.3 Surprisingly, 4RD-Cysless aggregation is not inhibited by tryptanthrin or its analogs.

We recently synthesized several potent, substoichiometric inhibitors of tau aggregation based on the natural product tryptanthrin, which itself robustly inhibits tau4RD aggregation. In exploring potential synergies or interactions between Zn^{2+} and tryptanthrin analogs, we made the serendipitous discovery that

4RD-Cysless is essentially completely resistant to inhibition by these small molecules, regardless of the presence or absence of Zn^{2+}. A concentration of 1.25 micromolar of tryptanthrin (1:4 molar ratio), which almost completely inhibits tau4RD aggregation, has no effect on the aggregation of 4RD-Cysless (Fig. 4.3A, SI. Fig. 4.1). This resistance extends to other more potent tryptanthrin analogs, including compound **TA-27**, which has an EC_{50} of 16 nM against tau4RD but does not delay 4RD-Cysless aggregation at 5 micromolar (Fig. 4.3B).

Comparison of 4RD-C291S with wild-type tau4RD and 4RD-Cysless reveals that 4RD-C291S behaves similarly to 4RD-Cysless and its aggregation is not inhibited by tryptanthrin (Fig. 4.4). This mutant lacks Cys291 but contains Cys322. In contrast, a comparison of 4RD-C322S with tau4RD and 4RD-Cysless in the presence of tryptanthrin reveals that 4RD-C322S aggregation is inhibited by tryptanthrin (Fig 4.4). This mutant lacks Cys322 but contains Cys291. The two single mutants display opposite profiles; removing Cys291 makes the construct resistant to tryptanthrin, but preserving Cys291 makes the construct susceptible to inhibition by tryptanthrin. In other words, Cys291 is essential to the tryptanthrin's mechanism of action.

4.3.4 Cys291 is close to the tryptanthrin binding site suggested by pulsed HDX-MS.

Tryptanthrin analogs were first identified as potential tau ligands through a virtual screening effort aimed at IDP targets like tau. Tryptanthrin was predicted to bind around residues 254-264. However, there are many uncertainties associated with modeling an IDP like tau4RD, and in the virtual screening process itself. Structural data are necessary to validate the computational prediction. Techniques such as X-ray crystallography and cryo-EM cannot shed light on the interactions between an IDP and a small molecule. NMR would be informative, except that the concentrations required are problematic due to compound solubility limitations. Instead, we turned to hydrogen/deuterium exchange mass spectrometry (HDX-MS).

HDX-MS relies on the principle that the exchange rate of polypeptide backbone amide protons with solvent molecules depends on peptide hydrogen bonding and solvent accessibility. Ligands binding to a specific site in an IDP like tau should decrease exchange locally while also potentially inducing more subtle changes in HDX of distal regions. In section 3.3.3, the binding site of tryptanthrin was suggested based upon decreased HDX localized to residues 285-290 when compared to the control state. While it was unexpected to see compound binding so apparent by pulsed HDX-MS, the effect is present in all detected redundant peptides (see SI Fig. 3.10.). This suggests that Cys291 contributes in some way to the high affinity of tryptanthrin and its analogs to this region within tau4RD, although the molecular details of the interaction cannot be resolved.

4.3.5 Cysless phenotype is dominant in seeding assays.

One of the hallmarks of tau fibril formation, like other amyloid aggregation processes, is the potential for seeded aggregation.[8,34,35] If a small amount of fibrillar material (a 'seed') is added at the start of an aggregation reaction, the seed can template fibril growth such that the normal lag phase is diminished or eliminated entirely, and the morphology of the resulting fibrils is highly influenced by the structure of the seed. Tryptanthrin and its analogs also inhibit seeded tau4RD aggregation, albeit about 10-fold less potently than the unseeded reaction.[22]

We explored how tau4RD's native cysteine residues affected the inhibition of seeded aggregation using a cross-seeded experiment design (Fig. 4.5A). When tau4RD aggregation was seeded with tau4RD fibrils in the presence vs. absence of tryptanthrin, the fibril elongation growth rate decreased modestly, as previously described. When 4RD-Cysless aggregation was seeded with 4RD-Cysless fibrils, tryptanthrin had no effect, as might be expected. When 4RD-Cysless aggregation was seeded with tau4RD fibrils, tryptanthrin again had no effect, consistent with a decreased affinity of the compound upon loss of the native Cys291. However, when tau4RD aggregation was seeded with 4RD-Cysless fibrils, tryptanthrin still had little to no effect. This was an unexpected finding: even though most of the protein in the reaction (tau4RD) was susceptible to inhibition, templating with a small amount of 4RD-Cysless was enough to confer resistance to tryptanthrin inhibition. In other words, the nucleating species of 4RD-Cysless aggregation must be structurally different enough from that of tau4RD that tryptanthrin is no longer able to bind efficiently, even when the native cysteine residues are present in excess in growing fibrils. This conclusion is supported by limited proteolysis with tandem mass spectrometry, which revealed that tau4RD fibrils and 4RD-Cysless fibrils have different trypsin/lys-C digestion profiles (Fig. 4.5B).

4.4 Discussion

Our observations here shed important light on the mechanism of action of novel tau aggregation inhibitors. Tryptanthrin and its analogs exert their effects by selectively targeting the aggregation nucleus or a close precursor. Mutation of Cys291 lowers the affinity of tryptanthrin for this target species and, in fact, changes its structure sufficiently so that the resulting aggregation pathway, whether in seeded or unseeded reactions, becomes resistant to tryptanthrin inhibition. This is consistent with the idea that tryptanthrin potency is highly dependent on the nature of the aggregation nucleus and should vary considerably for fibril formation induced by different cofactors. We observe, for example, that heparin-induced and polyphosphate-induced aggregation vary quite substantially in their sensitivity to tryptanthrin analogs (Fig. 4.6). Future studies that attempt to resolve structural differences in prefibrillar nucleating species or fibrillar intermediates of these various aggregation pathways could prove valuable in understanding the mechanisms of tryptanthrin analogs as well as other promising aggregation inhibitors.

4.5 Materials and Methods

4.5.1 Protein Expression and Purification

Tau4RD, 4RD-Cysless, 4RD-C291S, and 4RD-C322S were expressed and purified from *E. coli* BL-21 (DE3) in-house as recently described.[22] Tau4RD plasmid was gifted by the Rhoades lab at the University of Pennsylvania (Philadelphia, PA). 4RD-Cysless, 4RD-C291S, and 4RD-C322S plasmids were prepared by Gibson assembly. All mutations were confirmed by sequencing prior to protein expression. Protein constructs were purified through two Ni-NTA agarose column steps followed by fractionation with a 25 mL S200 extended gel filtration column. Protein purity was confirmed by precast 12% Bis-Tris SDS-PAGE gels (Invitrogen). Protein-containing fractions were concentrated, aliquoted, flash-frozen, and stored at -80 °C. Protein concentrations were determined by the Pierce BCA Protein Assay Kit (Thermo Fisher Scientific).

4.5.2 Aggregation Assays

4.5.2.1 Unseeded

Unseeded aggregation assays were performed as previously described with the following changes.[22] Protein and aggregation inducers (heparin, polyphosphate) were prepared at 2.105x the desired final concentration in a filtered (0.22 μm) aggregation buffer containing 20 mM MOPS, 50 mM NaCl, 1 mM TCEP, and 2.5 μM each of EDTA, EGTA, TPEN, pH 7.4. Tau constructs were thawed and diluted into aggregation buffer to which $ZnCl_2$ was spiked in combination with TA analogs (or equivalent volume of DMSO) for a combined volume of 460 μL per condition. DMSO content was 1% or less for all reactions. Per condition, 95 μL of tau construct sample was plated into each of n = 3 or 4 wells with a multi-channel pipette. 10 μL of filtered ThT (0.22 μm, 50 μM final concentration) or aggregation buffer was added to wells with a multi-channel pipette. Finally, 95 μL of aggregation inducer was added to each well. Final concentrations in the well were as follows (if applicable): 5 μM tau construct, 30 μM Zn^{2+}, 1.25 μM TA analog, 5 μM heparin, 10 μg/mL polyphosphate. The plate was covered with a polypropylene or polyolefin film and monitored by ThT fluorescence (λ_{ex} = 440 nm, λ_{em} = 485 nm) with a pre-heated (37 °C) BioTek Synergy HTX plate reader overnight (~17 h unless otherwise stated). Fluorescence readings were collected every 5 minutes after 1 minute of linear shaking at 540 rpm. All aggregation assays were performed with non-binding black 96-well flat-bottom plates (Corning). A blank sample without protein was prepared for each assay and used to correct baseline fluorescence.

4.5.2.2 Seeded

Seeded aggregation assays were performed with the components listed in unseeded assays above and as previously described[22] with the following changes. Pre-formed seeds were generated by harvesting the

appropriate fibrils (tau4RD, 4RD-Cysless) after 17 h of aggregation. Wells from unseeded aggregation assays were transferred to individual lo-bind snap-cap tubes (Eppendorf) and centrifuged at 21,000*g* for 30 min at 4 °C. 100 µL of supernatant was discarded, then 100 µL of fresh aggregation buffer was added to each tube. Seeds were generated by sonicating aliquots on ice for 5 rounds of 2 sec to disrupt amyloid fibrils. Seeds were added to aggregation assays at 5% (v/v). 10 µL of tau seeds or aggregation buffer was added to the wells after the addition of 85 µL of heparin (final heparin concentration remained 5 µM).

4.5.2.3 Determination of t_{50}

Non-linear least squares fitting in Prism 10.4 was used to determine t_{50}, the midpoint of the aggregation curve, for each condition according to the following equation:

$$F(t) = F(0) + \frac{(F_{max} - F(0))}{1 + e^{-k(t - t_{50})}} \qquad (1)$$

where $F(0)$ is the baseline fluorescence at the start of the start of the reaction, F_{max} is the condition-specific maximal fluorescence at the plateau, and k is a rate parameter that describes the steepness of the transition. Differences between t_{50} values were assessed for significance (alpha = 0.05) by one-way ANOVA.

4.5.3 Limited Proteolysis

4.5.3.1 Trypsin/Lys-C Digest

Tau constructs were aggregated in the absence of ThT as described above. After aggregation, fibrils were isolated by centrifugation as described above. Fibril pellets were isolated by removing 175 µL of supernatant from each aliquot. Trypsin/Lys-C Protease Mix (Pierce, MS-Grade) was resuspended at 0.5 mg/mL in PBS buffer pH 7.4 (20 mM phosphate, 150 mM NaCl, 0.02% sodium azide, 1 mM EDTA), aliquoted, and stored at -20 °C until use. 0.4 µg of Trypsin/Lys-C mix was added to each tube with minimal agitation of the fibril pellet. After a quiescent 30 min digestion at 37 °C, proteolysis was quenched, and fibrils were disrupted by the addition of 8 M urea, pH 2.5, followed by a 30-min incubation at 37 °C with orbital shaking (300 rpm). Samples were cooled to room temperature, flash-frozen, and stored at -80 °C until LC-MS/MS analysis.

4.5.3.2 LC-MS/MS

Samples were thawed at 5 °C for 4.5 minutes and injected using a custom LEAP robot integrated with an LC-MS system.[36] Peptides were trapped on a Waters XSelect CSH C18 trap cartridge column (2.1 x 5 mm 2.5 µm) and resolved over a CSH C18 column (1 x 50 mm 1.7 µM 130 Å) using a linear gradient of 5 to 35% B (A: 0.1% FA, 0.025% TFA, 5% ACN; B: CAN with 0.1% FA) over 10 minutes. Peptides were analyzed on a Thermo Orbitrap Ascend mass spectrometer with a 120,000 resolution. As described previously,[36] a series of washes was applied to the trap column between injections to minimize carry-over.

Data-dependent MS/MS acquisition was performed using rapid CID and HCD scans and processed in Byonic (Protein Metrics) with a digestion filter set to K/R and infinite missed cleavages. A score cutoff of 200 was used to identify peptides.

4.5.3.3 Peptide Mapping

Peptides identified from limited proteolysis-LC-MS/MS were filtered, sorted, and compared using an in-house Python script (available upon request). Briefly, each K/R position in the tau sequence was assessed for proteolysis by totaling the XIC of peptides with K/R in the C-terminal position. K/R positions with XIC signals less than 1e5 were assigned an XIC value of 0. The XIC for each K/R position (per sample) was then normalized to the average (mean) XIC of all K/R positions within the sample. Digests and analyses were performed in duplicate (biological replicates).

4.6 Figures

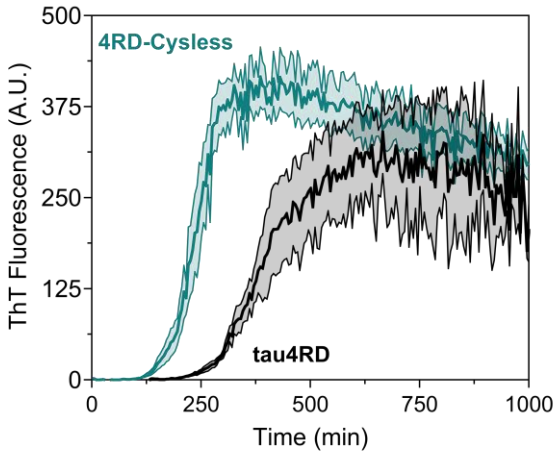

Figure 4.1: Wildtype tau4RD and 4RD-Cysless aggregation occur on similar timescales. ThT traces for heparin-induced tau4RD and 4RD-Cysless aggregation. While there is no significant difference in the t_{50} value between the two conditions here, significant differences in t_{50} were observed in other experiments. In general, 4RD-Cysless appears to aggregate twice as quickly as tau4RD.

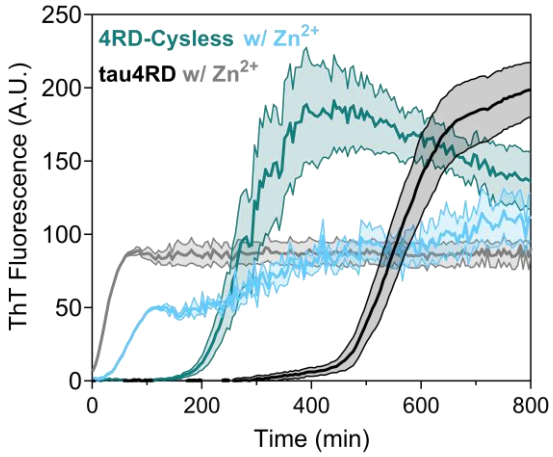

Figure 4.2: Zn^{2+} accelerates aggregation of tau4RD and 4RD-Cysless. ThT traces for heparin-induced tau4RD and 4RD-Cysless aggregation in the absence or presence of 30 μM Zn^{2+}. Zn^{2+} significantly accelerates the aggregation of both tau constructs; tau4RD aggregation is accelerated by approx. 21-fold and 4RD-Cysless by approx. 4-fold. See SI Fig. 4.2.

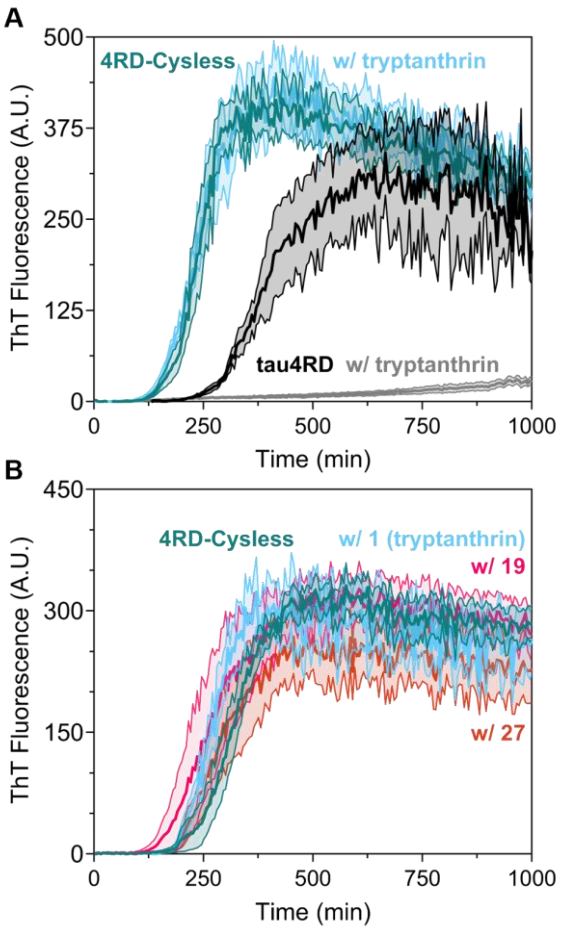

Figure 4.3: 4RD-Cysless aggregation is resistant to tryptanthrin inhibition. A) Tau4RD aggregation is almost completely abrogated by the addition of 1.25 μM (1:4 molar ratio) of tryptanthrin. 4RD-Cysless aggregation is unaffected by 1.25 μM tryptanthrin. B) 4RD-Cysless is resistant to tryptanthrin and its analogs **19** and **27**; none of the three compounds abrogate 4RD-Cysless aggregation at a 1:1 molar ratio, despite having an EC_{50} of 16 nM against tau4RD (**27**).

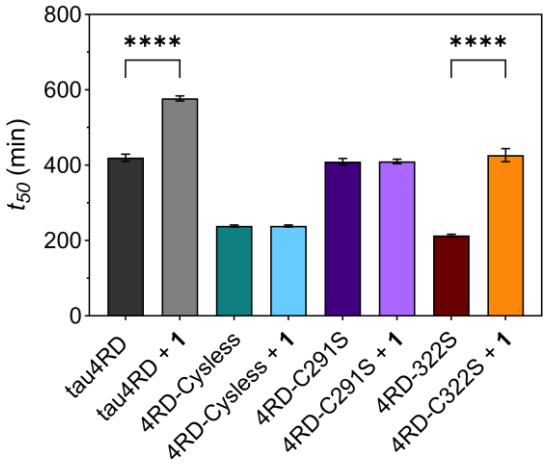

Figure 4.4: Single-cysteine mutants reveal that Cys291 is critical for tryptanthrin inhibition. Comparison of t50 values in the presence or absence of tryptanthrin (**1**) reveals that 4RD-C291S recapitulates the resistance to tryptanthrin inhibition seen in the double-mutant, 4RD-Cysless. Meanwhile, 4RD-C322S, which contains the native Cys291, is sensitive to tryptanthrin inhibition. See SI Fig. 4.3 for complete data.

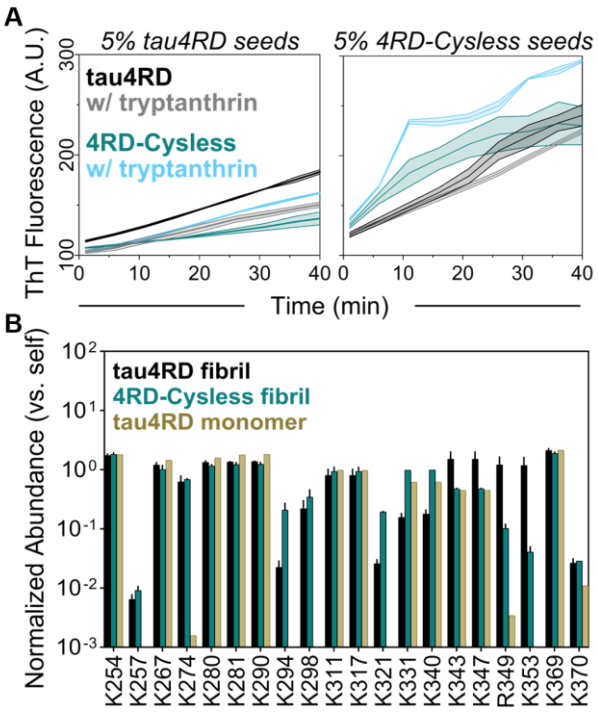

Figure 4.5: 4RD-Cysless and tau4RD form different aggregation nuclei. A) The addition of 5% (v/v) pre-formed fibrillar seeds bypasses the aggregation lag phase and allows observation of the elongation rate. The elongation rate of tau4RD seeded with tau4RD can be reduced by the addition of tryptanthrin. The elongation rate of 4RD-Cysless is not diminished by tryptanthrin (left). When 4RD-Cysless seeds are applied to tau4RD, tau4RD becomes resistant to the addition of tryptanthrin (right). As with tau4RD-seeded reactions, the elongation rate of 4RD-Cysless seeded with 4RD-Cysless seeds is not reduced by tryptanthrin. B) Trypsin/Lys-C limited proteolysis of tau4RD monomer, tau4RD fibrils, and 4RD-Cysless fibrils reveal different cleavage fingerprints, indicating that tau4RD and 4RD-Cysless form different fibril conformations.

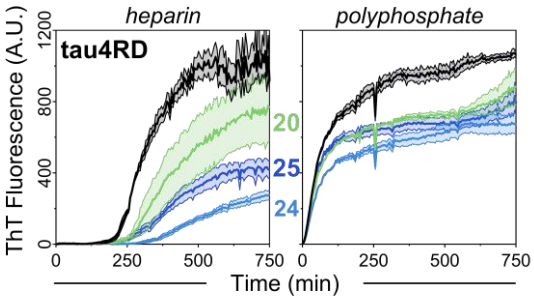

Figure 4.6: Sensitivity to tryptanthrins is dependent on aggregation nuclei. A) Tryptanthrin analogs **25** and **24** moderately inhibit and **20** mildly inhibits heparin-induced tau4RD aggregation. The effect is apparent both in the extension of the lag phase and in the reduction in the aggregation plateau. In contrast, all three analogs only mildly inhibit polyphosphate-induced tau4RD aggregation, and apparently through a different mechanism (note lack of lag phase).

4.7 Supplementary Material

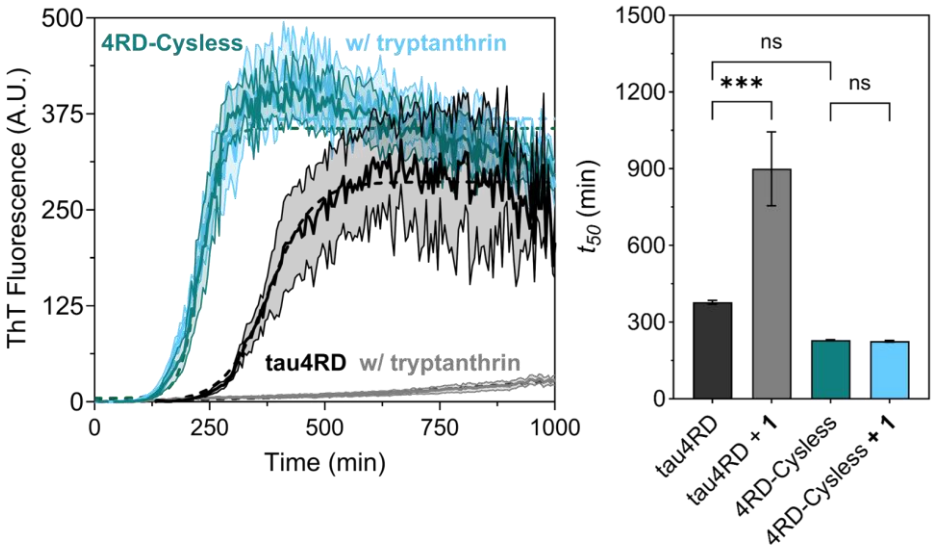

SI Fig. 4.1: Tau4RD and 4RD-Cysless simple sigmoidal fits and resulting t_{50} values. Related to Figs. 1 and 3A. Simple sigmoidal fits (eqn. 1) are marked with dashed lines. There is no significant difference between the t_{50} values of tau4RD and 4RD-Cysless. The addition of tryptanthrin (**1**) to tau4RD results in a significant increase in the t_{50}, while the same addition to 4RD-Cysless results in no change to the t_{50}. Significance assessed by one-way ANOVA (alpha = 0.05).

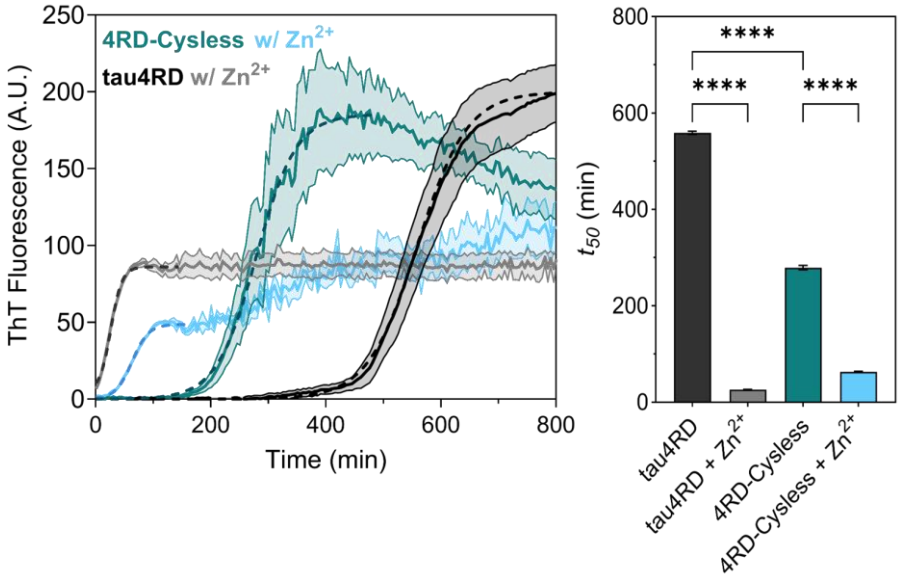

SI Fig. 4.2: Tau4RD and 4RD-Cysless simple sigmoidal fits and resulting t_{50} values in the presence of Zn^{2+}. Related to Fig. 4.2. Simple sigmoidal fits (eqn. 1) are marked with dashed lines. There is no significant difference between the t50 values of tau4RD and 4RD-Cysless. The addition of tryptanthrin (**1**) to tau4RD results in a significant increase in the t_{50}, while the same addition to 4RD-Cysless results in no change to the t_{50}. Significance assessed by one-way ANOVA (alpha = 0.05).

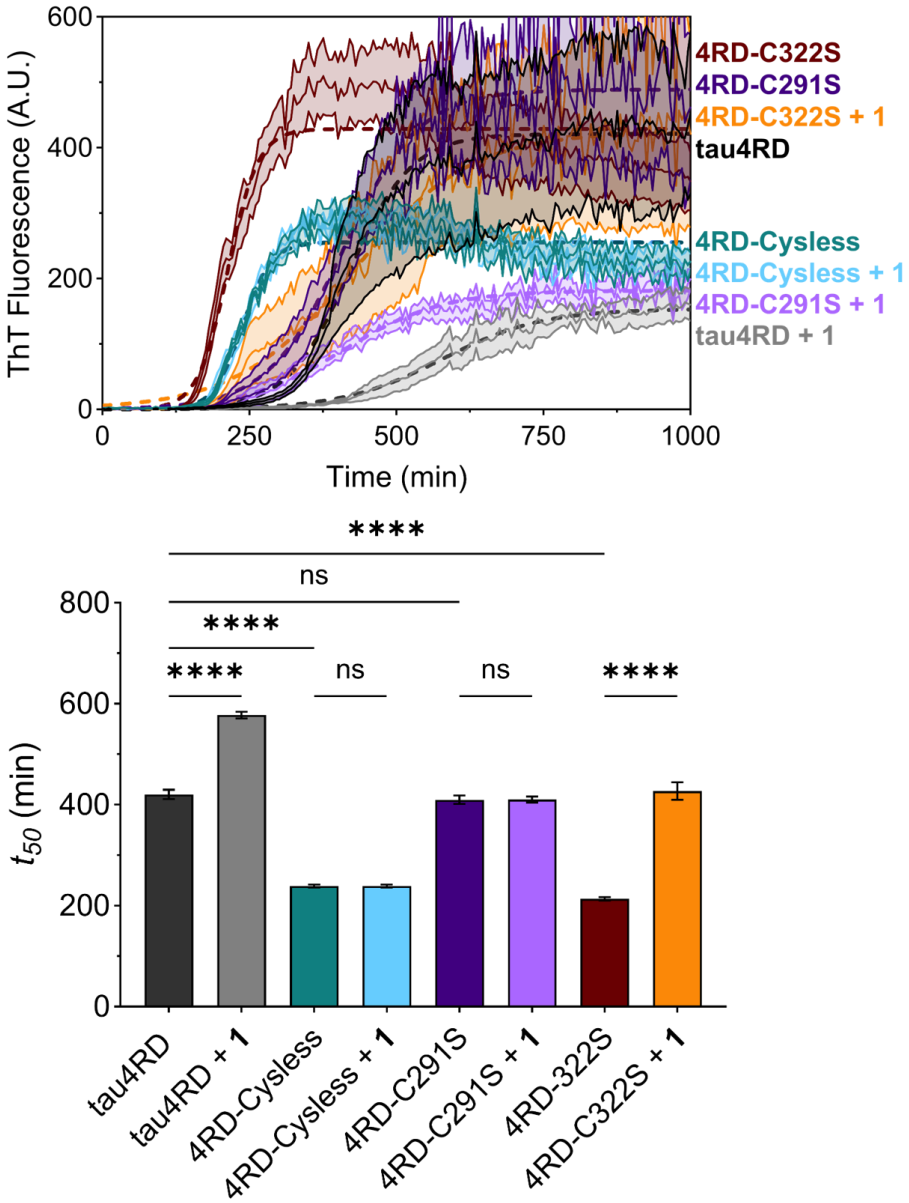

SI Fig. 4.3: Tau constructs simple sigmoidal fits and resulting t_{50} values in the presence of tryptanthrin. Related to Fig. 4. Simple sigmoidal fits (eqn. 1) are marked with dashed lines. Only tau4RD and 4RD-C322s are susceptible to inhibition by tryptanthrin. 4RD-Cysless and 4RD-C291S are not susceptible to tryptanthrin inhibition. Significance assessed by one-way ANOVA (alpha = 0.05).

4.8 References

(1) Zhang, Y.; Wu, K. M.; Yang, L.; Dong, Q.; Yu, J. T. Tauopathies: New Perspectives and Challenges. Mol. Neurodegener. 2022, 17 (1). https://doi.org/10.1186/s13024-022-00533-z.

(2) Limorenko, G.; Lashuel, H. A. Revisiting the Grammar of Tau Aggregation and Pathology Formation: How New Insights from Brain Pathology Are Shaping How We Study and Target Tauopathies. Chem. Soc. Rev. 2022, 51 (2), 513–565. https://doi.org/10.1039/D1CS00127B.

(3) Kanaan, N. M.; Grabinski, T. Neuronal and Glial Distribution of Tau Protein in the Adult Rat and Monkey. Front. Mol. Neurosci. 2021, 14, 607303. https://doi.org/10.3389/FNMOL.2021.607303/BIBTEX.

(4) Iqbal, K.; Liu, F.; Gong, C.-X.; Grundke-Iqbal, I. Tau in Alzheimer Disease and Related Tauopathies. Curr. Alzheimer Res. 2010, 7 (8), 656–664. https://doi.org/10.2174/156720510793611592.

(5) Hasegawa, M.; Wischik, C. M.; Harrington, C. Molecular Mechanisms in the Pathogenesis of Alzheimer's Disease and Tauopathies-Prion-Like Seeded Aggregation and Phosphorylation. Biomol. 2016 Vol 6 Page 24 2016, 6 (2), 24. https://doi.org/10.3390/BIOM6020024.

(6) Langerscheidt, F.; Wied, T.; Al Kabbani, M. A.; van Eimeren, T.; Wunderlich, G.; Zempel, H. Genetic Forms of Tauopathies: Inherited Causes and Implications of Alzheimer's Disease-like TAU Pathology in Primary and Secondary Tauopathies. J. Neurol. 2024, 271 (6), 2992. https://doi.org/10.1007/S00415-024-12314-3.

(7) Wickramasinghe, S. P.; Lempart, J.; Merens, H. E.; Murphy, J.; Huettemann, P.; Jakob, U.; Rhoades, E. Polyphosphate Initiates Tau Aggregation through Intra- and Intermolecular Scaffolding. Biophys. J. 2019, 117 (4), 717–728. https://doi.org/10.1016/J.BPJ.2019.07.028.

(8) Despres, C.; Di, J.; Cantrelle, F. X.; Li, Z.; Huvent, I.; Chambraud, B.; Zhao, J.; Chen, J.; Chen, S.; Lippens, G.; Zhang, F.; Linhardt, R.; Wang, C.; Klärner, F. G.; Schrader, T.; Landrieu, I.; Bitan, G.; Smet-Nocca, C. Major Differences between the Self-Assembly and Seeding Behavior of Heparin-Induced and in Vitro Phosphorylated Tau and Their Modulation by Potential Inhibitors. ACS Chem. Biol. 2019, 14 (6), 1363–1379. https://doi.org/10.1021/ACSCHEMBIO.9B00325/SUPPL_FILE/CB9B00325_SI_001.PDF.

(9) Montgomery, K. M.; Carroll, E. C.; Thwin, A. C.; Quddus, A. Y.; Hodges, P.; Southworth, D. R.; Gestwicki, J. E. Chemical Features of Polyanions Modulate Tau Aggregation and Conformational States. J. Am. Chem. Soc. 2023, 145 (7), 3926–3936. https://doi.org/10.1021/jacs.2c08004.

(10) Buchholz, S.; Zempel, H. The Six Brain-Specific TAU Isoforms and Their Role in Alzheimer's Disease and Related Neurodegenerative Dementia Syndromes. Alzheimers Dement. 2024, 20 (5), 3606–3628. https://doi.org/10.1002/ALZ.13784.

(11) Baggett, D. W.; Nath, A. The Rational Discovery of a Tau Aggregation Inhibitor. Biochemistry 2018, 57 (42), 6099–6107. https://doi.org/10.1021/ACS.BIOCHEM.8B00581/ASSET/IMAGES/LARGE/BI-2018-00581Y_0004.JPEG.

(12) Hwang, J. M.; Oh, T.; Kaneko, T.; Upton, A. M.; Franzblau, S. G.; Ma, Z.; Cho, S. N.; Kim, P. Design, Synthesis, and Structure-Activity Relationship Studies of Tryptanthrins as Antitubercular Agents. J. Nat. Prod. 2013, 76 (3), 354–367. https://doi.org/10.1021/NP3007167.

(13) Iwata, T.; Watanabe-Yanai, A.; Tamamura-Andoh, Y.; Arai, N.; Akiba, M.; Kusumoto, M. Tryptanthrin Reduces Campylobacter Jejuni Colonization in the Chicken Gut by a Bactericidal Mechanism. Appl. Environ. Microbiol. 2023, 89 (2). https://doi.org/10.1128/AEM.01701-22.

(14) Olson, J. A.; Terryn, R. J.; Stewart, E. L.; Baum, J. C.; Novak, M. J. New Insight into the Action of Tryptanthrins against Plasmodium Falciparum: Pharmacophore Identification via a Novel Submolecular QSAR Descriptor. J. Mol. Graph. Model. 2018, 80, 138–146. https://doi.org/10.1016/J.JMGM.2017.12.013.

(15) Bandekar, P. P.; Roopnarine, K. A.; Parekh, V. J.; Mitchell, T. R.; Novak, M. J.; Sinden, R. R. Antimicrobial Activity of Tryptanthrins in Escherichia Coli. J. Med. Chem. 2010, 53 (9), 3558–3565. https://doi.org/10.1021/JM901847F/ASSET/IMAGES/LARGE/JM-2009-01847F_0003.JPEG.
(16) Kirpotina, L. N.; Schepetkin, I. A.; Hammaker, D.; Kuhs, A.; Khlebnikov, A. I.; Quinn, M. T. Therapeutic Effects of Tryptanthrin and Tryptanthrin-6-Oxime in Models of Rheumatoid Arthritis. Front. Pharmacol. 2020, 11. https://doi.org/10.3389/FPHAR.2020.01145/PDF.
(17) Peng, J. W.; Yin, X. D.; Li, H.; Ma, K. Y.; Zhang, Z. J.; Zhou, R.; Wang, Y. L.; Hu, G. F.; Liu, Y. Q. Design, Synthesis, and Structure-Activity Relationship of Quinazolinone Derivatives as Potential Fungicides. J. Agric. Food Chem. 2021, 69 (16), 4604–4614. https://doi.org/10.1021/ACS.JAFC.0C05475.
(18) Hesse-Macabata, J.; Morgner, B.; Elsner, P.; Hipler, U. C.; Wiegand, C. Tryptanthrin Promotes Keratinocyte and Fibroblast Responses in Vitro after Infection with Trichophyton Benhamiae DSM6916. Sci. Rep. 2020, 10 (1). https://doi.org/10.1038/s41598-020-58773-2.
(19) Zou, Y.; Zhang, G.; Li, C.; Long, H.; Chen, D.; Li, Z.; Ouyang, G.; Zhang, W.; Zhang, Y.; Wang, Z. Discovery of Tryptanthrin and Its Derivatives and Its Activities against NSCLC In Vitro via Both Apoptosis and Autophagy Pathways. Int. J. Mol. Sci. 2023, 24 (2). https://doi.org/10.3390/ijms24021450.
(20) Yang, S.; Li, X.; Hu, F.; Li, Y.; Yang, Y.; Yan, J.; Kuang, C.; Yang, Q. Discovery of Tryptanthrin Derivatives as Potent Inhibitors of Indoleamine 2,3-Dioxygenase with Therapeutic Activity in Lewis Lung Cancer (LLC) Tumor-Bearing Mice. J. Med. Chem. 2013, 56 (21), 8321–8331. https://doi.org/10.1021/JM401195N/SUPPL_FILE/JM401195N_SI_001.PDF.
(21) Zeng, Q.; Luo, C.; Cho, J.; Lai, D.; Shen, X.; Zhang, X.; Zhou, W. Tryptanthrin Exerts Anti-Breast Cancer Effects Both in Vitro and in Vivo through Modulating the Inflammatory Tumor Microenvironment. Acta Pharm. 2021, 71 (2), 245–266. https://doi.org/10.2478/ACPH-2021-0020.
(22) James, E. I.; Baggett, D. W.; Chang, E.; Schachter, J.; Nixey, T.; Choi, K.; Guttman, M.; Nath, A. Tryptanthrin Analogs Substoichiometrically Inhibit Seeded and Unseeded Tau4RD Aggregation. eLife 2024, 13. https://doi.org/10.7554/ELIFE.98227.1.
(23) Di Noto, L.; DeTure, M. A.; Purich, D. L. Disulfide-Cross-Linked Tau and MAP2 Homodimers Readily Promote Microtubule Assembly. Mol. Cell Biol. Res. Commun. 1999, 2 (1), 71–76. https://doi.org/10.1006/MCBR.1999.0153.
(24) Barghorn, S.; Mandelkow, E. Toward a Unified Scheme for the Aggregation of Tau into Alzheimer Paired Helical Filaments. Biochemistry 2002, 41 (50), 14885–14896. https://doi.org/10.1021/BI026469J/ASSET/IMAGES/LARGE/BI026469JF00010.JPEG.
(25) Furukawa, Y.; Kaneko, K.; Nukina, N. Tau Protein Assembles into Isoform- and Disulfide-Dependent Polymorphic Fibrils with Distinct Structural Properties. J. Biol. Chem. 2011, 286 (31), 27236–27246. https://doi.org/10.1074/jbc.M111.248963.
(26) Bhattacharya, K.; Rank, K. B.; Evans, D. B.; Sharma, S. K. Role of Cysteine-291 and Cysteine-322 in the Polymerization of Human Tau into Alzheimer-like Filaments. Biochem. Biophys. Res. Commun. 2001, 285 (1), 20–26. https://doi.org/10.1006/BBRC.2001.5116.
(27) Schweers, O.; Mandelkow, E. M.; Biernat, J.; Mandelkow, E. Oxidation of Cysteine-322 in the Repeat Domain of Microtubule-Associated Protein Tau Controls the in Vitro Assembly of Paired Helical Filaments. Proc. Natl. Acad. Sci. 1995, 92 (18), 8463–8467. https://doi.org/10.1073/PNAS.92.18.8463.
(28) Mo, Z. Y.; Zhu, Y. Z.; Zhu, H. L.; Fan, J. B.; Chen, J.; Liang, Y. Low Micromolar Zinc Accelerates the Fibrillization of Human Tau via Bridging of Cys-291 and Cys-322. J. Biol. Chem. 2009, 284 (50), 34648–34657. https://doi.org/10.1074/JBC.M109.058883/ASSET/9CA7B656-171A-473E-9F01-2DD963DA3F10/MAIN.ASSETS/GR5.JPG.
(29) Huang, Y.; Wu, Z.; Cao, Y.; Lang, M.; Lu, B.; Zhou, B. Zinc Binding Directly Regulates Tau Toxicity Independent of Tau Hyperphosphorylation. Cell Rep. 2014, 8 (3), 831–842.

https://doi.org/10.1016/J.CELREP.2014.06.047/ATTACHMENT/AAD7BD54-C9E9-4158-A377-AFC96B6DB6BF/MMC2.PDF.
(30) Roman, A. Y.; Devred, F.; Byrne, D.; La Rocca, R.; Ninkina, N. N.; Peyrot, V.; Tsvetkov, P. O. Zinc Induces Temperature-Dependent Reversible Self-Assembly of Tau. J. Mol. Biol. 2019, 431 (4), 687–695. https://doi.org/10.1016/J.JMB.2018.12.008.
(31) Moreira, G. G.; Cristóvão, J. S.; Torres, V. M.; Carapeto, A. P.; Rodrigues, M. S.; Landrieu, I.; Cordeiro, C.; Gomes, C. M. Zinc Binding to Tau Influences Aggregation Kinetics and Oligomer Distribution. Int. J. Mol. Sci. 2019, 20 (23), 5979. https://doi.org/10.3390/IJMS20235979.
(32) Chowdhury, S. R.; Lu, H. P. Unraveling the Mechanism of Tau Protein Aggregation in Presence of Zinc Ion: The Earliest Step of Tau Aggregation. Chem. Phys. Impact 2022, 4. https://doi.org/10.1016/j.chphi.2021.100060.
(33) Lippi, S. L. P.; Neely, C. L. C.; Amaya, A. L. Trace Concentrations, Heavy Implications: Influences of Biometals on Major Brain Pathologies of Alzheimer's Disease. Int. J. Biochem. Cell Biol. 2022, 143, 106136. https://doi.org/10.1016/J.BIOCEL.2021.106136.
(34) Holmes, B. B.; Furman, J. L.; Mahan, T. E.; Yamasaki, T. R.; Mirbaha, H.; Eades, W. C.; Belaygorod, L.; Cairns, N. J.; Holtzman, D. M.; Diamond, M. I. Proteopathic Tau Seeding Predicts Tauopathy in Vivo. Proc. Natl. Acad. Sci. U. S. A. 2014, 111 (41), E4376–E4385. https://doi.org/10.1073/PNAS.1411649111/SUPPL_FILE/PNAS.201411649SI.PDF.
(35) Mirbaha, H.; Chen, D.; Mullapudi, V.; Terpack, S. J.; White, C. L.; Joachimiak, L. A.; Diamond, M. I. Seed-Competent Tau Monomer Initiates Pathology in a Tauopathy Mouse Model. J. Biol. Chem. 2022, 298 (8), 102163. https://doi.org/10.1016/J.JBC.2022.102163.
(36) Watson, M. J.; Harkewicz, R.; Hodge, E. A.; Vorauer, C.; Palmer, J.; Lee, K. K.; Guttman, M. Simple Platform for Automating Decoupled LC-MS Analysis of Hydrogen/Deuterium Exchange Samples. J. Am. Soc. Mass Spectrom. 2021, 32 (2), 597–600. https://doi.org/10.1021/JASMS.0C00341/SUPPL_FILE/JS0C00341_SI_001.PDF.

5. Chapter 5: Perspectives and Future Directions

5.1. Perspectives

Despite intensive study and attempts at therapeutic intervention, all-cause dementia remains debilitating for more than 6 million Americans and 55 million people worldwide.[1–3] Tau, an intrinsically disordered protein (IDP), is associated with many diseases classified as dementias, the most notable of which is Alzheimer's disease (AD, estimated 50-75% of dementia cases). This disease has disproportionate effects on the population that extend beyond the cognitive decline patients experience. Over 11 million people in the United States alone provide 18.4 billion hours of unpaid care for loved ones with AD, care which carries an estimated value of $350 billion per year.[1] Also of note, AD is more likely to affect marginalized communities; Black Americans suffer from AD at a rate twice that of similarly aged white Americans. The lifetime risk for AD at age 45 is twice as high for women as for men, and nearly two-thirds of U.S. AD patients are women. There is also data to suggest that gender and sexual minorities disproportionately suffer from AD, although stratifying the population for these studies is a new development.[1]

Looking beyond the U.S., the value of global dementia care is forecast to rise to $2.8 trillion dollars by 2030,[3] approximately equivalent to Italy's current GDP.[4] More than 60% of dementia patients live in low- and middle-income countries where accessing treatment and care is more challenging than in high-income countries. In fact, an estimated one-fifth to one-half of dementia cases are diagnosed in high-income countries, while only one-tenth of cases are diagnosed in low-income countries. There also appears to be a difference in care distribution between high- and low-income countries: informal care provided by family or friends occurs at *higher* rates in low-income countries than observed in North America and Western Europe,[2] a staggering fact when the number of informal carers in the U.S. is double the number of patients.

Over the years, there have been a handful of drugs approved for the treatment of AD and associated symptoms. Amongst these are small molecule drugs like cholinesterase inhibitors (e.g., donepezil, rivastigmine), which are effective for between 20 and 60% of patients, and memantine, an NMDA receptor antagonist that is effective for 10% of patients.[5] These treatments have been found to delay symptom progression by up to 6 months for patients with mild to severe AD in the U.S., although the E.U. only permits the use of cholinesterase inhibitors and restricts their prescription to the treatment of mild to moderate AD.[5] There is a dire need for additional therapeutics to treat AD, and many people were excited when aducanumab, the first monoclonal antibody (mAb) treatment for AD, was FDA-approved in 2021. Aducanamab was soon followed by lecanemab (2023) and donanemab (2024), all of which target various pathological states of amyloid-beta.[6–8] Evidence for the efficacy of these therapeutics was slim upon their approval, and subsequent meta-analysis has suggested that these drugs do not meet the minimum proposed

threshold for clinically meaningful change on AD assessment scales.[9] Ignoring their limited efficacy, these drugs also carry significant safety risks, calling into question their approval and prescription. It is evident that we are in desperate need of additional diagnostic and therapeutic compounds for AD.

5.2. Future Directions

IDPs such as tau offer a new avenue of exploration for AD drugs, although major gaps remain in our understanding of amyloid aggregation and how to target 'undruggable' IDP conformational ensembles. This knowledge gap arises mainly due to the challenge associated with studying IDPs, namely, their lack of structure. Historical approaches to structural biology are applicable to well-behaved (well-folded) proteins but fall short of capturing the dynamic interconversions inherent to IDP chains. As structural biology, computational tools, and instrumentation have advanced, so too has our understanding of IDPs. The research presented in this dissertation addresses questions directly related to the validity of applying traditional drug discovery approaches to a disordered target and highlights HDX-MS as a technique capable of discerning structural changes in small, soluble species during tau's aggregation.

In Chapter 2, we describe the discovery and subsequent SAR study of tryptanthrin and its analogs as potent inhibitors of tau4RD aggregation. This was the first report of tryptanthrin, a natural product with antimicrobial,[10] anti-inflammatory,[11] and anti-cancer activity,[12] as an anti-amyloid agent. Additionally, our work reports the most potent small molecule IDP effector to date, with one analog displaying an EC_{50} of 11 nM against heparin-induced tau4RD aggregation (Fig 2.3). The SAR study revealed that the principles behind changing a small portion of the molecular scaffold to change potency hold even against targets that are largely unstructured. Finally, the tryptanthrin family analogs inhibit nucleation, the first step of tau4RD aggregation. This could be an important advantage to pursue for future anti-amyloid drug discovery efforts; if one can inhibit nucleation, it may be possible to prevent or substantially delay amyloid aggregation. It would be interesting to apply tryptanthrin inhibitors to studies of prion-like tau seeding. Theoretically, tryptanthrin and its analogs should be more specific to tau than to other amyloidogenic IDPs (e.g., amyloid-beta, alpha-synuclein) because they were screened against a tau4RD conformational ensemble generated *in silico.* This would be a relatively straightforward set of experiments and would provide important feedback about the computational drug discovery pipeline (and its assumptions) that was developed in the Nath lab.

Chapter 3 addresses a major open question in amyloid research about the origin timeline of polymorphic amyloid fibrils. While the differences between mature fibrils are readily apparent by cryo-EM, there are few structural techniques that have both the resolution and capability of resolving dynamic intermediate species in the aggregation pathway. We applied pulsed HDX-MS to follow the structural changes associated with heparin- and polyphosphate-induced tau4RD aggregation. Remarkably, we observed multiple protected populations in the polyphosphate-induced condition after only 15 seconds of aggregation (Figs.

3.2/3.5). These populations developed in lockstep, indicating that they were separate and not interconverting species. Further, our data revealed that heparin- and polyphosphate-induced aggregation are different from the onset (Fig. 3.3). Because we were unable to disassemble fibrils to probe them by pulsed HDX-MS, we have assumed that no structural changes happen between the late soluble species (protofibrils) and the mature fibrils. It would be advantageous to probe the fibrils with fast photochemical oxidation of proteins (FPOP, reviewed in Ref. 13), a solution-based MS technique that provides complementary and orthogonal data to HDX-MS. Unlike deuterium, the hydroxyl label transferred to the side chains of the protein of interest during FPOP is not labile, which opens many avenues for disrupting the mature fibrils that would be too harsh for HDX-MS.

Returning to pulsed HDX-MS, the addition of tryptanthrin to either aggregation reaction did not change the structure of the intermediates observed, nor did it influence the relative population fractions of the two polyphosphate fibril morphs (Figs. 3.4/3.5). There is also data that suggests the binding site of tryptanthrin to tau4RD is near residues 285-290. While we have put significant effort toward building and testing a quenched-flow mixing apparatus capable of resolving HDX on the millisecond timescale to address this question, we have not been able to obtain a complete dataset. However, the many partial datasets we have generated also suggest that region of tau is differentially protected in the presence of tryptanthrin (data not shown). It would be advantageous to confirm whether this is indeed the tryptanthrin binding site, both to characterize the mechanism of tryptanthrin and to validate the computational screening approach by which it was discovered. The most straightforward approach to this question would be to continue with millisecond HDX studies of tau4RD and the tau constructs introduced in Chapter 4 (4RD-Cysless, 4RD-C291S, 4RD-C322S) in the presence of vehicle or tryptanthrin.

Finally, in Chapter 4, we serendipitously tied together the work from Chapters 2 and 3. We discovered that a cysteine-free tau4RD mutant (4RD-Cysless) is resistant to tryptanthrin inhibition, as well as inhibition by its more potent synthetic analogs (Fig. 4.3). Upon testing the single-cysteine mutants, we found that Cys291 is required for tryptanthrin inhibition, which aligns shockingly well with the binding site near residues 285-290 suggested by pulsed HDX-MS. Interestingly, 4RD-Cysless behavior seems to dominate over wildtype tau4RD and makes tau4RD aggregation resistant to tryptanthrin inhibition when seeded with 4RD-Cysless (Fig. 4.5). While this work clearly demonstrates that Cys291 plays a key role in tryptanthrin inhibition, it does not reveal tryptanthrin's mechanism of action. Additional experiments are necessary to determine how Cys291 confers susceptibility to tryptanthrin inhibition; structural studies by HDX-MS or cryo-EM could be informative, as well as studies of chain dynamics such as smFRET or FCS. Together, the work presented in this dissertation expands our understanding of tau's aggregation and presents it as an enticing drug target.

5.3. References

(1) *Alzheimer's Facts and Figures Report | Alzheimer's Association*. https://www.alz.org/alzheimers-dementia/facts-figures (accessed 2025-02-26).

(2) *ADI - Dementia statistics*. https://www.alzint.org/about/dementia-facts-figures/dementia-statistics/ (accessed 2025-02-26).

(3) *Dementia*. https://www.who.int/news-room/fact-sheets/detail/dementia (accessed 2025-02-26).

(4) *World Economic Outlook (October 2024) - GDP, current prices*. https://www.imf.org/external/datamapper/NGDPD@WEO (accessed 2025-02-26).

(5) Knopman, D. S.; Amieva, H.; Petersen, R. C.; Chételat, G.; Holtzman, D. M.; Hyman, B. T.; Nixon, R. A.; Jones, D. T. Alzheimer Disease. *Nature Reviews Disease Primers 2021 7:1* **2021**, *7* (1), 1–21. https://doi.org/10.1038/S41572-021-00269-Y.

(6) Riederer, F. Donanemab in Early Alzheimer's Disease. *Journal fur Neurologie, Neurochirurgie und Psychiatrie* **2021**, *22* (3), 142–143. https://doi.org/10.1056/NEJMOA2212948/SUPPL_FILE/NEJMOA2212948_DATA-SHARING.PDF.

(7) Sims, J. R.; Zimmer, J. A.; Evans, C. D.; Lu, M.; Ardayfio, P.; Sparks, J.; Wessels, A. M.; Shcherbinin, S.; Wang, H.; Monkul Nery, E. S.; Collins, E. C.; Solomon, P.; Salloway, S.; Apostolova, L. G.; Hansson, O.; Ritchie, C.; Brooks, D. A.; Mintun, M.; Skovronsky, D. M.; TRAILBLAZER-ALZ 2 Investigators. Donanemab in Early Symptomatic Alzheimer Disease: The TRAILBLAZER-ALZ 2 Randomized Clinical Trial. *JAMA* **2023**. https://doi.org/10.1001/jama.2023.13239.

(8) Lecanemab in Early Alzheimer's Disease. *New England Journal of Medicine* **2023**, *388* (17), 1630–1632. https://doi.org/10.1056/NEJMC2301380.

(9) Avgerinos, K. I.; Manolopoulos, A.; Ferrucci, L.; Kapogiannis, D. Critical Assessment of Anti-Amyloid-β Monoclonal Antibodies Effects in Alzheimer's Disease: A Systematic Review and Meta-Analysis Highlighting Target Engagement and Clinical Meaningfulness. *Scientific Reports 2024 14:1* **2024**, *14* (1), 1–12. https://doi.org/10.1038/S41598-024-75204-8.

(10) Bandekar, P. P.; Roopnarine, K. A.; Parekh, V. J.; Mitchell, T. R.; Novak, M. J.; Sinden, R. R. Antimicrobial Activity of Tryptanthrins in Escherichia Coli. *Journal of Medicinal Chemistry* **2010**, *53* (9), 3558–3565. https://doi.org/10.1021/JM901847F/ASSET/IMAGES/LARGE/JM-2009-01847F_0003.JPEG.

(11) Agafonova, I. G.; Moskovkina, T. V. Studies on Anti-Inflammatory Action of Tryptanthrin, Using a Model of DSS-Induced Colitis of Mice and Magnetic Resonance Imaging. *Applied Magnetic Resonance* **2015**, *46* (7), 781–791. https://doi.org/10.1007/S00723-015-0674-3.

(12) Zou, Y.; Zhang, G.; Li, C.; Long, H.; Chen, D.; Li, Z.; Ouyang, G.; Zhang, W.; Zhang, Y.; Wang, Z. Discovery of Tryptanthrin and Its Derivatives and Its Activities against NSCLC In Vitro via Both Apoptosis and Autophagy Pathways. *International Journal of Molecular Sciences* **2023**, *24* (2). https://doi.org/10.3390/ijms24021450.

(13) Liu, X. R.; Rempel, D. L.; Gross, M. L. Protein Higher-Order-Structure Determination by Fast Photochemical Oxidation of Proteins and Mass Spectrometry Analysis. *Nat Protoc* **2020**, *15* (12), 3942–3970. https://doi.org/10.1038/s41596-020-0396-3.